FIRE PERFORMANCE OF COLD-FORMED STEEL WALLS

by

Jean Carlos Batista Abreu

A dissertation submitted to Johns Hopkins University in conformity with the requirements for the degree of Doctor of Philosophy

Baltimore, Maryland

August 2015

Abstract

Fire is an important hazard to be considered in structural design. Therefore, rapid growth in the building industry demands lightweight construction to satisfy standardized design criteria that include fire resistance. As envisioned, performance-based fire design involves the development of models capable of predicting fire demands, heat transfer, and structural response of building components.

This dissertation is intended to provide technical information on the behavior, modeling and design of cold-formed steel (CFS) subjected to fire, grounded on experimental studies and engineering-based numerical analysis of CFS materials, members, connections, and systems at elevated temperatures. The experimental program presented herein includes tensile tests on CFS materials typically used in American and Brazilian building industries; connection tests to determine the stiffness of stud-to-sheathing connections; and column tests on bare and sheathed studs at elevated temperatures. Numerical analysis using the finite strip and finite element methods aims to provide a better understanding of the behavior of CFS members under fire. Numerical results are validated with experimental data, and used to judge the feasibility of current Direct Strength Method (DSM) column equations for fire design applications.

Proposed models include equations to estimate the mechanical properties and stress-strain relations for CFS at elevated temperatures, and retention factors for the stiffness of stud-to-sheathing connections. Fire design of CFS based on modest modification to the current DSM is also proposed.

Temperature-dependent material models are applied to the numerical study of CFS partition and load-bearing walls, using temperature data from standard fire tests. Results show the development of thermal bowing of walls, and joint opening between sheathing boards under simulated standard fire test conditions. These results potentially provide feedback to couple thermal and mechanical analyses of CFS wall systems.

The findings of this work pertain the growth of engineering-based structural analysis method, as a building block for the development of performance-based fire design of CFS structures. Research needs are identified and listed in this document.

Readers:

Dr. Benjamin W. Schafer (Advisor)
Dr. James K. Guest
Dr. Judith Mitrani-Reiser

Acknowledgements

It was very exciting and challenging to come to this country to pursue my academic, professional and personal goals. The support and advise of several individuals and institutions made my journey successful and enjoyable.

First, I need to thank the Department of Civil Engineering at Johns Hopkins University for giving me the opportunity of developing my research skills and providing the resources needed to satisfy the objectives of my research project. I also thank US Gypsum Corporation, Fundo de Apoio ao Ensino, à Pesquisa e à Extensão (FAEPEX) and Fundação de Amparo à Pesquisa do Estado de São Paulo (FAPESP) for their financial support.

The expert guidance and enthusiasm of my advisor, Benjamin W. Schafer, was invaluable, as well as the support of my mentors Luiz C. M. Vieira and Shahab Torabian. The environment in the lab was great! So, thank you all. Special thanks to Judith Mitrani-Reiser and James K. Guest for raising interesting questions and comments during research meetings, and for serving in my thesis committee.

Thank you family for your unconditional support despite not fully understanding what I was doing during these four years. Thank you Oscar and Isaura for celebrating with me and cheering me up all the time. Many thanks Diana for listening to every story, and always being by my side. Finally you dear son, Alfonso, thank you for helping me not to miss the deadline.

Table of contents

List of figures

List of tables

List of equations

Chapter 1 – Introduction

Engineers design structures to satisfy multiple criteria, life safety being the most primordial. Several loading conditions and environmental actions are carefully considered so that structures will (at least) guarantee safety when critical conditions arise. Even though engineering-based methods have been established and developed to account for the effect of dead, live, and environmental loads (including snow, wind, and earthquakes), structural design for fire safety seems to stay in its infancy. This fact awakens curiosity and brings several questions. First and probably the most common question would be: “how necessary is it to consider fire in structural design?” The answer to this question might be as simple as follows. The Federal Emergency Management Agency (FEMA) through the United States Fire Administration (USFA) has been publishing “Fire Estimates Summary” reports, based on data collected from all 50 states and the District of Columbia, currently participating in this effort. These reports provide statistics on overall fires and fire losses, related to property types, causes and consequences (Figure 1-1). For instance, estimates indicate that 364.5 thousand residential building fires occurred in 2011. This quantity corresponds to 29.1% of all fires occurring in the United States of America during the same year, being “outside fires” the most common (44.0% of all fires). Interestingly, “outside fires” contribute to only 2.3% of the deaths, 3.2% of the injuries and 7.8% of the losses. Residential building fires contributed to 75.7% of the deaths, 79.1% of the injuries and 52.2% of the losses. These percentages are equivalent to 2,450 deaths, 13,900 injuries and $6,651.4 millions lost in 2011 alone. As a reference, the 1906 San Francisco earthquake (and fire) -considered as one of the worst disasters in U.S.A. history- caused about 3,000 deaths; however, earthquakes with similar magnitude and intensity have return periods of a couple of hundred years. Other significant earthquakes occurred in the U.S.A. after the 1906 San Francisco earthquake caused as many as 165 deaths (i.e. the 1946 Alaska earthquake). Therefore, the number of fatalities due to residential fires is considerable and alarming. Daily activities such as cooking and smoking are identified as some of the main reported causes of fires in residential buildings.

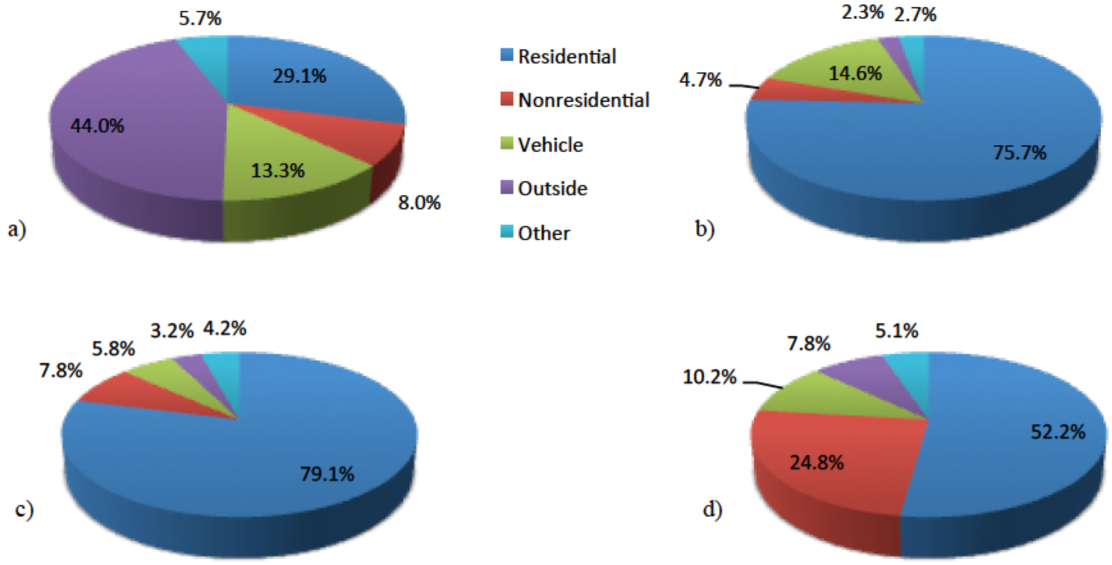

Figure 1-1: Fire loss in the United States during 2011 (FEMA, 2012). Percent of a) fires by general property type, b) deaths, c) injuries, and d) dollar loss (adjusted to 2011 dollars)

In general, fire protection can be provided through active and passive systems, and education. Active fire protection consists of items and systems that require an excitation to be activated, such as extinguishers, sprinklers and smoke detectors. Passive protection is provided by means of components that contain fires and slow their spread without the need of activation. Typical examples of passive fire protection systems are fire-resistant walls, floors and doors. Education is also a main component of fire protection; it includes the spread of information regarding the functioning of passive and active fire protection, and the development of a fire safety plan. Active and passive systems can provide redundancy, and they are also seen as complementary and not mutually replaceable. To illustrate this idea, consider the 1906 San Francisco earthquake and fire. By far, most of the damage and fatalities were due to the spread of uncontrolled fires propitiated by the lack of water after water main breaking during the shake. Under this situation, passive fire protection could control the spread of fires in building with no severe structural damage. In other extreme cases, the interaction of active and passive systems can be even detrimental if not contemplated in design. For instance, consider a compartment subjected to fire where sprinklers activate to extinguish the flames, but (simultaneously) saturate and deteriorate the gypsum of fire-resistant walls.

Now, how do we design passive fire protection systems? For many decades, passive fire protection has been based on prescriptive design, grounded on experimental results from standardized fire tests on individual assemblies. Specimens (with dimensions limited by testing conditions) are subjected to a time-temperature curve known as the "standard fire", which was developed based on conditions that reflect building constructions from about one century ago. Criticism regarding standard fire tests includes the advantage of having a consistent method to characterize systems based on the amount of time in which such systems are able to withstand the "standard fire" (i.e. fire rating). Contrastingly, standard fire tests do not seem to reflect the actual demands on typical building systems (including heating rates and peak temperatures), and do not account for the actual capacity of interconnected components able to transfer and redistribute loads in a system. Despite these significant limitations (among others discussed in this dissertation), prescriptive fire design predominates nowadays. Several catalogs provide information about the configuration of passive fire protection systems, including framing layout, bracing and sheathing to “guarantee” the stated fire ratings.

A different approach is embodied by performance-based fire design. This design method seeks to provide design solutions in response to predetermined objectives, including safety, functionality and economy. Safety is related to the level of fire protection needed, and could be defined based on the establishment of failure criteria such as insolation failure (e.g. lack of prevention of significant temperature increase in adjacent compartments), integrity failure (e.g. inability to containment of flames and smoke), and instability (i.e. partial or total collapse). Functionality is also a major design objective that denotes the ability of the structure to perform its intended nonstructural use after fire. Different criteria could be adopted to assess levels of functionality of systems, from fully operational conditions to partially functional, or even dysfunctional. Another main objective is to provide cost-effective design solutions (i.e. economy) considering the initial investment on fire protection systems, and the costs of maintenance and post-fire repairs. All these aspects are directly or indirectly related to the design and response of structural components, as well as nonstructural components. For example, the design of structural studs belonging to a load-bearing wall that is a main component of the fire protection system directly focuses on providing a cost-effective solution so that the subsystem does not collapse or compromises the functionality of the structure in case of fire. Safety may not be guaranteed if the gypsum boards crack, losing integrity and directly impacting on the load-carrying capacity of the studs by exposing them to higher temperatures, while losing the lateral restraint provided by sheathing boards. Therefore, the design of both, structural and nonstructural components is essential.

Performance-based fire design is generally seen as a sequence of processes starting with the definition and characterization of the hazard, normally based on some type of a fire model directly related to the characteristics of the structure to be designed (e.g. ventilation, amount of combustible materials, geometry, etc.). Then, heat transfer analysis is pursued to estimate the temperature field on structural and nonstructural components over time, based on the predetermined fire hazard, building geometry, and thermal properties of materials. Finally, the mechanical behavior of the structure is evaluated; considering temperature-dependent mechanical properties and other thermal effects based on the temperature history obtained from the heat transfer analysis. Therefore, the processes are unidirectional and sequentially coupled. However, this schema is only representative until the mechanical behavior takes a leading role on the system response. For instance, consider the following common but complex scenario. A partition wall is subjected to fire from one side; therefore, heat conduction occurs through the exposed gypsum boards and screws. In the wall cavity, rapid heat conduction occurs through the steel studs, and radiation and convection contribute to the increase of temperature on the unexposed gypsum boards. Meanwhile, gypsum boards dehydrate and therefore change their thermal and mechanical properties. Moisture migrates inside and outside the cavity, developing thermal gradients in the wall components. The paper sheets enclosing the gypsum cores eventually burn, allowing the gypsum boards to crack and fall-off. Due to increasing non-uniform temperature, the steel studs bow towards the heat source, opening the joints between gypsum boards, and consequently allowing flames and smoke to pass through the wall, and compromising the pre-established design objectives, including life safety. In this case, the mechanical response directly impacts the heat transfer. In a building system, deformations of structural components may lead to fracture of glass windows (for instance), allowing the fire to obtain more oxygen and grow. Therefore, the structural response may also impact and reshape the hazard. Additionally, the fire hazard and the structure are influenced by the emergency response system and the action of people during evacuation.

Although the problem is complex and includes coupled components (i.e. hazard, heat transfer and mechanical response), a simple performance metric such as time could be very powerful. Ideally, the design could answer questions related to the amount of time available to evacuate occupants, control or suppress the fire, and recover building and infrastructure functionality after a fire.

Under the broad topic presented in this introduction, this dissertation focuses on the response of cold-formed steel (CFS) structural and non-structural components at elevated temperatures. CFS assemblies are commonly used as primary passive fire protection systems, and therefore they are experimentally and numerically studied herein. This opening chapter provides an overview of the work presented in this dissertation, establishing research objectives, and presenting the methods used in this work.

1.1 Outline

Cold-formed steel (CFS) members are manufactured from cold bent sheet steel, approximately from 0.5 mm to 3.0 mm thick. The most common members are channels (tracks) and lipped channels (studs and joists), in addition to “Z”, tubular and hat sections. CFS stud and track are used extensively in buildings as the framing for interior partition walls, exterior curtain walls, and more recently as the complete load-bearing system (Allen 2004; Schafer 2011). CFS interior partition walls are framed with studs, have tracks at top and bottom, and are sheathed (most commonly) with gypsum wallboards (Figure 1-2). During a fire, partition walls serve as primary barriers to maintain building integrity and stability, and avoid the spread of fire and smoke between compartments. These wall assemblies are required to be “fire-rated” based on their ability to withstand a standardized “fire” test. The fire-resistance rating is expressed by the number of hours that the assembly maintains its integrity while containing gases and excessive temperature increases out of the compartment.

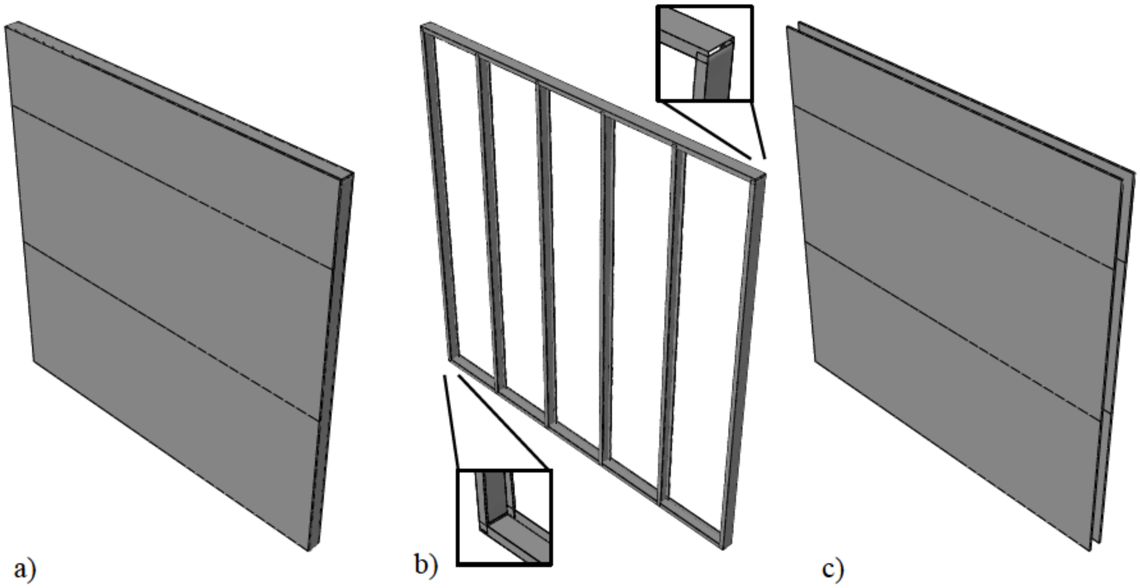

Figure 1-2: Cold-formed steel assembly, a) wall, b) CFS frame and c) sheathing boards

Industry has developed catalogs for prescriptive fire design based on experimental results from standard fire tests. From the catalogs, wall layouts and materials can be selected to provide a required fire rating (CFSEI 2012). These prescriptive solutions are critical to current design and represent an important review of the state of the art in their own right; however, the focus of this work is on enabling performance-based fire design, not additional prescriptive solutions.

To date, fire design for load-bearing CFS systems (where the complete structural system is framed from CFS members) has followed the same test-based, prescriptive detail driven approach that has been previously established for interior partition walls. However, given the wide variety of possible members and details, the prescriptive approach has several drawbacks, as discussed in Chapter 2. In addition, hot-rolled steel has demonstrated the possibilities and advantages of enabling performance-based fire design.

Recent research has taken the first steps towards establishing performance-based fire resistance of structures, including temperature-dependence of materials behavior, and thermal and structural response of members and sub-systems. Focusing on CFS walls, this dissertation is devoted to the study of CFS materials, connections, members and assemblies at elevated temperatures, to enable engineering-based analysis and design for fire.

1.2 Objectives

In general, this work focuses on the structural response of CFS wall components and systems at elevated temperatures, aiming to provide models to estimate material and connection behavior suitable for the analysis and design of CFS members and systems subjected to fire. The work presented in this dissertation intends to contribute towards the development of engineering-based structural analysis of CFS at elevated temperatures, as an essential building block for performance-based fire design.

The general objectives of this work are to:

- Characterize the temperature-dependent mechanical behavior of CFS materials commonly used in the building industry
- Study the degradation of stud-to-sheathing connections due to increasing temperatures
- Experimentally evaluate the response of bare and sheathed CFS members at elevated temperatures
- Provide advanced modeling of CFS wall systems subjected to fire, capable of generating meaningful feedback for heat transfer analysis, and potentially useful for future coupled thermo-mechanical analysis
- Evaluate the feasibility of current design methods for fire design of CFS
- Identify research needs for developing performance-based fire design of CFS

Specific objectives of this work include to:

- Develop temperature-dependent sets of equations to model the mechanical response of CFS material and connections
- Generate temperature-dependent stress-strain models for CFS material
- Provide a practical fire design solution based on current DSM formulation
- Estimate the magnitude and shape of thermal deformations in CFS walls subjected to fire for future coupled thermo-mechanical analysis
- Estimate the magnitude and shape of joint opening in walls under thermal gradients for future coupled thermo-mechanical analysis

1.3 Methods

In general, experimental work form the foundation of the work presented herein. Experiments were carried out in the structures laboratories at University of New Haven, in Connecticut, and University of Campinas, in Brazil. The experimental work includes 28 tensile tests, 40 column tests, and 54 connection tests at elevated temperatures. Numerical work using the finite strip method (Li and Schafer 2010) and finite element methods (ABAQUS 2013) were performed in the Thin-walled Structures Laboratory, at Johns Hopkins University, in Baltimore.

1.4 General overview

Literature review, results from experimental and numerical work, and proposed models and design are presented in the following chapters, and briefly summarized as follows.

Chapter 2 is a state-of-the-art review that discusses current research and recent findings on the fire performance of CFS. It includes results from experimental, numerical and analytical work to understand the response of CFS material, members and systems at elevated temperatures. The feasibility of current design methods and new proposed design methodologies are presented and evaluated in this chapter, and research needs are identified.

Chapter 3 presents an experimental work performed to characterize the mechanical behavior of CFS at elevated temperatures. This chapter describes the experimental program executed to obtain CFS temperature-dependent stress-strain relations, elastic modulus, yield stress and ultimate stress. CFS materials studied include ASTM A-653 and ZAR-345, with nominal yield stresses of 33 (230 MPa) ksi and 50 ksi (345 MPa). Retention factors for the mechanical properties of CFS are provided.

Chapter 4 depicts the experimental work completed to study the structural response of short and intermediate-length CFS bare and sheathed studs at elevated temperatures, up to 600°C. Sheathing materials included oriented strand boards, regular gypsum boards, and fire-rated gypsum boards. Experimental results show that sheathing potentially increases the axial strength of thin-walled studs, especially when distortional and global buckling modes have significant participation in their structural response. While temperature increases, CFS mechanical properties degrade, and the impact of sheathing bracing in the strength and stiffness of studs decays. Therefore, initially sheathed studs respond similar to bare studs at high temperatures. The suitability of current DSM equations along with empirical temperature-dependent mechanical properties to estimate the load-carrying capacity of CFS studs at uniform elevated temperatures is evaluated. This chapter shows that current design methods seem promising for performance-based fire design of CFS structures.

Stud-to-sheathing connections at elevated temperatures are experimentally studied in Chapter 5. Results from steady state in-plane fastener stiffness tests, and pull-through fastener stiffness tests are presented and discussed. Sheathing materials studied are similar to the materials used for stud tests in Chapter 4. This chapter aims to characterize the degradation of stud-to-sheathing connection stiffness with increasing temperature, and provide temperature-dependent retention factors to account for temperature effects when designing CFS sheathed studs following a recent methodology proposed by Schafer (2013), based on the work of Vieira (2011) and Peterman (2012).

In Chapter 6, proposed material and connection models from Chapters 3, and 5 are used to numerically study the behavior of bare and sheathed studs. First, sets of temperature-dependent equations are proposed to estimate strength and stiffness retention factors for CFS material and connections. Then, these equations are used to analyze the response of CFS members and estimate their load-carrying capacity at elevated temperatures. Numerical results from finite element models, and predictions from current DSM equations with proposed mechanical properties are compared against the experimental results presented in Chapter 4. The feasibility of current DSM equations to estimate the load-carrying capacity of sheathed members is judged, and design recommendations are presented.

Modeling recommendations presented in previous chapters are applied to the analysis of CFS partition and load-bearing walls at simulated standard fire test conditions, in Chapter 7. Advanced modeling through the finite element method is used to study the response of CFS systems at elevated temperatures. Numerical results are compared to experimental data provided by industry. The finite element models are capable of simulate material degradation with increasing temperature, and develop similar thermal deflections compared to experimental results. Commonly, structural model are sequentially coupled because they follow the results (e.g. temperature distributions) obtained from a heat transfer analysis, and no feedback is given from the structural response to the heat transfer. The advanced structural model presented in this chapter is capable of generating important feedback to thermal models, by providing estimates of the thermal bowing of walls, and the magnitude and shape of joint openings over time. This data potentially serves as a new source of information to feed models that predict the heat transfer through CFS systems without the need of arbitrarily calibrating thermal properties of materials.

Summary of research findings are provided in Chapter 8. Also, research needs are identified and presented.

References

American Institute of Steel Construction (AISC). Steel Construction Manual, Thirteen Edition. Appendix 4: Structural Design for Fire Conditions. United States of America, 2008.

American Society for Testing and Materials, ASTM E119-79, Standard Methods of Fire Tests of Building Construction and Materials.

International Code Council. (2012). International Building Code. Chapter 6. U.S.A, Country Club Hills, IL.

ABAQUS (2013). ABAQUS 6.13 Documentation. Providence, RI, USA.

Allen, D. (2004). Designing Cold-Formed Steel Mid-Rise Structures: Innovations for Cost-Effective and Attractive Projects. Structure: 17-19.

CFSEI (2012). Technical note on cold-formed steel. TECH-NOTE T100-12: Fire rated assemblies of cold-formed steel construction. Washington, DC.

Li, Z. and B. W. Schafer (2010). Buckling analysis of cold-formed steel members with general boundary conditions using CUFSM: conventional and constrained finite strip methods. Twentieth International Specialty Conference on Cold-Formed Steel Structures Saint Louis, Missouri, USA.

Peterman, K. D. (2012). Experiments on the stability of sheathed cold-formed steel stud under axial load and bending. M.S. Essay. Department of Civil Engineering, Johns Hopkins University.

Schafer, B. W. (2011). "Cold-formed steel structures around the world." Steel Construction 4(3): 141-149.

Schafer, B. W. (2013). Final Report: Sheathing Braced Design of Wall Studs. Washington, DC., Johns Hopkins University, prepared for the American Iron and Steel Institute.

Vieira, L. C. M. (2011). Behavior and design of sheathed cold-formed steel stud walls under compression. Civil Engineering Department. Baltimore, MD., Johns Hopkins University. Doctor of Philosophy.

Chapter 2 – Fire performance of cold-formed steel material, members and systems

CFS systems have become popular in building construction as both load-bearing and non-load-bearing, primarily due to their high strength-to-weight ratio and ease of construction. Consequently, design specifications and structural analysis tools have rapidly evolved to facilitate engineering design of these complex thin-walled members. However, in fires, prescriptive detailing and standardized testing assure the performance of CFS systems. Today, engineering knowledge is rapidly advancing, providing the opportunity to contemplate analysis-based design as an enabling tool for general performance-based engineering of CFS systems for fire.

This chapter combines and critiques existing research on CFS material, members, and assemblages at elevated temperatures; and complementary analysis and design methods necessary for the development of analysis-based design for CFS systems under fire. This review includes experimental results on mechanical and thermal properties, subsystem testing and computational simulations, and analysis models and exploratory methods for fire design, i.e., the building blocks towards performance-based fire design for CFS systems.

2.1 Fire demands and heat transfer analysis of cold-formed steel systems

Fundamental to determination of the fire resistance is establishing the fire demand and then propagating that demand to the underlying members. Ideally, performance-based fire design brings the demand (fire modeling), propagation (heat transfer), and capacity (strength at elevated temperatures) all into the realm of analysis. In such a situation the complete system may be designed for the desired fire performance with interactions between demand, propagation, and capacity fully included through analysis. Although the focus of this review is on capacity, demand and heat transfer is briefly reviewed here to establish the conditions under which the capacity is evaluated.

2.1.1 Fire demand

One of the first formal attempts to account for fire action on building structures emerged in 1918, when the ASTM standardized a time-temperature relationship (called the fire curve) to consistently evaluate the fire resistance of buildings. The fire curve was intended to represent a worst-case expected fire scenario, based on empirical data from timber construction (ASCE 2009). Similar time-temperature relationships have been implemented internationally. Typically, the fire curve seems weakly related to the actual time-temperature curve for a fire in a modern building. However, standard fire curves provide a consistent benchmark and their use is so pervasive that generally they are regarded as "fire demand" regardless of the specifics.

Parametric fire curves represent a modest generalization of the fire curve approach (EN 1991-1-2:2002). Typically, it is assumed that a building compartment is subjected to a uniform temperature distribution that follows the parametric fire curve. The curves include factors related to the compartment dimensions, size and number of openings, and amount of combustible materials, and result in a unique intensity and duration for the fire.

In general, parametric fire curves include a nonlinear heating phase followed by a linear cooling phase, while the standard fire is represented by an increasing curve (Figure 2-1).

Significant differences are observed between the standard fire, parametric and real fires. First, the duration of the standard fire is not specified. Instead, the temperature increases over time up to 1260 °C at 8 hours of fire exposure, and then it remains constant. However, temperatures eventually decrease in real (and parametric) fires. Also, the severity (i.e. measure of the fire intensity and duration) of the standard fire is unspecified, given that the standard curve does not decay. Additionally, the fire intensity (i.e. temperatures) and heating rates observed in real fires and standard fire curve are very different, given that the latter does not account for important factors such as the geometry of the compartment, actual fire load (both type and amount), ventilation (both size and location), ambient conditions (e.g. humidity), and thermal properties of materials.

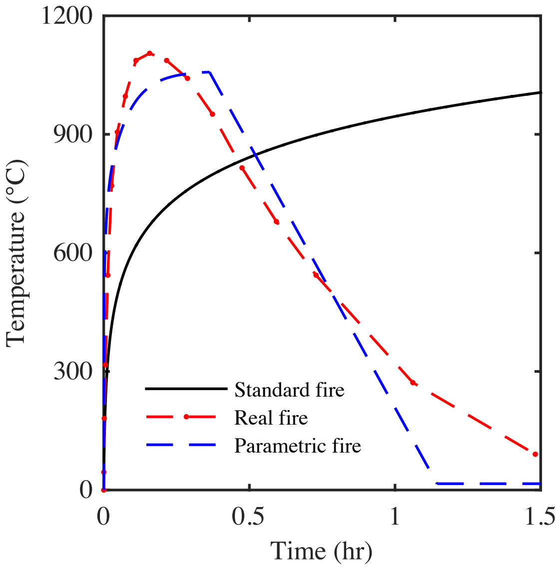

Figure 2-1: Example time-temperature fire curves

A further evolution of parametric fire curves is the use of “zone models” (Quintiere 1989). In zone models, the compartment is divided into multiple regions, each with its own uniform temperature distribution following a parameterized fire curve. Amongst other details, these models account for the fact that higher temperatures are observed in the upper zone of the compartment. The most sophisticated simulations adhere to computational fluid dynamics and at some level attempt to model actual fire dynamics. These models are used to predict the development of fire in a building structure (including fully three-dimensional models), incorporating flames and smoke propagation. Computational fluid dynamics simulations are complex; require a high level of expertise and relatively long computation times. Nonetheless, true performance-based design of fires relies on the long-term potential of this approach. Multiple software solutions are in current use, including PHOENICS (Spalding 1978), FDS (McGrattan 2002), SMARTFIRE (Ewer et al. 2008) and SOFIE (Rubini 2006).

2.1.2 Heat transfer

Once the thermal fire demands are established the next step is to propagate these demands to the structure itself through heat transfer analysis. For an actual fire, temperature distributions on CFS members are non-uniform and vary through the cross-sections and along the length. Fully three-dimensional heat transfer models of CFS assemblages are possible (Santos et al. 2013), but not common. Instead, simplified one-dimensional heat transfer models are generally used to estimate the temperature history across assemblages (walls, floors, etc.) subjected to fire action on one side (Sultan 1996; Alfawakhiri 2001; Keerthan and Mahendran 2013; Chen et al. 2013). These models require accurate thermal properties of all materials in the assemblage. Generally, the heat conduction through and radiation from the steel studs are ignored, and shrinkage, cracking and ablation processes of the gypsum boards are not explicitly modeled, although their effects are considered by modifying material thermal conductivity and specific heat. Also, moisture migration and hot air flow are ignored, thus thermal gradients along the length of the assemblage (i.e., height of the wall) are ignored. It is also common to make the simplifying assumption that the temperature varies linearly throughout the web of the CFS member in the assemblage, while the temperature of the flanges and lips are constant (Shahbazian and Wang 2013). See Section 5.2 for further discussion of modeling heat transfer in CFS assemblages.

2.2 Cold-formed steel material at elevated temperatures

During a fire, the temperature of structural members increases and, subsequently, material properties change. Mechanical properties of steel such as the elastic modulus, yield stress, and ultimate stress degrade with increasing temperature, thus steel members lose strength and stiffness. Thermal properties also vary with temperature, e.g. steel incurs phase transformations under highly elevated temperatures that significantly alter thermal response. Quantification of the temperature dependence of thermal and mechanical properties of sheet steel is a fundamental building block for predicting the response of CFS under fire.

2.2.1 Mechanical properties

Several research groups have studied mechanical properties of sheet steel at elevated temperatures (Lee et al. 2003; Chen and Young 2007; Ranawaka and Mahendran 2009a; Kankanamge and Mahendran 2011; Chen and Ye 2012). In general, tested specimens range from 0.50 mm [0.0188 in.] to 2.00 mm [0.0713 in.] thick, with yield strengths from 250 MPa [36 ksi] to 550 MPa [80 ksi] at ambient temperature. A typical experimental setup utilized by Chen and Ye (2012) is shown in Figure 2-2, including a MTS 810 for load application, a high-temperature axial extensometer MTS 634.25F-24 and temperature meters. Normally, the experimental results are presented as retention factors, which are ratios of a material property at elevated temperature with respect to the same property at ambient conditions. Retention factors vary among research efforts (Figure 2-3) and the proposed prediction equations differ as well (Figure 2-4). Differences are mainly attributed to the test method, strain rate, heating rate, material grade, and the criteria used to determine the yield stress - as discussed further below.

Tensile tests at elevated temperatures are traditionally conducted by either (a) steady-state, or (b) transient-state testing. During steady-state tests, the temperature on the specimen is increased to a given level and then, after the temperature becomes stable, external load is gradually applied until failure occurs. In contrast, during transient-state tests, the load is statically applied to the specimen, and the temperature is gradually increased until a failure criterion is met.

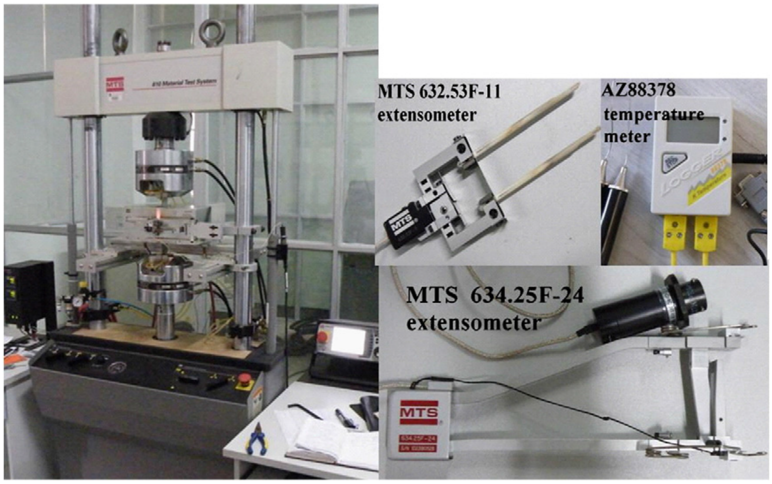

Figure 2-2: Experimental setup for steady-state and transient tests from Chen and Ye (2012)

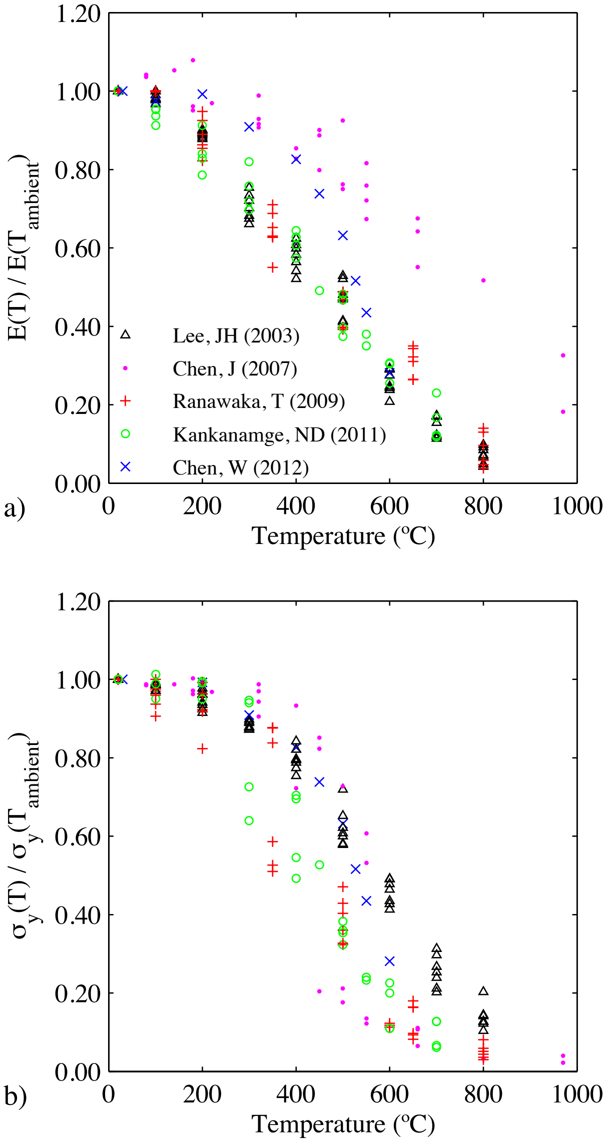

Figure 2-3: CFS retention factors for (a) elastic modulus and (b) yield strength from steady-state tests

Although the steady-state test is more popular (and generally easier to conduct), the transient-state test is considered more realistic as it is consistent with a member under an applied static load (e.g. a gravity loaded column) undergoing temperature increase, as in a fire (Outinen and Mäkeläinen 1999). In general, transient-state tests show a higher degradation than steady-state tests, e.g. see the retention for Young's modulus in Figure 2-5-a. Though common, the use of retention factors from steady-state tests may lead to overestimated stiffness and strength (Chen and Ye 2012).

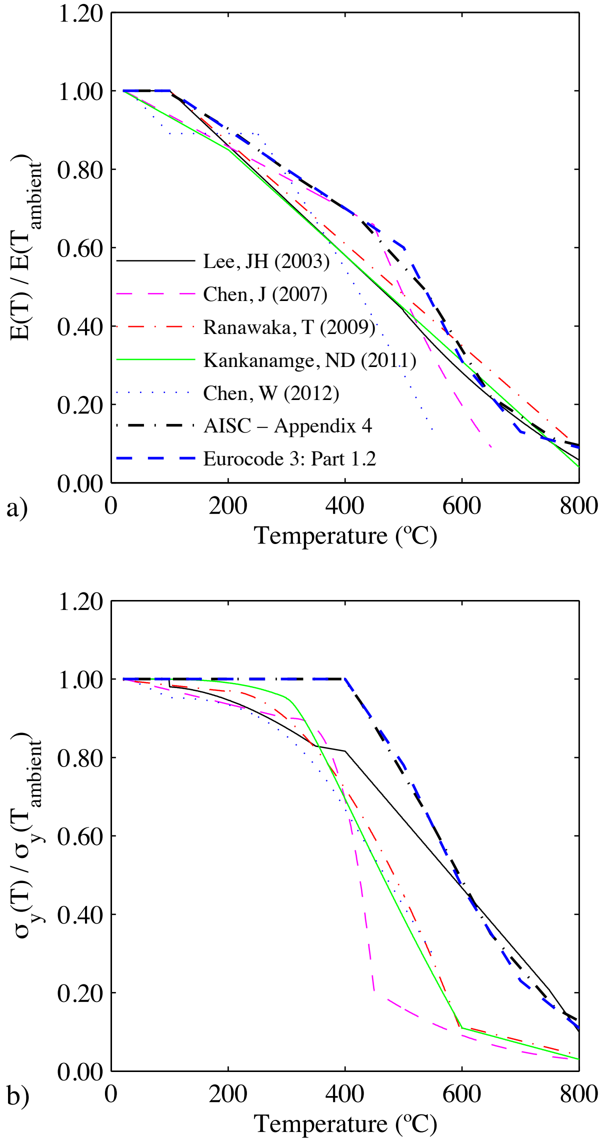

Figure 2-4: Proposed retention factors for (a) elastic modulus and (b) yield strength of steel

Strain rate, typically not influential for sheet steel at ambient temperatures under common loading or testing rates, might influence the results in strain-controlled steady-state tests at temperature. Figure 2-3 shows that retention factors obtained using a strain rate of 0.006 min^{-1} (Chen and Young 2007) are higher than the factors obtained using strain rates at about 0.003 min^{-1} (Lee et al. 2003; Ranawaka and Mahendran 2009[a]; Kankanamge and Mahendran 2011; Chen and Ye 2012). In general, higher strain rates lead to higher (stiffer) response (Cooke 1988). Additionally, retention factors for yield stress based on high strain rates often lead to yield and ultimate strengths at similar magnitudes (Kankanamge and Mahendran 2011). Thus, some care must be taken to insure strain rate is consistent with expected final use, when establishing retention factors.

High heating rates may also induce high strain rates during the heating process in transient-state tests (Outinen 2006). Expected heating rates for structural steel members with 2 hour fire rated protection and unprotected sections are approximately 5.0 ± 2.0 °C/min and 32.5 ± 7.5°C/min, respectively (Kodur et al. 2010). Typically, heating rates adopted in transient-state tests on CFS specimens vary from 10 to 20 °C/min. These values are not necessarily within the expected range during a fire, or even considered in computational simulations to predict the response of CFS structures. Figure 2-5-a shows that retention factors obtained using a heating rate of 100 °C/min (Chen and Young 2007) are higher than the factors obtained using 20 °C/min (Chen and Ye 2012). High heating rates result in high-predicted strengths since material damage may be delayed under rapid temperature increases (Bednarek and Kamocka 2006). Also, during tensile tests, the temperature is assumed to be uniform in the specimen, so it is important to provide enough time to stabilize the temperature and avoid significant thermal gradients. When the heating rate is high, it is more difficult to accurately monitor the temperature and guarantee a uniform distribution. In addition, heating rate alters the creep effect in sheet steel (Outinen 2006).

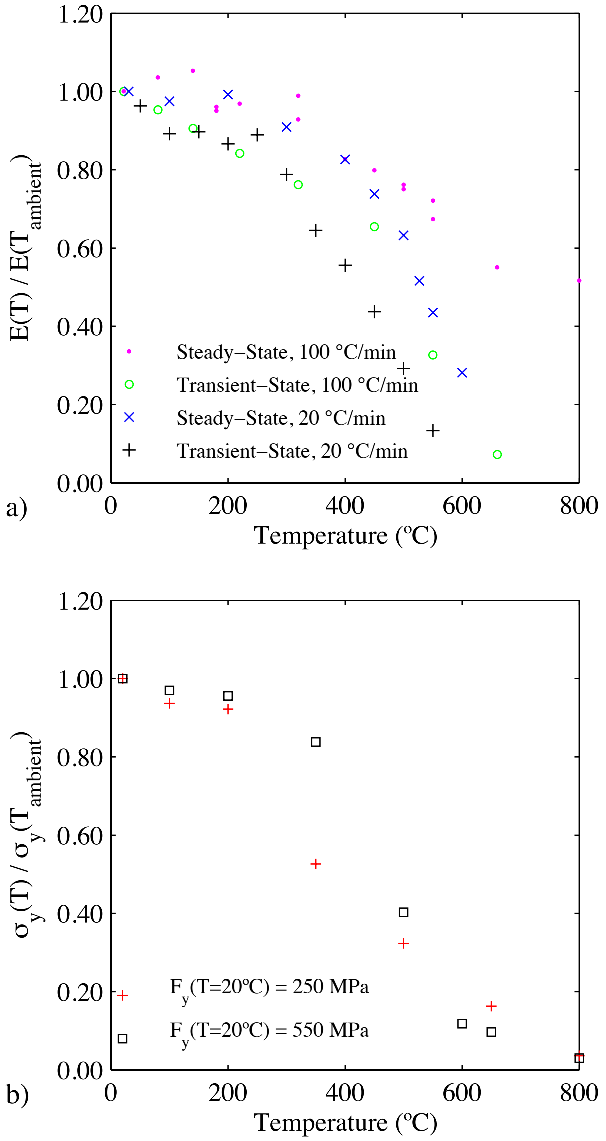

Figure 2-5: CFS retention factors for (a) elastic modulus from steady state and transient state tests, and (b) yield strength for different steels.

It has been posited that differences in chemical composition lead to different retention factors as a function of steel grade (Ranawaka and Mahendran 2009[a]). Young's modulus shows little dependence on steel grade, but retention factors for yield stress show a more complicated dependence. Researchers report that high strength steel (i.e. $F_y \sim 550$ MPa) is more efficient than common (low strength) steel grades at about 400 °C and above (Lee et al. 2003). However, the available experimental data is limited, and mixed. As shown in Figure 2-5-b, the transition temperatures from high to low retention factors may be different depending on steel grade, but overall retention factors for yield stress are similar across grades. Determining yield stress retention factors is itself dependent on strain level, heat level, and the formal method for determining yield stress. The retention factors vary according to the yield point and yield strain definitions. Usually, the yield point is based on the 0.2% offset strain. However, other offset strains might be adopted to define the yield point. For instance, AISC 2010 (Appendix 4) provides yield stress retention factors for hot-rolled steel based on 2% offset strain. In general, the larger the offset strain used to define the yield point, the closer the retention factors for yield and ultimate stresses are. Future work should fusion the actual material behavior in terms of material structure and phase transformations with the shape of the curves used to represent the degradation of mechanical properties with increasing temperatures.

Generally, temperature-dependent constitutive relations are based on the Ramberg-Osgood (1943) model:

$$\varepsilon(T) = \frac{\sigma(T)}{E(T)} + K(T)\left(\frac{\sigma(T)}{F_y(T)}\right)^{n(T)} \qquad \text{(Equation 2-1)}$$

Where $\varepsilon(T)$, $\sigma(T)$, $E(T)$ and $F_y(T)$ are the strain, stress, Young's modulus and yield stress at a temperature T (°C), respectively; and, K(T) and n(T) are parameters obtained from regression analysis. The Ramberg-Osgood strength coefficient, K(T), proposed by Chen and Young (2006^a; 2007) and Chen and Ye (2012) is 0.2%. According to temperature-dependent equations proposed by Mahendran and his colleagues, K(T) ranges from 0.08% to 0.31% (Ranawaka and Mahendran 2009a; Kankanamge and Mahendran 2011). In all cases, the 0.2% offset method was used to compute the yield stress used in Ramberg-Osgood equations. At ambient temperature (around 25 °C), typical Ramberg-Osgood hardening coefficients n(T) for cold-formed stainless steels range from 4.5 to 12.2 (Rasmussen 2003). However, n(T) computed from temperature-dependent equations ranges from 17.2 (Chen and Young 2007) to 57.6 (Ranawaka and Mahendran 2009a) at ambient temperature, for CFS carbon steel G550, under steady-state testing conditions. According to proposed equations, n(T) tends to decrease with increasing temperature, up to 450 °C. Then, up to 800 °C, n(T) ranges from 4.6 (Chen and Young 2007) to 24.8 (Chen and Ye 2012). Clearly, more work is needed to clarify the correct application of Ramberg-Osgood expressions under temperature for low carbon sheet steels.

Current steel design codes (AISC 2010; EN 1993-1-2:2005) provide retention factors for mechanical properties of steel at elevated temperatures, as shown in Figure 2-4. General trends for CFS specimens are consistent with the wider database of tested hot-rolled steels, but material and test method dependent scatter exists and, in some cases, particularly around 400°C, observed reductions of yield stress are far greater in CFS than in the code-based expressions for hot-rolled steel.

The manufacturing process for CFS sections can create significant changes in the material properties, particularly near the corners, in a phenomenon typically referred to as cold work of forming. This additional cold work of forming strength is gradually lost with increasing temperatures (Mäkeläinen and Outinen 1998; Lee et al. 2003), and completely disappears above 500°C (SCI 1993). However, CFS maintains its nominal yield strength without cold work of forming after heating and cooling (Outinen and Mäkeläinen 2004).

Other material properties such as density and Poisson's ratio of steel are commonly assumed to be constant (Kaitila 2002). Nevertheless, mass density slightly decreases (Costes 2004) and Poisson's ratio increases (Clark 1953) with temperature (see Figure 2-6). Prediction equations for the Poisson's ratio of CFS are not available; however, working directly from the available data may be useful to infer other constitutive parameters, such as shear modulus.

Significant limitations exist with the available data. At the most basic level, for use in the United States, the tested CFS does not conform to ASTM A1003 as specified in AISI S200-12. Further, the impact of temperature on residual stresses and strains has seen only limited study (Feng et al. 2003a; Lee et al. 2003). Since the cold-working process influences both explicit design expressions (cold work of forming) and implicit design expressions (the basic column curve) the impact of temperature (potentially similar to annealing) could be influential. The relatively common practice of cold-reducing the steel to a desired thickness has also not seen separate study for its effect on properties under temperature. CFS creep effects and behavior after the cooling phase have been scarcely studied (Outinen 2006). Moreover, unresolved issues at ambient temperature such as the difference in tensile and compressive yield strength in CFS (Karren 1970; Uribe 1969) also become more important as attempts to predict capacity are advanced.

In summary, research needs related to the mechanical properties include determining suitable heat rates that represent realistic fire conditions to study the material response during the heating and decaying phases of fire, and after cooling down. The influence of heat and load (or strain) rates on the mechanical properties at high temperatures needs to be studied, so that the advantages and disadvantages of different types of test (i.e. steady-state and transient) are better comprehended.

Attention should be paid to the chemical composition of specimens tested since the mechanical response seems to differ among different materials, and even for the same material before and after the cold-reducing process. Since mechanical properties at elevated temperatures might depend on the loading conditions, compression tests are also needed for material characterization. Data needs also include the Poisson's ratio, shear modulus, and characteristic stress-strain relations of CFS at elevated temperatures.

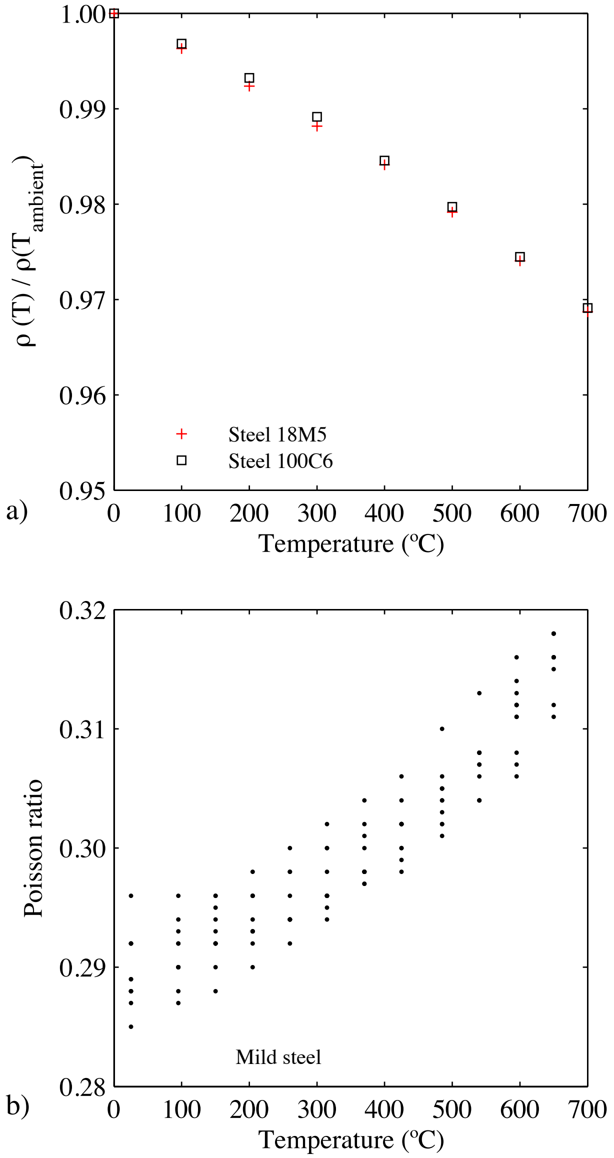

Figure 2-6: Temperature dependence of steel (a) density and (b) Poisson's ratio

2.2.2 Thermal properties

Thermal properties govern heat transfer and thermal deformations. Though important, they have seen less study than mechanical properties by the structural engineering community. At highly elevated temperature, steel may suffer a pearlite to austenite phase transformation, changing its internal crystal structure from body-centered cubic to face-centered cubic. During this transformation, no significant elongation (Chen and Ye 2012) or contraction (Cooke 1988) is observed. The temperature ranges at which these changes occur are sensitive to the chemical composition of the steel, but are generally high, and often higher than the temperatures at which structural failure is reached (Cooke 1988).

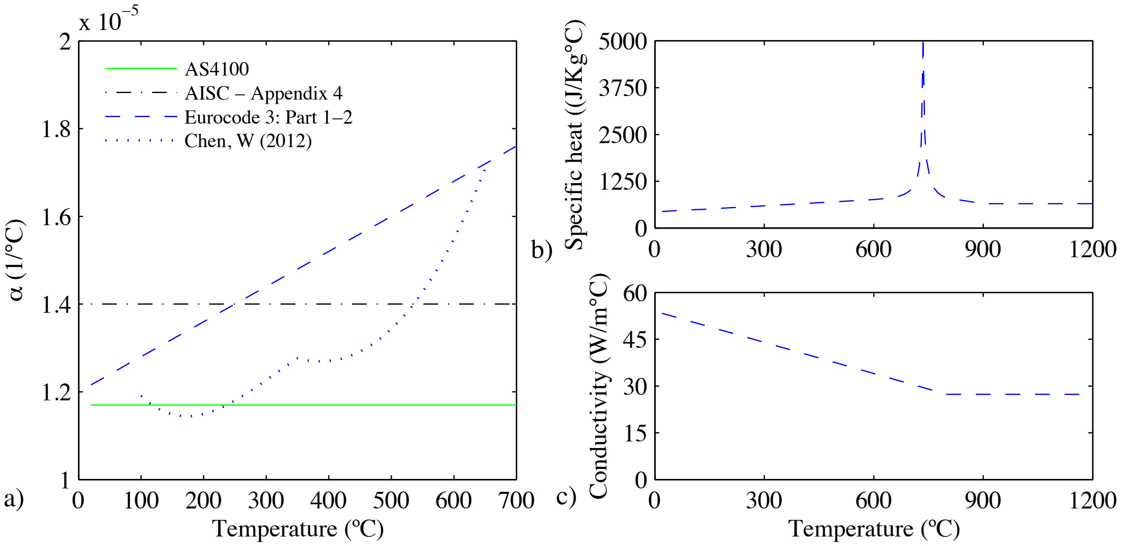

Figure 2-7: Steel at elevated temperatures (a) Thermal expansion coefficient, (b) specific heat, and (c) thermal conductivity

As illustrated in Figure 2-7, at temperatures below the phase transformation in carbon steel, thermal strains grow nonlinearly with increasing temperature; heat capacity increases with increasing temperature; and, conductivity decreases with increasing temperature. As shown in Figure 2-7-a, it is common in some codified solutions (AISC 2010, AS 4100-1998), to ignore the temperature dependence of the thermal expansion coefficient. This should be done with some care, as the thermal expansion coefficient governs the thermal strain field of structural members and (depending on the displacement boundary conditions) controls the magnitude and shape of thermal deformations.

Research needs include material testing to characterize the thermal conductivity, specific heat and thermal expansion coefficient of CFS at elevated temperatures, as well as the identification of critical temperatures at which phase transformation occur, and the thermal and mechanical properties of the material are altered.

2.3 Cold-formed steel members at elevated temperatures

The growing use of CFS in the construction industry has led to an increasing attention in the research community towards CFS performance under fire conditions. Thin-walled steel members are potentially more vulnerable to fire effects because of their high surface to volume ratio and relatively high thermal conductivity. If unprotected, these allow for rapid temperature increase, and consequently fast stiffness and strength degradation. Considering the temperature dependence of both mechanical and thermal properties, under realistic fire conditions, the stiffness, strength, and thermal elongation vary across the section of a member and along its length, creating a dynamically changing demand and capacity for the member.

CFS members, as conventionally employed in light steel framing, are unique: efficient in terms of strength-to-weight, but markedly more complex than typical hot-rolled steel members due to their thin-walled nature and related cross-section stability modes that must be accounted for in design. Strength prediction of thin-walled CFS members relies either on the Effective Width Method (EWM) or the Direct Strength Method (DSM) to account for local and/or distortional buckling (see e.g., AISI S100-12). DSM is preferred because it directly integrates (computational) elastic buckling analysis into the design process. This was originally envisioned as a means to handle the wide variety of different shapes that can be formed from sheet steel (Schafer 2006), but can be modified to include the wide variety of different stiffness properties within a cross-section due to temperature gradients in the section.

Currently, the design of CFS members under fire is based on standard fire tests results, under controlled laboratory conditions. Fire resistance is judged based on the amount of time that a member or assembly can withstand elevated temperatures without exceeding specific failure criteria. This quantity is correlated with the amount of available time for occupant's evacuation and firefighter's operation before structural failure. To enable a more engineered solution, research studies are generally focused on predicting the load-carrying capacity of members at elevated temperatures, typically using modifications to existing design methods. This approach aims to use this strength prediction coupled with heat transfer analysis and a given fire demand to establish the building fire performance.

2.3.1 Fire performance of columns

At ambient temperatures, the capacity of a CFS column must considers the interaction of local, distortional, and global buckling, as well as yielding. Under fire demand, all the buckling modes and yielding potentially become time and temperature dependent through the cross-section and along the length. In addition, due to thermal elongation and shift in the center of resistance from the changing mechanical properties, second-order P-d demands driven by thermal deformations can be important (Wang and Davies 2000).

Figure 2-8 shows a typical experimental setup used for column testing at elevated temperatures. A furnace located in a loading frame is used to increase the temperature before or after the column is subjected to axial stresses. Lateral deformations are not measured due to limitations of the test setup. Through a small observation window the specimen is observed during testing.

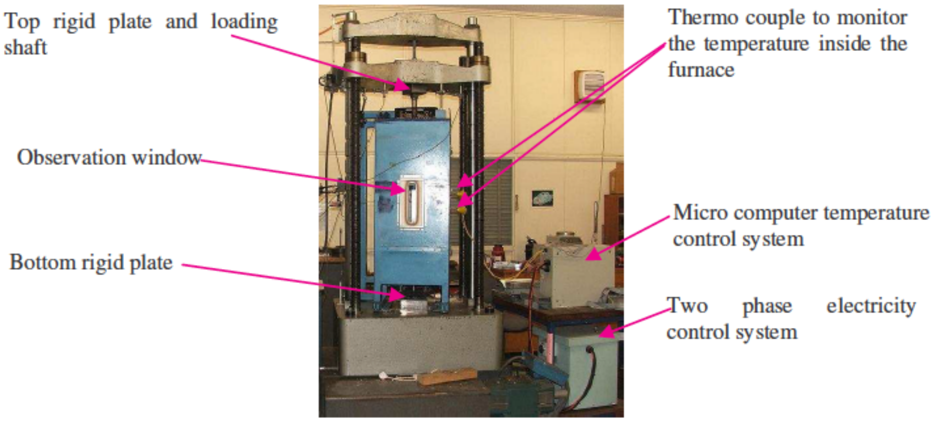

Figure 2-8: Experimental setup for column tests at elevated temperature from Heva and Mahendran (2008)

At ambient temperature certain modal interactions are generally considered (e.g., local-global) while others disregarded (e.g. local-distortional). Under thermal gradients these interactions can become far more complex (Batista-Abreu and Schafer 2013). For instance, experimental results qualitatively show that short columns with holes, dominated by local buckling at temperatures below 400°C, fail in distortional buckling at higher temperatures (Feng et al. 2003b). Further, short columns without holes dominated by distortional mode at temperatures below 400°C exhibit local-distortional-global (flexural) interaction at higher temperatures (Feng et al. 2003b). These evolutions of modal interaction, as a function of temperature, can be quantified through modal identification methods using the constrained finite strip method as a basis (Li et al. 2012).

Experimental data shows that the axial capacity of columns is reduced with increasing temperatures (Feng et al. 2003b). For instance, short columns develop substantial axial strength degradation after 200°C, withstanding about 15% of the failure load at ambient conditions at 700°C.

Computational mechanical models of CFS columns at elevated temperatures typically utilize shell finite elements, are only loosely coupled to thermal analyses, and focus on the impact of a uniform, elevated temperature on the collapse capacity of a CFS column (Feng et al. 2003c; Kaitila 2002; Ranawaka and Mahendran 2006; Chen and Young 2006b; Ranawaka and Mahendran 2009b). The models use temperature dependent mechanical properties for E, and Fy, typically based on testing conducted by the authors or on available retention factors (e.g, EN 1993-1-2:2005). Residual stresses are usually ignored (e.g. Ng and Gardner 2007) as they tend to diminish with increasing temperature (Ranawaka and Mahendran 2006; Lee 2004) and their influence on measured compressive ultimate load is negligible (Ranawaka and Mahendran 2010; Gardner and Nethercot 2004; Ellobody and Young 2005). In fact, this is consistent with findings at ambient temperatures as well (Schafer and Peköz 1998; Schafer et al. 2010).

Consistent with the thin-walled nature of the response, initial imperfections based on elastic buckling modes are typically included in the models. At ambient temperatures, significant progress has been made in realistic characterization of local, distortional, and global imperfections (Zeinoddini and Schafer 2012); however, at elevated temperatures, simpler approaches are typically employed for imperfection magnitudes: local ~t, distortional ~2t, global L/500, where t is the thickness and L the member length (Feng et al. 2004, Kaitila 2002; Ranawaka and Mahendran 2010). Under temperature gradients that are non-uniform through the cross-section, the necessity for fine-tuned imperfections is likely to be outweighed by the eccentricity in stiffness and the thermal bowing resulting from differential expansion (Feng and Wang 2005).

Work has also been completed on design methods for CFS columns at elevated temperatures. Under uniform temperature the DSM formulation (AISI S100-12 Appendix 1) with updated E(T) and related elastic buckling loads, and Fy(T) and related squash load have been used within the traditional DSM expressions with good success (Heva et al. 2008; Ranawaka and Mahendran 2009b). Thermal bowing is more pronounced under non-uniform temperature, and Shahbazian and Wang (2011b, a; 2012) have proposed modified DSM expressions and a new approach to determining the squash load capacity. The results are sensitive to the variation in the temperature across the section: temperature ratios between the exposed and unexposed flanges of 3.0, 2.0 and 1.5 at 120 minutes under a standard fire curve are utilized. Experimental data indicates actual temperature ratios are time dependent (see Figure 2-9) leading to further complications and a necessity to more directly couple the thermal and mechanical/design response. These temperature ratios were obtained through thermocouples located on the outside surface of the corners of lipped channels.

2.3.2 Fire performance of beams

Compared to columns, CFS beams under elevated temperature have seen relatively little study. Many of the challenges for columns are similar for beams: time-temperature dependence, altered buckling modes, modal interactions, and material yielding. Numerical investigations, based on shell finite element models, include work on lipped channels (Kankanamge and Mahendran 2008, 2012) and zee shapes (Lu et al. 2010). The models are subjected to uniform bending and analyzed with material properties consistent with uniformly elevated temperatures. Response is highly dependent on the end restraints, because they determine the development of compressive loads due to thermal elongation at initial stages of the fire action (Lu et al. 2011a), and tensile forces due to catenary action during the fire response. Lateral restraint provided by sheathing is critical at ambient temperatures and under elevated temperatures. Prediction equations for lateral-torsional buckling of channel sections have been proposed (Kankanamge and Mahendran 2012), but experimental and further numerical studies are needed.

In summary, existing research needs include the determination of realistic temperature distributions throughout the length and cross-section of CFS members. The structural response dynamically evolves as the temperature field changes; therefore, the study of mode interactions is important to understand the behavior of thin-walled members at elevated temperatures. Besides strength and stiffness degradation, structural members incur thermal deformations that would eventually lead to failure. Hence, the study of semi-rigid end restraints is crucial. In terms of experimental data, very limited information is available on the behavior single sections other than channels, and composite sections. Furthermore, design methods such as the Direct Strength Method and Effective Width Method have been validated for limited high temperature conditions; however this validation does not represent a sufficiently extensive range of possible scenarios.

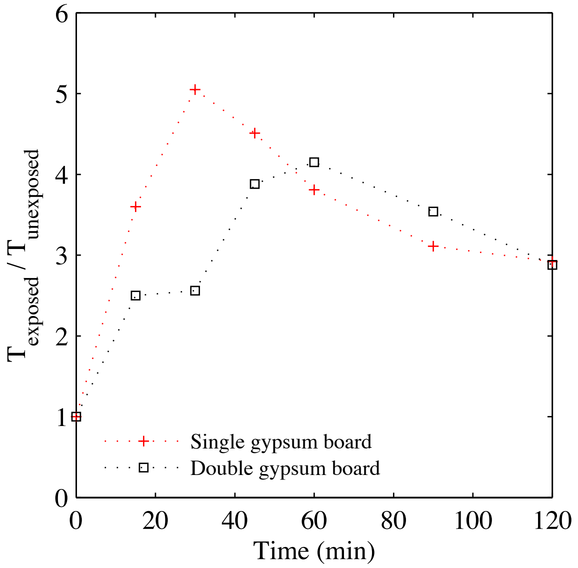

Figure 2-9: Temperature ratio between exposed and unexposed faces of a 100x54x15x1.2-lipped channel subjected to thermal load (cellulosic fire curve) on one flange (adapted from Feng et al. 2003a)

2.4 Cold-formed steel connections at elevated temperatures

Connections are critical in understanding the performance of CFS structures under elevated temperatures. At ambient temperatures a significant body of literature exists on bolted steel-to-steel connections, with more limited studies on other fasteners and sheet steel connected to other materials (wood products, gypsum products, concrete, etc.). The knowledge base is similar, but with less depth of results, for connection performance at elevated temperatures.

Young and his colleagues have studied bolted steel-to-steel connections relevant to CFS construction at elevated temperatures, including proposed reduction factors (Lim and

Young 2007), extensive (120 specimens) steady-state tests and analysis on single shear bolted connections (Yan and Young 2011a), and complementary (62 specimen) transient-state tests (Yan and Young 2011b). The tests and analysis show the dominance of bearing failures as long as the "3d" edge distance criteria is maintained, and also show that the use of reduced mechanical properties at elevated temperatures, but traditional ambient temperature strength equations, provides an adequate prediction of strength. Results show the capacity of connections is significantly reduced with increasing temperature. For instance, experimental data shows a degradation of the bearing strength of bolted moment connections up to 90% at 700°C, with respect to its capacity at ambient conditions.

Tests on screw fastened steel-to-steel connections in single shear under steady-state (Yan and Young 2012b) and transient-state (Yan and Young 2012c) conditions lead to similar findings as bolted connections. In addition, Lu et al. (2012) numerically studied shot-nailed and screwed connections, and again found that bearing failure of the thin steel sheet was the dominant failure mode. Design guidelines were provided to predict the capacity of shot-nailed (Lu et al. 2013), and screwed connections at elevated temperatures (Lu et al. 2011b).

In general, sheathed members are more stable and develop higher load-carrying capacity than unsheathed members. A methodology for sheathing-braced design of studs based on experimental data and discrete spring models is utilized at ambient conditions. However, studies on stud-to-sheathing connections at high temperatures are not currently found in the literature. Therefore, the feasibility of a similar methodology for fire design of CFS structures has not been judged. Research needs include the study of steel stud-to-sheathing connections at high temperatures. Additionally, the heat transfer through steel-to-steel and steel stud-to sheathing connections is relevant to understand the global behavior of CFS systems under fire.

2.5 Cold-formed steel assemblages at elevated temperatures

While CFS material and member performance under elevated temperature represents important building blocks for understanding fire resistance, it is complete CFS assemblages (i.e. walls and floors) that provide structural support and resist fire demands. The standard approach for assessing walls and floors is the performance in a standard fire test, as discussed in detail below. Industry has performed such testing extensively for CFS framing assemblages (CFSEI 2012). From the standpoint of the development of performance-based design, these tests provide benchmarks that the development of analysis-based approaches may be compared with. Thus, understanding the standard fire test and response of CFS assemblages is an important step in understanding full fire response, but must be coupled with more advanced fire demand and heat transfer models to provide a complete prediction of response.

2.5.1 Standard Fire Testing

The Standard Test Methods for Fire Tests of Building Construction and Materials (ASTM E119-12a) are the most commonly referenced methods for fire testing of CFS assemblages. Equivalent, or similar, test standards also exist (UL 263; ISO 834-1:1999). The fire curve used in ASTM E119-12a was developed in 1918 (Manzello 2008a), is equivalent to UL 263, and has a higher initial rate of temperature rise compared to the ISO 834-1:1999 fire curve. Thus, for short test durations, the ASTM E119-12a fire curve is more severe. However, fire curves have been strongly criticized due to the difference found between standard curves and fire curves measured in real compartment fires, both in terms of severity and duration. In this sense, the fire resistance specified for an assembly through standard testing may be different from the real response of the structure (Lane 2000). The worth of the standard test is more in its comparison to past practice, that in its absolute response.

A standard fire test is illustrated in Figure 2-10. The specimens (wall or floors) are subjected to a specific and prescriptive time-temperature curve (Figure 2-10-a). Thermocouples are strategically located on the specimens and they are monitored throughout the test (Figure 2-10-b and c). Fire resistance is defined by the time until "the maximum temperature increase on the unexposed side of the wall exceeds 181°C (325°F); the average temperature increase on the unexposed side of the wall exceeds 139°C (250°F); a breach occurs in the wall that allows hot gases from the furnace to penetrate and ignite a cotton target on the unexposed side of the wall; or, the wall is unable to maintain its design load." (ASTM E119-12a). Test setup and response for typical tests are provided in Figure 2-10-d-f for a wall and Figure 2-10-g-i for a floor.

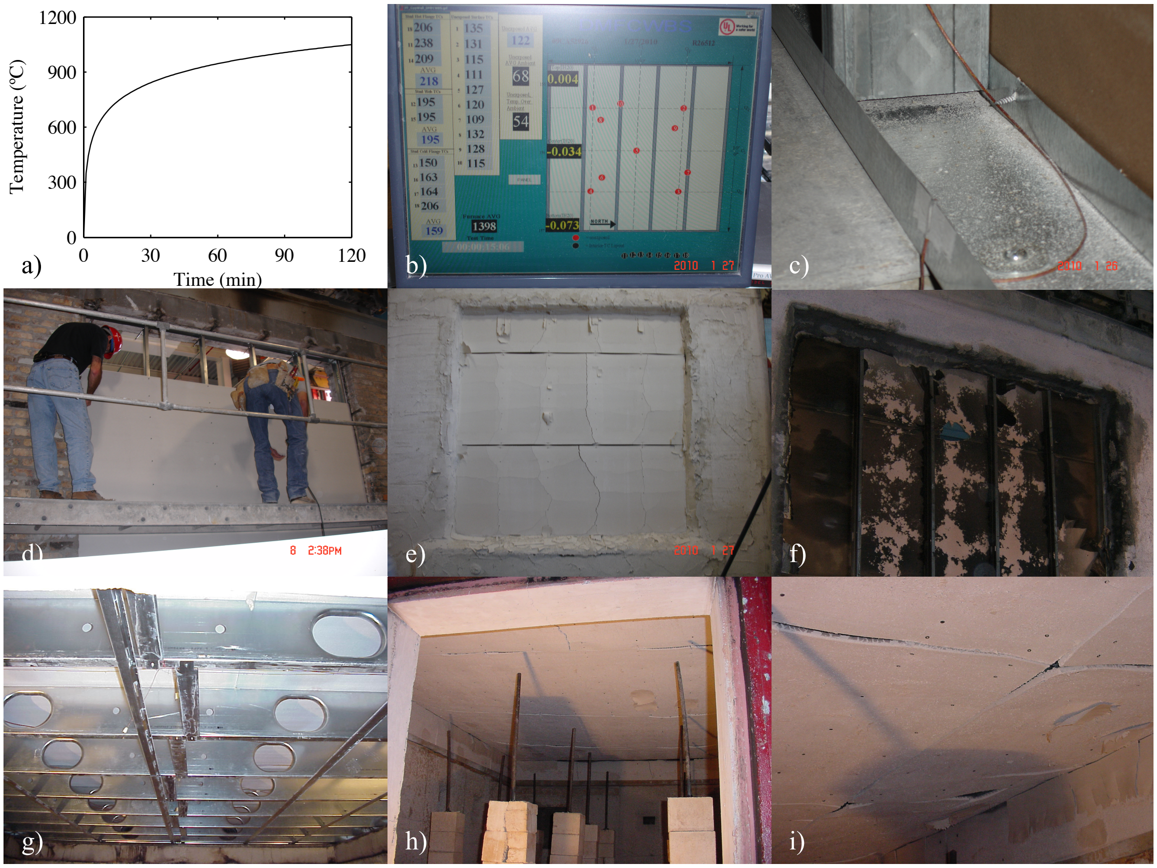

Figure 2-10: Proprietary ASTM E119 fire test results on walls (d-f) and floors (g-i) provided by ClarkDietrich Building Systems (a) prescriptive time-temperature curve, (b) thermocouple readings from wall test, (c) thermocouple installation, (d) installation of wall in furnace, (e) wall exterior during test, (f) wall interior and calcined gypsum board after test, (g) proprietary floor system showing blocking and strapping of joists (h) underneath floor before test, (i) after test

Criticisms of the standard fire test are well summarized by Grosshandler (2007): “The maximum size of the wall system is limited by the size of the furnace. The load conditions for the test specimen may not adequately mimic field use. The thermal environment of the furnace does not mimic a real fire. The tests reveal no fundamental information about the performance of the specimen and provide little guidance on how to improve performance. The furnaces themselves are not standardized; hence, the same specimen could receive different ratings if tested in two different facilities. Ratings are based upon a single test, with no way to quantify the uncertainty or safety factor.” In many ways the fact that “the tests reveal no fundamental information about the performance of the specimen" is the most damning and demonstrates how current practice provides no path towards significant improvement or change when driven by the standard fire test.

Even to use standard fire testing to advance basic modeling can be challenging since little, if any, of the specific data (thermocouple readings, deformations, etc.) is available in the public domain. Further, the pass/fail nature of the test has precluded studies focused on better understanding behavior. For example, the interaction between damage due to structural loads and degrading strength under realistic fire conditions has not been studied in detail.

By analyzing the data generated from standard fire tests, Ingberg (1928) developed a method to approximate the fire resistance time of a structure under a real fire, based on the fire resistance of a structure under standard fire conditions. This methodology compares the severities of real and standard fires, quantified as the areas under both fire curves. Other methods attempt to estimate "real" fire resistance rating based on the maximum temperatures that structural members develop. In general, these methodologies do not explicitly account for factors such as the type of combustible, geometry of the compartment, ventilation conditions, and heat release rate. Equations used to estimate the fire resistance rating are based on regression of limited experimental data related to tests with specific configurations and materials. Additionally, these methodologies do not consider the effect of loading conditions on the structural members, and the variation of temperature throughout the compartment.

2.5.2 Fire performance of walls

Performance of CFS walls in standard fire testing is summarized in CFSEI (2012). For both partition walls and for load bearing walls, the fire rating is largely a function of the thickness and number of gypsum (or similar) wallboards. Thus, the primary interest in research has been on the heat transfer aspects of the gypsum wallboard under the standard fire curve. The role of the fasteners as a thermal bridge, the role of the cross-section stiffness with respect to thermal bowing of the wall and local flange deformations, and the role of lost axial capacity due to decreased bracing stiffness from the wallboard as the board burns and undergoes calcination (or is saturated by a sprinkler) are important, but have seen little or no study.

The performance of the wallboard itself directly drives the thermal response and indirectly influences the mechanical response of the system. Wallboards consist of a pressed gypsum (and glass fiber) core, covered with thick sheets of paper. The sheets of paper maintain the integrity of the gypsum core even when it cracks, until they burn at about 200°C to 300°C. Dehydration of gypsum plasterboards initiates at 100°C (Gerlich 1995; Ngu 2004), when water boils, leading to increased porosity and a considerable drop of thermal conductivity (Rahmanian 2011). For instance, calcination of the gypsum board is complete after 20 minutes at 400°C, resulting in ~20% density reduction and ~80% loss of material strength (Cramer et al. 2003), as shown in Figure 2-11. Gypsum board damage depends on the maximum temperature reached and the rate of temperature increase and its relations to the moisture flow, ablation and cracking processes (Ariyanayagam and Mahendran 2012). Alternatives to gypsum wallboards such as bolivian magnesium and calcium silicate boards have shown better fire resistances (Chen et al. 2012), but are associated with increased cost.

Available data on thermo-mechanical properties of gypsum boards is commonly derived from research on lightweight wood construction. Thermal properties (i.e. specific heat, thermal conductivity, contraction and mass loss) of types X, C, F and R gypsum boards are available in the literature (Bakhtiary et al. 2000; Bénichou and Sultan 2005; Manzello et al. 2008a; Manzello et al. 2008b; Thomas 2002). Variability in the chemical composition and testing conditions (e.g. heating rate) of gypsum leads to scattered thermal properties results (Wakili and Hugi 2009). However, the chemical composition of the tested gypsum boards is not commonly stated in experimental reports. Modified thermal properties to implicitly account for mass transfer (e.g. water migration and re-condensation) and ablation process have also been proposed (Ang and Wang 2004).

Data on the mechanical properties of gypsum boards is scarce. Fuller (1990) showed the stiffness and strength of gypsum boards decays by 80% at 120 °C, after calcination. Similarly, Cramer et al. (2003) reported the variation of the elastic modulus, bending strength and thermal expansion coefficient along and across type X gypsum boards, up to 400 °C, after 60 minutes of fire exposure. Furthermore, Rahmanian (2011) reported the elastic modulus, bending and compressive strengths, and proposed linear stress-strain relations for standard and glass-fiber reinforced gypsum boards at elevated temperatures.

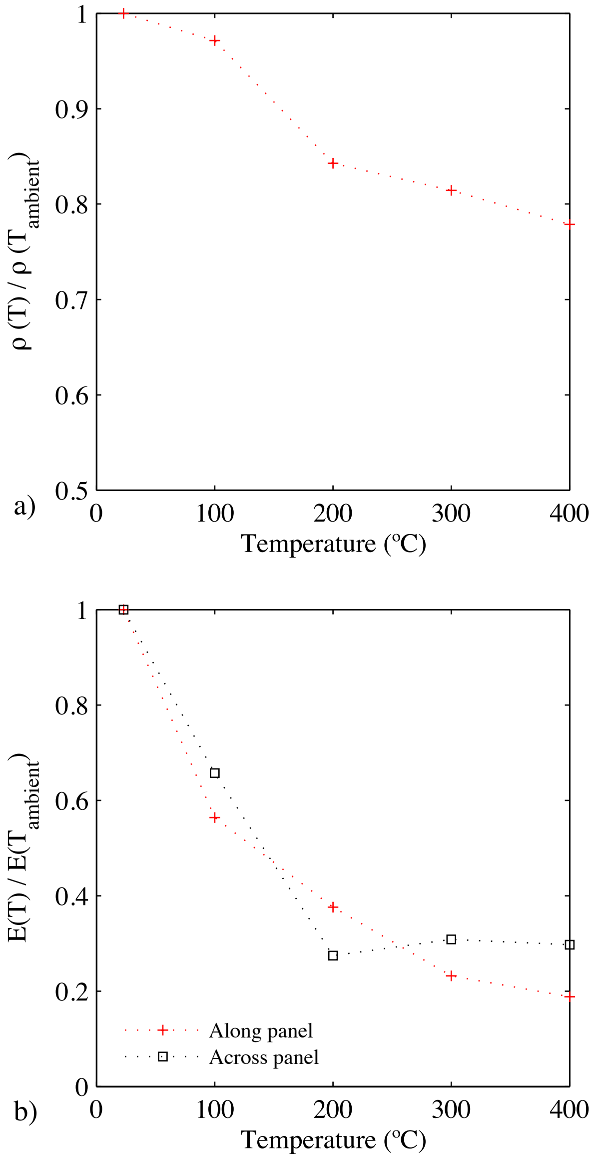

Figure 2-11: Temperature dependence of type X gypsum board (a) density and (b) elastic modulus retention (adapted form Cramer et al. 2003)

CFS walls commonly contain cavity insulation for climate and sound control. In general, cavity insulation obstructs heat dissipation in the cavity, causing a faster temperature increase in the exposed face of the wall, while delaying the temperature increase in the unexposed face (Alfawakhiri and Sultan 2001). Whether or not this change in the heat transfer is beneficial or detrimental is an open question. Research indicates glass or cellulose fiber cavity insulation has little affect, but mineral fiber insulation generally increases fire resistance (Sultan and Lougheed 2002, Feng et al. 2003d). However, others conclude cavity insulation is generally detrimental to strength (Kolarkar 2010). Alternatives to cavity insulation have been explored by Mahendran and his colleagues, including glass and rock fiber external insulation and external insulation sandwiched between gypsum boards. Fire performance for these systems can be excellent (Kolarkar and Mahendran 2008, 2012; Gunalan and Mahendran 2010; Keerthan and Mahendran 2012, 2013).

2.5.3 Performance of Floors

CFSEI (2012) summarizes available sources for prescriptive fire design of CFS floor systems; however, only limited information on the behavior of CFS floor-ceiling systems is available. Sultan et al. (1998) tested five floor specimens with CFS joists and gypsum board sheathing under standard fire conditions. It was observed that thermal bowing of the steel joists governs floor deflections until run-away occurs. In general, local buckling at the top flange of the joists near mid-span, and subsequent inelastic mechanism formation led to structural failure. Conclusions indicate that cavity insulation has a detrimental effect on the fire resistance of floor systems especially when the insulation melts, allowing the CFS joists to be completely exposed to fire after the gypsum falls off. The ability of the sheathing boards to remain in place governs the overall fire resistance of CFS floor assemblies (Alfawakhiri and Sultan 2001).

Baleshan and Mahendran (2010) tested three floor-ceiling systems looking at the advantages of using sandwiched insulation on the ceiling side of the CFS frame instead of cavity insulation. Results demonstrate that sandwiched insulation improves the fire resistance of floor systems by mitigating convective and radiative heat transfer from the external heat source to the CFS joists. It was observed that gypsum boards prevented lateral-torsional buckling of the joists during the tests. At high temperatures, local buckling along the CFS joist was prevalent, and pronounced crippling occurred near the supports. However, this implies a more expensive solution since two layers of boards are used to sandwich the insulation material.

The list of research needs related to CFS assemblages is exhaustive, as detailed in the previous sections. These needs begin with the characterization of fire demands based on realistic fire scenarios. Then, the actual heat transfer throughout the elements of the assemblage should be understood. The development of more accurate tridimensional and simplified heat transfer models is essential to enable coupled thermo-mechanical models useful for engineering-based analysis method. Furthermore, the study of the degradation of the capacity of the assemblage itself, and its interaction with the entire system is necessary for the development of a performance-based design method.

2.6 The case for performance-based fire design of cold-formed steel systems

Fire represents one of the most important hazards that building structures must be designed against. Most of the modern regulatory framework around building structures originated in response to the great fires of the late 19th and early 20th century. Today, this regulatory framework supports material standards that have adopted reliability-based design methods that largely bring other building hazards (snow, wind, conventional dead and live load) into a risk consistent framework. For complex hazards such as earthquakes, the risk consistent methodology has been extended to cover multiple performance objectives, always insuring society's concern of minimizing life safety risk, but enabling and incentivizing engineers and building owners to consider higher levels of performance. This performance-based design approach is largely seen as the future, and provides the best potential for risk consistent multi-hazard design.

Fire resistance of buildings framed from CFS is guaranteed through prescriptive codes and the standardized test. While the level of safety has generally been found acceptable, the lack of an engineering/analysis-based approach to fire resistance of CFS structures impedes progress and stifles innovation, summarized here across four broad categories. First, the cost to industry, particularly for ASTM E119 testing, is high and as a result little improvements are sought or found in even basic CFS wall and floor designs. Second, system-level mechanisms that provide enhanced resistance to fire through re-distribution of load are neither conceptualized, nor tested, nor designed in CFS structures due to lack of knowledge to complete such an approach and lack of financial reward for the engineer to do so. Third, risk consistent multi-hazard based design with fire is largely impossible since fire cannot be reasonably integrated with other hazards without a means to analyze the structure. Fourth, and finally, as multiple parties work to re-envision buildings to be greener and more sustainable the current prescriptive approach to fire means fire protection is added as a constraint with a small set of known solutions instead of integrated within the larger optimization that needs to be performed.

Preliminary work on performance-based fire resistance has begun internationally, but it is still limited. Positive strides in this direction include codification of engineering/analysis-based methods that predict the response of structures under fire demands such as those recently adopted for hot-rolled steel (AISC 2010 Appendix 4). However, similar progress has not been made in this direction for CFS structures. These structures provide a compelling and challenging framework for advancing performance-based fire resistance. Compelling, because a significant percentage of the modern building stock uses CFS framed walls with gypsum board for interior fire resistance; when these same walls are load bearing, as in a highly efficient CFS framed building, additional considerations arise. Challenging, because the thin-walled nature of CFS members complicates conventional design significantly and at elevated temperatures the stability response is further modified and must be understood.

Significant challenges remain to developing a complete performance-based fire engineering solution for CFS structures; including: more realistic fire models; deeper understanding of the temperature dependence of CFS, gypsum, and connector thermal properties; three dimensional heat transfer models including gypsum board deterioration (dehydration, cracking, and ablation) processes; improved one-dimensional heat transfer models for design; better understanding of strength and stiffness degradation of CFS and connected wallboards at elevated temperatures, considering the influence of the test method, strain and heating rates and chemical composition; verified coupled thermo-mechanical models that accurately predict the response of CFS elements and subsystems; experimental research at large scale on CFS building structures, including fire development, cooling phase behavior and residual strength, and element and subsystems interactions; performance-based methods for CFS fire design; structural optimization of load-bearing and non-load-bearing fire protection systems; and multi-hazard building response and mitigation, including fire after earthquake and fire after blast.

Although work remains, the basic building blocks for analysis-based fire resistance of CFS building assemblages and structures are in place, and performance-based fire design for CFS structures can now be pursued. Prescriptive solutions under standard fire testing provide a variety of immediately available options for design, but are restricting innovation in CFS assemblages and systems and ultimately place fire outside of the risk-consistent framework that has been developed for other building natural hazards. Ideally, performance-based fire design brings the demand (fire modeling), propagation (heat transfer), and capacity (strength at elevated temperatures) all into the realm of analysis. This review briefly summarized current efforts in fire modeling and heat transfer. For capacity determination, the chapter provides detailed reviews and composite data on the temperature dependence of sheet steels commonly used in CFS, members formed from CFS, and wall and floor assemblages framed from CFS. Available data is compared, along with existing codified provisions for other steels, and recommendations are provided for modeling and expected performance whenever possible. Codified provisions for analysis-based fire design of CFS will enable performance-based fire engineering of

CFS structures and should be a near term goal. Work remains to provide detailed capacity predictions fully coupled with three-dimensional building models and simulated fires, but already this possibility exists for researchers, and in the future for designers as well.

References

Alfawakhiri F (2001) Behaviour of cold-formed-steel-framed walls and floors in standard fire resistance tests. Carleton University, Ottawa, Ontario, Canada

Alfawakhiri F, Sultan MA (2001) Numerical modelling of steel members subjected to severe thermal loads. National Research Council Canada, Canada

Allen D (2004) Designing Cold-Formed Steel Mid-Rise Structures: Innovations for Cost-Effective and Attractive Projects, Structure

American Institute of Steel Construction (AISC) Specification for Structural Steel Buildings, Appendix 4: Structural Design for Fire Conditions. United States of America, 2010

American Iron and Steel Institute, AISI Standard, AISI S100-12. North American Standard For Cold-Formed Steel Framing – General Provisions

American Iron and Steel Institute, AISI Standard, AISI S100-12. North American Specification for the Design of Cold-formed Steel Structural Members

American Society for Testing and Materials, ASTM E119-12a, Standard Methods of Fire Tests for Fire Tests of Building Construction and Materials

American Society of Civil Engineers (ASCE) Performance-based design of structural steel for fire conditions: a calculation methodology. Reston, VA, 2009

Ang CN, Wang YC (2004) The effect of water movement on specific heat of gypsum plasterboard in heat transfer analysis under natural fire exposure. Construction and Building Materials 18 (7):505-515.

Ariyanayagam AD, Mahendran M (2012) Fire tests of load bearing steel stud walls exposed to real building fires. Paper presented at the 7th International Conference on Structures in Fire, Zurich, Switzerland, June 6-8

Bakhtiary SB, Jafarpoor F, Firoozyar F (2000) Thermal and mechanical properties of fire-resistant gypsum plasters. Asian Journal of Civil Engineering (Building and Housing) 1 (2):67-82

Baleshan B, Mahendran M (2010) Full scale fire tests of a new light gauge steel floor-ceiling system. Paper presented at the 4th International Conference on Steel & Composite Structures, Sydney, 21-23 July 2010

Batista-Abreu JC, Schafer BW (2013) Stability of cold-formed steel compression members under thermal gradients. In: Annual Stability Conference Structural Stability Research Council St. Louis, Missouri, pp 136-154

Bednarek Z, Kamocka R (2006) The heating rate impact on parameters characteristic of steel behaviour under fire conditions. Journal of Civil Engineering and Management 12 (4):269-275. doi:10.1080/13923730.2006.9636403

Bénichou N, Sultan MA (2005) Thermal properties of lightweight-framed construction components at elevated temperatures. Fire and Materials 29 (3):165-179. doi:10.1002/fam.880

British Standard Institution (BSI). BS5950 structural use of steel work in building-part 8: code of practice for fire resistant design. London, UK, 1990

cold-formed steelEI (2012) Technical note on cold-formed steel. TECH-NOTE T100-12: Fire rated assemblies of cold-formed steel construction. Washington, DC

Chen J, Young B (2006a) Corner properties of cold-formed steel sections at elevated temperatures. Thin-Walled Structures 44 (2) : 216-223.

Chen J, Young B (2006b) Design of cold-formed steel lipped channel columns at elevated temperatures. Paper presented at the Stability and ductility of steel structures, Lisbon, Portugal

Chen J, Young B (2007) Experimental investigation of cold-formed steel material at elevated temperatures. Thin-Walled Structures 45 (1):96-110.

Chen W, Ye J (2012) Mechanical properties of G550 cold-formed steel under transient and steady state conditions. Journal of Constructional Steel Research 73 (0):1-11.

Chen W, Ye J, Bai Y, Zhao X (2013) Thermal and mechanical modeling of load-bearing cold-formed steel wall systems in fire, Journal of Structural Engineering.

Chen W, Ye J, Bai Y, Zhao X (2012) Full-scale fire experiments on load-bearing cold-formed steel walls lined with different panels. Journal of Constructional Steel Research 79 (0):242-254

Clark CL (1953) High-temperature alloys. Pitman Metallurgy Series. Pitman Publishing Corporation, Toronto

Cooke GME (1988) An introduction to the mechanical properties of structural steel at elevated temperatures. Fire Safety Journal 13 (1):45-54

Costes F (2004) Modélisation thermomécanique tridimensionnelle par éléments finis de la coulée continue d’aciers, Ecole Nationale Supérieure des Mines de Paris, France

Cramer SM, Friday OM, White RH, Sriprutkiat G Mechanical properties of gypsum board at elevated temperatures. In: Fire and materials 2003: 8th International

Conference, San Francisco, CA, USA, 2003. Interscience Communications Limited, pp 33-42

Ellobody E, Young B (2005) Structural performance of cold-formed high strength stainless steel columns. Journal of Constructional Steel Research 61 (12):1631-1649

European Committee for Standardization (CEN). Eurocode 1: Actions on Structures Part 1-2: General actions – Actions on structures exposed to fire, EN 1991-1-2:2002, Brussels, 2002

European Committee for Standardization (CEN). Eurocode 3: Design of steel structures. Part 1-2: General rules - Structural fire design, EN 1993-1-2:2005, Brussels, 2005

Ewer J, Jia F, Grandison A, Galea E, Patel M (2008) SMARTFIRE V4.1: User Guide and Technical Manual - SMARTFIRE Tutorials. University of Greenwich, United Kingdom

Feng M, Wang YC (2005) An analysis of the structural behaviour of axially loaded full-scale cold-formed thin-walled steel structural panels tested under fire conditions. Thin-Walled Structures 43 (2):291-332

Feng M, Wang YC, Davies JM (2003a) Axial strength of cold-formed thin-walled steel channels under non-uniform temperatures in fire. Fire Safety Journal 38 (8):679-707. doi:10.1016/s0379-7112(03)00070-5

Feng M, Wang YC, Davies JM (2003b) Structural behaviour of cold-formed thin-walled short steel channel columns at elevated temperatures. Part 1: experiments. Thin-Walled Structures 41 (6):543-570. doi:10.1016/s0263-8231(03)00002-8

Feng M, Wang YC, Davies JM (2003c) Structural behaviour of cold-formed thin-walled short steel channel columns at elevated temperatures. Part 2: Design calculations and numerical analysis. Thin-Walled Structures 41 (6):571-594. doi:10.1016/s0263-8231(03)00003-x

Feng M, Wang YC, Davies JM (2003d) Thermal performance of cold-formed thin-walled steel panel systems in fire. Fire Safety Journal 38 (4):365-394. doi:10.1016/s0379-7112(02)00090-5

Feng M, Wang YC, Davies JM (2004) A numerical imperfection sensitivity study of cold-formed thin-walled tubular steel columns at uniform elevated temperatures. Thin-Walled Structures 42 (4):533-555

Fuller JJ (1990) Predicting the Thermo-Mechanical Behavior of A Gypsum-To-Wood Nailed Connection. Oregon State University

Gardner L, Nethercot D (2004) Numerical Modeling of Stainless Steel Structural Components—A Consistent Approach. Journal of Structural Engineering 130 (10):1586-1601. doi:10.1061/(ASCE)0733-9445(2004)130:10(1586)

Gerlich JT (1995) Design of Loadbearing Light Steel Frame Walls for Fire Resistance. vol Fire Engineering Research Report 95/3. School of Engineering, University of Canterbury, Christchurch, New Zealand

Grosshandler WL (2007) Fire Resistance Proficiency Testing of Gypsum/Steel-Stud Wall Assemblies, in Technical Memorandum of PWRI 4075; Wind and Seismic Effects. U.S./Japan Natural Resources Development Program (UJNR). Joint Meeting, 39th. Technical Memorandum of PWRI 4075. Tsukuba, Japan

Gunalan S, Mahendran M (2010) Structural and Fire Behaviour of a New Light Gauge Steel Wall System. Paper presented at the Structures in Fire: Sixth International Conference, PA

Heva B, Yasintha D, Mahendran M (2008) Local Buckling Tests of Cold-formed Steel Compression Members at Elevated Temperatures. Paper presented at the 5th International Conference on Thin-walled Structures - ICTWS 2008 : Innovations in Thin-walled Structures, Gold Coast, Australia

International Code Council. (2012). International Building Code. Chapter 6. Country Club Hills, IL

International Organization for Standardization (ISO), Fire Resistance Tests - Elements in Building Construction, ISO 834-1:1999

Kaitila O (2002) Finite element modelling of cold-formed steel members at high temperatures. Helsinki University of Technology, Espoo, Finland

Kankanamge ND, Mahendran M (2008) Numerical studies of cold-formed steel beams subject to lateral-torsional torsional buckling at elevated temperatures. Paper presented at the Fifth International Conference on Thin-Walled Structures, Brisbane, Australia

Kankanamge ND, Mahendran M (2011) Mechanical properties of cold-formed steels at elevated temperatures. Thin-Walled Structures 49 (1):26-44

Kankanamge ND, Mahendran M (2012) Behaviour and design of cold-formed steel beams subject to lateral–torsional buckling at elevated temperatures. Thin-Walled Structures 61 (0):213-228

Karren KW (1970) Corner properties of cold-formed steel structural members. Effects of cold work in cold-formed steel structural members, vol 70-1. Cornell Engineering Research Bulletin, NY

Keerthan P, Mahendran M (2012) Numerical modelling of load bearing LSF walls under fire conditions. Paper presented at the 7th International Conference on Structures in Fire, Zurich, Switzerland, June 6-8

Keerthan P, Mahendran M (2013) Thermal Performance of Composite Panels Under Fire Conditions Using Numerical Studies: Plasterboards, Rockwool, Glass Fibre and Cellulose Insulations. Fire Technol 49 (2):329-356. doi:10.1007/s10694-012-0269-6

Kodur V, Dwaikat M, Fike R (2010) High-Temperature Properties of Steel for Fire Resistance Modeling of Structures. Journal of Materials in Civil Engineering 22 (5):423-434. doi:10.1061/(asce)mt.1943-5533.0000041

Kolarkar P, Mahendran M (2008) Thermal performance of plasterboard lined steel stud walls. Paper presented at the 19th International Specialty Conference on Cold-Formed Steel Structures St. Louis, MO

Kolarkar P, Mahendran M (2012) Experimental studies of non-load bearing steel wall systems under fire conditions. Fire Safety Journal 53 (0):85-104

Kolarkar PN (2010) Structural and Thermal Performance of Cold-formed Steel Stud Wall Systems under Fire Conditions. Queensland University of Technology, Australia

Lane B (2000) Performance-Based Design for Fire Resistance. Modern Steel Construction. American Institute of Steel Construction

Lee JH (2004) Local buckling behaviour and design of Colf-formed steel compression members at elevated temperatues. Queensland University of Technology

Lee JH, Mahendran M, Makelainen P (2003) Prediction of mechanical properties of light gauge steels at elevated temperatures. Journal of Constructional Steel Research 59 (12):1517-1532. doi:10.1016/s0143-974x(03)00087-7

Li Z, Batista Abreu JC, Adany S, Schafer BW (2012) Cold-formed steel member stability and the constrained finite strip method. Paper presented at the The 6th International Conference on Coupled Instabilities in Metal Structures, Glasgow, United Kingdom

Li Z, Schafer BW (2010) Buckling analysis of cold-formed steel members with general boundary conditions using CUFSM: conventional and constrained finite strip methods. Paper presented at the Twentieth International Specialty Conference on Cold-Formed Steel Structures Saint Louis, MO

Lim JBP, Young B (2007) Effects of elevated temperatures on bolted moment-connections between cold-formed steel members. Engineering Structures 29 (10):2419-2427

Lu W, Ma Z, Mäkeläinen P, Outinen J (2012) Behaviour of shear connectors in cold-formed steel sheeting at ambient and elevated temperatures. Thin-Walled Structures 61 (0):229-238

Lu W, Ma Z, Mäkeläinen P, Outinen J (2013) Design of shot nailed steel sheeting connection at ambient and elevated temperatures. Engineering Structures 49 (0):963-972

Lu W, Makelainen P, Outinen J (2010) Numerical investigation of cold-formed steel purlin in fire. Journal of Structural Mechanics 43 (1):12-24

Lu W, Makelainen P, Outinen J (2011a) Behaviour of cold-formed Z-shaped steel purlin in fire. Paper presented at the Civil Engineering ’11 - 3rd International Scientific Conference, Jelgava

Lu W, Mäkeläinen P, Outinen J, Ma Z (2011b) Design of screwed steel sheeting connection at ambient and elevated temperatures. Thin-Walled Structures 49 (12):1526-1533

Luecke WE, McColskey JD, McCowan CN, Banovic SW, Fields RJ, Foecke T, Siewert TA, Gayle FW (2005) Mechanical Properties of Structural Steels (Draft). Federal Building and Fire Safety Investigation of the World Trade Center Disaster NIST NCSTAR 1-3D (Draft). U.S. Government Printing Office, Washington, DC

Mäkeläinen P, Outinen J (1998) Mechanical properties of an austenitic stainless steel at elevated temperatures. Journal of Constructional Steel Research 46 (1–3):455

Manzello SL, Park SH, Mizukami T, Bentz DP (2004) Measurement of thermal properties of gypsum board at elevated temperatures. Paper presented at the Fifth International Conference Structures in Fire (SiF’08), Nanyang Technological University, Singapure, 28-30 May, 2008

Manzello SL, W.L. Grosshandler, and T. Mizukami (2008a) Furnace Testing of Full-Scale GypsumSteel Stud Non-Load Bearing Wall Assemblies: Results of Multi-Laboratory Testing in Canada, Japan and USA. Paper presented at the Structures in Fire (SiF'08), Singapore

Manzello SL, Park SH, Mizukami T, Bentz DP (2008b) Measurement of thermal properties of gypsum board at elevated temperatures. Paper presented at the Fifth International Conference Structures in Fire (SiF'08), Nanyang Technological University, Singapure, 28-30 May, 2008

McGrattan KBF, G. P.; Floyd, J. E.; Hostikka, S.; Prasad, K. R. (2002) Fire Dynamics Simulator (Version 3): Users Guide. NISTIR 6784, 2002 Ed. U.S. Department of Commerce. National Institute of Standards and Technology

Ng KT, Gardner L (2007) Buckling of stainless steel columns and beams in fire. Engineering Structures 29 (5):717-730

Ngu CN (2004) Calcination of Gypsum Plasterboard under Fire Exposure. Fire Engineering Research Report 04/6. Department of Civil Engineering, University of Canterbury. University of Canterbury, Christchurch, New Zealand

Outinen J (2006) Mechanical Properties of Structural Steel at High Temperatures and after Cooling Down. Doctoral Dissertation, Helsinki University of Technology Espoo, Finland

Outinen J, Mäkeläinen P (1999) Mechanical Properties of an Austenitic Stainless Steel at Elevated Temperatures. In: Chan SL, Teng JG (eds) Advances in Steel Structures (ICASS '99). Elsevier, Oxford, pp 1063-1069. doi:10.1016/b978-008043015-7/50124-x

Outinen J, Mäkeläinen P (2004) Mechanical properties of structural steel at elevated temperatures and after cooling down. Fire and Materials 28 (2-4):237-251

Quintiere JG (1989) Fundamentals of Enclosure Fire "Zone" Models. Journal of Fire Protection Engineering 1(3): 99-119

Rahmanian I (2011) Thermal and mechanical properties of gypsum boards and their influence on fire resistance of gypsum board based systems. University of Manchester, England

Ramberg W, Osgood WR (1943) Description of stress-strain curves by three parameters. Technical Notes. National Advisory Committee for Aeronautics, Washington, DC

Ranawaka T, Mahendran M (2006) Finite element analyses of cold-formed steel columns subject to distortional buckling under simulated fire conditions. Paper presented at the Stability and ductility of steel structures, Lisbon, Portugal

Ranawaka T, Mahendran M (2009a) Experimental study of the mechanical properties of light gauge cold-formed steels at elevated temperatures. Fire Safety Journal 44 (2):219-229. doi:10.1016/j.firesaf.2008.06.006

Ranawaka T, Mahendran M (2009b) Distortional buckling tests of cold-formed steel compression members at elevated temperatures. Journal of Constructional Steel Research 65 (2):249-259. doi:10.1016/j.jcsr.2008.09.002

Ranawaka T, Mahendran M (2010) Numerical modelling of light gauge cold-formed steel compression members subjected to distortional buckling at elevated temperatures. Thin-Walled Structures 48 (4-5):334-344. doi:10.1016/j.tws.2009.11.004

Rasmussen KJR (2003) Full-range stress–strain curves for stainless steel alloys. Journal of Constructional Steel Research 59 (1):47-61. doi:http://dx.doi.org/10.1016/S0143-974X(02)00018-4

Rubini P (2006) Simulation of Fires in Enclosure (SOFIE). Cranfield University, United Kingdom

Santos P, Martins C, da Silva LS, Bragança L (2013) Thermal performance of lightweight steel framed wall: The importance of flanking thermal losses. Journal of Building Physics. doi:10.1177/1744259113499212

Schafer BW (2006) Review: The Direct Strength Method of Cold-Formed Steel Member Design. Paper presented at the Stability and Ductility of Steel Structures, Lisbon, Portugal

Schafer BW, Li Z, Moen CD (2010) Computational modeling of cold-formed steel. Thin-Walled Structures 48 (10–11):752-762.

Schafer BW (2011). Cold-formed steel structures around the world: A review of recent advances in applications, analysis and design. ECCS, Steel Construction. 4 (3) 141-149. (DOI: 10.1002/stco.201110019)

Schafer BW, Peköz T (1998) Computational modeling of cold-formed steel: characterizing geometric imperfections and residual stresses. Journal of Constructional Steel Research 47 (3):193-210

SCI (1993) Building Design using Cold Formed Steel Sections: Fire Protection. British Library Cataloguing-in-Publication Data. Silwood Park, Ascot

Shahbazian A, Wang YC (2011a) Application of the Direct Strength Method to local buckling resistance of thin-walled steel members with non-uniform elevated temperatures under axial compression. Thin-Walled Structures 49 (12):1573-1583

Shahbazian A, Wang YC (2011b) Calculating the global buckling resistance of thin-walled steel members with uniform and non-uniform elevated temperatures under axial compression. Thin-Walled Structures 49 (11):1415-1428.

Shahbazian A, Wang YC (2012) Direct Strength Method for calculating distortional buckling capacity of cold-formed thin-walled steel columns with uniform and non-uniform elevated temperatures. Thin-Walled Structures 53 (0):188-199

Shahbazian A, Wang YC (2013) A simplified approach for calculating temperatures in axially loaded cold-formed thin-walled steel studs in wall panel assemblies exposed to fire from one side. Thin-Walled Structures 64 (0):60-72

Spalding B (1978) PHOENICS. Concentration Heat And Momentum Limited, London, UK

Standards Australia (AS), S.A. AS 4100-1998. Steel Structures. Sydney, Australia

Sultan M (1996) A model for predicting heat transfer through noninsulated unloaded steel-stud gypsum board wall assemblies exposed to fire. Fire Technol 32 (3):239-259. doi:10.1007/bf01040217

Sultan MA, Lougheed GD (2002) Results of Fire Resistance Tests on Full-Scale Gypsum Board Wall Assemblies. Internal Report, Institute for Research in Construction, vol 833. National Research Council Canada, Canada

Thomas G (2002) Thermal properties of gypsum plasterboard at high temperatures. Fire and Materials 26:37-45. doi:10.1002/fam.786

Underwriters Laboratories Inc. (UL), Standard for Safety for Fire Tests of Building Construction and Materials, UL 263. Northbrook, Illinois, Thirteenth Edition, 2003

Uribe J (1969) Aspects of the effects of cold-forming on the properties and performance of light-gage structural members. vol Report No. 333. Department of Structural Engineering, Cornell University, Ithaca, NY

Wakili KG, Hugi E (2009) Four Types of Gypsum Plaster Boards and their Thermophysical Properties Under Fire Condition. Journal of Fire Sciences 27 (1):27-43. doi:10.1177/0734904108094514

Wang YC, Davies JM (2000) Design of thin-walled steel channel columns in fire using Eurocode 3 Part 1.3, Structures in Fire, Copenhagen, Denmark

Yan S, Young B (2011a) Tests of single shear bolted connections of thin sheet steels at elevated temperatures—Part I: Steady state tests. Thin-Walled Structures 49 (10):1320-1333

Yan S, Young B (2011b) Tests of single shear bolted connections of thin sheet steels at elevated temperatures—Part II: Transient state tests. Thin-Walled Structures 49 (10):1334-1340

Yan S, Young B (2012a) Bearing factors for single shear bolted connections of thin sheet steels at elevated temperatures. Thin-Walled Structures 52 (0):126-142

Yan S, Young B (2012b) Screwed connections of thin sheet steels at elevated temperatures – Part I: Steady state tests. Engineering Structures 35 (0):234-243

Yan S, Young B (2012c) Screwed connections of thin sheet steels at elevated temperatures – Part II: Transient state tests. Engineering Structures 35 (0):228-233

Zeinoddini VM, Schafer BW (2012) Simulation of geometric imperfections in cold-formed steel members using spectral representation approach. Thin-Walled Structures 60 (0):105-117

Chapter 3 – Experiments on cold-formed steel material at elevated temperatures

Understanding the temperature dependence of CFS material properties is a necessary step towards the development of a rational engineering design method. As temperature increases, steel members lose strength and stiffness, retaining only a fraction of their original capacity. This material degradation is commonly pondered through the use of retention factors. In general, retention factors for the mechanical properties of CFS at elevated temperatures are provided by design codes and standards, but based on studies on hot-rolled steel (AISC 2008, AS 1998, BSI 1990, CEN 2005). However, CFS members develop faster heating rates and have higher thermal conductivity than hot-rolled steel members. Moreover, when heated, CFS loses the strength gained through cold work in the forming process (Lee et al. 2003). Consequently, retention factors from hot-rolled steel may overestimate the capacity of CFS material under fire. This brings the need of the development of retention factors for CFS based on experiments on such material.

Strength retention factors may vary within different types of steels, according to their chemical composition. Although CFS structural and non-structural members are manufactured from low (~227MPa [33ksi]), intermediate (~345MPa [50ksi]), and high strength (~552MPa [80ksi]) steels, previous research has been mainly dedicated to intermediate to high-strength materials. Available data on the mechanical behavior of CFS is limited and exhibits significant scatter across research groups. Discrepancies may be ascribed to differences in test methods, strain and heating rates used in experiments, and criteria to post-process experimental data (Batista Abreu et al. 2014).

This chapter presents an experimental investigation on the mechanical behavior of CFS through steady-state experiments, with the objective of providing retention factors and constitutive relations for this material. In total, 21 specimens were tested, including ASTM A653 and NBR 7008 ZAR-35 CFSs.

3.1 Experimental investigation on ASTM A653 cold-formed steel

Tensile test on ASTM A653 CFS, a material typically used in lightweight building constructions in North America, were performed in the Structural Engineering Laboratory, at the University of New Haven, in Connecticut.

3.1.1 Test method

Different techniques may be used to evaluate the degradation of mechanical properties and temperature dependence of stress-strain relations of building materials under fire. The most popular technique is the steady-state test in which the specimen is heated up to a target temperature and then, after the temperature is stable and uniform in the material, tensile load is gradually applied until a failure criterion is met. Another common technique is the transient-state test in which the specimen is subjected to a static load and then heated up progressively until it fails. Continuous stress-strain curves can be directly obtained from steady-state tests. However, after transient-state tests, stress-strain curves are constructed from temperature-strain curves recorded at several stress levels. This construction process may induce errors in the subsequently computed mechanical properties, particularly in the determination of the elastic modulus, if an insufficient amount of data is used to compute the initial slope of stress-strain curves.

Most of the data reported in the literature employs steady-state test protocols since it avoids heat rate dependence; allows a more accurate acquisition of mechanical properties with available technology; and is generally easier to conduct. Consequently, this experimental investigation adopted the strain-controlled steady-state test method.

As discussed in Section 2.2.1, the selection of the heating rate is relevant and has a significant impact on the experimental results, especially in transient state test. Given that CFS members are typically sheathed with gypsum boards as part of the fire protection system, the heating rate assumed in this experimental investigation is related to the heating rate the steel frame experiences during a standard fire. Recognizing that the heating rate is time-dependent during fire, an average heating rate was chosen to perform the steady-state tests. Also, the heating rate varies in the cross-section of CFS members, and along their length. For instance, during a standard fire test, the exposed and unexposed flanges of a stud experience average heating rates at mid-height around 9.7 °C/min and 8.7 °C/min, respectively, if the wall has no cavity insulation. When cavity insulation is included, this average values increase to 10.7 °C/min and 10.2 °C/min, respectively. Undoubtedly, the peak heating rates will be very different depending on the presence and type of cavity insulation, but the average rates are not. Considering this range of average values, the heating rate adopted in the steady-state tests was 10.0 °C/min.

3.1.2 Cold-formed steel specimens

Thin-walled specimens were cut from the web of CFS 600S162 structural studs (according to AISI S200-2012 nomenclature). The specimens were formed from ASTM A653 steel, with nominal yield stress of 230 MPa [33 ksi] and thickness of 1.44 mm [0.0566 in.], and nominal yield stress of 345 MPa [50 ksi] and thicknesses of 2.58 mm [0.1017 in.], and 1.15 mm [0.0451 in.]. The specimens were flat and had two holes for pinned connections (Figure 3-1). The dimensions of the tensile specimens follow the standard test method for tension testing of metallic materials (ASTM E8/E8M-11). The metal thickness and gage width of the specimens were measured at three points within their gage lengths using a micrometer. These measurements were used to compute the initial cross-sectional area of the specimens for further stress calculations. A total of 21 specimens were tested.

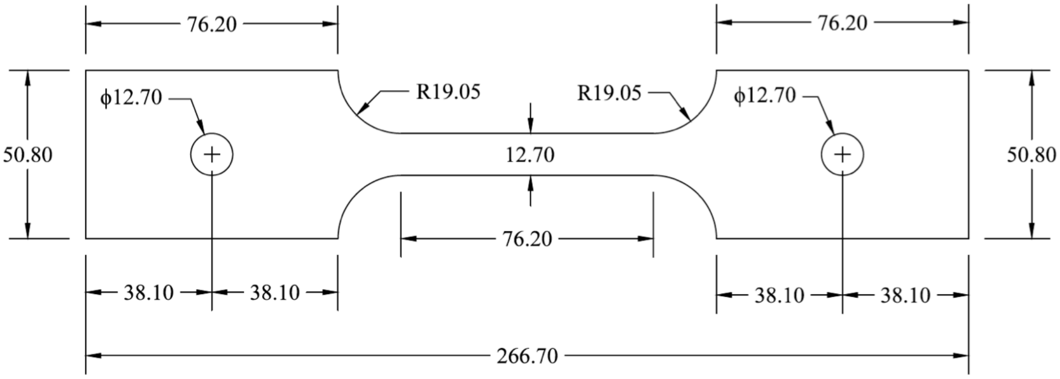

Figure 3-1: Tension test specimen dimensions (mm)

3.1.3 Test setup and procedure

An ATS 3710A furnace with maximum temperatures of 621°C [1150°F] was employed in the testing (Figure 3-2-a). The specimens were located inside the furnace and connected to MTS 647 hydraulic wedge grips on a MTS 810 load frame through high temperature stainless steel bars with pins, as illustrated in Figure 3-2. These bars transmitted the load to the specimens, avoiding eccentricity. A MTS 634 axial extensometer was used to measure the changes along the length of the specimens while the axial load was applied (Figure 3-2-c). The extensometer was connected outside the furnace to a high-temperature steel mounting which was attached to the specimen inside the furnace, within its gage length (Figure 3-2-d).

After placing the specimen and calibrating the load cell and extensometer, the specimen was heated up at an average rate of 10 °C/min. During the heating process, free thermal expansion was allowed by releasing the bottom grip. The temperature levels in this study were 20 °C, 100 °C, 200 °C, 300 °C, 400 °C, 500 °C and 600 °C. Temperature was monitored by two type-K thermocouples. One thermocouple was attached to the specimen and the other was used to measure air temperature inside the furnace. After the target temperature was stable, the specimens were maintained under constant temperature for a period of 10 minutes, approximately. The extensometer was recalibrated to zero and then the load was applied by controlling the displacement of the hydraulic grip until fracture occurred. The strain rate was set to 0.003 mm/mm/min per ASTM E21-09.

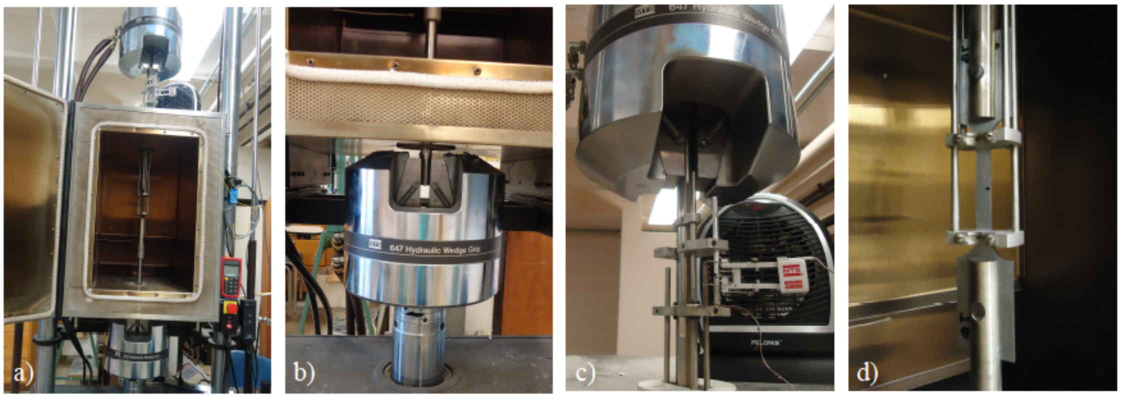

Figure 3-2: Tension test setup (a) ATS 3710A furnace, (b) extension rods attached to MTS 647 hydraulic grips to transmit load, (c) MTS 634 axial extensometer on top of the furnace, and (d) mounting system attached to a CFS specimen inside the furnace

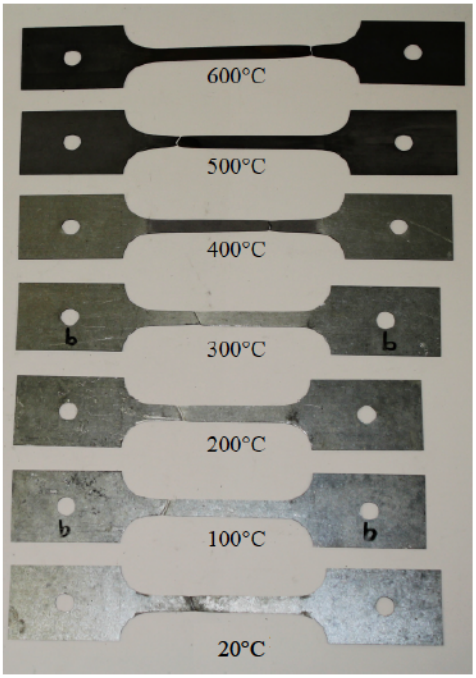

Figure 3-3: CFS specimens after high-temperature tensile test

3.1.4 Steady-state test results

Figure 3-3 shows the fractured 2.58 mm [0.1017 in.] thick CFS specimens with nominal yield strength of 345 MPa [50 ksi], at temperatures from 20 °C to 600 °C. Visually, large elongation of the specimens is observed at 300 °C and higher temperatures.

Stress-strain curves at ambient temperature (i.e. 20 °C) show a clear linear-elastic region followed by a yield plateau (see Figure 3-4). These characteristics are not evident at 200 °C and higher temperatures, as the elastic limit disappears and the nonlinearity of the stress-strain curve becomes predominant. Consequently, the elastic modulus computed as the initial slope of the σ-ε curve may not be as representative of the stress-strain relationship as it is for ambient conditions, even for relatively small strain levels.

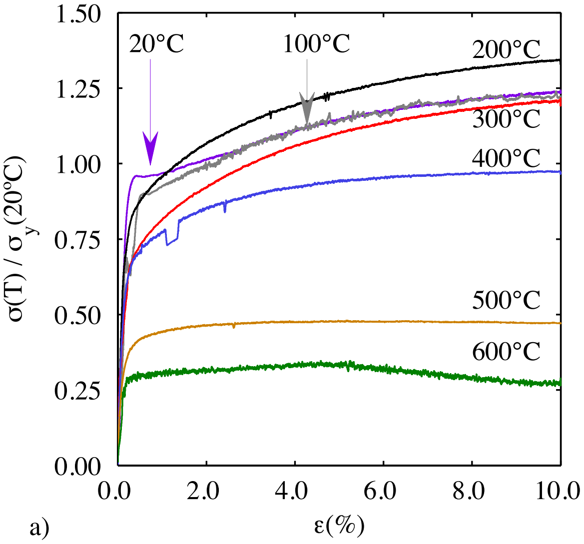

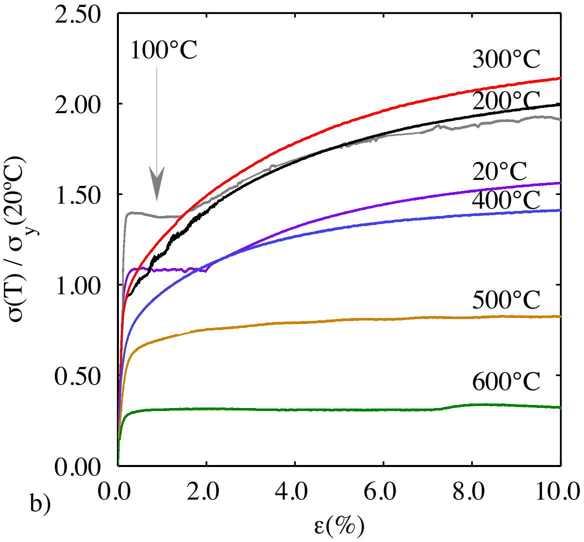

Figure 3-4: CFS stress-strain curves at ambient and elevated temperatures, from tensile specimens with nominal yield stresses of (a) 345 MPa [50 ksi] and (b) 230 MPa [33 ksi]

In most cases, CFS specimens with nominal yield stress of 230 MPa [33 ksi] developed high stresses between 200 °C and 300 °C compared to the ambient case. At this temperature range, the specimens did not develop significant elongation and necking. Figure 3-5 shows that the total elongation (computed as the percentage of change in length of the specimen within the gage length) decreases with respect to the ambient case when the specimens are heated at 100 °C and 200 °C. This material behavior may relate to blue brittleness development, evidenced by the blue colored oxidation film observed in the fracture section of specimens. Blue brittleness is an accelerated strain-aging phenomenon that occurs in a particular temperature range (which depends on the chemical composition of steel) due to an increase of dislocation density. This phenomenon causes an increased apparent strength and reduced ductility and toughness (Dolzhenkov 1971).

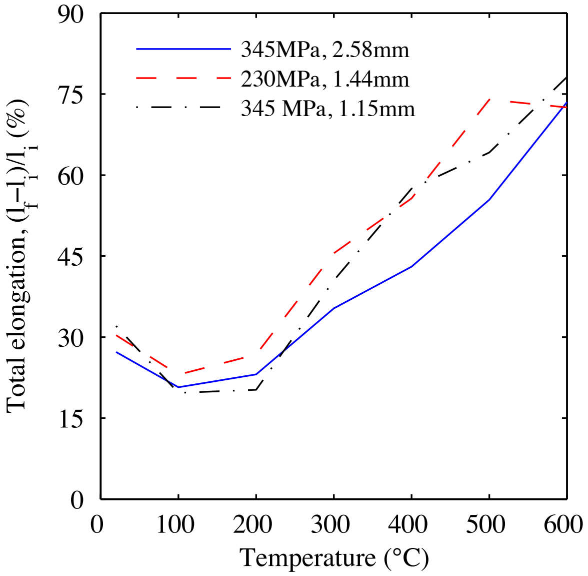

Figure 3-5: Total elongation of the tensile specimens at elevated temperatures

The elastic modulus was obtained by calculating the initial slope of the stress-strain curves, fitting the curve up to 0.1% strain. At ambient temperature, the nominal elastic modulus is 203 GPa [29500 ksi]. The yield stress was computed using the 0.2% offset method and the corresponding slope (i.e. temperature-dependent elastic modulus). The ultimate stress was taken as the maximum stress read during testing. Results for CFS ASTM A653 with nominal stress of 345 MPa [50 ksi] and 230 MPa [33 ksi] are shown in Table 3-1 and Table 3-2, respectively. Appendix A, Figures A-1, 2 and 3 show stress-strain curves for each specimen.

Table 3-1: Retention factors for the elastic modulus, yield stress and ultimate stress of ASTM A653 with nominal yield stress of 345 MPa [50 ksi]

T (°C)	t = 2.58 mm [0.1017 in.]			t = 1.15 mm [0.0451 in.]		
	$\frac{E(T)}{E(20°C)}$	$\frac{\sigma_y(T)}{\sigma_y(20°C)}$	$\frac{\sigma_u(T)}{\sigma_u(20°C)}$	$\frac{E(T)}{E(20°C)}$	$\frac{\sigma_y(T)}{\sigma_y(20°C)}$	$\frac{\sigma_u(T)}{\sigma_u(20°C)}$
20	1.000	1.000	1.000	1.000	1.000	1.000
100	0.869	0.929	0.962	0.915	0.948	1.016
200	0.831	0.891	1.050	0.986	0.834	1.097
300	0.702	0.716	0.880	0.771	0.761	1.095
400	0.578	0.748	0.727	0.689	0.631	0.798
500	0.420	0.431	0.366	0.450	0.382	0.378
600	0.352	0.424	0.345	0.378	0.164	0.194

Table 3-2: Retention factors for the elastic modulus, yield stress and ultimate stress of ASTM A653 with nominal yield stress of 230 MPa [33 ksi]

T (°C)	t = 1.44 mm [0.0566 in.]		
	$\frac{E(T)}{E(20°C)}$	$\frac{\sigma_y(T)}{\sigma_y(20°C)}$	$\frac{\sigma_u(T)}{\sigma_u(20°C)}$
20	1.000	1.000	1.000
100	0.899	1.318	1.239
200	0.876	0.948	1.402
300	0.700	1.024	1.468
400	0.618	0.745	0.950
500	0.385	0.606	0.534
600	0.363	0.291	0.226

3.2 Experimental investigation on ZAR-345 cold-formed steel

Tensile test on CFS ZAR-345, a material used in civil constructions in Brazil, were performed in the Civil Engineering Laboratory, at the University of Campinas, Brazil. ZAR-345 is equivalent to the ASTM A653 steel, commonly used in North America. The chemical composition of ZAR-345 and ASTM A653 is shown in Table 3-3. A total of 7 specimens made with ZAR-345 were tested.

3.2.1 Test method

This experimental investigation implemented the strain-controlled steady-state test method with a heating rate of 10.0 °C/min to 20 °C/min, comparable with the tensile test at elevated temperatures on ASTM A653, shown in section 3.1.

3.2.2 Cold-formed steel specimens

Specimens were taken from the web of CFS lipped channels with web, flanges, and lips measuring 153, 43, and 13 mm, respectively, nominal yield strengths of 345 MPa [50 ksi], and thickness of 1.55 mm [0.0610 in.]. The specimens were flat and had two holes for pinned connections (Figure 3-6). The dimensions of the tensile specimens follow the standard test method for tension testing of metallic materials (ASTM E8/E8M-11). The metal thickness and gage width of the specimens were measured at three points using a micrometer, and this measurements were used to compute the initial cross-sectional area and stresses.

Table 3-3: Chemical composition of CFS materials (CSN 2006)

Material nomenclature F_y (MPa [ksi])	Chemical composition (maximum %)		
	C	P	S
ASTM A653 (230 [33])	0.20	0.04	0.04
ASTM A653 (345 [50])	0.40	0.20	0.04
NBR 7008 ZAR-345 (345 [50])	0.20	0.20	0.04

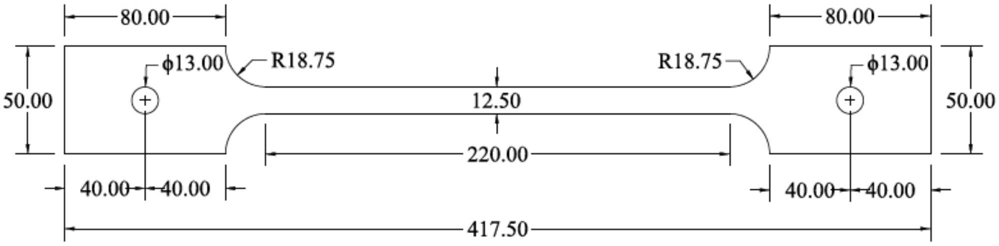

Figure 3-6: Tension test specimen dimensions (mm)

3.2.3 Test setup and procedure

The specimens were connected to MTS 680 high-temperature grips on a MTS load frame model 312.21 through high-temperature stainless steel pin connections, as illustrated in Figure 3-7. A MTS 652.01 high-temperature furnace with a MTS 490.83 controller was used in the testing (Figure 3-7-b). A MTS 632 high-temperature extensometer was employed to measure strains while the tension load was applied to the specimen inside the furnace (Figure 3-7-c). The extensometer was directly in contact with the specimen through ceramic extension rods (Figure 3-7-d).

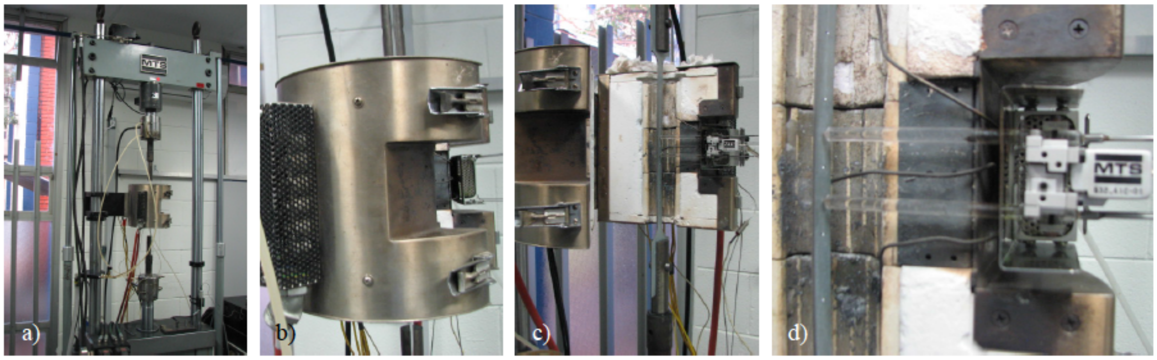

Figure 3-7: Tension test setup (a) MTS 312.21 frame and (b) MTS 652.01 furnace, (c) CFS specimens inside furnace, and (d) MTS 632 high-temperature extensometer attached to specimen

After placing the specimens and calibrating the load cell and extensometer, the specimens were heated up at a rate of 10 °C/min to 20 °C/min. During the heating process, thermal expansion was allowed by keeping a small tensile stress (about 2% of the nominal yield stress) on the specimen. The temperatures of study were 20 °C, 200 °C, 300 °C, 400 °C, 500 °C, 600 °C and 700 °C. The temperature of the furnace was monitored by type-K thermocouples. After the target temperature was stable, the specimens were maintained at constant temperature for a period of 10 minutes, approximately. The extensometer was recalibrated to zero and then the load was applied by controlling the displacement of the hydraulic grip until fracture occurred. The strain rate was set to 0.005 mm/mm/min, per ASTM E21-09.

3.2.4 Steady-state test results

Figure 3-8 shows the fractured 1.55 mm [0.0610 in.] thick CFS specimens with nominal yield strength of 345 MPa [50 ksi], at temperatures from 20 °C to 700 °C. Visually, noticeable necking is observed at 500 °C and higher temperatures.

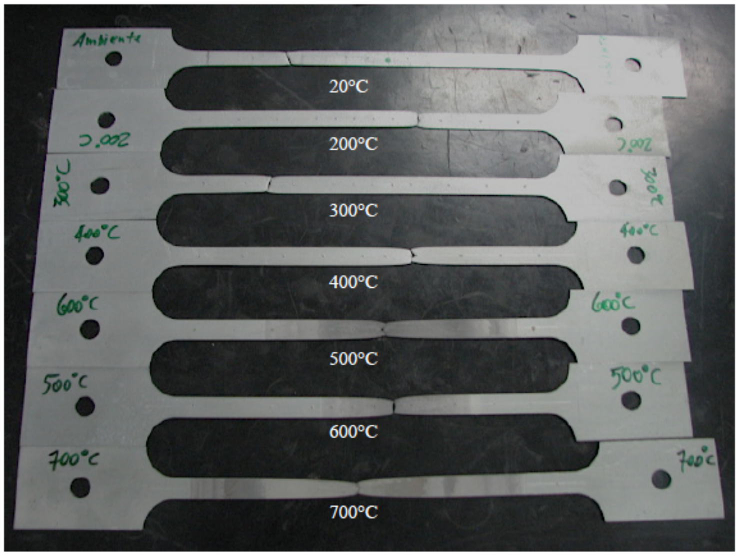

Figure 3-8: CFS specimens after high-temperature tensile test

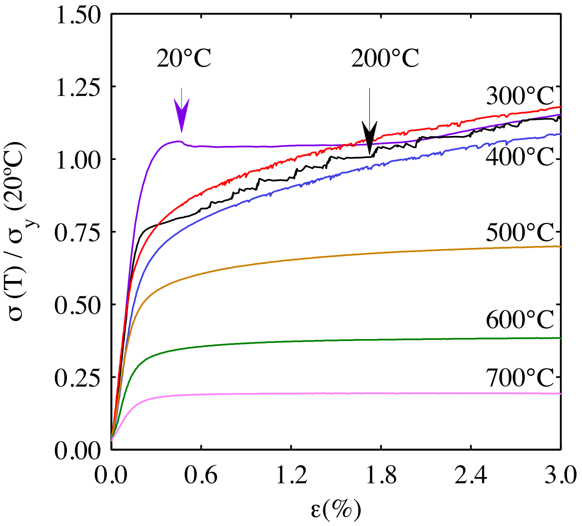

Figure 3-9: CFS stress-strain curves at ambient and elevated temperatures, from tensile specimens with nominal yield stresses of 345 MPa [50 ksi]

Stress-strain curves for ZAR-345 are similar to the curves obtained for A653: there is a clear linear-elastic region followed by a yield plateau at ambient temperature; and nonlinear response is notorious at 300 °C and higher temperatures. Figure 3-10 shows the total elongation computed as the change in length of the specimen (within a gage length of 50 mm) with increasing temperature, from 20 °C to 700 °C. At 300 °C this maximum elongation is small compared to the ambient case.

The elastic modulus was obtained by calculating the initial slope of the stress-strain curves, fitting the curve up to 0.1% strain. At ambient temperature, the nominal elastic modulus is 203 GPa [29500 ksi]. The yield stress was computed using the 0.2% offset method and the corresponding slope (i.e. temperature-dependent elastic modulus). The ultimate stress was taken as the maximum stress read during testing. Results for CFS NBR 7008 ZAR-345 with nominal stress of 345 MPa [50 ksi] are shown in Table 3-4. Appendix A, Figures A-4 shows stress-strain curves for each specimen.

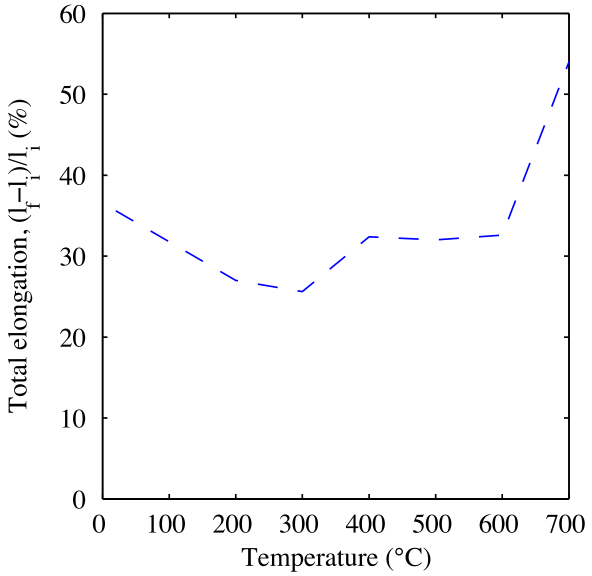

Figure 3-10: Total elongation of the tensile specimens at elevated temperatures

Table 3-4: Retention factors for the elastic modulus, yield stress and ultimate stress of ZAR-345 with nominal yield stress of 345 MPa [50 ksi]

T (°C)	t = 1.55 mm [0.6102 in.]		
	$\frac{E(T)}{E(20°C)}$	$\frac{\sigma_y(T)}{\sigma_y(20°C)}$	$\frac{\sigma_u(T)}{\sigma_u(20°C)}$
20	1.000	1.000	1.000
200	0.873	0.741	0.927
300	0.910	0.757	0.925
400	0.684	0.690	0.931
500	0.642	0.532	0.552
600	0.369	0.317	0.319
700	0.165	0.174	0.166

References

CSN (2006), Catalogo Zincados, Companhia Siderúrgica Nacional, Sao Paulo, Brazil

Chapter 4 – Experiments on cold-formed steel studs under compression at elevated temperatures

CFS members are broadly used as framing components in non-load-bearing and load-bearing systems. Typical walls are assembled with thin-walled studs connected to top and bottom tracks through screws, and then sheathed with gypsum wallboards or oriented strand boards (OSB). In cases required by building codes, fire-rated gypsum boards are also used to sheath the cold-formed steel framing and to assist in mitigating the spread of fire and smoke among building compartments.

In general, sheathing provides (among other benefits) lateral restraint to cold-formed steel members at screw locations, potentially increasing their load-carrying capacity. Vieira (2011) investigated the behavior of sheathed cold-formed steel studs at ambient temperatures under compression and concluded that sheathing braces the studs, allowing only local buckling, by restraining distortional and global buckling modes. This beneficial effect was experimentally and analytically characterized, and translated into a design formulation to determine the strength of sheathed wall assemblies (Schafer 2013). The proposed method was validated for cold-formed steel systems at ambient temperature.

In case of fire, the temperature of exposed assemblies increases producing a deterioration of the mechanical properties of structural and sheathing materials. Investigations on the behavior of stud-to-sheathing connections at elevated temperatures are limited in the current literature; consequently, the feasibility of a complete methodology for cold-formed steel system fire design has not yet been judged (Batista Abreu et al. 2014).

Gypsum wallboards consist of a core of pressed gypsum, enclosed by sheets of paper. At elevated temperatures, gypsum wallboards burn and suffer calcination, therefore decreasing the bracing stiffness provided to the studs. The deterioration process starts with dehydration of gypsum at about 100 °C (Gerlich 1995), when the void fraction of the material increases and its thermal conductivity drops (Rahmanian 2011). Then, at about 200 °C to 300 °C, the paper cover burns and thus the ability of the wallboard to remain integral progressively vanishes. During this heating process, the wallboard loses its structural strength (Cramer et al. 2003).

OSB is formed by blending rectangular wood strands and adhesives, then compressed in multiple layers. Besides burning and producing an enormous amount of smoke, the mechanical properties of OSB degrade at elevated temperatures. For example, OSB retains about 24% of its bending strength at 200 °C (Sinha et al. 2011).

In general, the response of sheathing determines the thermal response of cold-formed steel assemblies, and has a direct impact on the structural response of the system. For instance, the loss of lateral bracing may cause weakness in load-bearing members, influencing the stability of the structure. Aiming to understand response of sheathed studs under fire, this chapter presents an experimental investigation on the behavior of single sheathed studs subjected to axial load, at elevated temperatures. The specimens studied are similar to those tested at ambient temperature by Vieira Jr et al. (2011).

4.1 Experimental investigation on cold-formed steel bare and sheathed studs

Compression test specimens and test procedure are depicted in this section.

4.1.1 Test specimens

Cold-formed steel specimens consisted of single 0.60 m [23.62 in.] or 1.00 m [39.37 in.] long studs connected to 0.50 m [19.69 in.] long tracks. The studs were lipped channels with web, flanges, and lips nominally measuring 153 mm [6.02 in.], 43 mm [1.69 in.], and 13 mm [0.51 in.], respectively; while the tracks were unlipped channel sections with similar dimensions. The thickness of all cold-formed steel sections was 1.55 mm [0.061 in.].

Stud and track flanges were connected with single screws #10 3/4” (19.1 mm) at each side, in both ends (Figure 4-1-a). Therefore, the cold-formed steel studs were allowed to experience rotation about their minor-axis, reflecting partially-restrained end conditions. Regular gypsum boards (GYP), fire rated gypsum boards (FRG), or OSB were used as sheathing materials (Figure 4-1-b). Gypsum boards were connected to cold-formed steel sections through #6 1-5/8” (41.3 mm) screws although #8 1 15/16” (49.2 mm) screws were used for stud-to-OSB connections. The average thickness of OSB and gypsum boards (both GYP and FRG) was 11.5 mm [0.45 in.] and 12.7 mm [0.50 in.], respectively.

Five configurations were studied according to the sheathing condition (or material used) at each side of the stud, and named as follows: BARE-BARE, OSB-OSB, GYP-OSB, GYP-GYP, and FRG-FRG. For instance, GYP-OSB denotes that the cold-formed steel stud was sheathed with gypsum board on one side, and oriented strand board on the other side.

At room temperature (i.e. 20°C approximately), the average moisture content of OSB and gypsum (both GYP and FRG) was 3% and 12%, respectively. Bare specimens and specimens sheathed with (GYP or FRG) gypsum were tested at 20, 200, 400 and 600 °C. Specimens sheathed with OSB, either in one or two sides, were tested at 20, 100, 200 and 250 °C. In summary, cold-formed steel specimens with two stud lengths and five different sheathing conditions were tested at four temperatures levels. Therefore, a total of forty tests were completed.

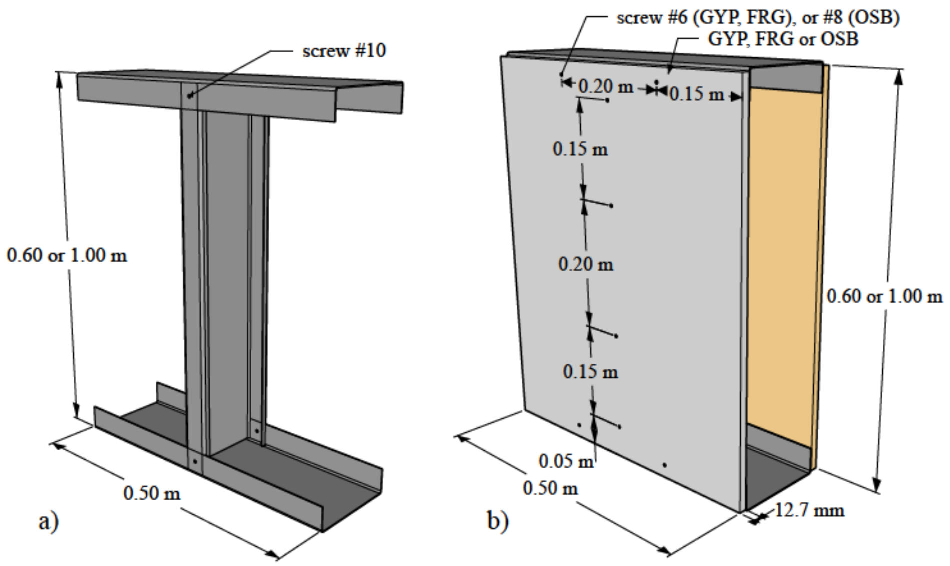

Figure 4-1: CFS stud specimens a) bare and b) sheathed

4.1.2 Test setup and procedure

After aligning the specimens in the structural testing frame (Figure 4-2-a), an electric furnace was activated to set the temperature to a predetermined value (Figure 4-2-b). The heating rate was defined as 10 °C/min, and the temperature of the furnace was controlled through type-K thermocouples. The temperature of the specimen was measured at three cross-sections: located at mid-height, 12.5 cm [4.92 in.] from the top of the top track, and 12.5 cm [4.92 in.] from the bottom of the bottom track. At each location, type-K thermocouples were attached to the middle of both flanges. Additionally, a type-K thermocouple was attached to the web center, at mid-height. In total, 7 thermocouples reported the temperatures of the steel studs. Thermal expansion was allowed during the heating phase of the experiment.

Once the temperatures reached the predetermined value and were stable for about 20 minutes, axial load was applied to the top of the specimen at a rate of 0.01 mm/sec, approximately. Two 153.0 mm [6.02 in.] wide, 304.8 mm [12.00 in.] long, and 12.7 mm [0.50 in.] thick steel plates were located on the web of the top track and under the web of the bottom track. These thick plates were used to transfer the load directly to the tracks and avoid direct bearing of the sheathing. The load was recorded through a load cell placed under the specimen, outside of the furnace. Two linear variable differential transducers (LVDT) were used to measure the vertical displacement at the top of the specimen during the test. The temperatures of the load cell and LVDT was monitored with laser temperature sensors to guarantee they would not increase significantly over room temperature. Axial load was applied until collapse (Figure 4-2-c).

4.1.3 Experimental results from compression tests at elevated temperatures

Axial load and displacement of bare and sheathed specimens, at ambient temperature, are plotted in Figure 4-3. Short members (i.e. 0.60 m [23.62 in.] long) show a slight variation of the peak load among bare and sheathed specimens (Figure 4-3-a). For these short studs, the dominant failure mode corresponds to local buckling of the web. By adding sheathing, distortional and global buckling effects are restricted; however the local buckling of the web continues to govern the response. In contrast, intermediate-length specimens (i.e. 1.00 m [39.37 in.] long) exhibited an increased load-carrying capacity by adding sheathing, regardless of the sheathing material (whether it is gypsum or OSB). The response of the intermediate-length studs was governed by global-local interactions, and high participation of distortional buckling mode. Therefore, by adding sheathing and constraining the rotation of the flanges and minor-axis buckling, the capacity of the studs increased at least 15% compared to the bare case. Vieira Jr. et al. (2011) obtained similar results at ambient conditions. Load-displacement curves of CFS studs at elevated temperatures are provided in Appendix B.

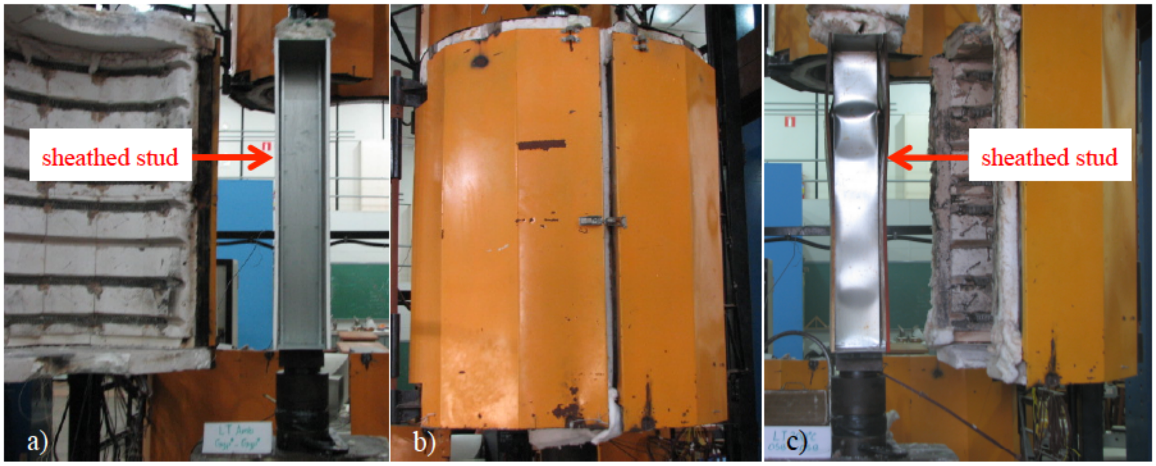

Figure 4-2: Experimental setup: a) sheathed specimen alignment before testing, b) electric furnace during testing, and c) sheathed specimen after testing

By increasing the temperature, the load-carrying capacity of the specimen decays due to degradation of the mechanical properties of cold-formed steel. Additionally, high temperatures alter the properties of the sheathing materials, consequently reducing their ability to brace the stud and constraint distortional and global buckling modes. Figure 4-4 shows the case of intermediate-length cold-formed steel studs sheathed with FRG. Both stiffness and strength are considerably reduced with increasing temperature. For instance, the load-carrying capacity reduces to 30 % of its initial value, at 600 °C.

Short specimens showed comparable axial strength regardless of their sheathing conditions at every temperature (Figure 4-5). The load-carrying capacity reduced mainly due to degradation of the steel. Intermediate-length studs showed higher capacity when sheathed at every temperature compared to the bare members, up to 600 °C (Figure 4-6). However, the strength increase due to sheathing was observed to vary with increasing temperature.

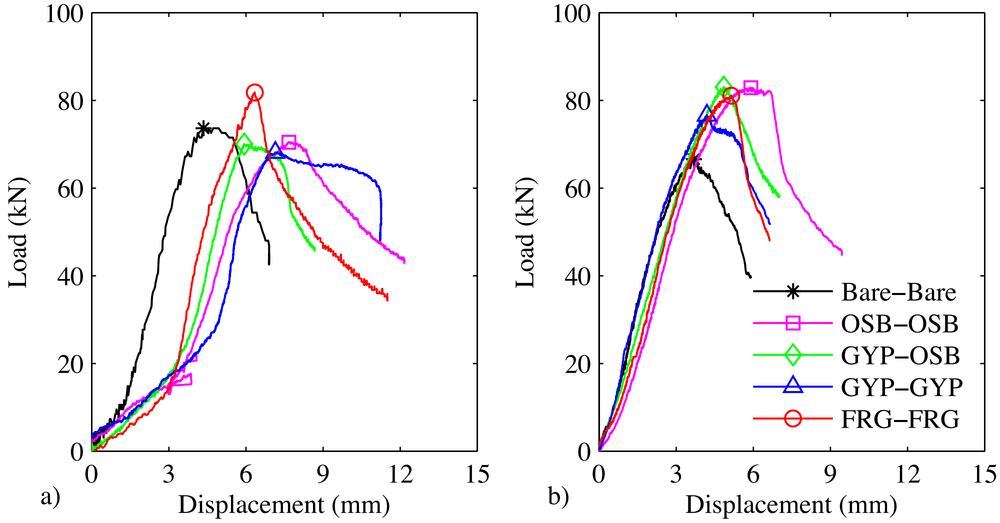

Figure 4-3: Axial load versus displacement of a) 0.6 m [23.62 in.] and b) 1.0 m [39.37 in.] long cold-formed steel studs at 20 °C

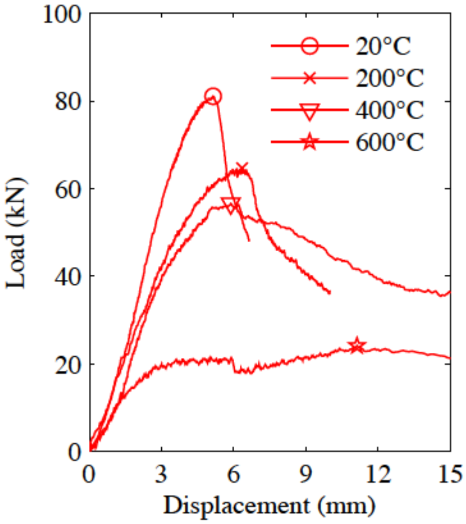

Figure 4-4: Axial load versus displacement of 1.0 m [39.37 in.] long studs sheathed with fire-rated gypsum

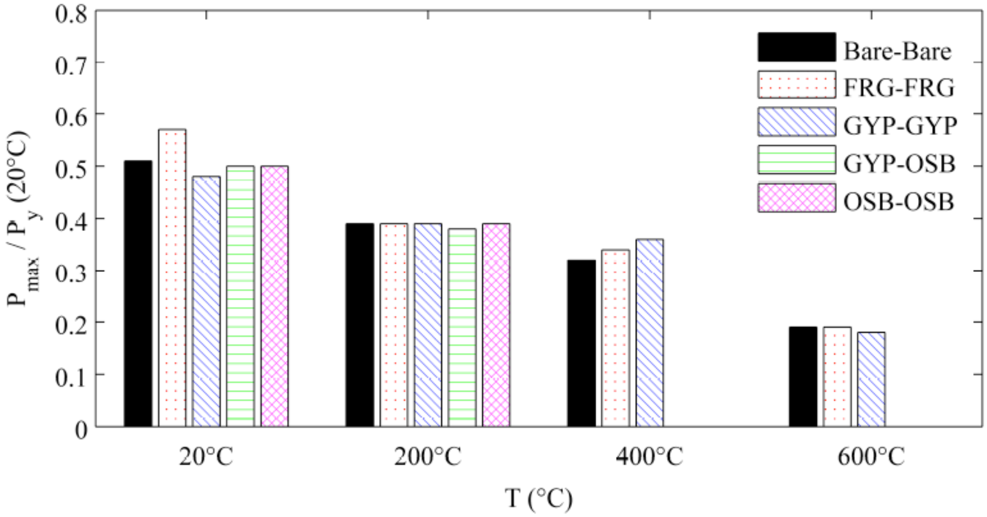

Figure 4-5: Normalized ultimate load of 0.6 m [23.62 in.] long studs with temperature

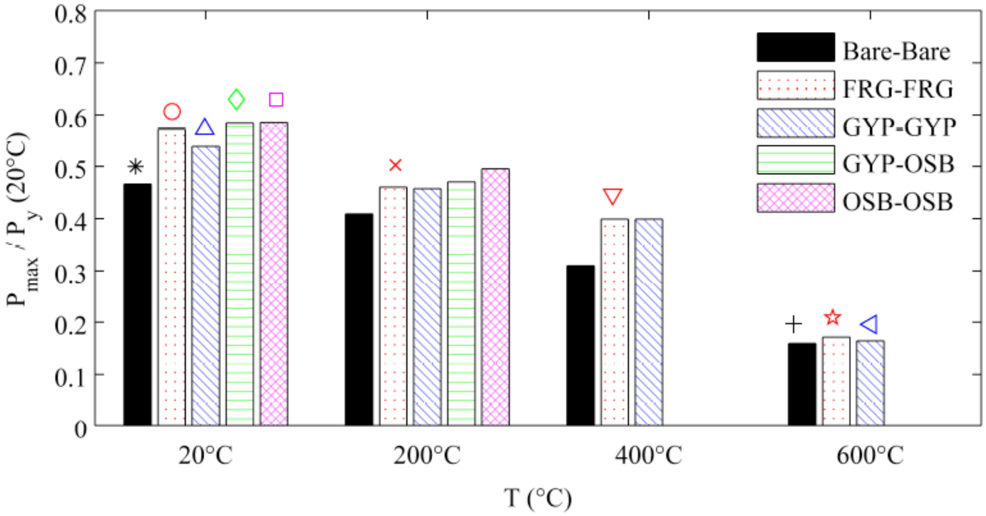

Figure 4-6: Normalized ultimate load of 1.0 m [39.37 in.] long studs with temperature

Significant damage of the sheathing was noticed when increasing the temperature. The gypsum wallboards produced a noticeable amount of water steam and smoke after reaching 115 °C and 250 °C, respectively. The paper used to maintain the integrity of the gypsum was mostly burned at about 400 °C; therefore, at high temperatures, the sheathing capacity relied only on dehydrated and damaged gypsum. Smoke was observed after OSB reached 200 °C, approximately; and at 250 °C the amount of smoke was substantial.

Gypsum boards were significantly cracked after testing sheathed specimens at 600 °C. Results show that at 600 °C the difference between the strength of sheathed and bare specimens is small (Figure 4-7).

4.2 Discussion

Although the load-carrying capacity of short studs governed by local buckling was not significantly improved by adding sheathing boards, the strength of intermediate-length members was improved. This increase in strength tends to disappear as the sheathing board degrades with rising temperature. Figure 4-8 shows intermediate-length bare members after test, with noticeable deformations about the minor-axis, and localized deformations at mid-height. Similar sheathed studs at elevated temperatures show localized deformations at the ends and web buckling along the member, up to 400 °C. At 600 °C, the sheathed studs become “unsheathed” after a significant part of the gypsum spalls off; thus, both the bare and sheathed specimens show similar deformed shapes (Figures 4-8-d and 4-8-h).

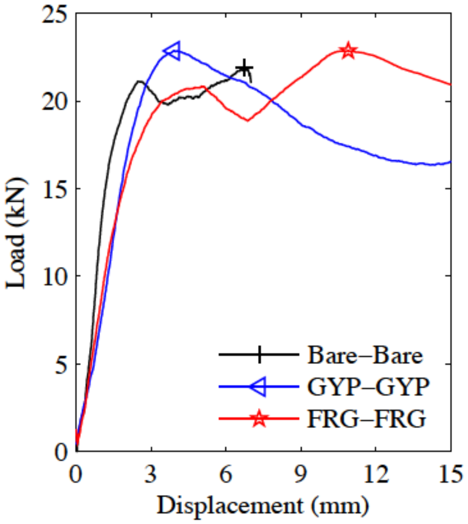

Figure 4-7: Axial load versus displacement of 1.0 m [39.37 in.] long studs at 600°C

Figure 4-8: 1.0 m [39.37 in.] long specimens after testing:
bare studs tested at a) 20°C, b) 200°C, c) 400°C and d) 600°C, and
studs sheathed with fire-rated gypsum tested at e) 20°C, f) 200°C, g) 400°C and h) 600°C

The normalized axial strength of intermediate-length studs is plotted in Figure 4-9-a. The experimental results were fit, and then compared. A strength increase was predicted at several temperatures as the percentage of additional load-carrying capacity gained by the specimen when sheathed. Results are plotted in Figure 4-9-b. The vertical axis "Strength increase (%)" was calculated as the ratio between the difference of the ultimate loads of sheathed and bare studs, and the ultimate load of the bare studs. The figure shows that the strength increase due to sheathing at ambient temperature is 20.0 % on average. This strength increase decays linearly with temperature down to 5.5 % at 600 °C. The regression line shown in Figure 4-9-b provides an estimate of the strength increase due to sheathing with temperature.

To quantify the lateral stiffness provided by the sheathing boards, additional tests were performed at high temperatures, similar to those completed by Vieira Jr. and Schafer (2012) at ambient temperature. Chapter 5 includes the study of the lateral stiffness of sheathed CFS studs at elevated temperatures based on experimental results.

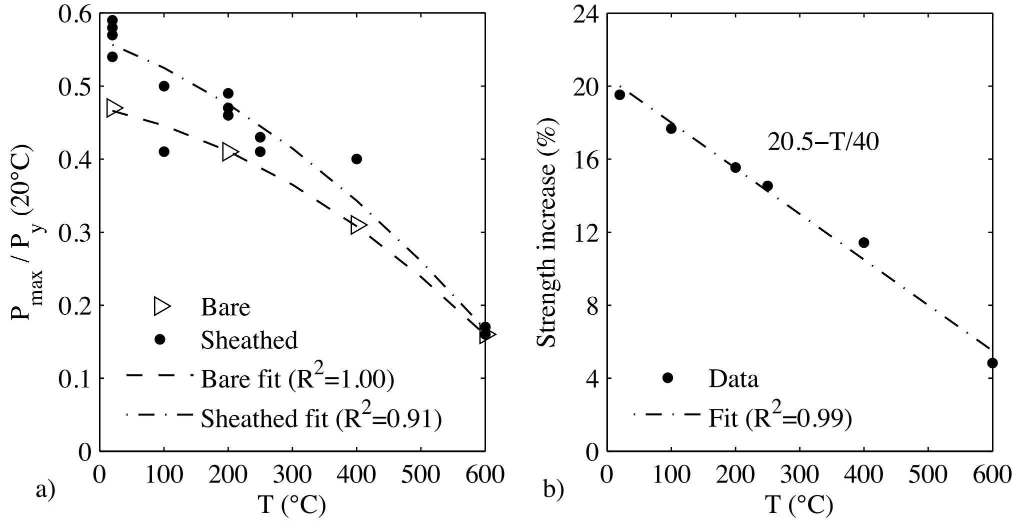

Figure 4-9: a) Degradation of the axial strength of bare and sheathed 1.0 m [39.37 in.] long studs, and b) loss of strength increase obtained through sheathing with temperature

References

Batista Abreu J, Vieira L, Abu-Hamd M, Schafer B (2014) Review: development of performance-based fire design for cold-formed steel. Fire Science Reviews 3 (1):1

Cramer S, Friday O, White R, Sriprutkiat G (2003) Mechanical Properties Of Gypsum Board At Elevated Temperatures. Fire And Materials 2003: 8th International Conference:33 - 42

Gerlich JT (1995) Design of Loadbearing Light Steel Frame Walls for Fire Resistance. vol Fire Engineering Research Report 95/3. School of Engineering, University of Canterbury, Christchurch, New Zealand

Rahmanian I (2011) Thermal and mechanical properties of gypsum boards and their influence on fire resistance of gypsum board based systems. University of Manchester, England

Schafer BW (2013) Final Report: Sheathing Braced Design of Wall Studs. Johns Hopkins University, prepared for the American Iron and Steel Institute, Washington, DC.

Sinha A, Nairn J, Gupta R (2011) Thermal degradation of bending strength of plywood and oriented strand board: a kinetics approach. Wood Sci Technol 45 (2):315-330. doi:10.1007/s00226-010-0329-3

Vieira Jr LCM, Schafer BW (2012) Lateral stiffness and strength of sheathing braced cold-formed steel stud walls. Engineering Structures 37 (0):205-213. doi:http://dx.doi.org/10.1016/j.engstruct.2011.12.029

Vieira Jr LCM, Shifferaw Y, Schafer BW (2011) Experiments on sheathed cold-formed steel studs in compression. Journal of Constructional Steel Research 67 (10):1554-1566. doi:http://dx.doi.org/10.1016/j.jcsr.2011.03.029

Vieira LCM (2011) Behavior and design of sheathed cold-formed steel stud walls under compression. Johns Hopkins University, Baltimore, MD.

Chapter 5 – Experiments on stud-to-sheathing connections at elevated temperatures

The stability and strength of cold-formed steel members significantly depends on the boundary conditions, including restraints along the member length. Sheathing provides these restraints at screw locations, increasing the load-carrying capacity of the thin-walled members and stabilizing them against distortional and global buckling. Vieira Jr and Schafer (2012) characterized the stiffness provided by sheathing through small-scale tests, considering different studs, fasteners, sheathing materials, and spacing between connectors. Then, a simple analytical model to estimate the stiffness provided by the sheathing and stud-to-sheathing connection was developed. Based on this model, Schafer (2013) provided a design formulation to determine the strength of sheathed walls. The design formulation was validated at normal (i.e. 20 °C and 65 % humidity), saturated, and dry (i.e. after keeping sheathing at 103 °C during 7 days) conditions. However, the effect of elevated temperatures was not included.

During a fire, sheathing plays a major role: sheathing boards control the amount of heat transferred from one compartment to another, and through the CFS members; the passage of smoke and flames through a wall depends on the damage of the board (e.g. cracking or joint opening) governed by the mechanical response of the system at elevated temperatures; and, the load-carrying capacity and stability of the CFS members significantly rely on the restrains provided by sheathing. In other words, sheathing governs the thermal response and has a strong impact on the mechanical response of the system.

This chapter focuses on the degradation of the translational (lateral) stiffness and pull-through fastener stiffness at the stud-to-sheathing fastener locations, at elevated temperatures. A total of 54 tests were carried out at temperatures from 20°C to 400 °C. This chapter studies the effect of elevated temperatures on sheathing bracing, and provides temperature-dependent retention factors to be used along with the design formulation for sheathed walls by Schafer (2013).

5.1 Experimental investigation on the in-plane lateral stiffness of stud-to-sheathing connections at elevated temperatures

CFS walls contain thin-walled members braced by sheathing boards usually composed of gypsum, fire-rated gypsum or oriented strand board. Along the wall height, self-drilled screws are used to connect CFS studs and sheathing boards at regular intervals. When the studs are loaded under compression and/or heated up under fire, stud-to-sheathing connections develop forces contributing to the load-carrying capacity and stability of the system. The stiffness provided by the connection is classified as rotational and translational both in-plane and out-of-plane. In-plane translational (or lateral) stiffness is activated by a relative shear between the stud flange and the sheathing caused by weak-axis flexural, or torsional buckling. The in-plane translational stiffness consists of direct diaphragm resistance, and tilting and bearing fastener resistance (as described by (Vieira Jr and Schafer 2012)).

A total of 26 tests were completed to experimentally obtain the in-plane lateral stiffness of stud-to-sheathing connections, with the objective of determining the degradation of the connection stiffness with increasing temperature.

5.1.1 Test specimens

Specimens consisted of two 12 in. long lipped channels with web, flanges, and lips nominally measuring 153 mm [6.02 in.], 43 mm [1.69 in.], and 13 mm [0.51 in.], respectively. The thickness of the cold-formed steel sections was 1.55 mm [0.061 in.]. Each flange was connected to 12 in. x 12 in. pieces of sheathing boards at two locations. Screws #6 1-5/8" (41.3 mm) and #8 1 15/16" (49.2 mm) were used to connect 11.5 mm [0.45 in.] thick gypsum boards (both regular gypsum and fire rated gypsum) and 12.7 mm [0.50 in.] thick OSB, respectively (Figure 5-1). The webs of the CFS channels were perforated in the middle to allow for the passage of high-temperature steel extension rods used to apply the load (Figure 5.2-a).

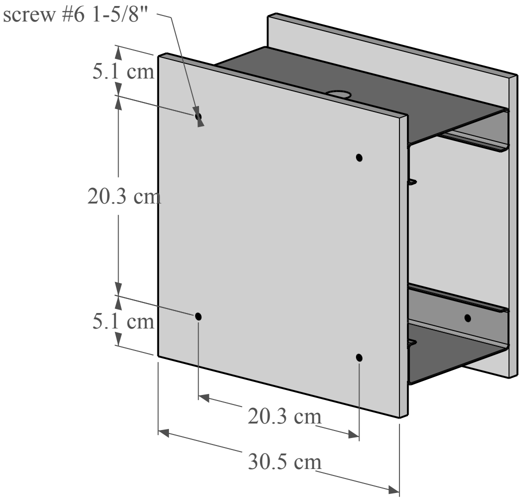

Figure 5-1: Sketch of specimen for in-plane lateral stiffness tests

5.1.2 Test setup and procedure

The test method followed Winter's methodology for determining the translational stiffness of stud-to-sheathing connections. Two steel plates were used to restrain the web of each CFS channel, as illustrated in Figure 5-2-a. The 3/8 in. [0.95 cm] thick plates sandwiched the thin web, minimizing bending of the CFS member. These plates were connected at 4 locations (Figure 5-2-b), using bolts with a diameter of 5/8 in. [0.95 cm]. High-temperature steel extension rods connected to the plates were used to apply the load to the specimen.

After the specimen was constructed (Figure 5-3-a), environmental moisture and temperature were measured (Table C-1, Appendix C). Steady-state test were conducted. First, the temperature of the specimen was increase inside an electric furnace with internal dimensions of 15.75 in. x 15.75 in. x 15.75 in. [40 cm x 40 cm x 40 cm], as shown in Figure 5-.3-b. The heating rate was 10 °C/min, approximately. A set of 7 type-K thermocouples (TC) was used to measure the temperature of the specimens (Figure 5-4). TC1, TC6 and TC7 were located on the external surface of the boards; TC2, TC3 and TC4 measured the temperature inside the gypsum board in the middle of the thickness; and, TC5 measured the temperature on the internal surface of a board at mid-height. An additional thermocouple was used to monitor air temperature at the center of the furnace. The specimen was free to deform during the heating phase. Once the temperature reads from all thermocouples were stable and reached the target temperature, vertical displacement was gradually applied to the specimen through a hydraulic device.

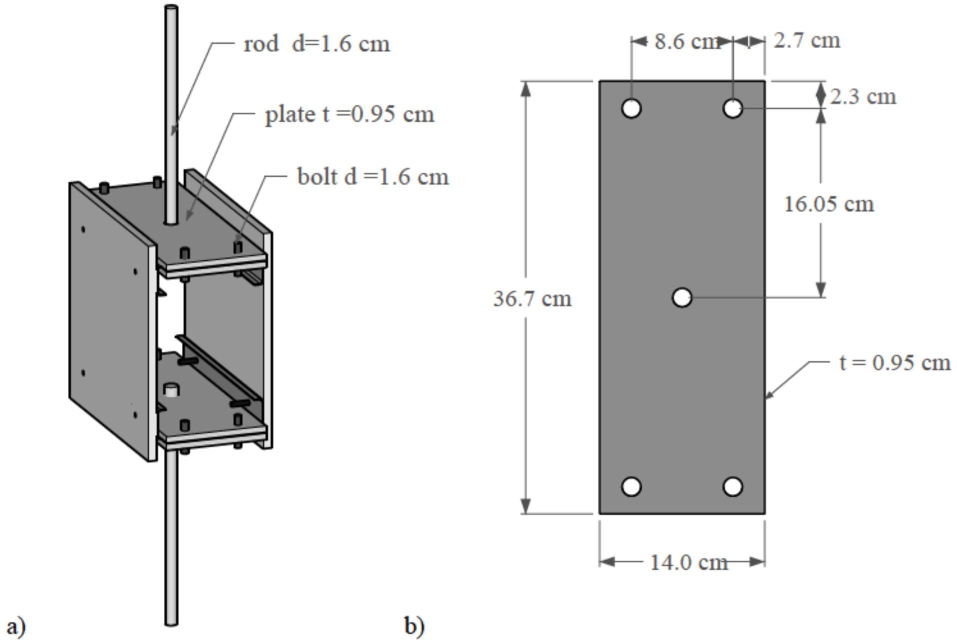

Figure 5-2: a) Test setup for in-plane lateral stiffness tests, and b) dimensions of plates

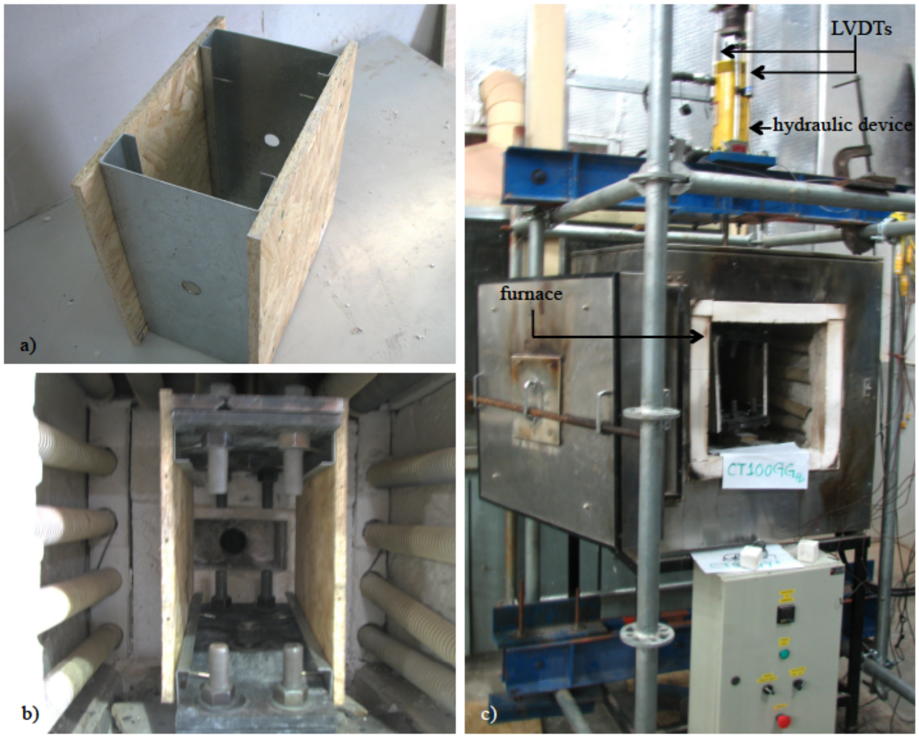

Figure 5-3: In-plane lateral stiffness test a) OSB specimen before testing, b) OSB specimen inside electric furnace, c) electric furnace and testing frame

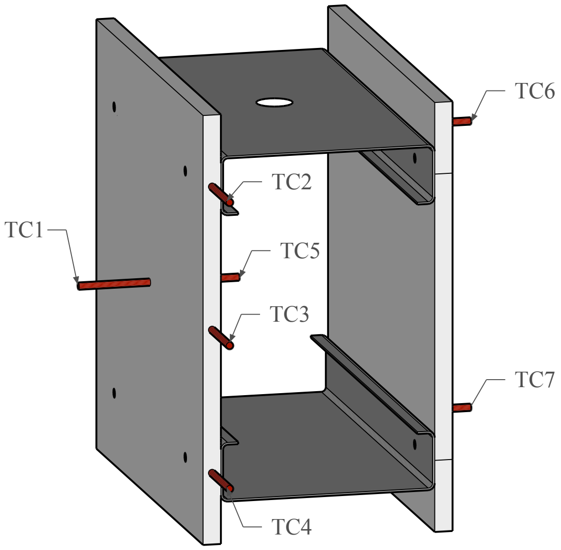

Figure 5-4: Thermocouple distribution on the specimen

A load cell placed under the furnace was used to measure forces with a precision of 0.0003 kgf. Two LVDTs placed outside the furnace were used to measure the vertical displacements (Figure 5-3-c). Load was applied until failure occurred, considering a significant drop on the load measured.

5.1.3 Experimental results from in-plane lateral stiffness tests at elevated temperatures

Load versus displacement curves were obtained for each test, corresponding to a sheathing material and temperature. Figure 5-5 shows the results corresponding to gypsum specimens. All curves are provided in Appendix C.

The maximum load the specimen withstood during testing (P_{max}) significantly drops from 100 °C to 200 °C. Between this temperature range, dehydration of the gypsum occurs. P_{max} tends to be developed at smaller displacements with increasing temperature;

therefore, the connection requires less mechanical energy to reach its load-carrying capacity as the temperature increases.

The lateral stiffness of the stud-to-sheathing connection was computed through the secant and tangent method. In the secant method, the slope of a secant intersecting 40% of the maximum load was computed (i.e. k_S). This method has been commonly used in the past. In the tangent method, a similar approach by Vieira (2011) was utilized. The tangent stiffness defines the stiffness of the linear branch of the load-displacement curve. The tangent stiffness (i.e. k_T) was computed by segmenting the curve into groups of at least 30 points; fitting them to a linear curve; and obtaining the maximum slope of all the segments. This tangent method avoids assuming low stiffness resulting from initial accommodation of the specimen, or early degradation at or before 40% of the maximum load. In general, the tangent stiffness is moderately larger than the secant stiffness, and has been found appropriate for designing CFS walls at ambient temperature. In general, both secant stiffness and tangent stiffness degrade with increasing temperature for all sheathing materials studied (Table 5.1).

The effect of time of high temperature exposure is also important since dehydration of the board is not instantaneous, and affects the strength and stiffness of the connection. Six gypsum specimens were tested at 100 °C, varying the time of exposure to high temperature before applying load. Results are provided in Table 5-1 (specimens CT100G1-6).

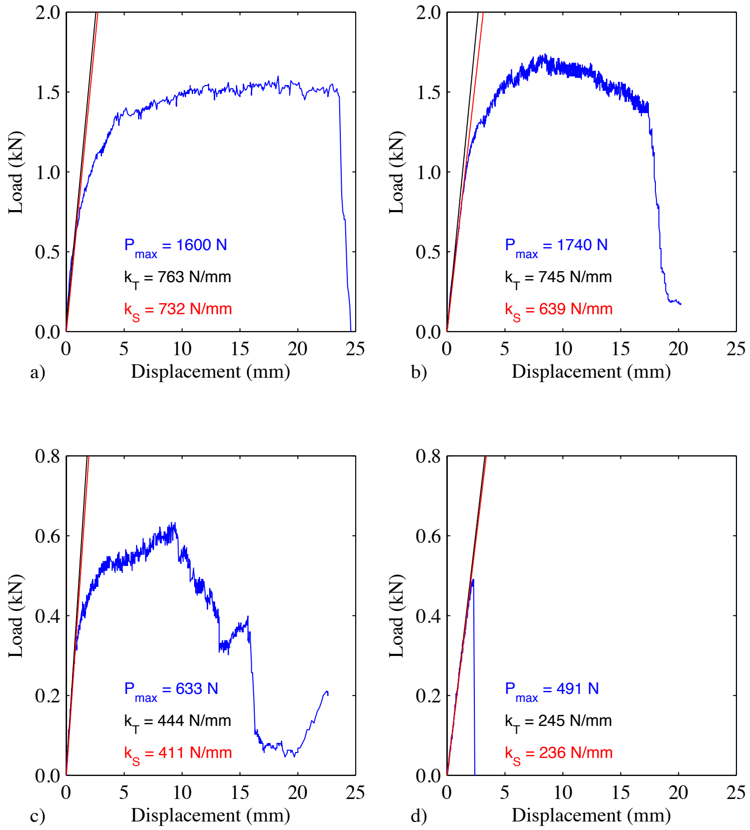

Figure 5-5: Tensile load versus displacement of in-plane lateral stiffness test gypsum specimens, tested after 20 minutes at a) 20 °C, b) 100 °C, c) 200 °C, and d) 300 °C

Average results at ambient conditions are compared against results from similar tests reported in the literature (Vieira 2011; Peterman and Schafer 2013). Despite of differences in material properties and geometry of specimens, experimental values are comparable in most cases.

Regardless the type of material, bearing failure was observed at 20 °C and 100 °C, except for OSB specimens at 100 °C that developed shear fracture of the screws. At temperatures above 100 °C, specimens incurred sheathing fracture, except for gypsum specimens at 200 °C that developed noticeable tearing, OSB specimens at 200 °C that failed due to screw shear fracture, and OSB specimens at 250 °C that failed due to bearing (Figures C-13, C-14 and C-15 in Appendix C).

Table 5.1: Results of in-plane lateral stiffness tests with increasing temperature

Sheathing	Test	T (°C)	t (min)	k_T (N/mm)	k_S (N/mm)	T_{max} (N)
Gypsum	CT20G1	20	20	763	732	1600
	CT20G2	20	20	974	590	1750
	CT100G1	100	10	707	461	2370
	CT100G2	100	10	720	578	2130
	CT100G3	100	20	743	593	2210
	CT100G4	100	20	745	639	1740
	CT100G5	100	30	586	450	2460
	CT100G6	100	40	516	446	2010
	CT200G1	200	20	498	377	662
	CT200G2	200	20	444	411	633
	CT300G1	300	20	245	236	491
	CT300G2	300	20	206	189	511
Fire-rated gypsum	CT20Y1	20	20	625	568	2740
	CT100Y1	100	20	678	481	3300
	CT300Y1	300	20	265	193	1270
	CT400Y1	400	20	-	-	26
Oriented strand board	CT20O1	20	20	1518	1275	9200
	CT20O2	20	20	1513	1238	8720
	CT100O1	100	20	1430	1084	6490
	CT100O2	100	20	1214	894	5970
	CT200O1	200	20	720	584	5860
	CT200O2	200	20	672	569	5650
	CT250O1	250	20	1059	940	3540
	CT250O2	250	20	931	816	3670
	CT350O1	350	20	698	633	473
	CT350O2	350	20	626	541	500

Table 5-3: Average in-plane lateral stiffness test results at ambient temperature

Material	Author	k_T (kN/mm)	k_S (kN/mm)	P_{max} (kN)
Gypsum	Batista	0.9	0.7	1.7
	Peterman	-	1.2	2.2
	Vieira	0.9	0.8	1.3
OSB	Batista	1.5	1.3	9.0
	Peterman	-	3.0	8.7
	Vieira	2.4	1.6	9.2

5.1.4 Discussion

A general trend is observed in results of in-plane lateral stiffness tests: both strength and stiffness of stud-to-sheathing connections degrade with increasing temperature. Figure 5-6 shows temperature-dependent tangent and secant stiffness of gypsum, fire-rated gypsum and OSB specimens, normalized to stiffness values at ambient temperature (i.e. 20 °C). The normalized values represent in-plane lateral stiffness retention factors. The rate of degradation with temperature is similar for gypsum and fire-rated gypsum; however, gypsum boards show higher degradation with increasing temperature compared to fire-rated gypsum and OSB (Figure 5-6-d).

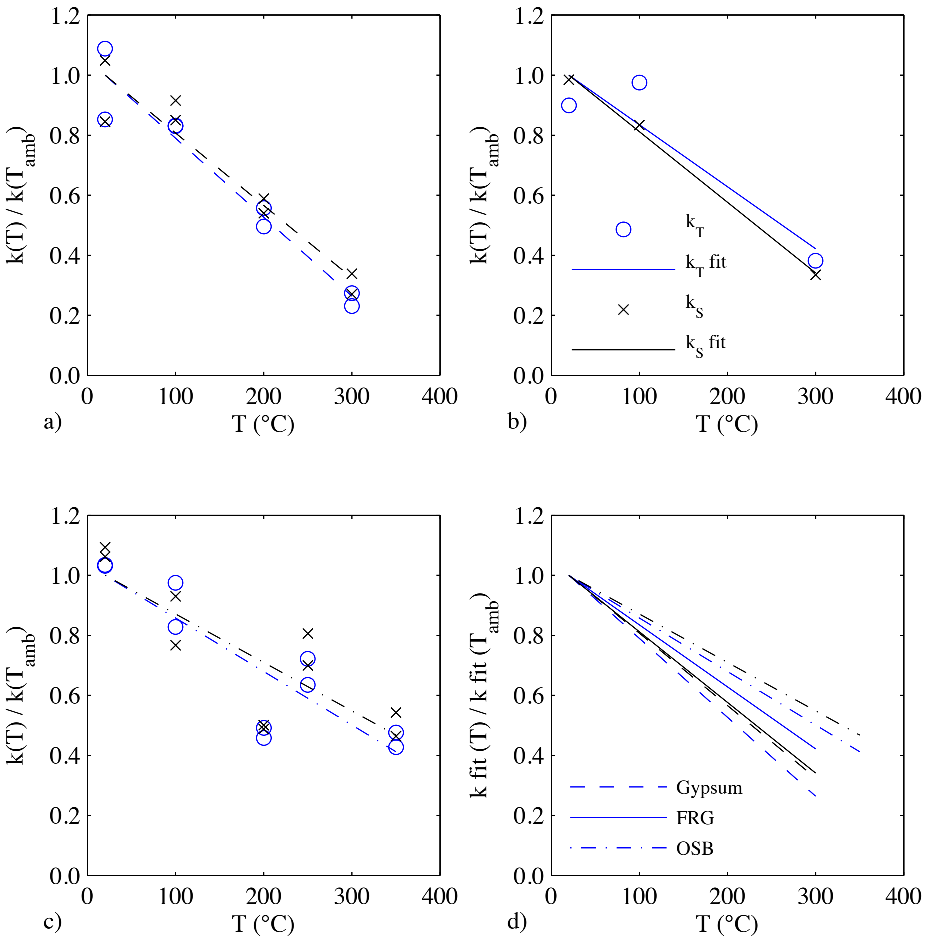

Figure 5-6: In-plane lateral tangent stiffness "k_T" (blue) and secant stiffness "k_S" (black) degradation with increasing temperature for a) gypsum specimens, b) fire-rated gypsum specimens, and c) oriented strand board specimens, and d) comparison of fitted results

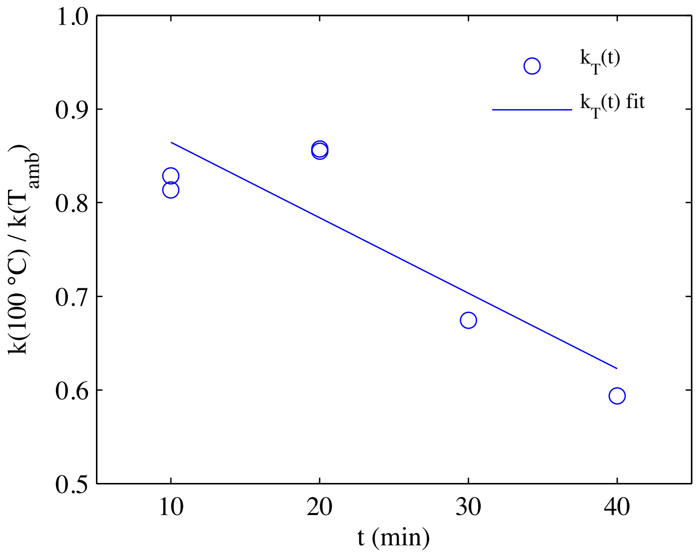

Figure 5-7: In-plane lateral stiffness degradation at 100 °C with time of gypsum specimens

Through the method used to obtain the tangent stiffness of the connection, it is observed a degradation of the in-plane lateral stiffness at 100 °C with increasing time of high temperature exposure, from 10 to 40 minutes (Figure 5-7). This degradation is associated with the dehydration processes occurring in the gypsum board. While losing moisture, gypsum loses strength and stiffness. This augmented degradation with increasing time of fire exposure suggests that retention factors do not only depend on the temperature of the material but also on the heating rates. Future work should focus on the determination of strength and stiffness at elevated temperatures in relation to time of fire exposure or heating rates. Ideally, materials will be tested following time-temperature curves that represent realistic heating conditions.

5.2 Experimental investigation on the pull-through fastener stiffness of stud-to-sheathing connections at elevated temperatures

The objective of the tests presented in this section is to experimentally obtain the stiffness of fastener connections when the fastener is pulled, forcing the head of the fastener to pass through the board. Pull-through and bearing are dominant failure modes experimentally characterized at ambient conditions (Peterman and Schafer 2013). These failure modes were also observed in sheathed stud testing at elevated temperatures described in Chapter 4 (Figure 5-8). For instance, when distortional buckling occurs, the flanges of CFS studs rotate in or out their original position. The screws connected to the board develop forces in the connection while restraining this rotation. Aiming to characterize the degradation of the pull-through fastener stiffness of stud-to-sheathing connections, a total of 28 tests were completed using different materials at temperatures ranging from ambient (20 °C approximately) to 300 °C.

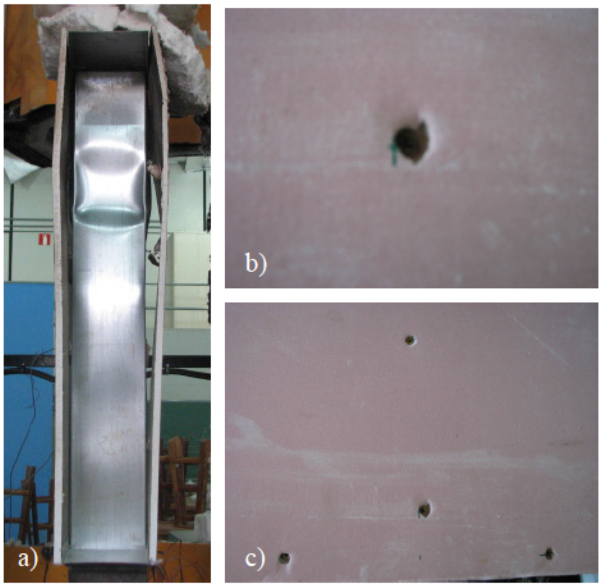

Figure 5-8: Fastener pull-through failure during compression test of sheathed stud at elevated temperature, a) sheathed stud after test, and holes at b) mid-height and c) bottom connections due to fastener pull-through

5.2.1 Test specimens

Specimens were created with 4 in. x 4 in. [10 cm x 10 cm] pieces of sheathing boards composed of gypsum, fire-rated gypsum or OSB. A single screw was self-drilled in the center of each piece of board. Screws #6 1-5/8" (41.3 mm) were used for 11.5 mm [0.45 in.] thick gypsum and fire-rated gypsum boards; and screws #8 1 15/16" (49.2 mm) were used for 12.7 mm [0.50 in.] thick OSB boards. Figure 5-9 shows a specimen for pull-through fastener stiffness test.

Figure 5-9: OSB specimen for pull-through fastener stiffness test

5.2.2 Test setup and procedure

Specimens were place inside a steel hollow tube 6 in. x 6 in. x 6 in. [15.2 cm x 15.2 cm x 15.2 cm], 0.5 in. [1.3 cm] thick (Figure 5-10-a). The tip of the screw passed a 1 in. [2.5 cm] diameter hole on the hollow section, and was screwed inside a 5/8 in. [1.6 cm] diameter high-temperature steel rod. The steel hollow tube was anchored at the base to restrain its displacement. Therefore, by applying load to the steel rod, the screw was pulled up and the piece of board developed contact forces against the steel tube (Figure 5-10-b). Ambient temperature and moisture level of the specimens were recorded right before testing (Table D-1, Appendix D).

The test procedure followed the steady state method. First, the temperature was raised with a rate about 10 °C/min, until reaching the target temperature. Three type-K thermocouples were used to measure the temperature of the specimen. Two of them were inserted in the middle of the thickness of the board, and the other was placed between the surface of the board and the steel hollow tube. An additional type-K thermocouple was used to measure air temperature inside the hollow steel tube. Once the temperature reads reached the target temperature and were stable for 20 minutes, vertical displacement of the high-temperature steel rod was applied at about 0.01 mm/sec (0.0004 in./sec) using a hydraulic device, consequently pulling up the screw. A load cell placed under the furnace was used to measure forces with a precision of 0.0003 kgf (0.0007 lbf). Two LVDTs were used to measure vertical displacement, as illustrated in Figure 5-3-c. The tests were finished once the load reading was significantly low after the load peak.

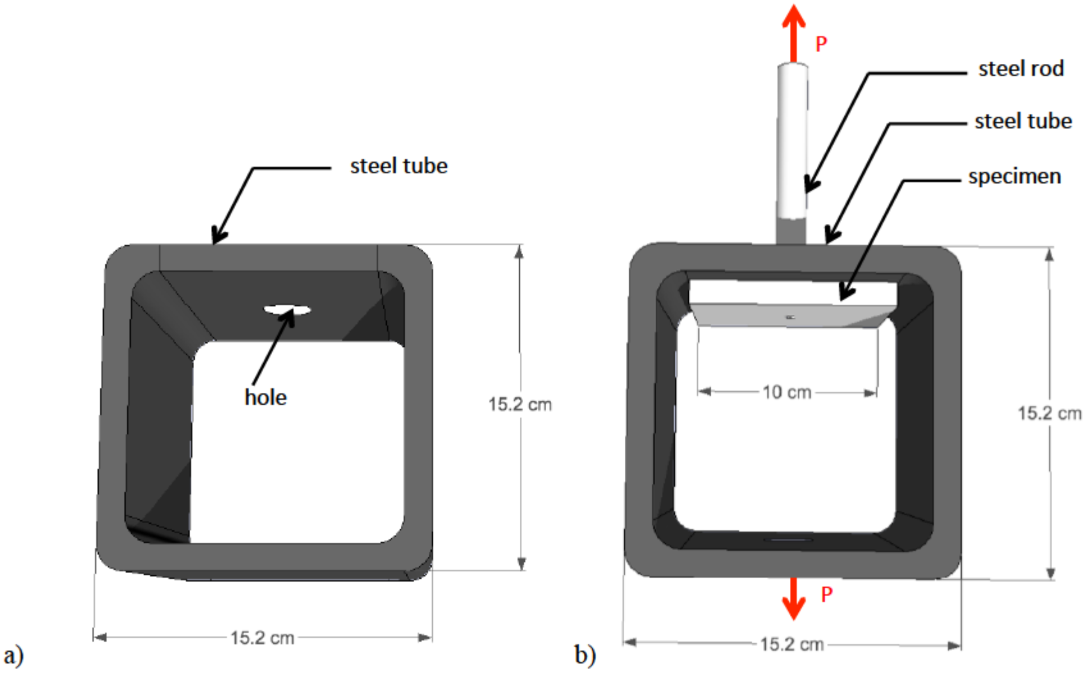

Figure 5-10: Pull-through fastener stiffness test setup, a) steel tube, and b) specimen connected to high-temperature steel rod

5.2.3 Experimental results from pull-through fastener stiffness tests at elevated temperatures

Load-displacement curves were constructed with experimental data (Appendix D). Figure 5-11 shows the results for gypsum specimens tested at 20 °C, 100 °C, 200 °C, and 300 °C, after 20 minutes of exposure to elevated temperature. A significant drop of maximum load (P_{max}) is observed from 100 °C to 200 °C, due to gypsum dehydration. Both, gypsum and fire-rated gypsum, develop ultimate strengths at 100 °C higher than their strength at ambient conditions (compare peaks in Figure 5-11-a and b, and see Table 5.3). Further investigation is needed to relate this observed strength gain at 100 °C in relation to the material behavior of gypsum and paper at this temperature.

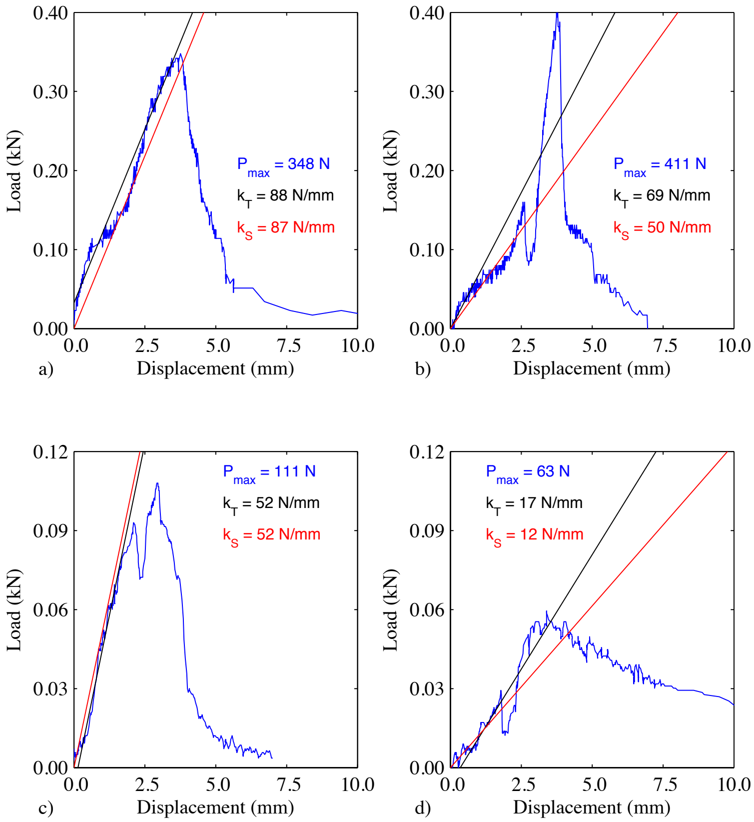

Figure 5-11: Tensile load versus displacement of pull-through fastener stiffness test gypsum specimens, tested after 20 minutes at a) 20 °C, b) 100 °C, c) 200 °C, and d) 300 °C

Tangent and secant stiffness values were computed using the same method described in Section 5.1.3. Results are provided in Table 5.3.

Table 5.3: Results of fastener pull-through stiffness tests with increasing temperature

Sheathing	Test	T (°C)	t (min)	k_T (N/mm)	k_S (N/mm)	T_{max} (N)
Gypsum	FT20G1	20	20	88	87	348
	FT20G2	20	20	118	111	359
	FT100G1	100	10	95	63	513
	FT100G2	100	10	77	54	542
	FT100G3	100	20	69	50	411
	FT100G4	100	20	70	42	422
	FT100G5	100	30	67	60	337
	FT100G6	100	40	64	55	308
	FT200G1	200	20	46	34	108
	FT200G2	200	20	52	52	111
	FT300G1	300	20	9	8	34
	FT300G2	300	20	17	12	63
Fire-rated gypsum	FT20Y1	20	20	124	96	422
	FT20Y2	20	20	151	141	530
	FT100Y1	100	20	64	54	593
	FT100Y2	100	20	68	57	445
	FT200Y1	200	20	72	70	165
	FT200Y2	200	20	69	68	165
	FT300Y1	300	20	38	20	131
	FT300Y2	300	20	27	22	165
Oriented strand board	FT20O1	20	20	571	469	1080
	FT20O2	20	20	795	518	1430
	FT100O1	100	20	666	426	1030
	FT100O2	100	20	495	352	776
	FT200O1	200	20	369	203	553
	FT200O2	200	20	397	228	633
	FT300O1	300	20	15	13	137
	FT300O2	300	20	10	10	86

5.2.4 Discussion

In general, tangent stiffness is moderately higher than the secant in cases when early degradation of the connection occurs (before and around 40% of the peak load). Pull-through fastener stiffness degrades significantly with increasing temperature, caused by degradation of the sheathing material.

Figures 5-12 provides temperature-dependent pull-through fastener stiffness (both secant and tangent) normalized to results at ambient temperature (i.e. 20 °C) for gypsum, fire-rated gypsum and OSB specimens, respectively. Fire-rated gypsum specimens developed higher stiffness and strength retention at elevated temperatures. OSB develops faster degradation of pull-through fastener stiffness compared to gypsum and fire-rated gypsum.

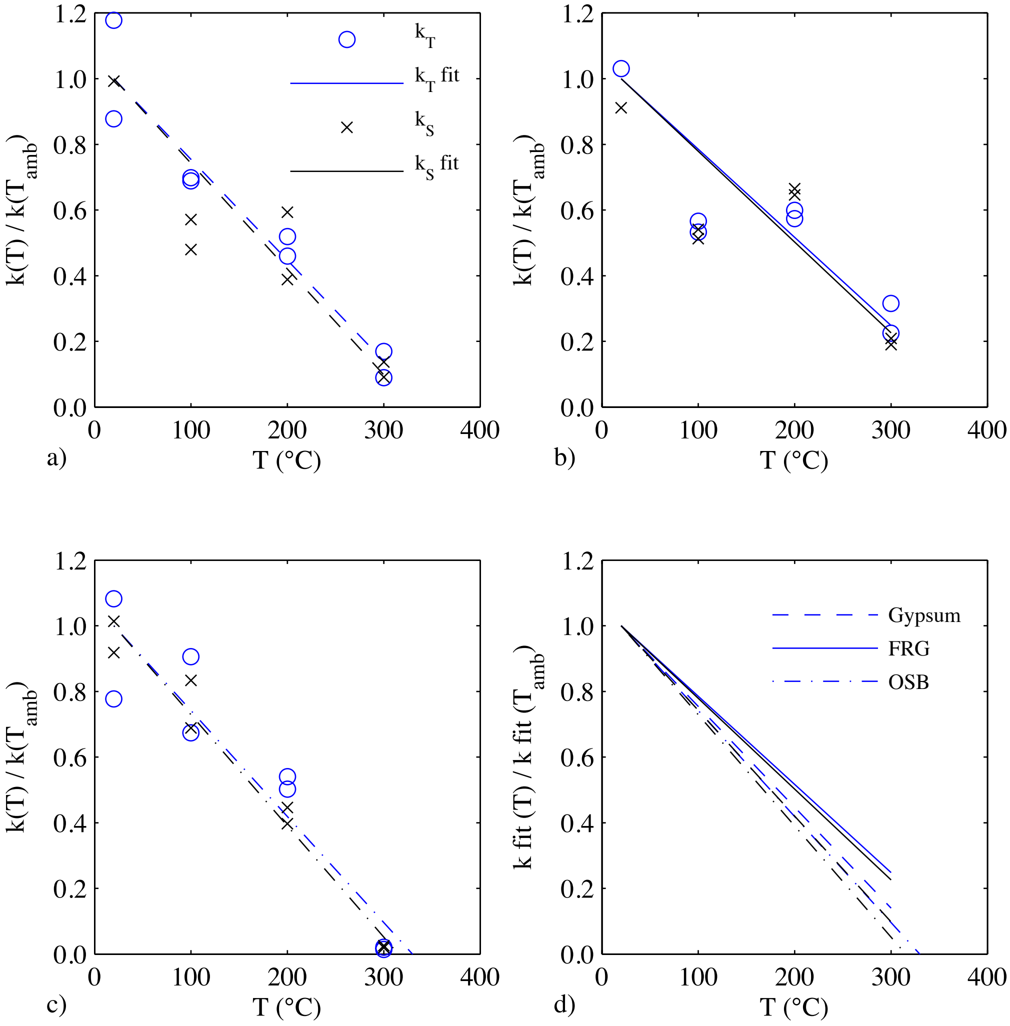

Figure 5-12: Fastener pull-through tangent stiffness "k_T" (blue) and secant stiffness "k_S" (black) degradation with increasing temperature for a) gypsum specimens, b) fire-rated gypsum specimens, and c) oriented strand board specimens, and d) comparison of fitted results

Results for gypsum and fire-rated gypsum are similar: there is a rapid stiffness degradation from 20 °C to 100 °C, and from 200 °C to 300 °C. Between, 100 °C and 200 °C the stiffness does not change significantly. Notice at about 100 °C gypsum dehydrates and at after 200 °C the paper enclosing the gypsum core burns. Results suggest that after gypsum dehydration and before the paper burns, the pull-through fastener stiffness remains quite constant.

Figures 5-13 show time-dependent retention factors for gypsum specimens at 100 °C. Results show that stiffness retention decreases by increasing the time of exposure to elevated temperature. Similar to in-plane lateral stiffness tests, this results imply that the degradation of material strength and stiffness not only depends on the maximum temperature of the material but also on the time of exposure to such temperature (i.e. time-temperature history).

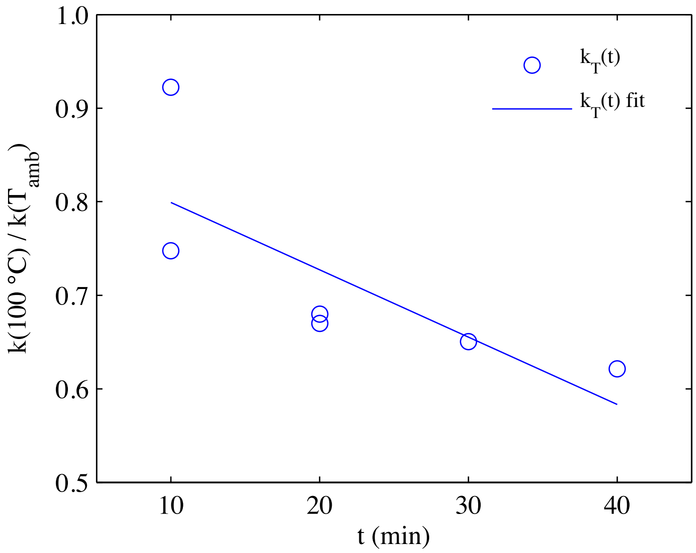

Figure 5-13 Fastener pull-through stiffness degradation at 100 °C with time of gypsum specimens

References

Peterman, K. D. and B. W. Schafer (2013). Hysteretic shear response of fasteners connecting sheathing to cold-formed steel studs. CFS NEES Research Report 04.

Schafer, B. W. (2013). Final Report: Sheathing Braced Design of Wall Studs. Washington, DC., Johns Hopkins University, prepared for the American Iron and Steel Institute.

Vieira Jr, L. C. M. and B. W. Schafer (2012). "Lateral stiffness and strength of sheathing braced cold-formed steel stud walls." Engineering Structures 37(0): 205-213.

Vieira, L. C. M. (2011). Behavior and design of sheathed cold-formed steel stud walls under compression. Civil Engineering Department. Baltimore, MD., Johns Hopkins University. Doctor of Philosophy.

Chapter 6 – Modeling and design of cold-formed steel material and members at elevated temperatures

This chapter provides models to estimate the mechanical properties of CFS at elevated temperatures, including retention factors for the elastic modulus, yield stress and ultimate stress, and temperature-dependent stress-strain relations based on modified Ramberg-Osgood equations, based on the experimental study presented in Chapter 3. Also, retention factors for the stiffness of stud-to-sheathing connections are proposed, based on experimental results depicted in Chapter 5. Material models are then used to analyze bare and sheathed CFS studs at elevated temperatures, and judge the feasibility of current and proposed design methods for fire design applications. Results are compared against experimental results discussed in Chapter 4.

6.1 Modeling temperature-dependent cold-formed steel material

Analysis and design of CFS members and systems require the understanding of material behavior. For fire design applications, this material behavior needs to be characterized in terms of temperature, since increasing temperatures tend to degrade mechanical properties of CFS. This section provides CFS material model through a set of equations suitable to estimate the effect of elevated temperatures on the mechanical properties of CFS. Equations are based on experimental results on CFS specimens.

6.1.1 Retention factors for cold-formed steel mechanical properties at elevated temperatures

Retention factors for the elastic modulus, yield stress and ultimate stress obtained through tensile tests at elevated temperatures were presented in Chapter 3 (Tables 3.1, 3.2 and 3.4). These retention factors are used to build temperature-dependent equations to estimate the mechanical behavior of CFS at elevated temperatures. Subsequently, mechanical properties are used to construct stress-strain models based on Ramberg-Osgood equations.

Figure 6-1-a shows the retention factors for the elastic modulus of CFS at elevated temperatures (i.e. temperature-dependent elastic modulus normalized to the elastic modulus at ambient conditions). Equations 6-1 and 6-2 are proposed to estimate the elastic modulus at elevated temperatures. Similarly, retention factors for the yield stress and ultimate stress along with proposed curves are provided in Figures 6-2-a and 6-3-a. Equations 6-3 and 6-4 estimate the yield stress, and Equations 6-5, 6-6 and 6-7 estimate the ultimate stress of CFS at elevated temperatures. The proposed equations are compared against retention factors available in AISC and Eurocode in Figures 6-1-b, 6-2-b and 6-3-b. Retention factors from AISC are intended for hot-rolled steel, while the retention factors from Eurocode are specifically used for CFS; therefore, retention factors for the yield stress, and ultimate stress of hot-rolled steel and CFS are different. Eurocode assumes no mechanical degradation of CFS before 100 °C, which is (in general) unconservative compared to experimental results.

An increase of the ultimate stress up to 300 °C was observed in CFS specimens with nominal yield stress of 227 MPa [33ksi] (Figure 6-3-a). This strength increase did not occur in specimens with nominal yield stress of 345 MPa [50 ksi]. The difference might be attributed to differences in chemical composition, and phase transformations originated during the heating process. Further research is needed to better understand the changes in mechanical behavior of CFS at elevated temperature in term of chemical structure and behavior. Conservatively, retention factors for the ultimate stress of CFS is assumed to be 1.00 up to 300 °C.

The following equations are proposed to estimate temperature-dependent mechanical properties of CFS.

For the elastic modulus:

$$20^{\circ}C \leq T \leq 300^{\circ}C \rightarrow \frac{E(T)}{E(T_{amb})} = 1.015 - 0.00075T \quad \text{(Equation 6-1)}$$

$$300^{\circ}C \leq T \leq 700^{\circ}C \rightarrow \frac{E(T)}{E(T_{amb})} = 1.219 - 0.00143T \quad \text{(Equation 6-2)}$$

For the yield stress:

$$20^{\circ}C \leq T \leq 300^{\circ}C \rightarrow \frac{F_y(T)}{F_y(T_{amb})} = 1.013 - 0.00065T \quad \text{(Equation 6-3)}$$

$$300^{\circ}C \leq T \leq 700^{\circ}C \rightarrow \frac{F_y(T)}{F_y(T_{amb})} = 1.337 - 0.00173T \quad \text{(Equation 6-4)}$$

For the ultimate stress:

$$20°C \le T \le 300°C \rightarrow \frac{F_u(T)}{F_u(T_{amb})} = 1.000 \qquad \text{(Equation 6-5)}$$

$$300°C \le T \le 600°C \rightarrow \frac{F_u(T)}{F_u(T_{amb})} = 1.756 - 0.00252T \qquad \text{(Equation 6-6)}$$

$$600°C \le T \le 700°C \rightarrow \frac{F_u(T)}{F_u(T_{amb})} = 0.874 - 0.00105T \qquad \text{(Equation 6-7)}$$

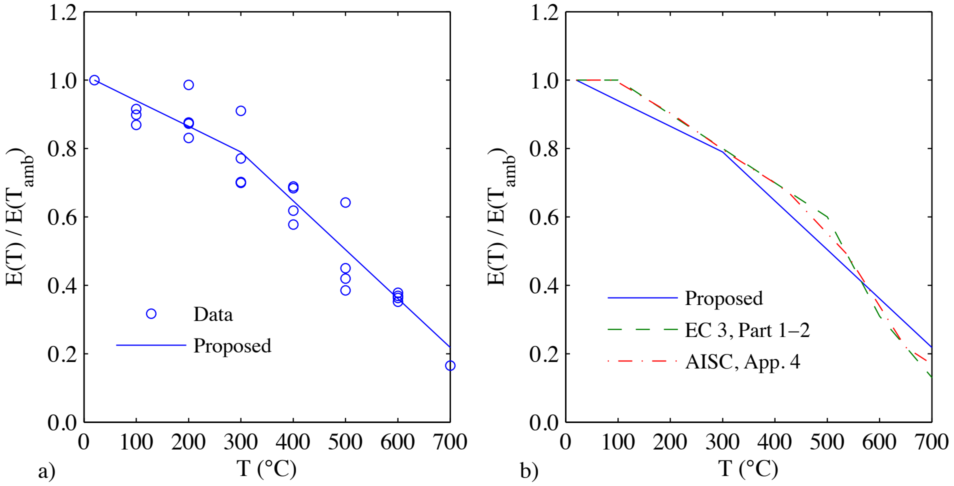

a) b)

Figure 6-1: Retention factors for the elastic modulus of CFS at elevated temperatures, a) experimental data and proposed equation, b) proposed equation and codified equations for steel

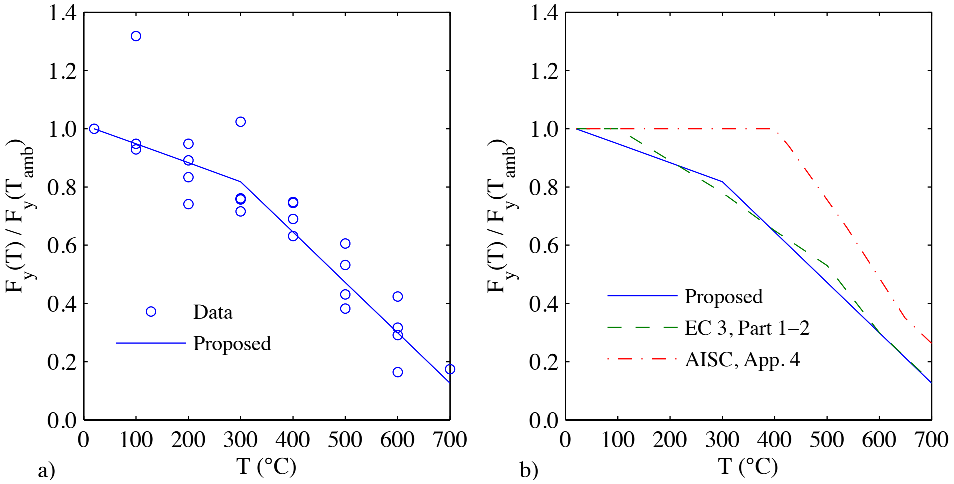

a) b)

Figure 6-2: Retention factors for the yield stress of CFS at elevated temperatures, a) experimental data and proposed equation, b) proposed equation and codified equations for steel

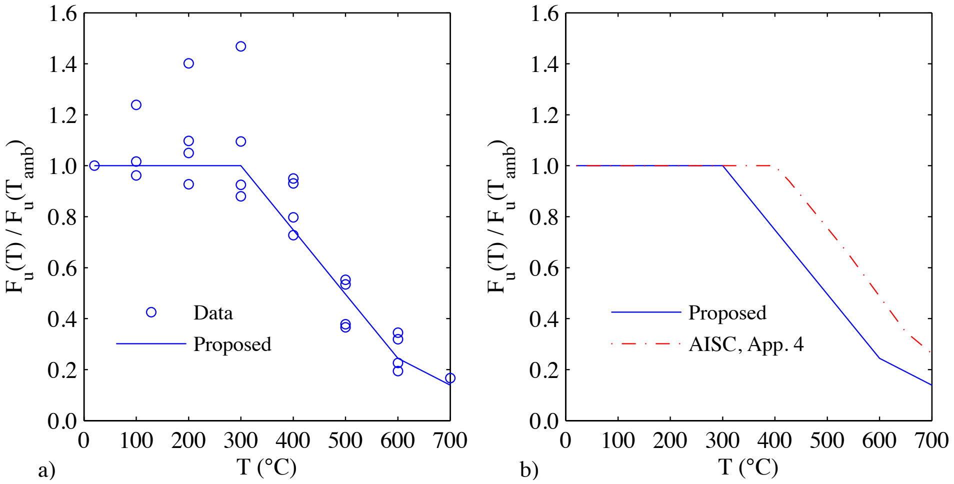

Figure 6-3: Retention factors for the ultimate stress of CFS at elevated temperatures, a) experimental data and proposed equation, b) proposed equation and codified equations for steel

6.1.2 Stress-strain relations for CFS at elevated temperatures

The temperature-dependent stress (σ) - strain (ε) data was fitted to the following modified Ramberg-Osgood equation (rewritten Equation 2-1):

$$\varepsilon(T) = \frac{\sigma(T)}{E(T)} + K(T)\left(\frac{\sigma(T)}{F_y(T)}\right)^{n(T)} \qquad \text{(Equation 6-8)}$$

The elastic modulus (E) and yield stress (Fy) at a given temperature (T) can be computed with Equations 6-1 to 6-7. Ramberg-Osgood parameters (“K” and “n”) were obtained by fitting experimental stress-strain curves to Equations 6-8. Results are provided in Table 6-1, and stress-strain curves are plotted in Figure 6-4. The hardening parameter “n” significantly increases from 400 °C to 700 °C, and reaches a minimum at 300 °C.

Table 6-1: Ramberg-Osgood parameters from curve fitting

T (°C)	K (T)	n(T)
100	1.040E-02	8.331
200	3.840E-03	7.602
300	6.931E-03	6.615
400	1.937E-04	14.870
500	5.108E-02	22.390
600	9.898E-04	36.000
700	6.250E-10	50.960

Table 6-2: Ramberg-Osgood parameters from curve fitting, with K=0.002

T (°C)	n(T)
100	15.240
200	9.285
300	10.070
400	8.920
500	29.001
600	29.020
700	15.861

Considering that the yield stress was obtained through the 0.2% offset method, stress-strain data was fitted to Equation 6-8 with the Ramberg-Osgood strength parameter (K) set to 0.002. Therefore, the strain computed at a stress equal to the 0.2% offset-stress matches the yield strain. The resulting Ramberg-Osgood hardening parameters are shown in Table 6-2, and stress-strain curves are shown in Figure 6-5. The temperature dependent Ramberg-Osgood hardening parameters n(T) were fitted to:

$$n(T) = aT^2 + bT + c \qquad \text{(Equation 6-9)}$$

Constants a, b and c are provided in Table 6-3. The minimum Ramberg-Osgood hardening parameters predicted by Equation 6.9 occurs around 300 °C, reflecting that hardening is more pronounced within this temperature range, as observed in Figure 3-4.

Equation 6-9 predicts a Ramberg-Osgood hardening parameter "n" for CFS equals to 19.9 at ambient temperature; this value may be contrasted against stainless steels that have a typical n between 4.45 and 12.2 (Rasmussen 2003).

Table 6-3: Constants for Ramberg-Osgood hardening parameter (Equation 6-9)

	T (°C)	a ($\times10^{-4}$) ($1/°C^2$)	*b* ($\times10^{-2}$) (1/°C)	c
n(T)	[20, 400]	1.201	-7.824	21.429
	(400, 700]	-8.310	93.494	-231.667

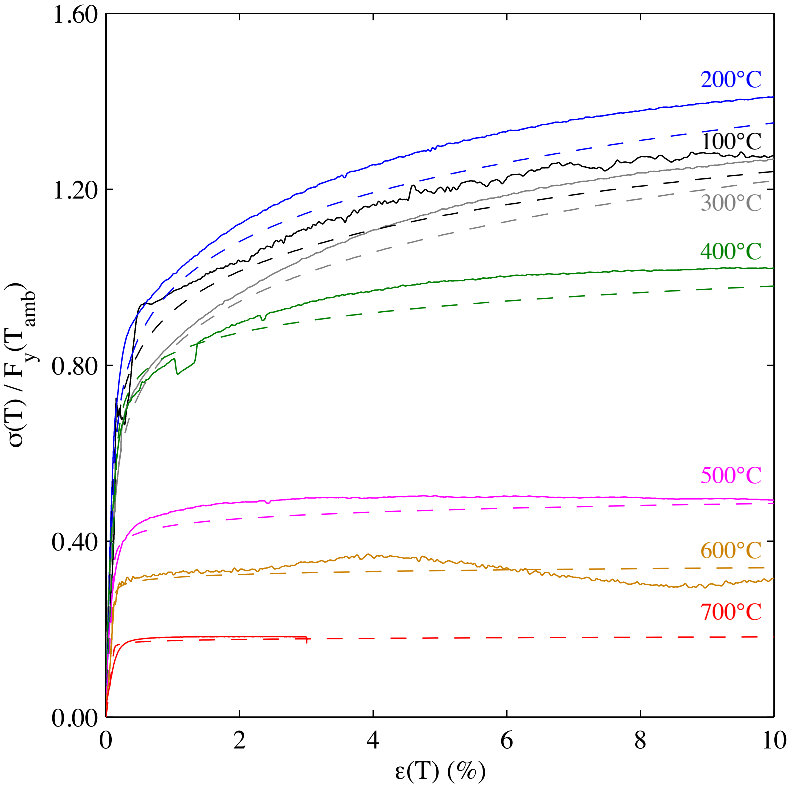

Figure 6-4: Stress strain data (solid lines) and Equation 6.8 (dashed lines) using temperature-dependent Ramberg-Osgood parameters (i.e. "n" and "k")

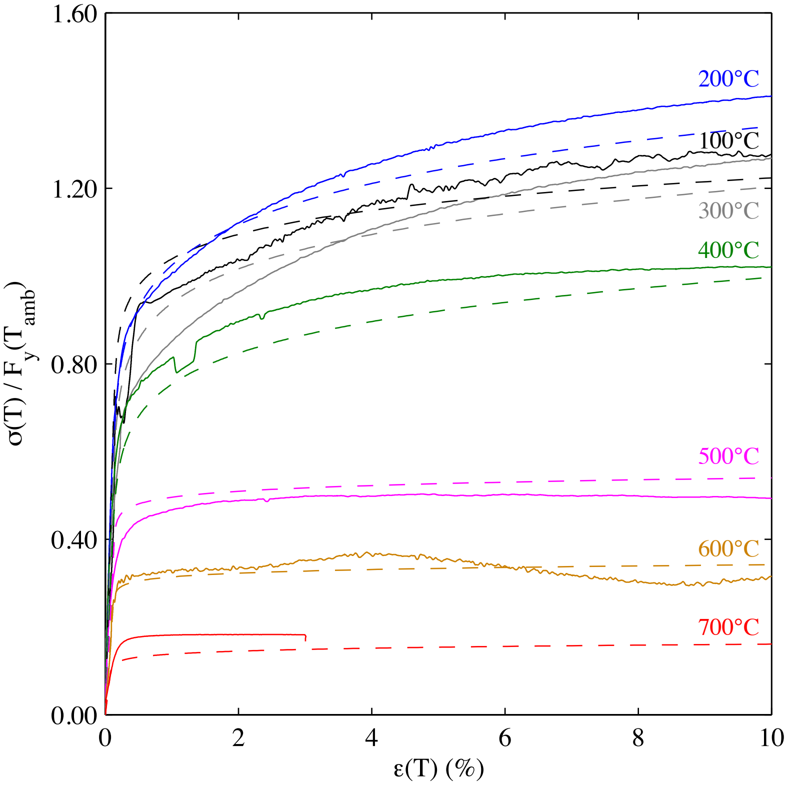

Figure 6-5: Stress strain data (solid lines) and Equation 6.8 (dashed lines) using Ramberg-Osgood parameters “K=0.002” and temperature-dependent “n”

Figure 6-6 provides Ramberg-Osgood parameters for CFS available in the literature and proposed in this chapter. Chen and Ye (2012) adopted a constant Ramberg-Osgood strength parameter equivalent to the offset strain used to compute the yield stress (i.e. K=0.002). Consequently, the predicted strain at a stress equal to the yield stress coincides with the yield strain. Other researchers (Lee, Mahendran et al. 2003; Ranawaka and Mahendran 2009; Kankanamge and Mahendran 2011) have proposed temperature dependent Ramberg-Osgood strength parameters in the range of 3.8×10-6 to 1.1×10-2, even though the yield stresses were determined based on the 0.2% offset method corresponding to 2.0×10-3 (Figure 6-6-a). Therefore, the predicted yield strain do not coincide with the strain at which the predicted yield stress occurs.

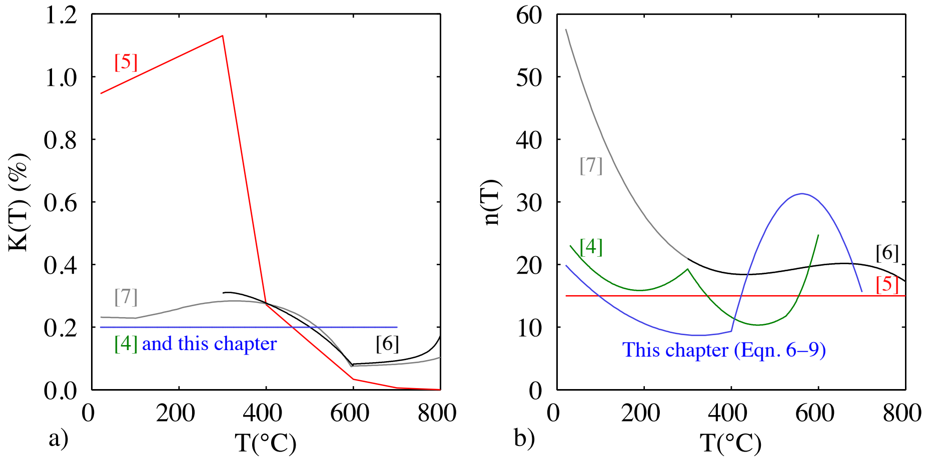

Figure 6-6: Temperature-dependent Ramberg-Osgood a) strength and b) hardening parameters

Significant variability is observed in predicted Ramberg-Osgood hardening parameters (Figure 6-6-b). A large value of "n" implies a flatter stress-strain curve, and therefore small strain hardening. In general, the hardening parameter initially decreases with increasing temperature up to 200 °C; tends to increase from 460 °C to 560 °C; and decreases from 650 °C. Compared to the case at ambient temperature, Figure 6-6-b implies a more pronounced hardening between 200 °C and 400 °C, while negligible hardening is observed at higher temperatures. Further research is necessary to determine accurate Ramberg-Osgood parameters by looking at the actual strength and strain hardening based on the development of dislocation in the crystal structure at elevated temperatures.

A satisfactory agreement is observed between the temperature-dependent stress-strain curves from experimental data and the proposed Ramberg-Osgood equation (Figure 6-7). Stress-strain prediction equations have initial slopes and plastic strains corresponding to the predicted elastic moduli and yield stresses. Maximum stresses can be limited to the ultimate stress computed through Equations 6-5, 6-6 and 6-7.

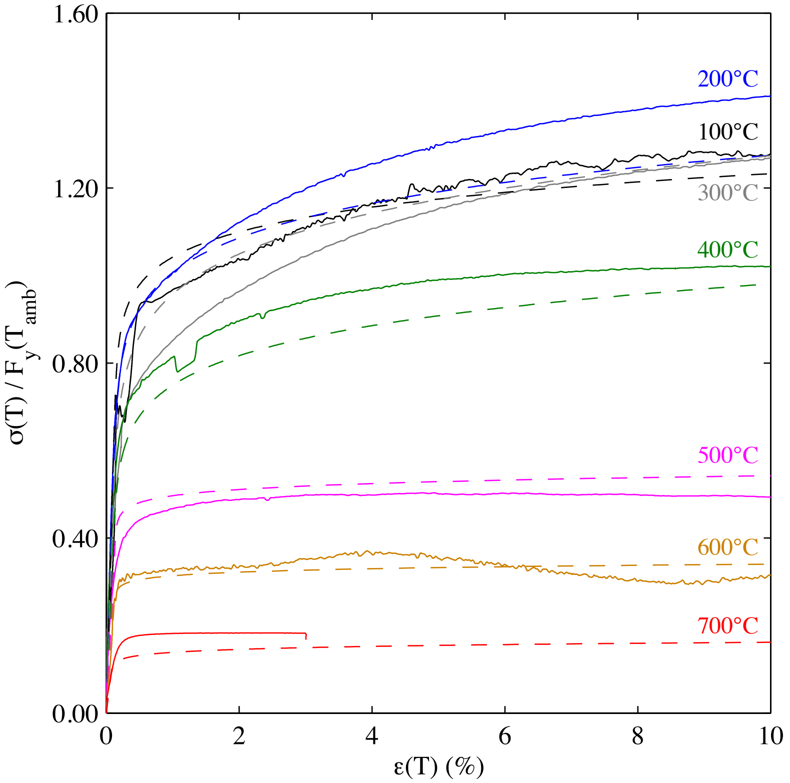

Figure 6-7: Stress strain data (solid lines) and Equation 6.8 (dashed lines) using Ramberg-Osgood parameters "k=0.002" and fitted temperature-dependent "n" (Equation 6.9)

6.1.3 Design equations for CFS mechanical properties

Temperature-dependent CFS material can be modeled following previous sections. Retention factors for mechanical properties of CFS can be obtained with Equations 6-1 to 6-7, and stress-strain relations can be constructed with Equation 6-8 and Equation 6-9 along with Table 6-3, assuming the strength parameter "K" equals to the offset strain used to compute the yield stress (i.e. K=0.002).

6.2 Modeling temperature-dependent stud-to-sheathing connections

Retention factors for the stud-to-sheathing connection stiffness were developed in Chapter 5, based on experimental results from in-plane lateral stiffness tests and fastener pull-through tests.

This section provides equations to determine retention factors according to the temperature of the connection. These equations can be used to account for strength and stiffness degradation of stud-to-sheathing connections with increasing temperatures (in degrees Celsius).

The objective of this work is to enable the analysis and design of sheathed CFS members at elevated temperatures using the methodology proposed by Schafer (2013), based on the experimental work of Vieira (2011) and Peterman (2012), and the temperature-dependent retention factors presented in this section.

6.2.1 Retention factors for in-plane lateral stiffness

The following equations were obtained by fitting experimental data provided in Chapter 5, and extrapolating the data by estimating zero in-plane lateral stiffness at 600 °C. This estimation is based on the fact that bare and sheathed CFS studs have similar strengths at 600 °C (Figure 4-7). Retention factors were computed as the ratio of the stiffness obtained elevated temperature and the stiffness obtained at ambient temperature. Stiffness was computed using secant method at 40% of the maximum load, and using the tangent method described in Section 5.1.3. Equations are provided for secant stiffness and tangent stiffness. Equations are expressed in terms of localized stiffness at the fastener (i.e. “k_{xl}”).

The following equations provide retention factors for the local in-plane lateral secant stiffness.

For gypsum boards:

$$\frac{k_{xl}\left(T\right)}{k_{xl}\left(T_{amb}\right)}=\begin{cases}1.048-0.0024T & if\ 20°C\le T\le 300°C\\ 0.660-0.0011T & if\ 300°C<T\le 600°C\\ 0 & if\ T>600°C\end{cases}\qquad\text{(Equation 6-10)}$$

For fire-rated gypsum boards:

$$\frac{k_{xl}\left(T\right)}{k_{xl}\left(T_{amb}\right)}=\begin{cases}1.048-0.0024T & if\ 20°C\le T\le 300°C\\ 0.660-0.0011T & if\ 300°C<T\le 600°C\\ 0 & if\ T>600°C\end{cases}\qquad\text{(Equation 6-11)}$$

For OSB:

$$\frac{k_{xl}\left(T\right)}{k_{xl}\left(T_{amb}\right)}=\begin{cases}1.032-0.0016T & if\ 20°C\le T\le 350°C\\ 1.102-0.0018T & if\ 350°C<T\le 600°C\\ 0 & if\ T>600°C\end{cases}\qquad\text{(Equation 6-12)}$$

The following equations provide retention factors for the local in-plane lateral tangent stiffness.

For gypsum boards:

$$\frac{k_{xl}\left(T\right)}{k_{xl}\left(T_{amb}\right)}=\begin{cases}1.052-0.0026T & if\ 20°C \le T \le 300°C\\ 0.542-0.0009T & if\ 300°C < T \le 600°C\\ 0 & if\ T > 600°C\end{cases} \qquad \text{(Equation 6-13)}$$

For fire-rated gypsum boards:

$$\frac{k_{xl}\left(T\right)}{k_{xl}\left(T_{amb}\right)}=\begin{cases}1.042-0.0021T & if\ 20°C \le T \le 300°C\\ 0.802-0.0013T & if\ 300°C < T \le 600°C\\ 0 & if\ T > 600°C\end{cases} \qquad \text{(Equation 6-14)}$$

For OSB:

$$\frac{k_{xl}\left(T\right)}{k_{xl}\left(T_{amb}\right)}=\begin{cases}1.036-0.0018T & if\ 20°C \le T \le 350°C\\ 0.966-0.0016T & if\ 350°C < T \le 600°C\\ 0 & if\ T > 600°C\end{cases} \qquad \text{(Equation 6-15)}$$

The following equation provides retention factors for the local in-plane lateral tangent stiffness over time of exposure to 100 °C. It applies to CFS members sheathed with gypsum board with 10 to 40 minutes of exposure to elevated temperature. Equation 6-16 implies that further research is needed to characterize retention factors based on time-temperature history, instead of maximum temperature only.

$$\frac{k_{xl}\left(t,T=100°C\right)}{k_{xl}\left(T_{amb}\right)}=0.945-0.0081t \qquad \text{(Equation 6-16)}$$

6.2.2 Retention factors for fastener pull-through stiffness

The following equations were obtained by fitting experimental data provided in Chapter 5, and extrapolating the data by estimating zero fastener pull-through stiffness at 600 °C. This estimation is based on the fact that bare and sheathed CFS studs have similar strengths at 600 °C (Figure 4-7). Retention factors were computed as the ratio of the stiffness obtained elevated temperature and the stiffness obtained at ambient temperature. Stiffness was computed using secant method at 40% of the maximum load, and using the tangent method described in Section 5.2.3. Equations are provided for secant stiffness and tangent stiffness. Since the pull-through stiffness is directly related to the rotational restraint that sheathing provides to the studs, equations are expressed in terms of rotational stiffness (i.e. "k_ϕ"). The following equations provide retention factors for the rotational secant stiffness.

For gypsum boards:

$$\frac{k_\phi(T)}{k_\phi(T_{amb})} = \begin{cases} 1.064 - 0.0032T & if\ 20°C \le T \le 300°C \\ 0.194 - 0.0003T & if\ 300°C < T \le 600°C \\ 0 & if\ T > 600°C \end{cases} \qquad \text{(Equation 6-17)}$$

For fire-rated gypsum boards:

$$\frac{k_\phi(T)}{k_\phi(T_{amb})} = \begin{cases} 1.056 - 0.0028T & if\ 20°C \le T \le 300°C \\ 0.426 - 0.0007T & if\ 300°C < T \le 600°C \\ 0 & if\ T > 600°C \end{cases} \qquad \text{(Equation 6-18)}$$

For OSB:

$$\frac{k_\phi(T)}{k_\phi(T_{amb})}=\begin{cases}1.068-0.0034T & \text{if } 20°C \le T \le 300°C\\ 0.078-0.0001T & \text{if } 300°C < T \le 600°C\\ 0 & \text{if } T > 600°C\end{cases} \qquad \text{(Equation 6-19)}$$

The following equations provide retention factors for the rotational tangent stiffness.

For gypsum boards with 20 °C ≤ T ≤ 300 °C:

$$\frac{k_\phi(T)}{k_\phi(T_{amb})}=\begin{cases}1.062-0.0031T & \text{if } 20°C \le T \le 300°C\\ 0.252-0.0004T & \text{if } 300°C < T \le 600°C\\ 0 & \text{if } T > 600°C\end{cases} \qquad \text{(Equation 6-20)}$$

For fire-rated gypsum boards with 20 °C ≤ T ≤ 300 °C:

$$\frac{k_\phi(T)}{k_\phi(T_{amb})}=\begin{cases}1.054-0.0027T & \text{if } 20°C \le T \le 300°C\\ 0.484-0.0008T & \text{if } 300°C < T \le 600°C\\ 0 & \text{if } T > 600°C\end{cases} \qquad \text{(Equation 6-21)}$$

For OSB with 20 °C ≤ T ≤ 300 °C:

$$\frac{k_\phi(T)}{k_\phi(T_{amb})}=\begin{cases}1.064-0.0032T & \text{if } 20°C \le T \le 300°C\\ 0.194-0.0003T & \text{if } 300°C < T \le 600°C\\ 0 & \text{if } T > 600°C\end{cases} \qquad \text{(Equation 6-22)}$$

The following equation provides retention factors for the rotational tangent stiffness over time of exposure to 100 °C. It applies to CFS members sheathed with gypsum board with 10 to 40 minutes of exposure to elevated temperature. Equation 6-23 implies that further research is needed to characterize retention factors based on time-temperature history, instead of maximum temperature only.

$$\frac{k_{\phi}\left(t, T=100^{\circ}C\right)}{k_{\phi}\left(T_{amb}\right)} = 0.871 - 0.0072t \qquad \text{(Equation 6-23)}$$

Equations 6-16 and 6-23 imply that the stud-to-sheathing connection stiffness of CFS members sheathed with gypsum boards is completely degraded after 2 hours of exposure to 100 °C. In general, Equations from Section 6.2 indicate that pull-through (or rotational) stiffness degrades faster than the in-plane lateral stiffness of stud-to-sheathing connections with increasing temperature, regardless the type of sheathing material.

6.2.3 Design equations for stud-to-sheathing connections

Consistently with the design formulation proposed by Schafer (2013), secant stiffness will be used. Therefore, retention factors from Equations 6-10 to 6-12 are proposed to estimate the in-plane lateral stiffness, and retention factors from Equations 6-17 to 6-19 are proposed to estimate rotational stiffness at elevated temperatures.

6.3 Design and modeling of bare CFS studs at uniform elevated temperatures

Using the mechanical properties of CFS proposed in Section 6.1, the load-carrying capacity of CFS studs experimentally studied in Chapter 4 are estimated in this section. The analysis consist on computing the elastic buckling loads at elevated temperatures, and using the Direct Strength Method to compute the strength of bare CFS studs. Results are compared against experimental results, and finite element analysis results. This section aims to explore the feasibility of current design method (i.e. DSM) for fire design applications using temperature-dependent mechanical properties.

6.3.1 Elastic buckling loads for bare CFS studs at uniform elevated temperatures

CUFSM (Li and Schafer 2010) was used to compute elastic buckling loads for the member with dimension depicted in Section 4.1.1. Mechanical properties (i.e. elastic modulus) for finite strip analysis were computed using retention factors from Equations 6-1 and 6-2. Shear modulus was computed assuming homogeneous and isotropic material, and constant Poisson's ratio equal to 0.3. The elastic modulus and yield stresses at ambient temperature used for DSM calculations were taken from experiments depicted in Chapter 3, and shown in Table 6-4. The cross-sectional are of the studs is 0.6132 in.^{2} (396 mm^2), and the squash load "P_y" was computed as the product of this area and the yield stress at each temperature (Equation 6-24).

$$P_y\left(T\right) = A_g F_y\left(T\right) \qquad \text{(Equation 6-24)}$$

Results from finite strip analysis (in CUFSM) are provided in Table 6-5. The half-wave lengths for local and distortional buckling are 3.83 in. (97.3 mm) and 14.31 in. (363.5 mm), respectively. Global buckling loads were obtained at 24 in. (0.6 m) and 40 in. (1.0 m). Typical mode shapes are shown in Figure 6-8, and signature curves at each temperature are provided in Figure 6-9.

Table 6-4: Mechanical properties used for elastic buckling and DSM calculations

T (°C)	E ksi (GPa)	G ksi (GPa)	F_y ksi (MPa)	P_y Kip (kN)
20	27106 (186.9)	10425 (71.9)	52.9 (364.7)	32.44 (144.3)
200	23447 (161.7)	9018 (62.2)	46.7 (322.0)	28.64 (127.4)
400	17538 (120.9)	6745 (46.5)	34.1 (235.1)	20.92 (93.1)
600	9785 (67.5)	3764 (26.0)	15.8 (108.9)	9.70 (43.1)

Table 6-5: Elastic-buckling stresses used for DSM calculations

T (°C)	σ_l ksi (MPa)	σ_d ksi (MPa)	$\sigma_{e\,L=24in.}$ ksi (MPa)	$\sigma_{e\,L=40in.}$ ksi (MPa)
20	15.89 (109.5)	23.05 (159.0)	154.15 (1062.8)	58.68 (404.6)
200	13.74 (94.7)	19.97 (137.7)	133.34 (919.4)	50.76 (350.0)
400	10.28 (70.9)	14.94 (103.0)	99.74 (687.7)	37.97 (261.8)
600	5.73 (39.5)	8.34 (57.5)	55.65 (383.7)	21.18 (146.1)

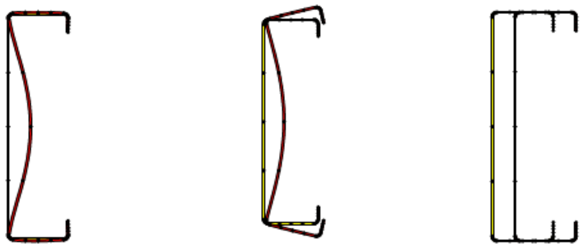
a) b) c)

Figure 6-8: a) Local, b) distortional and c) global mode shapes from CUFSM

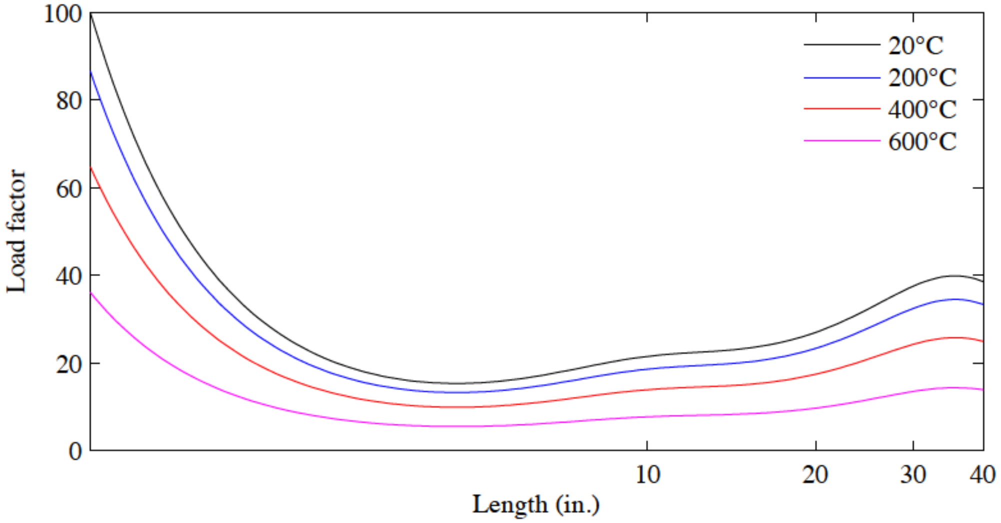

Figure 6-9: Signature curves from CUFSM

6.3.2 Direct-strength method for bare CFS studs at uniform elevated temperatures

The axial strength of bare studs was estimated through current DSM equations from AISI-S100-12 Appendix-1, using temperature-dependent mechanical properties. Nominal loads are provided in Table 6-6.

Normalized axial strength of bare specimens are provided in Figure 6-10 along with DSM predictions. In general, current DSM equations provide satisfactory and slightly conservative estimates; therefore, they are suitable for estimating the load-carrying capacity of CFS studs at uniform elevated temperatures (Heva 2008; Ranawaka and Mahendran 2009). However, adequate CFS mechanical properties should be used in the calculations.

Table 6-6: Nominal buckling loads obtained from DSM calculations

T (°C)	P_{nl} Kip (kN)	P_{nd} Kip (kN)	$P_{ne\ L=24in.}$ Kip (kN)	$P_{ne\ L=40in.}$ Kip (kN)
20	16.59 (73.8)	16.71 (74.3)	28.10 (125.0)	22.24 (98.9)
200	14.51 (64.5)	14.62 (65.0)	24.74 (110.0)	19.49 (86.7)
400	10.71 (47.7)	10.81 (48.1)	18.13 (80.7)	14.36 (63.9)
600	5.39 (24.0)	5.48 (24.4)	8.61 (38.3)	7.10 (31.6)

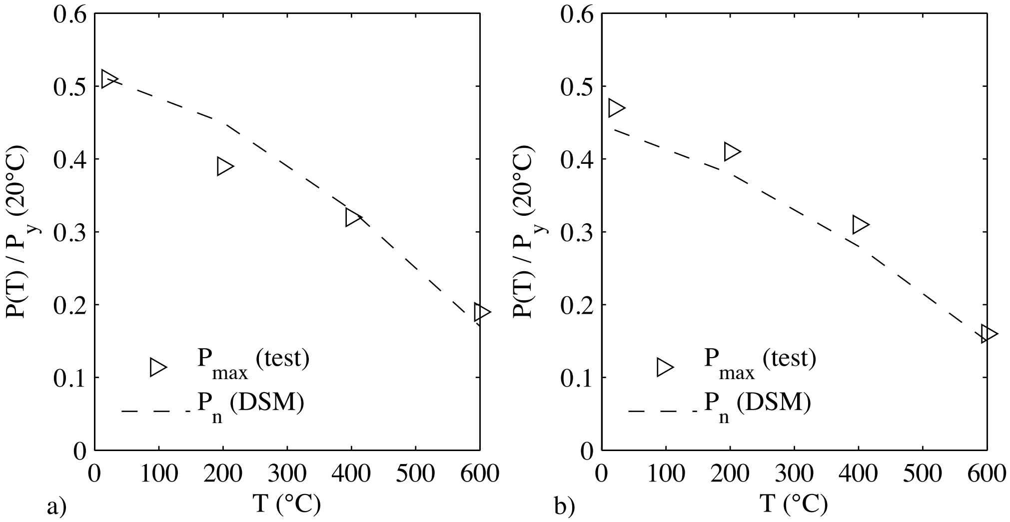

Figure 6-10: DSM predictions versus experimental results for a) 0.6 m and b) 1.0 m long bare studs

6.3.3 Modeling CFS studs at uniform elevated temperatures through FEM

ABAQUS (ABAQUS 2013) was used to analyze bare studs, using temperature-dependent mechanical properties.

The initial geometry of the studs follows the dimensions in Section 4.1.1, and geometric imperfections based on field measurements from Zeinoddini and Schafer (2012) were included, including local, distortional, bow and camber with magnitudes of 0.47t, 1.03t, L/2242 and L/3477, respectively. Shell elements S9R5 were utilized in the simulation. The model included the stud and track, connected through rigid connectors at screw locations (see Section 4.1.1), shown in Figure 6-11-a and b. Friction contact was defined between the ends of the stud and the web of the tracks to reflect the conditions of the experiments.

The analysis consisted of two steps. The first step simulated the heating process, based on uniform temperature increase and a thermal expansion coefficient linearly increasing from 1.20×10-5 (1/°C) at 20 °C to 1.65×10-5 (1/°C) at 600 °C. Free thermal expansion was allowed to reflect test conditions. After reaching the target temperature, a loading step was executed. Load was applied through axial displacement compressing the stud from the top, and restraining the displacement of the web of the bottom track. Buckling modes of short and intermediate-length studs are shown in Figure 6-11.

Load-displacement curves from test and numerical simulations are similar (Figure 6-11-c). The maximum load obtained from the collapsed analysis is show in Figure 6-12, and compared against experimental results and DSM predictions. A reasonable agreement is found among collapse analysis results, DSM predictions and experimental results.

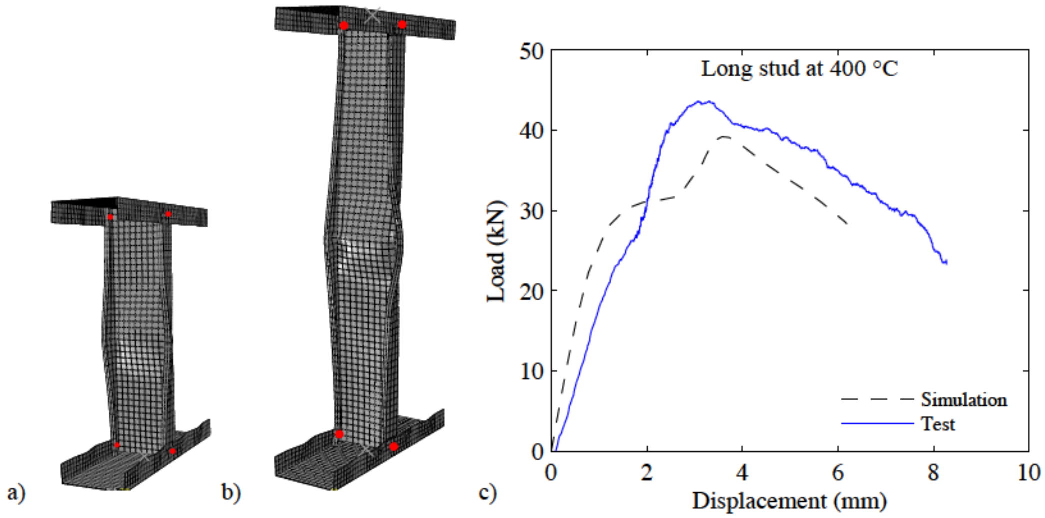

Figure 6-11: Mesh and deformed shapes from collapse analysis of CFS specimens with length of a) 0.6 m [24 in.] and b) 1.0 m [40 in.] showing screw locations (red dots), and c) load-displacement curve for long specimen at 400 °C from test and numerical simulation

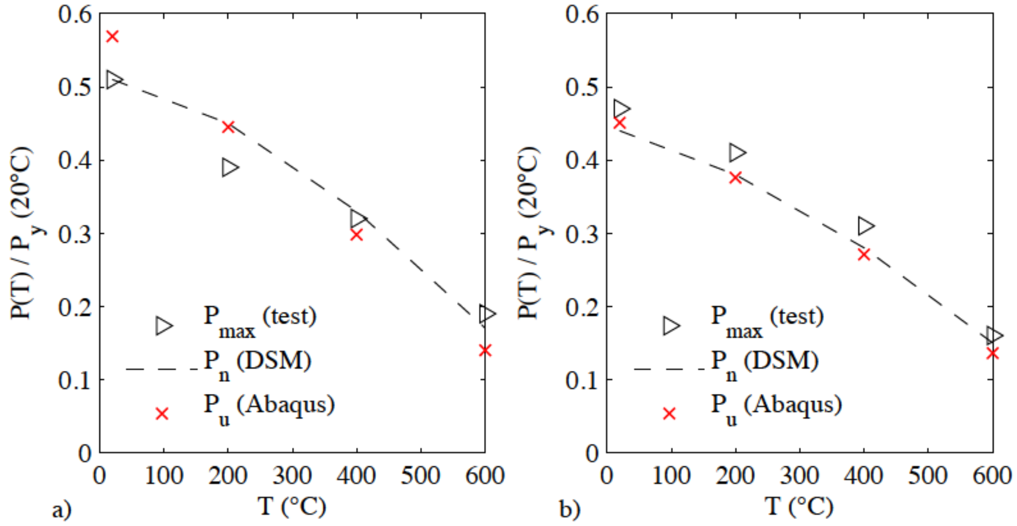

Figure 6-12: ABAQUS results versus DSM predictions and experimental results for a) 0.6 m and b) 1.0 m long bare studs

6.4 Design and modeling of sheathed CFS studs at uniform elevated temperatures

Current DSM equations with temperature-dependent CFS mechanical properties and connection stiffness were used to estimate the load-carrying capacity of sheathed CFS studs at elevated temperatures.

Material properties used in the finite strip analysis were similar to those presented in Table 6-4, based on Equations 6-1 and 6-2 and experimental results from Chapter 3. The geometry of the studs was taken from Chapter 4. Experimental in-plane lateral stiffness results were included in the finite strip analysis (see Chapter 5). Sheathing materials include gypsum boards, fire-rated gypsum boards, and OSB.

6.4.1 Elastic buckling analysis of sheathed CFS studs at uniform elevated temperatures

The local connection stiffness was obtained from the experimental secant stiffness shown in Table 5.1. Average values at each temperature were used. It is assumed the four fasteners connecting the boards to the top CFS stud are springs in parallel; the four fasteners connecting the boards to the bottom CFS stud are springs in parallel, too; and the top fasteners are in series with the bottom fasteners. Therefore, the local fastener stiffness was computed as the test stiffness divided by two, considering the applied load was equally distributed in the four fasteners, and the displacements in the top connection are equal to the displacements experienced in the bottom. In CUFSM, the "foundation stiffness" flag was activated, since the stiffness values provided correspond to a stiffness distributed along the length of the CFS member. Consequently, the stiffness values entered to CUFSM are the local fastener stiffness divided by the distance between fasteners (i.e. 20 cm from Figure 4.1). Foundation stiffness values for CUFSM are provided in Table 6-7. Simply supported boundary conditions were assumed to reflect test conditions. Traditional signature curve solution was adopted.

Results show similar buckling modes to those presented in Figure 6-8, except for the case of studs sheathed with gypsum board in one side and OSB in the other, for which the global modes became lateral-torsional instead of minor-axis buckling.

Table 6-7: Foundation stiffness values for finite strip analysis in CUFSM

Sheathing material	T (°C)	k_x (T) Kip/in/in (kN/mm/mm)
Gypsum	20	0.240 (1.067)
	100	0.223 (0.994)
	200	0.143 (0.636)
	300	0.077 (0.343)
Fire-rated gypsum	20	0.206 (0.917)
	100	0.174 (0.776)
	300	0.070 (0.311)
OSB	20	0.456 (2.028)
	100	0.359 (1.596)
	200	0.209 (0.930)
	250	0.319 (1.417)
	350	0.213 (0.947)

6.4.2 Direct-strength method for sheathed CFS studs at uniform elevated temperatures

Current DSM equations with temperature dependent squash load, and elastic buckling loads from CUFSM were used to estimate the load carrying capacity of sheathed studs. Results are shown in Figures 6-13 to 6-16. Satisfactory agreement between DSM predictions and experimental results is observed. Squash and critical loads at elevated temperatures are provided in Appendix E.

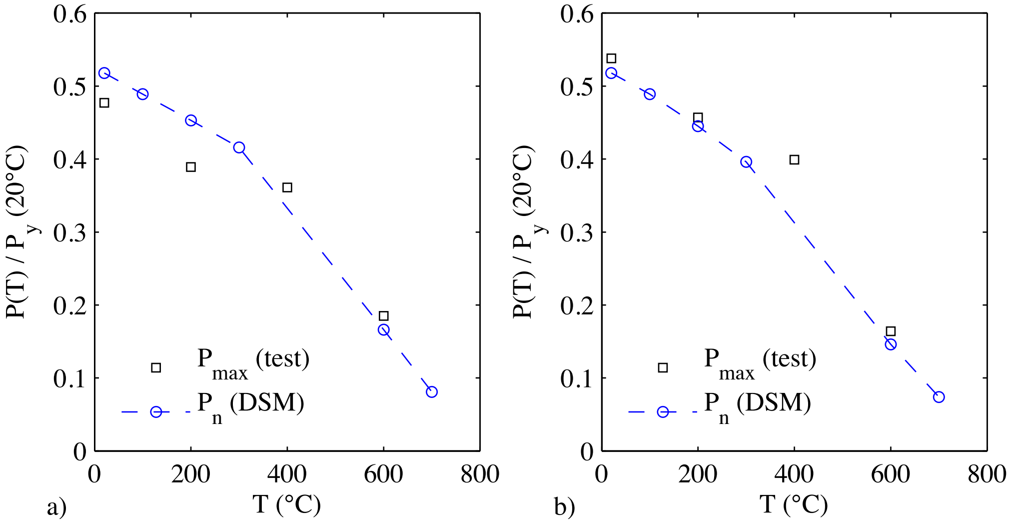

a) b)

Figure 6-13: DSM predictions versus experimental results for a) 0.6 m and b) 1.0 m long studs sheathed with gypsum boards on both sides

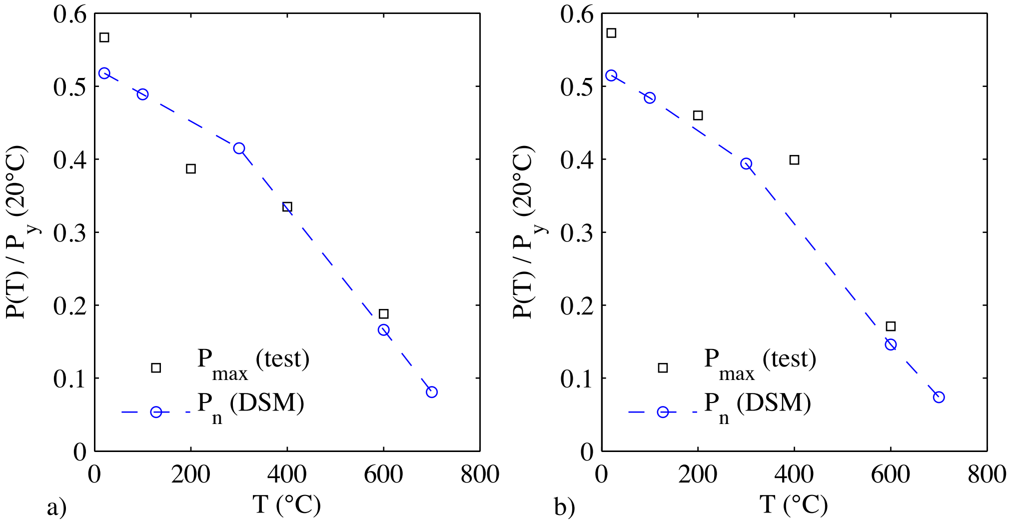

a) b)

Figure 6-14: DSM predictions versus experimental results for a) 0.6 m and b) 1.0 m long studs sheathed with fire-rated gypsum boards on both sides

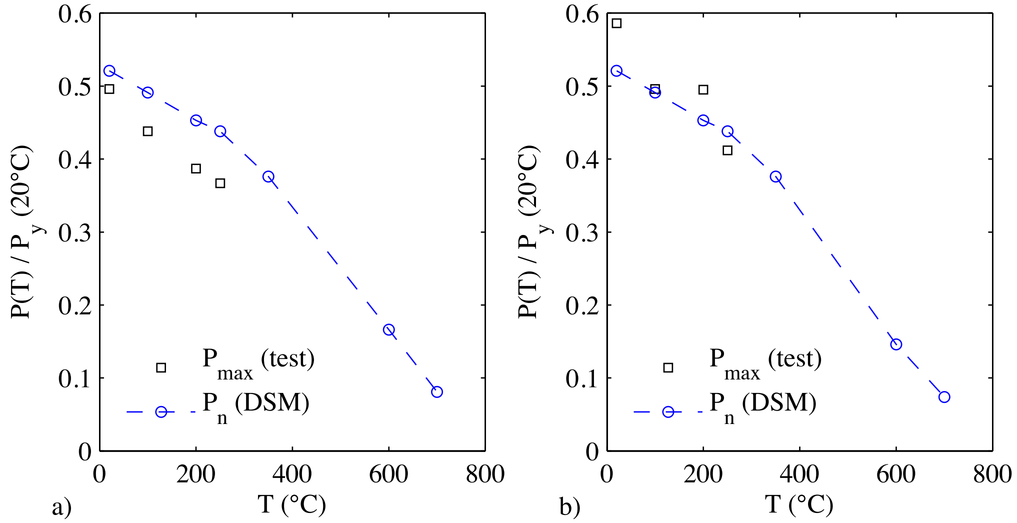

Figure 6-15: DSM predictions versus experimental results for a) 0.6 m and b) 1.0 m long studs sheathed with OSB on both sides

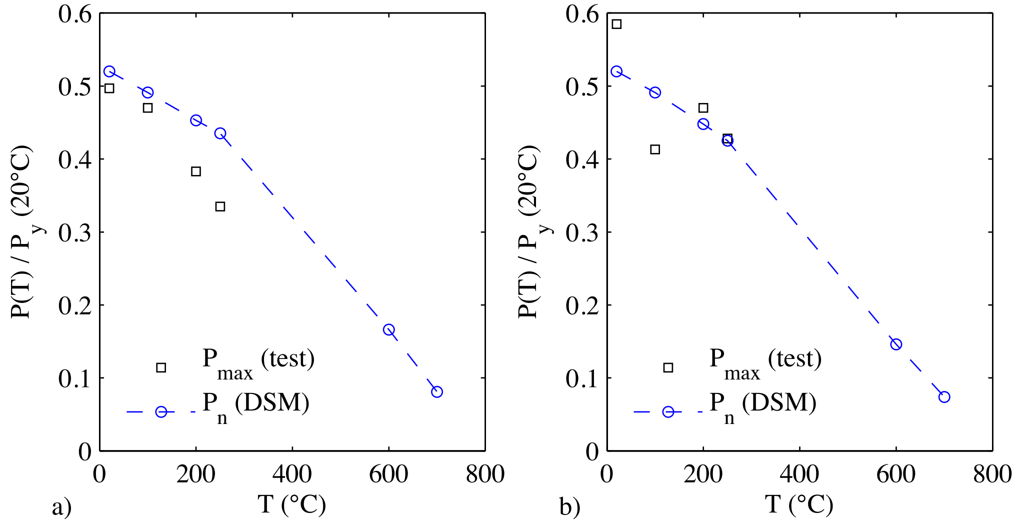

Figure 6-16: DSM predictions versus experimental results for a) 0.6 m and b) 1.0 m long studs sheathed with gypsum boards on one side and OSB on the other side

6.5 Modeling CFS studs with thermal gradients

CFS framing members are typically used in partition and load-bearing walls, between sheathing boards and surrounded by insulation. When fire occurs in a building compartment, the wall system is commonly heated on the exposed side, and heat is transferred to the unexposed side. This condition creates a non-uniform temperature distribution in the steel members, developing stiffness and strength variations throughout the member section and length, over time.

This section focuses on the analysis of CFS compression members with thermal gradients, including geometric imperfections and residual stresses. The main objective of this study is to judge the feasibility of current DSM equations to be used for fire design of compression members under non-uniform temperature distributions, and explore a simplified approach to predict the axial strength of thin-walled columns through current DSM equations.

6.5.1 Geometry, initial imperfections and residual stresses

The load carrying capacity of CFS compression members was computed through finite element GMNIA, using ABAQUS (ABAQUS 2013), and current DSM equations. The cross-section analyzed in this study corresponds to a thin-walled cold-formed steel lipped channel designated as a 400S200-54, with dimensions shown in Figure 6-17. In total, 360 finite element models were analyzed, considering two temperature profiles at multiple times of fire exposure, with lengths varying from 4 in. (101.6 mm) to 96 in. (2438.4 mm), pinned end conditions, and residual stresses and geometric imperfections as described herein.

Initial geometric imperfections were modeled based on superposition of elastic buckling modes with magnitudes proposed by Zeinoddini and Schafer (2012). The statistical values for local, distortional, and global imperfection magnitudes are provided in Table 6-8.

Residual stresses and strains were determined from the mechanics-based method proposed by Moen, Igusa et al. (2008). The prediction method suggests only corner residual stresses and plastic strains need to be considered. Residual stresses in the flat parts of the 400S200-54 can be ignored due to relatively large yield stress (e.g. 345 MPa or 50 ksi) and small thickness (e.g. 0.0566 in. or 1.44 mm). Effective strains and residual stresses included in the finite element models (FEM) are shown in Figure 6-18. The statistical mean of the coil radius (i.e. 474 mm) was assumed in the calculations. Due to corner bending, a maximum true plastic strain of 25% was included.

Quadrilateral shell elements with nine nodes and five degrees of freedom per node (S9R5), with thirty-one through-thickness integration points were used in the simulations.

Table 6-8: Imperfection magnitudes from Zeinoddini and Schafer (2012)

Case	Local (δ_o/t)	Distortional (δ_o/t)	Bow (L/δ_o)	Camber (L/δ_o)
25th percentile	0.17	0.43	4755	6295
50th percentile	0.31	0.75	2909	4010
75th percentile	0.54	1.14	1659	2887
95th percentile	1.02	3.06	845	1472

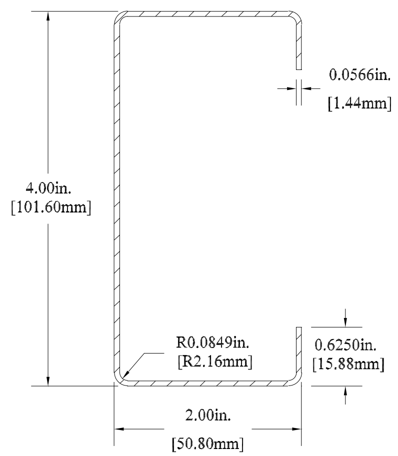

Figure 6-17: Section 400S200-54 dimensions (SSMA 2011, AISI-S200-12)

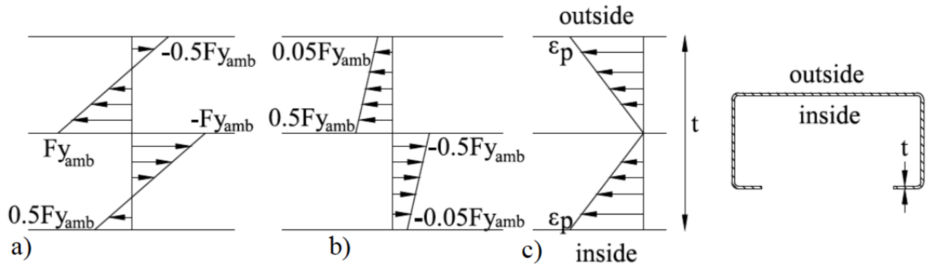

Figure 6-18: Residual stresses in the (a) transverse and (b) longitudinal directions, and (c) effective plastic strains in corner regions of thin-walled members

6.5.2 Temperature distribution and thermal gradients

Several models have been proposed to study the heat transfer problem in CFS systems (see Section 2.1.2). In this section, the non-uniform temperature distributions on the thin-walled studs were obtained through thermal analysis and validated experimentally by Feng, Wang et al. (2003). Two temperature profiles for lipped channels presented by Feng, Wang et al. (2003) were used to simulate the fire action on the structural members, as shown in Figures 6-19 and 6-20. Temperature profile 1 resulted from fire exposure on one side of a CFS wall with a single layer of gypsum board sheathing; while temperature profile 2 was obtained from a similar system with a double layer of gypsum board sheathing.

Temperature profile 1 shows higher temperatures and thermal gradients over time compared to temperature profile 2 (Figure 6-21), thus it is expected to provoke faster degradation of the load-carrying capacity of the structural members.

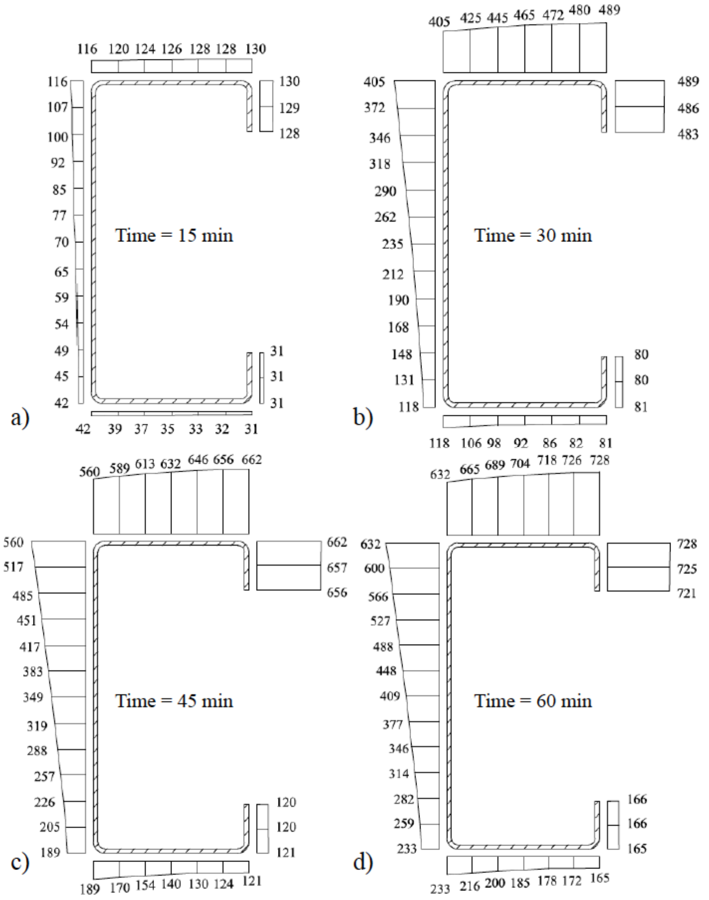

Figure 6-19: Temperature profile 1 - CFS wall with single layer of gypsum board sheathing exposed to the standard fire curve on one side, from (Feng, Wang et al. 2003)

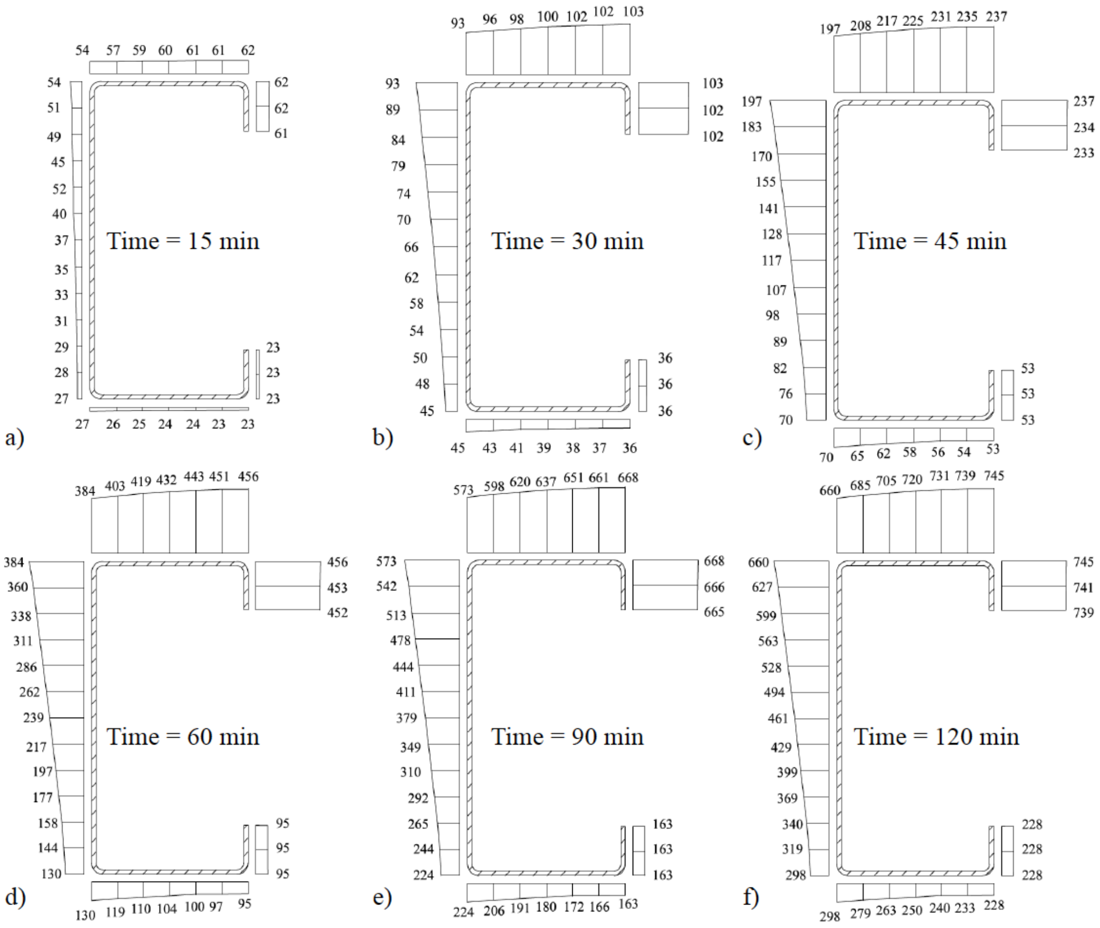

Figure 6-20: Temperature profile 2 - CFS wall with double layers of gypsum board sheathing exposed to the standard fire curve on one side, from (Feng, Wang et al. 2003)

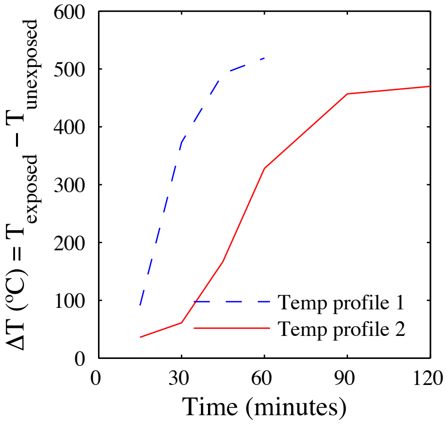

Figure 6-21: Temperature difference between exposed and unexposed flanges of a 400S200-54 stud over time, for temperature profiles 1 and 2

6.5.3 Mechanical properties for FEA and DSM calculations

This numerical study was finalized before completing the experimental program presented in previous chapter; therefore, material properties from other researchers cited herein were utilized.

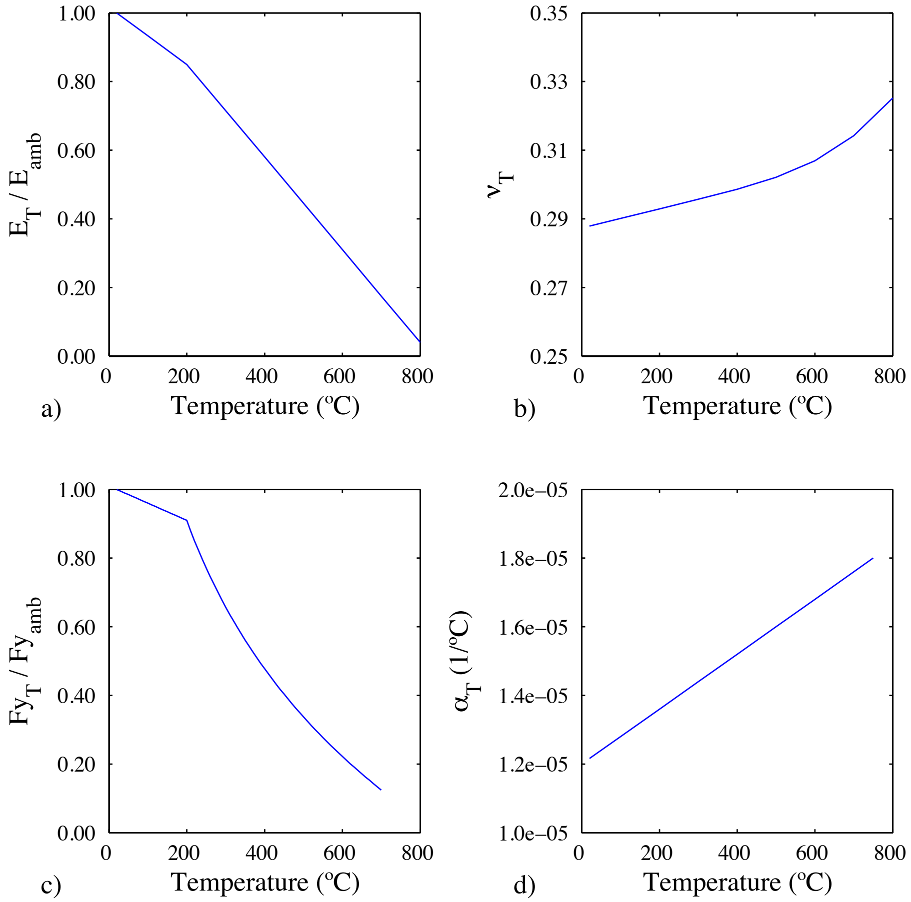

Figure 6-22: Mechanical properties of steel at elevated temperatures. (a) Retention factor for the elastic modulus (Kankanamge and Mahendran 2011), (b) Poisson's ratio (Luecke, McColskey et al. 2005), (c) retention factors for the yield stress (Kankanamge and Mahendran 2011), and (d) thermal expansion coefficient

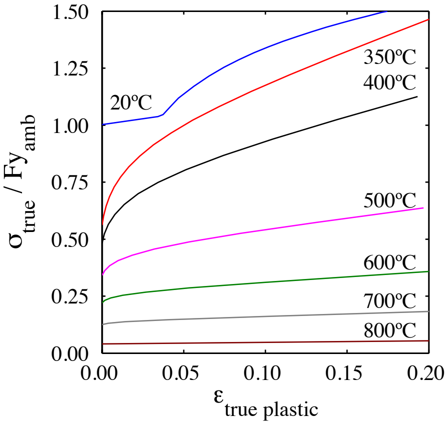

Figure 6-23: Normalized true stress versus plastic true strain (Kankanamge and Mahendran 2011)

Computational models included the degradation of the strength and stiffness according experimental results on CFS specimens from Kankanamge and Mahendran (2011) similar to results presented in Section 6.1, and variations of the Poisson's ratio and thermal expansion coefficient from Luecke, McColskey et al. (2005) and Eurocode 3: Part 1-2, respectively (Figure 6-22). Temperature-dependent true stress versus plastic true strain curves computed from engineering stress-strain prediction equations from Kankanamge and Mahendran (2011) are shown in Figure 6-23 and are utilized in the analysis.

6.5.4 Effect of residual stresses and imperfections of CFS studs under thermal gradients

The inclusion of residual stresses and plastic strains in the analysis results in a slight increase in the load-carrying capacity of the CFS column (up to 7.6% for 400S200-54 columns with temperature profile 2, at 60 minutes). However, their effect is less significant as the slenderness of the member increases, which is the case of long columns or members subjected to very high temperatures (Figure 6-24-a).

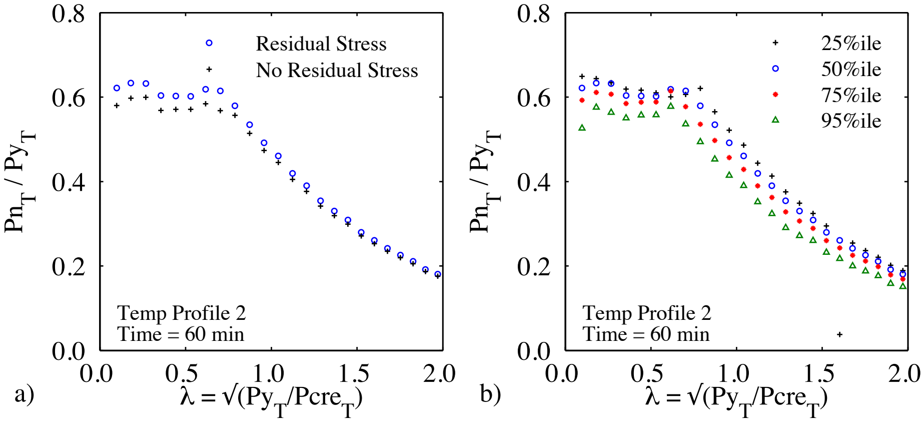

Figure 6-24: Strength curves for 400S200-54 columns under temperature profile 2, at 60 minutes of fire exposure. Variation of column strength with (a) residual stresses, and (b) imperfection magnitudes

Collapse analyses with several imperfection magnitudes were performed, considering temperature profile 2, at 60 minutes of fire exposure (Figure 6-24-b). Compared to the cases with imperfection magnitudes corresponding to the 50th percentile, the axial capacity of members with imperfection magnitudes in the 25th percentile resulted in at most 7.1% higher loads. In contrast, the axial capacity of members with imperfections corresponding to the 75th and 95th percentiles resulted in, at most, 7.5% and 17.9% lower loads, respectively. Consistent with the ambient case, results indicate the larger the imperfections the lower the axial capacity of compression members – and this reality holds with temperature. Imperfection magnitudes of the 50th percentile are used in the following simulations.

6.5.5 Results from GMNIA and DSM equations

The nominal axial capacity of compression members was computed through shell finite element collapse analysis and compared with DSM predictions. For DSM, elastic buckling loads (i.e. local, distortional, and global) were computed through CUFSM (Li and Schafer 2010). Temperature dependent material properties were included in the finite strip analysis. The temperature-dependent squash load was computed assuming a weighted average yield stress “$F_y(T)$”, or using the minimum yield stress of the cross-section “$F_{y\,min}$”. Following the temperature distribution of profiles 1 and 2, the squash load degrades over time (Figure 6-25-a). Simultaneously, the slenderness of columns, even at the same physical length, increases with temperature (over time), since the degradation of the elastic buckling load governs the response (Figure 6-25-b). In other words, columns become more slender and have a lower squash load as temperature (or time) increases. This fact is reflected in typical DSM slenderness vs. strength curves: a point of the curve corresponding to a structural member with a specific geometry (cross-section and length) moves “down” losing load-carrying capacity, and to the “right” becoming more slender, as the temperature (time) increases.

At ambient temperature, results from GMNIA collapse analysis and DSM are comparable (Figure 6-26), as expected. However, at elevated non-uniform temperatures, DSM column equations overestimate the load-carrying capacity of the compression members under thermal gradients, due to thermal bowing and second order effects. Figures 6-27 and 6-28 shows the column strength curves of members with temperature distributions based on profiles 1 and 2, respectively. The plots show the strength of columns is reduced and their slenderness is increased as time elapses (and temperature increases). Figure 6-29 shows the failure mode of the columns becomes unsymmetrical due to non-uniform material strength and stiffness, and modal interactions are more pronounced (Batista-Abreu and Schafer 2013).

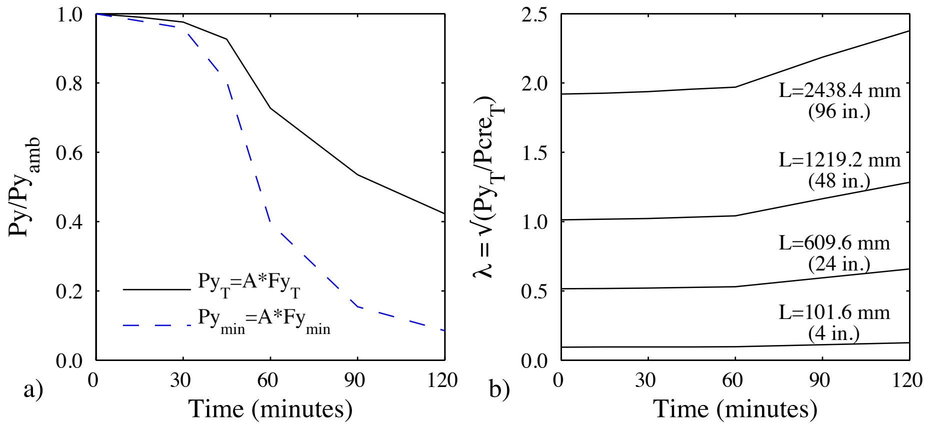

Figure 6-25: Variation of the (a) squash load computed with average (Fy_T) and minimum (Fy_{min}) yield stresses, and (b) slenderness of columns with temperature profile 2

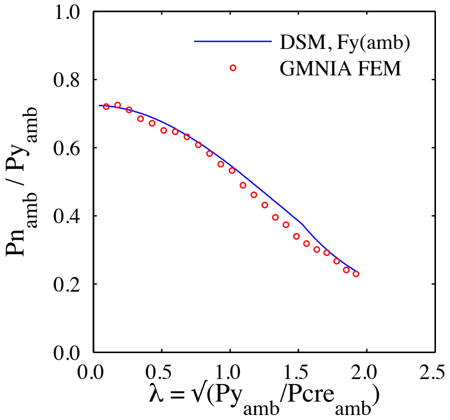

Figure 6-26: Column strength curve at ambient temperature

An alternative DSM approach to estimate the nominal axial strength of CFS columns consists in computing the squash load as the product of the cross-sectional area and the minimum yield stress of the section ($F_{y\ min}$). This is similar to the use first yield criteria in bending (M_y) instead of the fully plastic bending moment (M_p). This reduced squash load ($P_{y\ min}$) is then used in DSM equations to estimate the load-carrying capacity of columns. Although this approach penalizes the overall yield strength of the member, results show the predicted axial capacity is only modestly conservative compared to collapse analysis results (Figures 6-30 and 6-31). However, if this criterion were utilized to compute the slenderness of the column, equations would suggest slenderness ratios less than the actual values. Essentially, this approach allows the yielding failure to have a more dominant role in the prediction of the structural response.

DSM results based on squash load derived from the minimum yield stress ($P_{y\ min}$) are presented in Figures 6-32 and 6-33, and compared to GMNIA collapse analysis results. Normalization of the axial strength and slenderness ratios are based on ambient temperature conditions. The degradation of the axial strength with increasing temperature is not proportional among members with different physical lengths (or ambient slenderness) since failure modes evolve while temperature increases. However, in all cases the axial strength predicted by current DSM equations are similar to results form GMNIA.

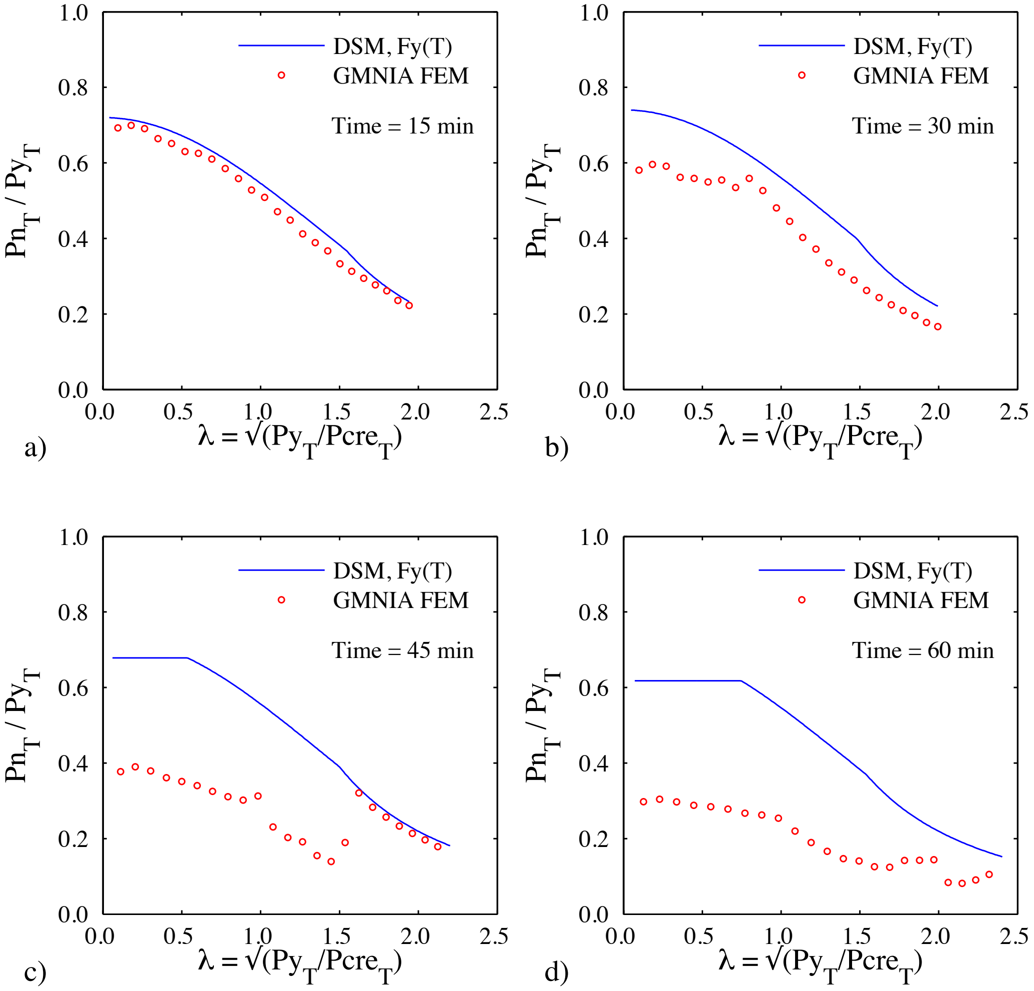

Figure 6-27: DSM predictions based on weighted average squash load (P_{yT}) and GMNIA results normalized with weighted average squash load (P_{yT}), corresponding to temperature profile 1

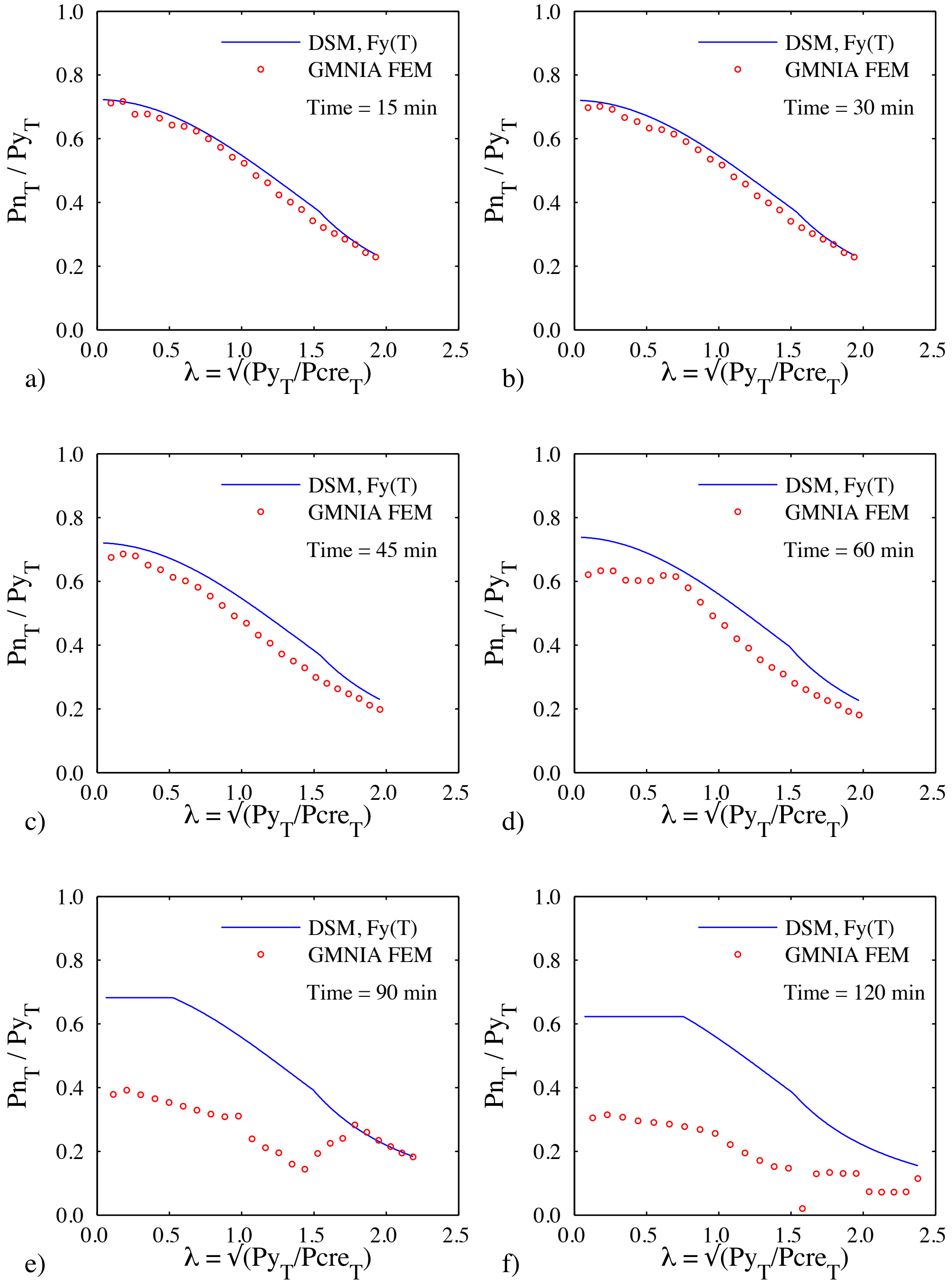

Figure 6-28: DSM predictions based on weighted average squash load (P_{yT}) and GMNIA results normalized with weighted average squash load (P_{yT}), corresponding to temperature profile 2

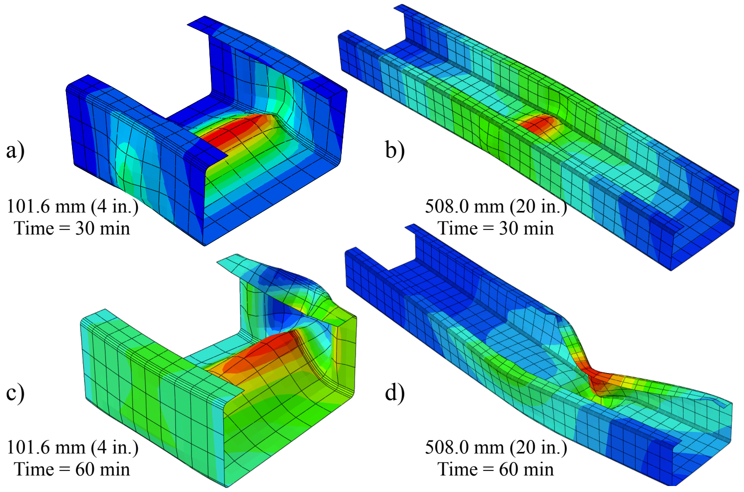

Figure 6-29: Deformed shapes of CFS members with temperature profile 2, 101.6 mm (4 in.) long columns at (a) 30 minutes and (b) 60 minutes, and 508.0 mm (20 in.) long columns at (c) 30 minutes and (d) 60 minutes of fire exposure

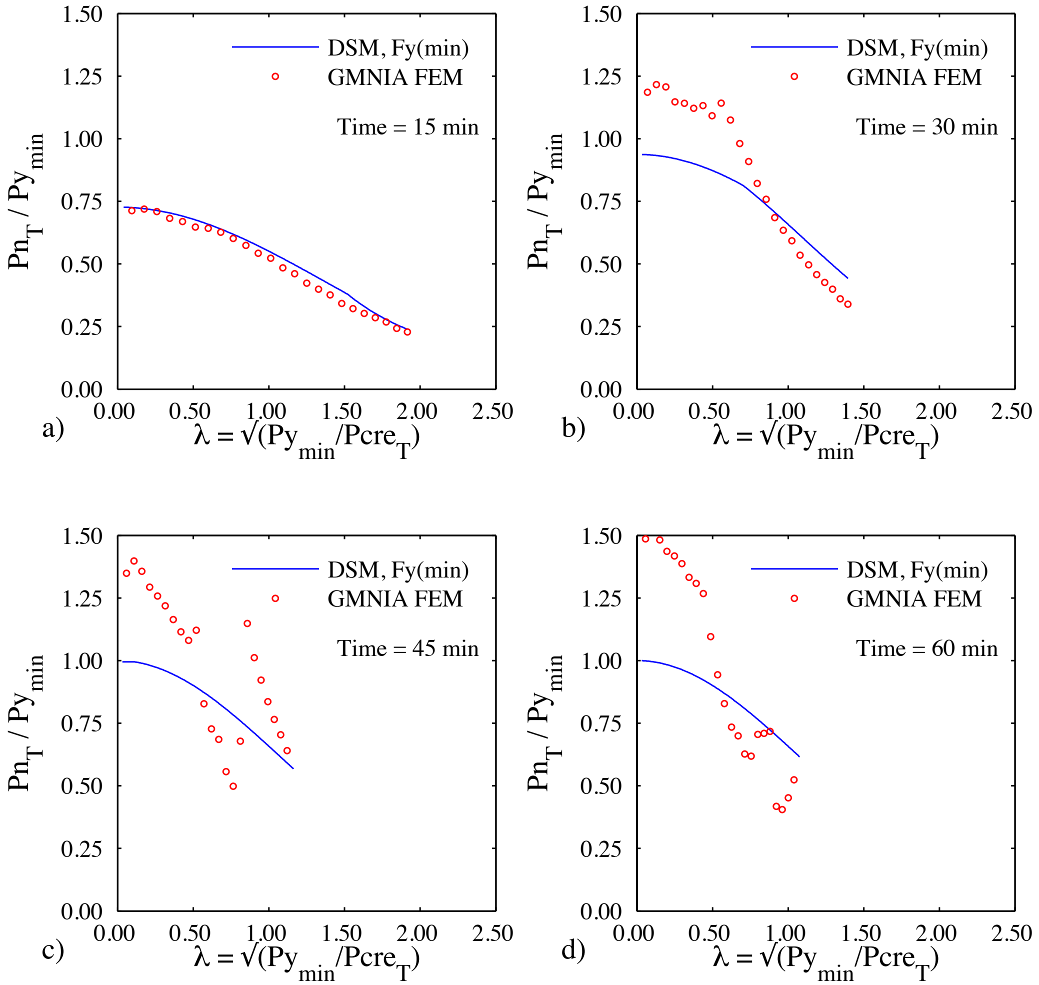

Figure 6-30: DSM predictions based on minimum squash load ($A_g \times F_{y\ min}$) and GMNIA results normalized with minimum squash load ($A_g \times F_{y\ min}$), corresponding to temperature profile 1

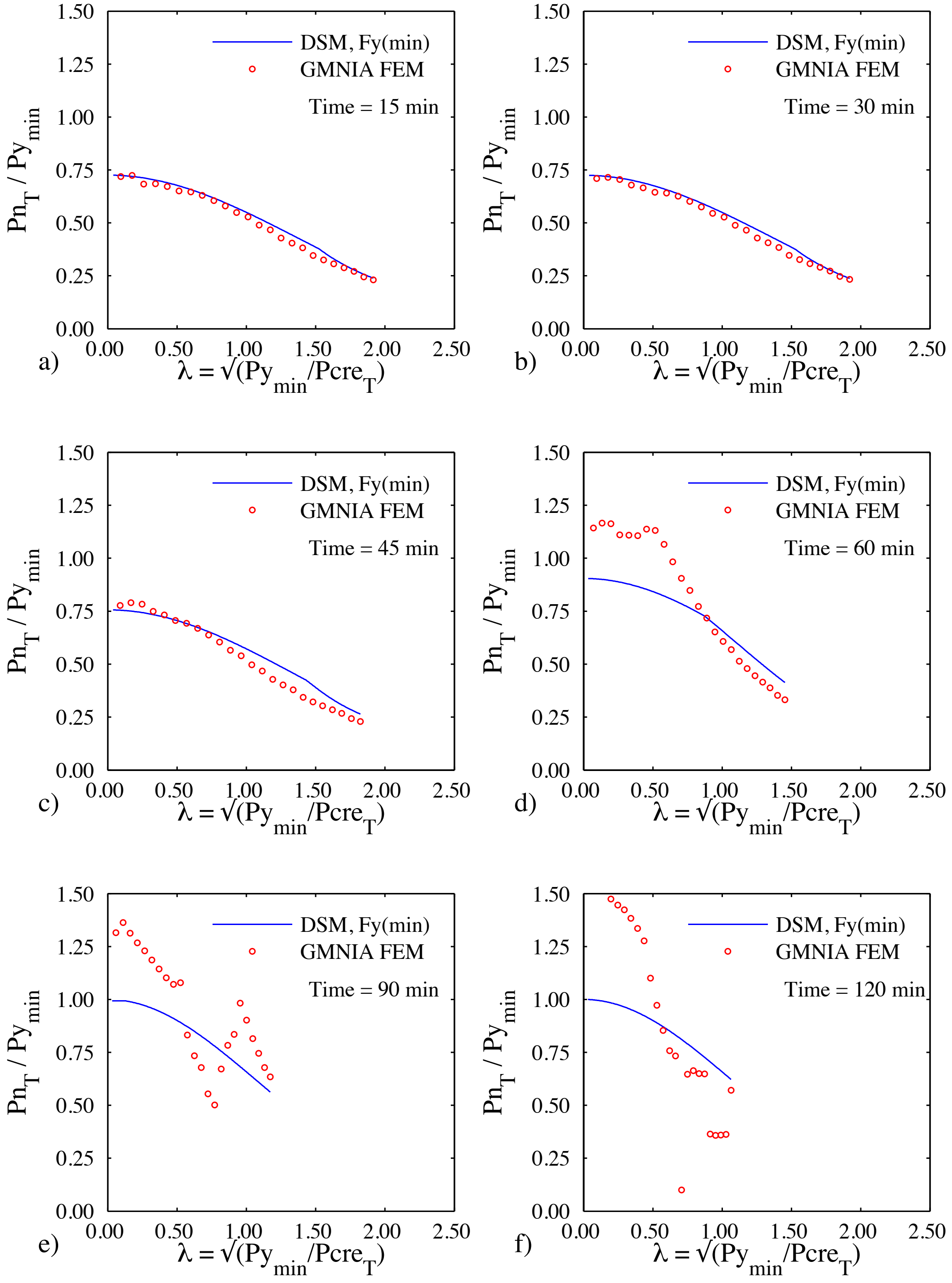

Figure 6-31: DSM predictions based on minimum squash load ($A_g \times F_{y\,min}$) and GMNIA results normalized with minimum squash load ($A_g \times F_{y\,min}$), corresponding to temperature profile 2

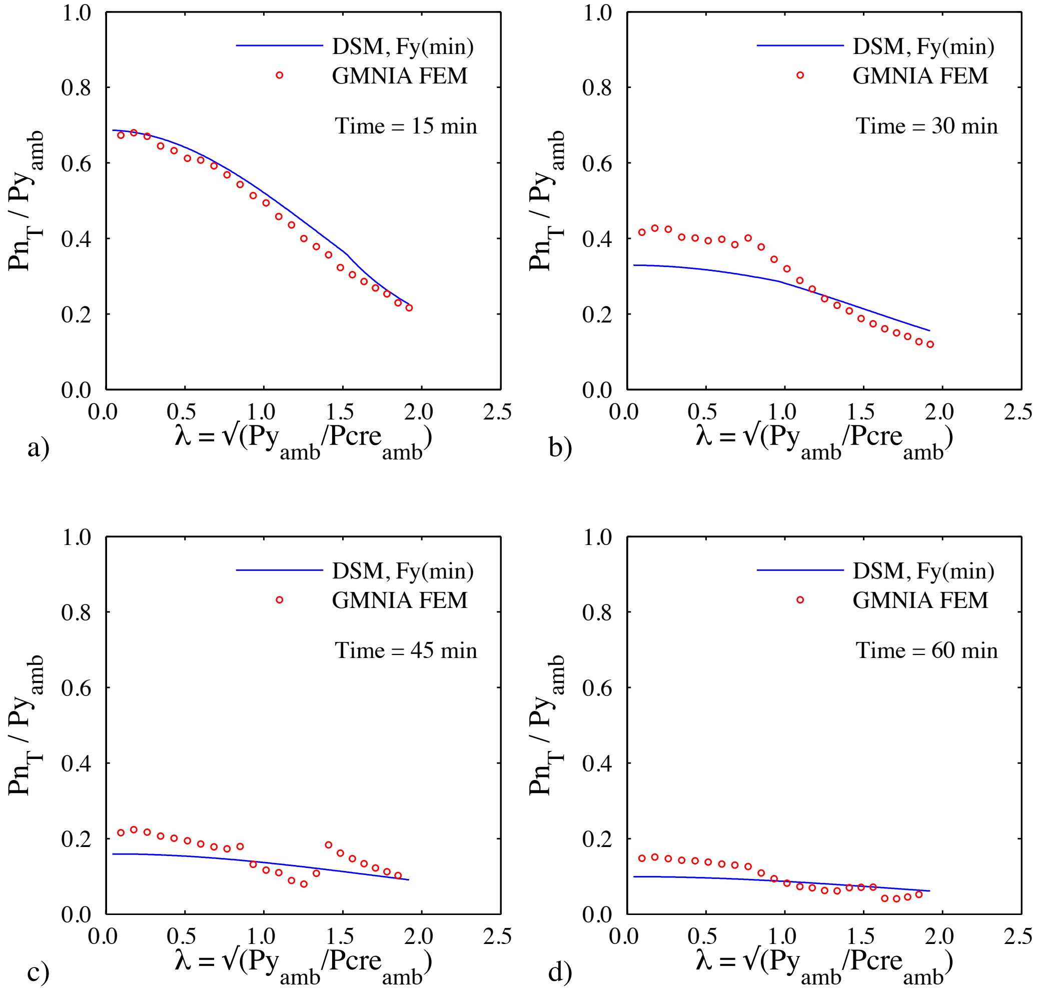

Figure 6-32: DSM predictions based on minimum squash load ($A_g \times F_{y\ min}$) and GMNIA results normalized with ambient squash load ($A_g \times F_{y\ amb}$), corresponding to temperature profile 1

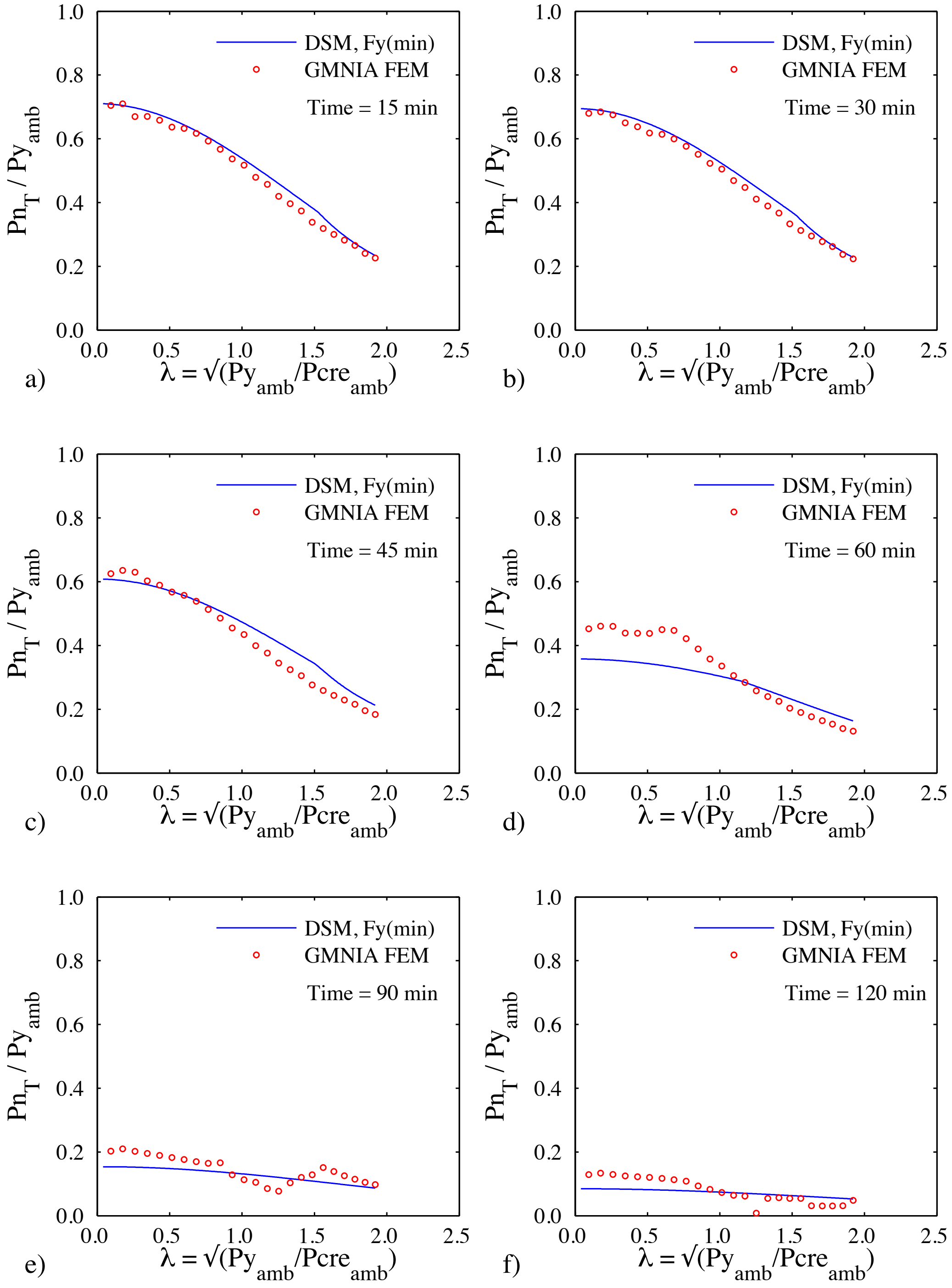

Figure 6-33: DSM predictions based on minimum squash load ($A_g \times F_{y\,min}$) and GMNIA results normalized with ambient squash load ($A_g \times F_{y\,amb}$), corresponding to temperature profile 2

In summary, results show that CFS columns lose strength and become more slender with increasing temperature due to degradation of mechanical properties and thermal deformations. Final collapse is unsymmetric, exhibits noticeable minor-axis bending due to thermal bowing, and includes coupled buckling modes. Comparisons of the results with the DSM are completed. Elastic stability is established at a specific time (t) for a given temperature profile (T) around the section through computational finite strip analysis. Two methods are considered for establishing the squash load, one uses a weighted average: $P_{yT}=\Sigma A_i F_{yi}(t,T)$ and considers the variation around the section; and the second simply uses the minimum yield stress: $P_{y\ min}=A_g \times \min(F_y(t,T))$. Current DSM column are not modified. The weighted average approach (P_{yT}) is rational, but leads to unconservative strength predictions. The minimum squash load method ($P_{y\ min}$) is shown to provide modestly conservative solutions across the study, and is simple to implement. Additional work remains to explore coupled heat transfer analysis, varied members and boundary conditions (for both heat transfer and structural response), and the impact of coupled modes in the response.

6.6 Comparison to proposed modified DSM by Shahbazian and Wang (2014)

Shahbazian and Wang (2014) proposed a method to evaluate the thermo-mechanical performance of CFS. The method estimates the temperature distribution on the CFS members based on a specific fire (time-temperature) curve, and then, estimates their load-carrying capacity. The heat transfer analysis is two-dimensional; so, it ignores thermal gradient along the length of the studs. The analysis assumes constant temperature in lips and flanges, and linear temperature variation on the web of the studs. After the temperature distribution on the stud is obtained, the load-carrying capacity is estimated through a set of modified DSM equation obtained from fitting FEA results. The structural analysis start with a redefinition of the squash load “P_y”, obtained from interaction curves of axial load and bending moment. The bending moment is developed as a result of the thermal bowing occurring on member subjected to thermal gradients, and the shift of the center of resistance due to non-uniform mechanical properties on the cross-section of the stud. Shahbazian and Wang (2014) concluded that current DSM equations do not provide accurate results when analyzing members subjected to elevated temperatures and thermal gradients. Therefore, new interaction equations (similar to current DSM equations) were proposed, and found accurate compared to FEA results.

6.6.1 Modified DSM predictions

Equations proposed by Shahbazian and Wang (2014) were used to estimate the load-carrying capacity of studs studied experimentally in Chapter 4, and analyzed with current DSM equations in Section 6.3. Shahbazian and Wang’s equations were developed to account for the effect of elevated temperatures and thermal gradients on the cross-sections of thin-walled CFS members. In general, those equations are capable of accounting for the shift of the center of resistance and second order effects due to thermal bowing in bare thin-walled members.

In this section, Shahbazian and Wang’s equations are used to analyze CFS members subjected to uniform elevated temperatures to assess the feasibility of these equations for the design of members without thermal bowing (or small temperature gradients). Mechanical properties proposed in Section 6.1.1 were utilized.

Figure 6-34 provides experimental results versus DSM predictions based on current equations and modified equations proposed by Shahbazian and Wang (2014). A satisfactory agreement between experimental results and current DSM equations is observed as observed in Figure6-34, and previously discussed in Section 6.3. However, predictions by Shahbazian and Wang (2014) provide very conservative results for both short and intermediate-length studs. On average, modified DSM equations estimate a load-carrying capacity 35% lower than experimental results. Therefore, current DSM equations without modifications are recommended for the analysis of CFS studs at uniform elevated temperatures.

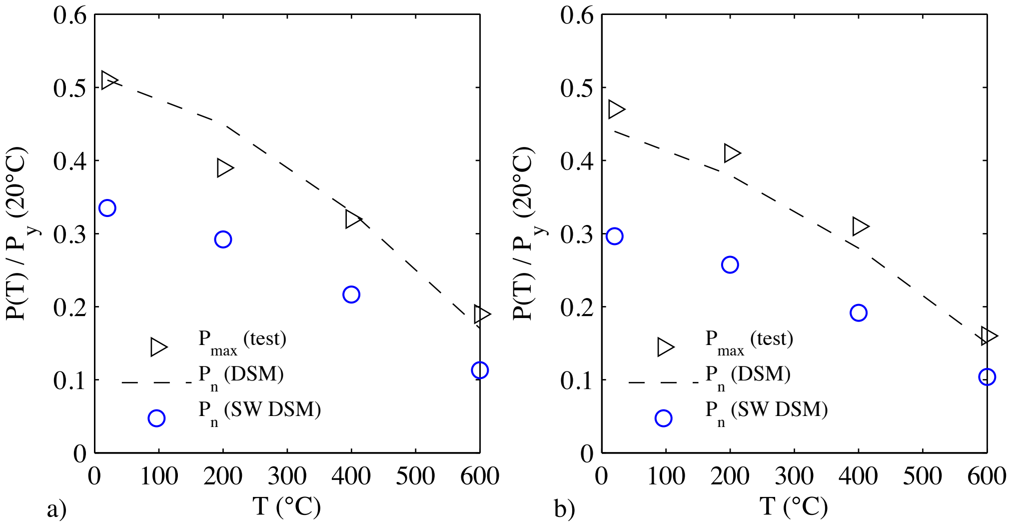

Figure 6-34: Experimental load-carrying capacity of studs, and predictions from current DSM equations and modified DSM equations proposed by Wang and Shahbazian (SW DSM), a) 0.6 m and b) 1.0 m long bare studs

References

American Institute of Steel Construction (AISC). Steel Construction Manual, Thirteen Edition. Appendix 4: Structural Design for Fire Conditions. United States of America, 2008.

American Iron and Steel Institute, AISI Standard, AISI S100-2012. North American Specification for the Design of Cold-formed Steel Structural Members. Appendix 1.

American Iron and Steel Institute, AISI Standard, AISI S200-2012. North American Standard For Cold-Formed Steel Framing – General Provisions 2012 Edition.

EN 1993-1-2 (2005). Eurocode 3: Design of steel structures - Part 1-2: General rules. Structural fire design. Brussels, 2005.

ABAQUS (2013). ABAQUS 6.13 Documentation. Providence, RI, USA.

Batista-Abreu, J. C. and B. W. Schafer (2013). Stability of cold-formed steel compression members under thermal gradients. Annual Stability Conference Structural Stability Research Council St. Louis, Missouri.

Chen, W. and J. Ye (2012). "Mechanical properties of G550 cold-formed steel under transient and steady state conditions." Journal of Constructional Steel Research 73(0): 1-11.

Feng, M., Y. C. Wang, et al. (2003). "Axial strength of cold-formed thin-walled steel channels under non-uniform temperatures in fire." Fire Safety Journal 38(8): 679-707.

Feng, M., Y. C. Wang, et al. (2003). "Thermal performance of cold-formed thin-walled steel panel systems in fire." Fire Safety Journal 38(4): 365-394.

Heva, B. (2008). Behaviour and design of cold-formed steel compression members at elevated temperatures. School of Urban Developments. Australia., Queensland University of Technology. Doctor of Philosophy.

Kankanamge, N. D. and M. Mahendran (2011). "Mechanical properties of cold-formed steels at elevated temperatures." Thin-Walled Structures 49(1): 26-44.

Lee, J., M. Mahendran, et al. (2003). "Prediction of mechanical properties of light gauge steels at elevated temperatures." J Constructional Steel Res 59(12): 1517 - 1532.

Li, Z. and B. W. Schafer (2010). Buckling analysis of cold-formed steel members with general boundary conditions using CUFSM: conventional and constrained finite strip methods. Twentieth International Specialty Conference on Cold-Formed Steel Structures Saint Louis, Missouri, USA.

Luecke, W. E., J. D. McColskey, et al. (2005). Mechanical Properties of Structural Steels (Draft). Federal Building and Fire Safety Investigation of the World Trade Center Disaster NIST NCSTAR 1-3D (Draft). U. S. D. o. Commerce. Washington, DC, U.S. Government Printing Office.

Moen, C. D., T. Igusa, et al. (2008). "Prediction of residual stresses and strains in cold-formed steel members." Thin-Walled Structures 46(11): 1274-1289.

Peterman, K. D. (2012). Experiments on the stability of sheathed cold-formed steel stud under axial load and bending. M.S. Essay. Department of Civil Engineering, Johns Hopkins University.

Ranawaka, T. and M. Mahendran (2009). "Distortional buckling tests of cold-formed steel compression members at elevated temperatures." J Construct Steel Res 65(2): 249 - 259.

Ranawaka, T. and M. Mahendran (2009). "Experimental study of the mechanical properties of light gauge cold-formed steels at elevated temperatures." Fire Safety Journal 44(2): 219-229.

Rasmussen, K. (2003). "Full-range stress-strain curves for stainless steel alloys." J Construct Steel Res 59(1): 47 - 61.

Schafer, B. W. (2013). Final Report: Sheathing Braced Design of Wall Studs. Washington, DC., Johns Hopkins University, prepared for the American Iron and Steel Institute.

Shahbazian, A. and Y. C. Wang (2014). Performance-based fire resistance design method for wall panel assemblies using thin-walled steel sectios. The Structural Engineer. 94: 52-62.

Vieira, L. C. M. (2011). Behavior and design of sheathed cold-formed steel stud walls under compression. Civil Engineering Department. Baltimore, MD., Johns Hopkins University. Doctor of Philosophy.

Zeinoddini, V. M. and B. W. Schafer (2012). "Simulation of geometric imperfections in cold-formed steel members using spectral representation approach." Thin-Walled Structures 60(0): 105-117.

Chapter 7 – Applications: Advanced modeling of cold-formed steel walls at elevated temperatures

Design equations proposed in Chapter 6 are used to model and analyze CFS walls subjected to standard fire tests, both non-load-bearing and load-bearing. This study aims to show that advanced modeling of CFS systems under fire is possible and provides satisfactory results if realistic material models and other modeling parameters are utilized. Also, this chapter provides original insight on the development of thermal bowing and opening of joints between gypsum boards during standard fire tests. Numerical models are validated against experimental results from CFS walls standard fire tests.

Understanding the behavior of CFS wall assemblies at elevated temperatures is the main step towards the optimization of these systems. In essence, two main aspects motivate this work from the point of view of the industry. First, in repeated standard tests, it is observed that CFS wall assemblies underperform compared to wood systems at elevated temperatures with similar layout and gypsum boards. The CFS industry seeks becoming more competitive by providing similar or better fire resistance ratings compared to the wood industry, and this can be achieved by first understanding the behavior of CFS studs and their effect on the entire wall system. Second, sustainable (or green) building constructions seek leaving a lighter footprint on the environment, and this can be achieved by optimizing (or reducing) the amount of materials used. In the design of fire-resistant structures, sustainability means reducing the thickness of gypsum boards. The simplest question is how can we reduce gypsum board thickness while maintaining the same or increasing the fire resistance of wall assemblies.

The advanced modeling presented herein is meant to provide new information on the response of CFS wall assemblies at elevated temperatures. The following sections describe the modeling parameters used in the finite element models, validation of numerical results, and parametric study to explore the system response.

7.1 Application 1: Modeling cold-formed steel partition walls in standard fire tests

This section focuses on the response of non-load bearing walls used to avoid spread of fire and smoke between compartments. Usually, partition walls consist of a CFS frames with equidistant vertical lipped channels (i.e. studs), and horizontal channels at the top and bottom (i.e. tracks). The flanges of the studs are usually connected to the flanges of the tracks by screws, or by sliding/frictional connections. Gypsum boards enclose the CFS frames, and act as the main components to provide fire resistance. Wall model components are illustrated in Figure 7-1.

7.1.1 Geometry and initial imperfections of CFS frame

Typical CFS wall geometry is considered (Figure 7-2). The frame is 10 ft. (3.05 m) by 10 ft. (3.05 m), and has 6 lipped channel studs, and two channel tracks. The length of the tracks is 120 in. (304.8 cm), and the length of the studs is 119.25 in. (302.9 cm), since small gaps exist between the ends of the studs and the web of the tracks. The gaps measure 0.50 in. (1.3 cm) and 0.25 in. (0.6 cm) in the top and bottom, respectively (Figure 7-1).

The centerline dimensions of web, flange and thickness of studs and tracks are 3.60 in. (9.14 cm), 1.23 in. (3.12 cm), and 0.0188 in. (0.478 mm), respectively. The centerline dimension of the lips of studs is 0.188 in. (0.48 cm).

Initial imperfections are included in the stud model, following magnitudes recommended by Zeinoddini and Schafer (2012).

Gypsum boards are usually 4 ft. wide (1.22 m); therefore, several boards are used to cover each side of the CFS frame. In Figure 7-3, Board 1 is 2 ft. (0.61 m) wide, and Boards 3 and 4 are 4 ft. (1.22 m) wide. The thickness of gypsum boards is 0.61 in. (15.5 mm).

In ABAQUS (ABAQUS 2013), quadrilateral shell elements with reduced integration and large-strain formulation “S4R” were used to model CFS members and gypsum boards. Studs and tracks consisted of 5656 and 8120 elements, respectively. Each element of the studs and tracks (i.e. web, flange and lip) were discretized into 4 elements. Gypsum boards 2 and 3 were modeled with 360 elements each, while Board 1 was modeled with 180 elements. The boards at each side of the CFS frame were modeled similarly.

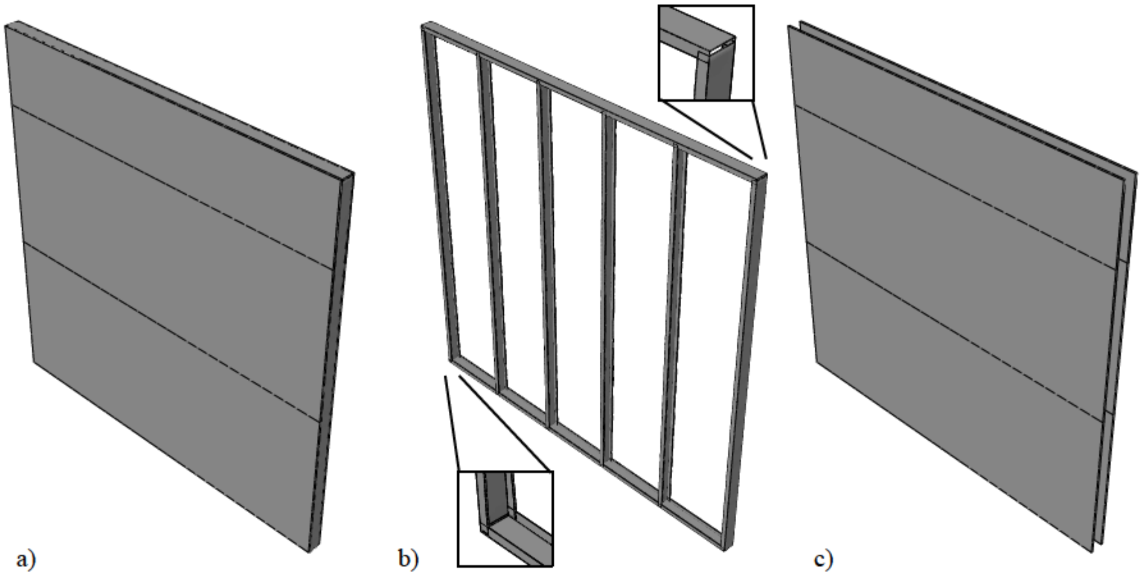

Figure 7-1: Wall model components, a) Wall model, b) CFS frame, and c) gypsum boards

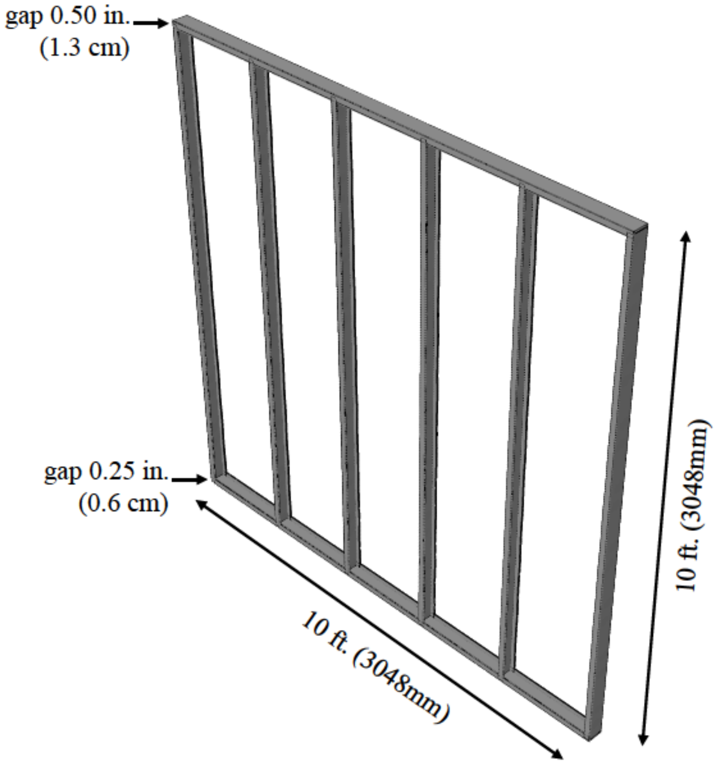

Figure 7-2: CFS frame model geometry

Connectors were modeled at screw locations, along the flanges of studs and tracks at 8 in. (20.32 cm) from screws, and 4 in. (10.16 cm) from board edges (Figure 7-4). Additional connectors on stud flanges were modeled at 1 in. (2.54 cm) from board joints. Connectors were modeled as rigid beams, by tying nodes at the center of CFS flanges and adjacent nodes on the boards, within a radius of 1.8 mm.

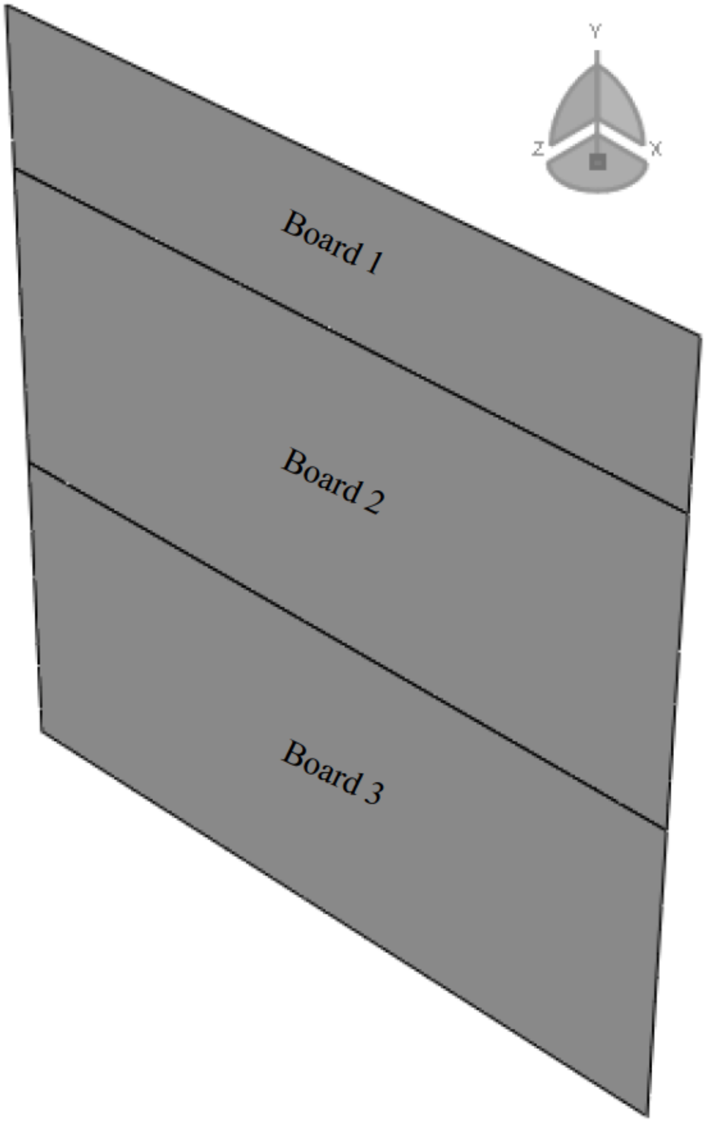

Figure 7-3: Gypsum boards layout

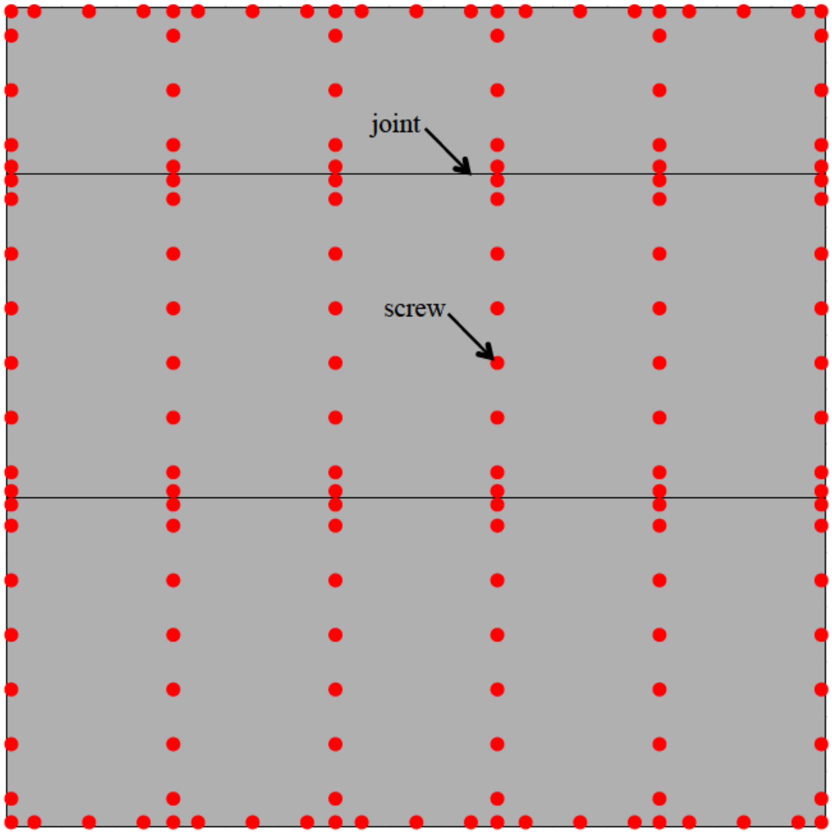

Figure 7-4: Gypsum boards and fastener distribution in the model

The web of the bottom track was restricted to displacements in all directions. The web of the top track was allowed to displace only in the vertical direction, to allow thermal expansion on the studs. The web of the studs at the left and right sides of the wall were not allowed to displace in the in-plane horizontal direction. These boundary conditions intend to reflect real displacement restrictions during tests.

7.1.2 Temperature distribution on CFS partition wall

Temperature distribution can be obtained through heat transfer analysis. However, current models do not reflect the effect of structural deformations and damage of components on the heat transfer analysis. For this model, time-temperature curves were obtained experimentally to study the structural response of the system based on accurate temperature data. During standard fire test, the temperature of the furnace is controlled and the temperatures on the studs and gypsum boards are measured (Figure 7-5). The temperature of the flanges was measured. The temperature of the lips was assumed to be similar to the temperature of the flanges since steel has a high thermal conductivity and the lips are small and thin. The temperature of the web of the studs was assume to vary linearly, and calculated based on the measured flanges temperatures. The temperature distribution on the studs reflects the thermal gradient measured during test (Figure 7-6).

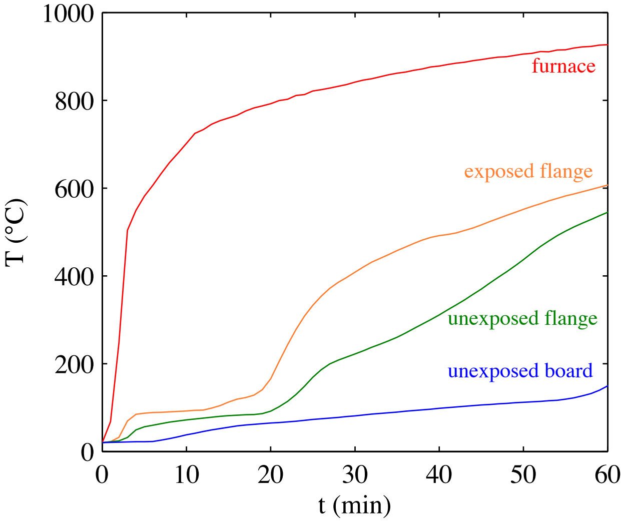

Figure 7-5: Temperature data from standard fire test (from proprietary manufacturer data)

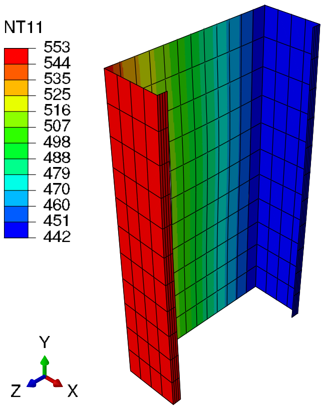

Figure 7-6: Temperature distribution on a CFS stud (°C)

7.1.3 Modeling mechanical properties of materials

CFS material model follows equations proposed in Chapter 6, assuming elastic modulus and yield stress at ambient temperature of 29500 ksi (203.4 GPa) and 33 ksi (228 MPa), respectively. The thermal expansion coefficient of CFS is 1.2×10-5 1/°C, and the Poisson's ratio is 0.3.

Retention factors for the mechanical properties and thermal expansion of gypsum are based on results by Cramer, Friday et al. (2003). Figure 7-7 shows the degradation of the elastic modulus of gypsum boards. Retention factors were fitted and extrapolated to 600 °C. It was assumed a linear decay of the retention factors from 0.05 at 600 °C to 0.01 at 1000 °C. Homogeneous material was assumed in the model with elastic modulus at ambient temperature of 690 MPa (100 ksi), with Poisson's ratio equal to 0.3. The thermal expansion coefficient was assumed constant -1.60×10^{-6} 1/°C after 400 °C.

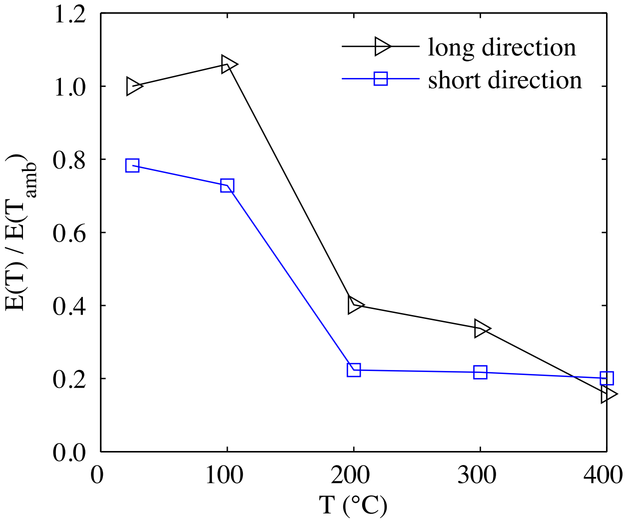

Figure 7-7: Retention factors for the elastic modulus of gypsum (Cramer, Friday et al. 2003)

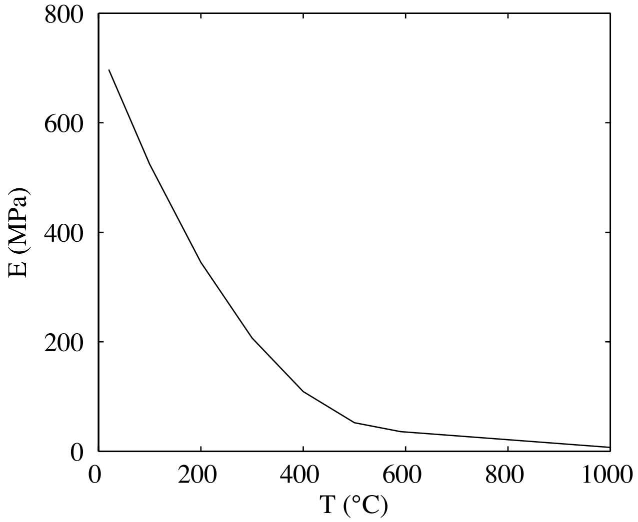

Figure 7-8: Elastic modulus of gypsum used in numerical models

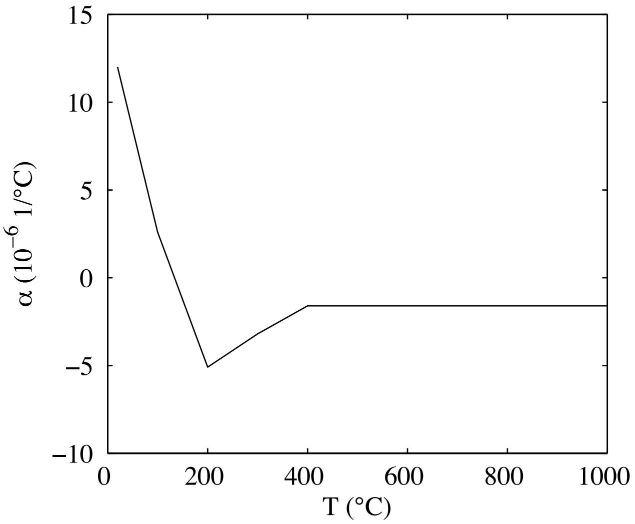

Figure 7-9: Thermal expansion coefficient of gypsum used in numerical models

7.1.4 Numerical results from finite element analysis

Stress distribution, thermal bowing and joint opening are the main outputs obtained from numerical simulations. Von Mises stresses on the CFS frame do not exceed the yield stress of the material at ambient conditions (Figure 7-10). The stress distribution of a single stud is shown in Figure 7-11. Lower stresses are developed on the exposed flange compared to the unexposed flange, due to higher temperature and therefore more pronounced material degradation. Interaction of local and distortional buckling modes is observed.

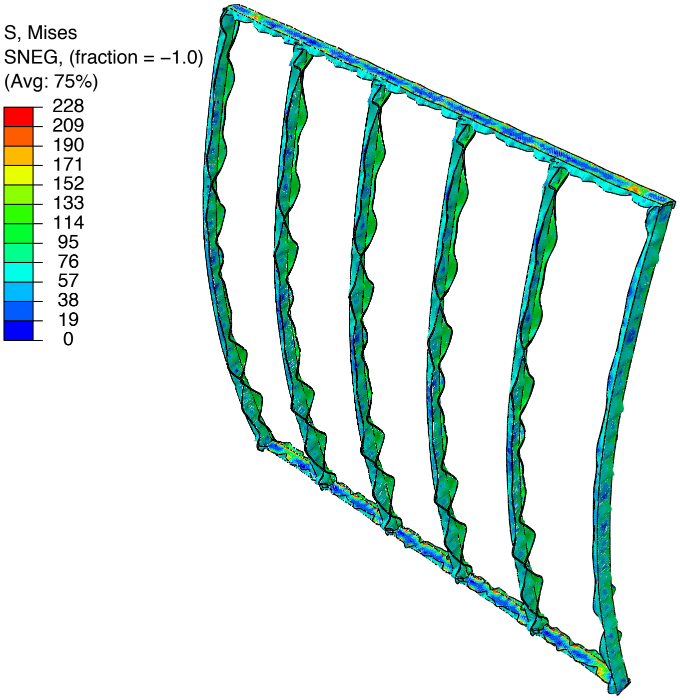

Figure 7-10: Von Mises stresses in CFS frame (MPa) at 60 min, displacements scale is 1:5

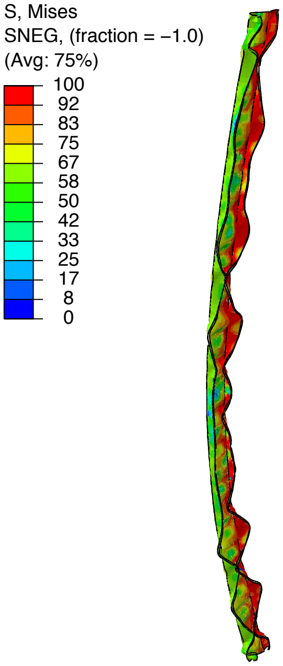

Figure 7-11: Von Mises stresses in CFS stud (MPa) at 60 min, displacements scale is 1:5

The CFS frame bows towards the furnace due to thermal gradients causing larger thermal expansion on the exposed flanges compared to the unexposed flanges. Thermal bowing of the wall develops large out-of-plane displacement at mid-height (Figure 7-12). Out-of-plane displacements on the unexposed side were obtained at the center of the wall, and at quarter-points at midheigth (both left and right). These values are compared against experimental data from two standard fire tests on CFS partition walls with similar geometry and materials modeled (Figure 7-13). Relatively small displacements are observed after 20 minutes of exposure to standard fire. Then, large velocity develops from 20 to 30 minutes. Out-of-plane displacements tend to slightly decrease after peak due to reduction of thermal gradient between studs flanges. The numerical model predicts maximum out-of-plane displacements around 56 mm, while 41 mm and 52 mm where measured in two similar tests.

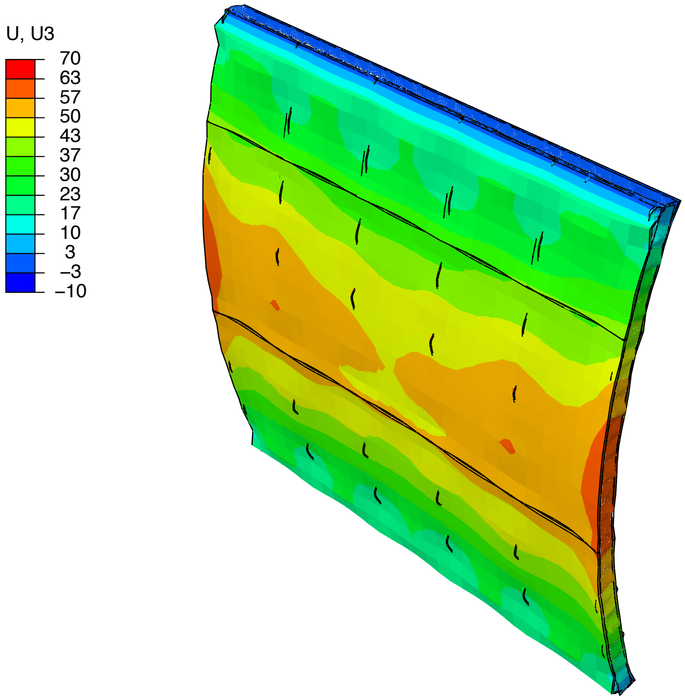

Figure 7-12: Out-of-plane displacements of wall model (mm) at 60 min, displacements scale is 1:5

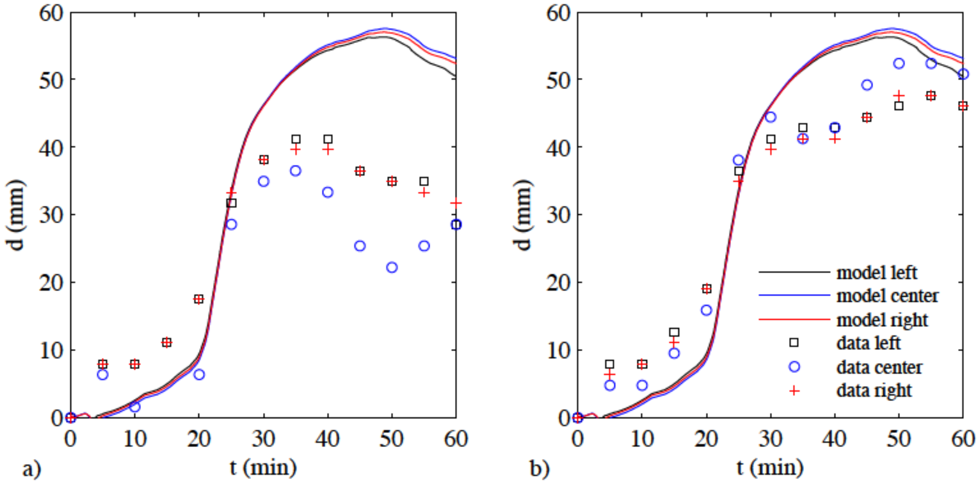

Figure 7-13: Out-of-plane displacements of wall model at mid-height (solid lines) compared to experimental data (markers) from a) test #1 and b) test #2 (from proprietary manufacturer data)

During the heating process and subsequent thermal bowing, it is observed that joints between sheathing boards open up on the exposed side of the walls (Figure 7-14). Normally, joint openings on the unexposed side of walls are not visible, compared to the joint openings developed on the expose boards (Figure 7-15). These openings allow a rapid passage of hot gases from the furnace to the wall cavity, consequently accelerating the heat transfer though the studs and unexposed boards. A more extreme case is presented in Figure 2-10-f in which the exposed gypsum boards are almost completely damaged by the fire, and the CFS studs are directly exposed to the elevated temperatures from the furnace compromising the fire resistance of the system.

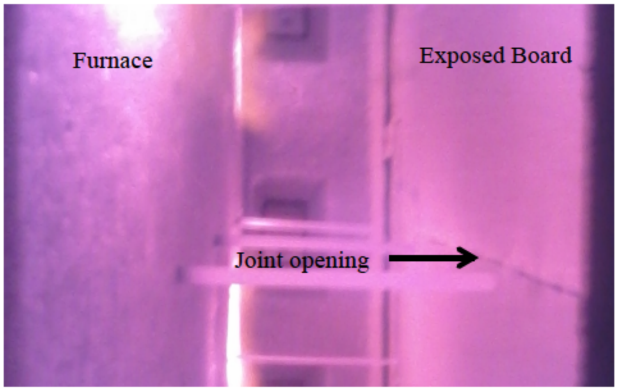

Figure 7-14: Joint opening on exposed side of a CFS wall during test

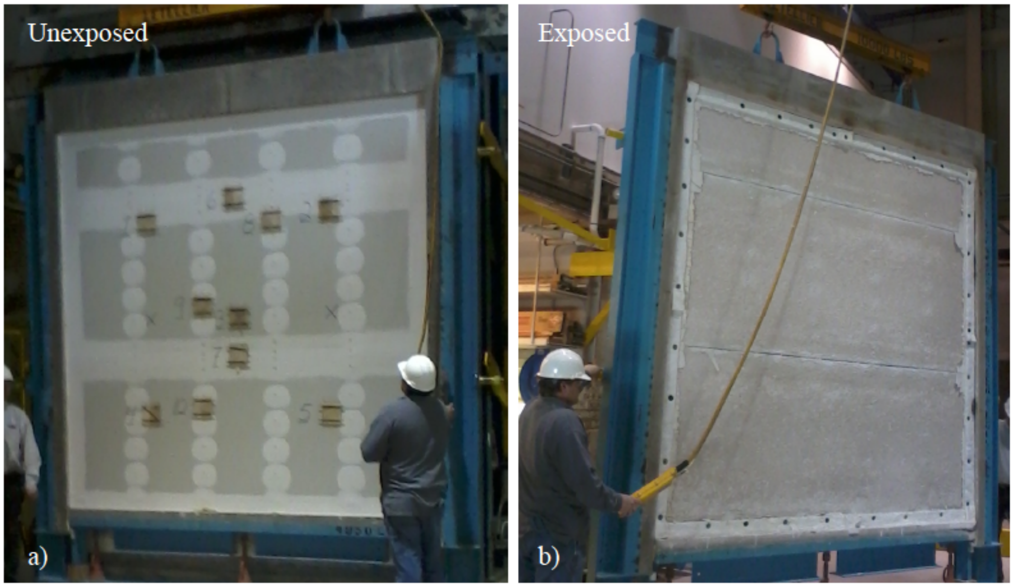

Figure 7-15: a) Unexposed and b) exposed boards after standard fire test

In standard fire tests and numerical results, it is observed that joint openings develop between studs. At stud locations the opening is minimum since a larger concentration of screws is present. Maximum joint openings tend to occur in the middle of two consecutive studs (Figure 7-16). Characterizing the size of this opening is very important since they contribute to a faster heat transfer through the wall system attempting to the fire protection of the system. This rapid heat transfer is translated into higher temperatures on the unexposed side of the wall potentially provoking ignition in adjacent compartments. Also, this opening could allow the passage of hot gases (including smoke) and flames. Additionally, rapid temperature increase in the wall cavity would produce higher temperatures on the studs; more degraded mechanical properties; and larger thermal deformations. To account for the effect of damage of the gypsum boards and joint opening, current models proposed arbitrarily calibrate thermal properties validated for a certain test. This limited approach leads to dissimilar models from different research groups. Instead, the model proposed in this chapter estimates the magnitude and shape of joint openings that can be directly included in heat transfer analysis (Figure 7-17). Joint opening of about 1 mm is observed in the model at about 4 minutes of exposure to the standard fire curve. Maximum opening about 5 mm is developed between 50 min and 60 minutes. In this model, the bottom joints develop slightly larger joint openings after 20 minutes.

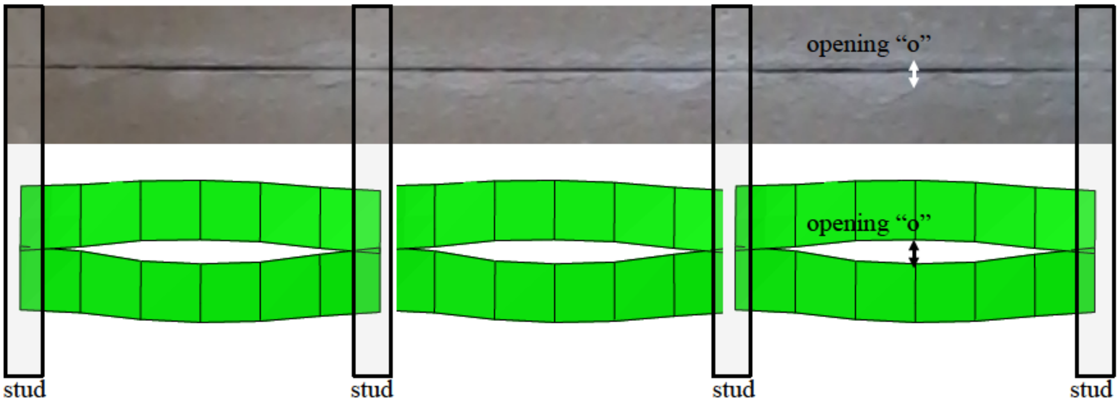

Figure 7-16: Illustration of joint opening observed during test and numerical model (scale 1:10)

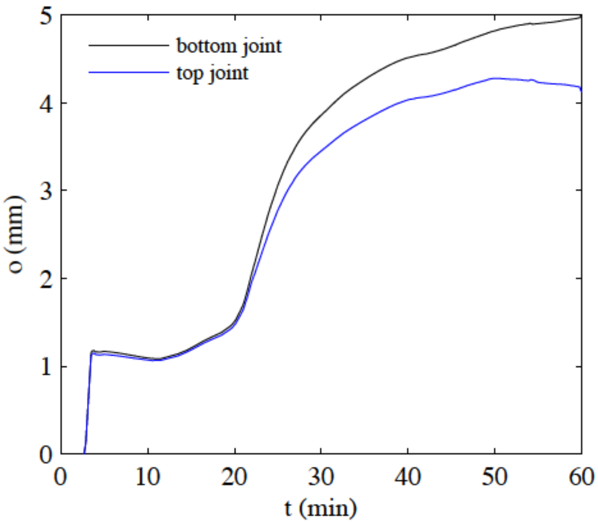

Figure 7-17: Magnitude of joint openings "o" at the middle of bottom and top joints

7.1.5 Parametric study of partition walls under standard fire test

In this section, results from parametric studies are presented. First, using the same retention factors shown in Figure 7-8 and varying the elastic modulus of gypsum at ambient conditions from 700 MPa [102 ksi] to 1200 MPa [174 ksi], the elastic moduli at elevated temperatures are computed and used to predict the out-of-plane displacements in the middle of the wall. Figure 7-18 shows the results. Similar bowing up to 30 minutes are obtained, regardless the elastic modulus; however, the maximum out-of-plane displacements slightly decrease from 55 mm [2.17 in.] to 48 mm [1.89 in.], by increasing the elastic modulus of gypsum from 700 MPa [102 ksi] to 1200 MPa [174 ksi].

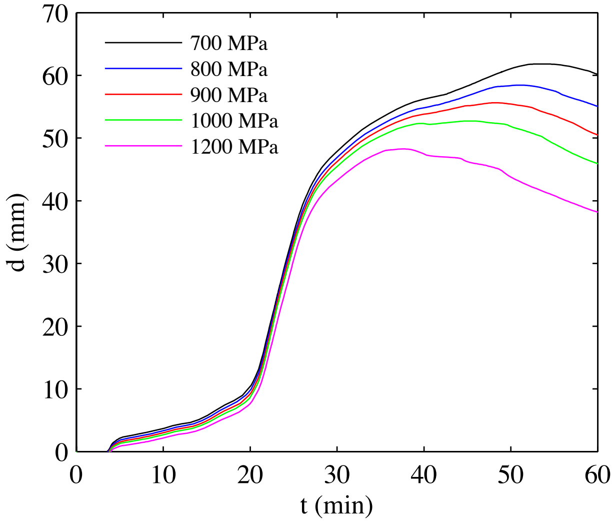

Figure 7-18: Maximum out-of-plane displacement of CFS walls

Changing the elastic modulus does not significantly change the magnitude of the thermal bowing of walls. In other words, formulating gypsum boards with higher stiffness at ambient conditions but similar retention factors does not lead to a significant change on the structural response of the wall. A more significant impact on the thermal bowing is obtained when changing the retention factors, even thought the elastic modulus of gypsum at ambient conditions is unchanged.

A logistic sigmoid function was used to model the retention factors for the elastic modulus of gypsum (Equation 7-1), with coefficients provided in Table 7-1. Model PE1 corresponds to the simulation based on retention factors from Figure 7-8 fitted to the following logistic sigmoid function.

$$\frac{E(T)}{E(T_{amb})} = \frac{A_1}{1+e^{A_2(T-A_3)}} + A_4$$

(Equation 7-1)

In Equation 7-1, “A4” is set to 0.01, so the retention factor at 1000 °C is about 0.01. The steepness of the curve “A2” was set to 0.007123 (1/°C) in all cases, based on calibration of the base case PE1. “A1” and “A3” vary such that, at 400 °C, the retention factors from models PE1, PE2, PE3, PE4, PE5 and PE6 are about 0.15, 0.20, 0.25, 0.30, 0.40, and 0.45, respectively. Retention factors for each model are provided in Figure 7-19. The black line represents the case studied in Section 7.1.4.

Figure 7-20 shows that increasing the retention of the elastic modulus of gypsum at elevated temperatures could significantly decrease the thermal bowing of walls subjected to fire from one side. A similar effect is observed on the magnitude of joint opening (Figure 7-21). It implies that the retention of the elastic modulus of gypsum boards at elevated temperatures plays an important role on the development of thermal bowing and joint openings (Figure 7-22).

Table 7-1: Logistic sigmoid function coefficients

Model	A_1	A_3 (°C)
PE1	1.60	80
PE2	1.44	135
PE3	1.25	200
PE4	1.20	240
PE5	1.10	300
PE6	1.08	350

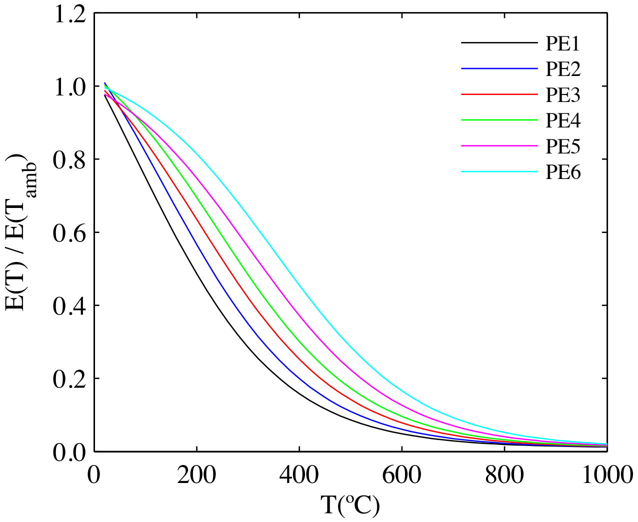

Figure 7-19: Logistic functions to model the retention factors for elastic modulus of gypsum boards

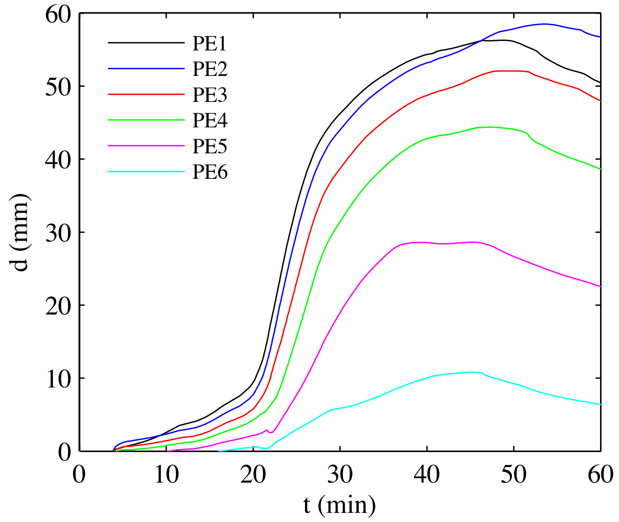

Figure 7-20: Out-of-plane displacements of CFS walls with different retention factors for the elastic modulus of gypsum boards

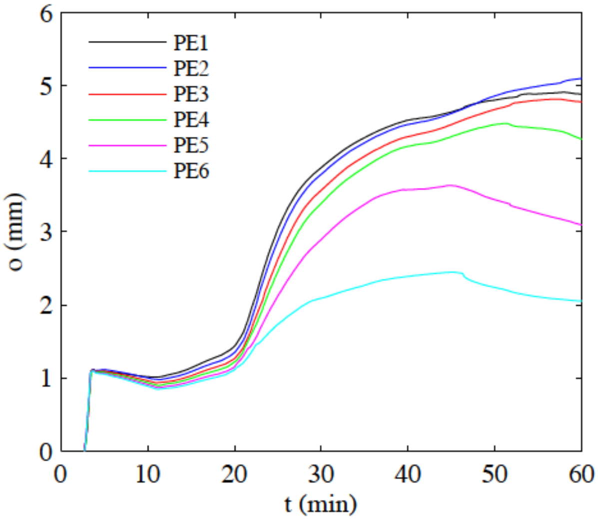

Figure 7-21: Joint opening in CFS walls with different retention factors for the elastic modulus of gypsum boards

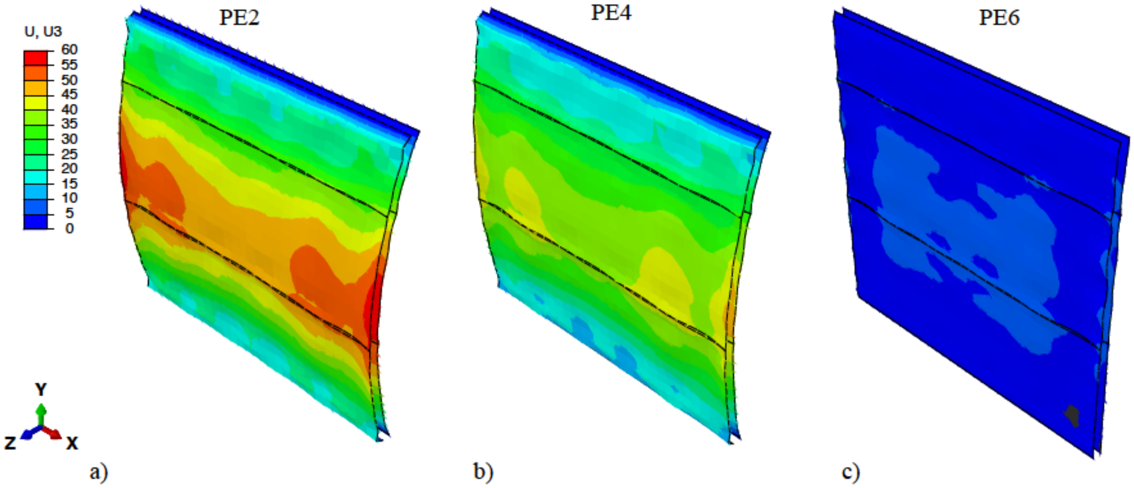

Figure 7-22: Contour plots of the out-of-plane displacement of walls during simulated standard fire test at 60 minutes, models a) PE2, b) PE4, and c) PE6

Another variable in play for the design of CFS walls as main components of the fire protection system is the steel grade of the studs. Usually, studs with nominal yield stress of 33 ksi and 50 ksi are used in the American building industry. Figures 7-23 and 7-24 show that changing the strength of the studs does not have a significant impact of the structural response of non-load-bearing walls subjected to standard fire tests.

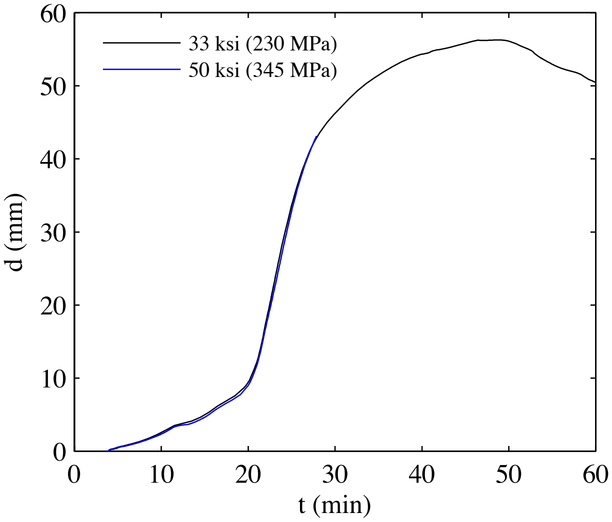

Figure 7-23: Out-of-plane displacements of CFS walls with different CFS materials

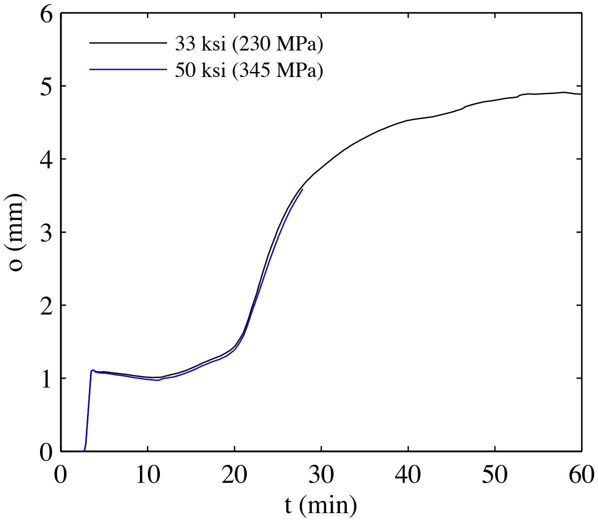

Figure 7-24: Joint opening of CFS walls with different CFS materials

7.2 Application 2: Modeling cold-formed steel load-bearing walls in standard fire tests

The model presented in Section 7.1 can be used to study the response of load-bearing walls at elevated temperatures. In order to represent transient conditions for which thermal action occurs after the system is loaded, an additional step need to be included in the finite element simulation before increasing the temperature of the system.

The loads to be applied can be determined from service loads expected in typical CFS load-bearing walls, or proper load combinations can be used. The load can be distributed according to the number of studs and their tributary area, and applied at the top of the studs. After applying completing the load step, the structural members will be stresses and deformed. Then, the temperature step can be activated.

Mechanical properties do not need to be modified. The thickness of CFS members could be increased given that load-bearing members are generally thicker than the members used in partition walls.

The study can include to main parameters. First, the amount of load applied to the system before fire action could be studied. Second, the temperature input can be varied to look at the effects of different fires on the load-bearing system.

Future work will be dedicated to the study of load-bearing systems at elevated temperatures through advance numerical modeling with the objective of understanding the response of load-bearing systems and optimize their fire resistance. The work provided herein establishes that such an approach is possible, and likely to provide useful predictions of fire and structural performance.

References

ABAQUS (2013). ABAQUS 6.13 Documentation. Providence, RI, USA.

Zeinoddini, V. M. and B. W. Schafer (2012). "Simulation of geometric imperfections in cold-formed steel members using spectral representation approach." Thin-Walled Structures 60(0): 105-117.

Chapter 8 – Summary, conclusions and future work

Performance-based fire design for CFS systems is in its infancy; however, this approach is largely seen as the future, and provides the best potential for risk consistent multi-hazard design. Three main components are identified for the development of the traditional engineering aspects for a performance-based design framework: realistic fire models, accurate thermal analysis, and engineering-based structural analysis and design. These components impact each other, so understanding their interaction and codependence its fundamental.

The research presented in this dissertation is mainly focused on engineering-based structural analysis and design of CFS, given a known temperature distribution on the structural components. This work aims to provide a better understanding on the structural behavior of CFS at elevated temperatures, including material, connection, member, and system response. The main contributions of this work satisfy the research objectives established in Chapter 1, and are summarized in this chapter.

In the state-of-the-art review presented in Chapter 2, key research needs relevant to the development of performance-based fire design of CFS are identified, and reviewed herein.

The accurate estimation of the fire resistance of structures first relies on the ability to understand the demands on the system, including loading conditions and potential fire scenarios. Realistic fires models should consider measures of fire severity adapted to the characteristics of modern building constructions such as geometry, amount and type of combustible materials, number and size of openings, thermal properties of materials, and compartment use. Fire curves should depend on the type of building construction, accounting for the fact that CFS structures and their response to fire are significantly different to wood or concrete structures, and their behavior. Furthermore, fire models should be coupled to the thermal and structural models, in such way that they obtain and provide feedback depending of the response of the structure over time.

Currently, sequentially coupled thermal and mechanical analyses are used to study building response. The way this coupling works is unilateral, so that the outputs from the heat transfer analysis (e.g. temperature field) is used as an input for the structural analysis. Therefore, the heat transfer affects the structural response, but the structural behavior (e.g. deformations and damage) does not affect the heat transfer. This method is not realistic and is based on crude assumptions and arbitrarily calibrated thermal properties that are eventually “validated” against limited experimental data. Ideally, heat transfer analysis would be fully coupled to the structural analysis, so that the thermal response is updated as the structure is heated, deformed and damaged.

Mechanical properties of CFS obtained experimentally were presented in Chapter 3. Temperature-dependent stress-strain curves and retention factors for the elastic modulus, yield stress and ultimate stress were obtained from experimental data. Experiments performed in different facilities and test setups provided similar results under comparable testing parameters, including specimen dimensions, and heating and loading rates. Much of the scatter observed in experimental results seems to be related to material grade, and therefore chemical composition of materials. Future work includes the study of mechanical properties of CFS at elevated temperatures, considering the chemical composition. Study of the variability of experimental results depending on the testing method whether it is steady state or transient state is also important. When comparing experimental data available in the literature, it was not found a consistent methodology to post-process experimental data, potentially causing much of the scatter observed among different research groups. Consistent guidelines for data post-processing should be developed and widely adopted.

Chapter 4 presented an experimental study to analyze the behavior of short and intermediate-length CFS bare and sheathed studs at elevated temperatures, up to 600 °C. Sheathing materials included OSB, regular gypsum boards and fire-rated gypsum boards. Experimental results show that sheathing potentially increases the axial strength of thin-walled studs, especially when distortional and global buckling modes have significant participation in their structural response. While temperature increases, CFS mechanical properties degrade, and the impact of sheathing bracing in the strength and stiffness of studs decays. Therefore, initially sheathed studs respond similar to bare studs at high temperatures. Current DSM equations along with empirical temperature-dependent mechanical properties were found suitable to estimate the load-carrying capacity of CFS at uniform elevated temperatures. Therefore, current design methods seem promising for performance-based fire design of CFS structures. Future work includes the characterization of steel-to-steel connections, and the study of long members governed by global buckling.

Chapter 5 focused on the stiffness of stud-to-sheathing connections at elevated temperatures. In-plane lateral stiffness tests and pull-through fastener stiffness tests performed at elevated temperatures are used to characterize the degradation of connection stiffness. Specimen's materials included gypsum, fire-rated gypsum and OSBS. Different degradation rates were observed among different materials, for both lateral-stiffness test and fastener-stiffness tests. Also, stiffness degradation at 100 °C increases as the time of exposure to elevated temperature on gypsum specimens increases.

Material and connection stiffness models based on experimental results were proposed in Chapter 6. The models consist of sets of temperature-dependent equations to obtain retention factors for the elastic modulus, yield stress, and ultimate stress. Stress-strain proposed models are based on modified Ramberg-Osgood equations. Similarly, equations to determine retention factors for the stud-to-sheathing connection stiffness are provided. Retention factors could be used for the design of sheathed studs at elevated temperature. Chapter 6 also showed that current DSM equations with realistic mechanical properties at elevated temperatures provide reasonable predictions of the load-carrying capacity of bare and sheathed studs. Modified DSM equations available in the literature are found to be very conservative, and underestimate member strength at elevated temperatures. The feasibility of the proposed method should be evaluated for other types of CFS sections and loading conditions.

Proposed models are applied to the analysis of CFS partition and load-bearing walls in Chapter 7. Advanced finite element nonlinear analyses include temperature-dependent mechanical properties, geometric imperfections, and interaction between CFS and sheathing materials. Thermal bowing from numerical results are compared against experimental data. The models are used to predict wall deflections due to thermal gradients, and joint opening between sheathing boards over time, following time-temperature curves from experimental results. Parametric studies were performed to identify key parameters controlling the thermal bowing and joint opening in CFS walls in standard fire tests. Research needs include the ability of fully coupling the structural behavior to the heat transfer analysis of the system.

Engineering-based modeling and design of CFS wall systems at elevated temperatures are possible, based on adequate material models, and current analysis tools and design methods. Material and connection models are proposed in this dissertation. Analysis and design method based on current DSM methodology is validated and therefore proposed herein. Finally, an advanced numerical model of CFS wall systems is presented and used to understand the response of CFS wall assemblies at elevated temperatures.

Future research for the development of realistic fire models, accurate heat transfer analysis tools, and fully coupled structural analysis are needed to enable performance-based fire design of CFS structures. Future work will also be dedicated to cross-section optimization to create sustainable design solutions able to withstand fire demands.

Appendix A: Stress-strain curves from high-temperature tension tests on cold-formed steel specimens

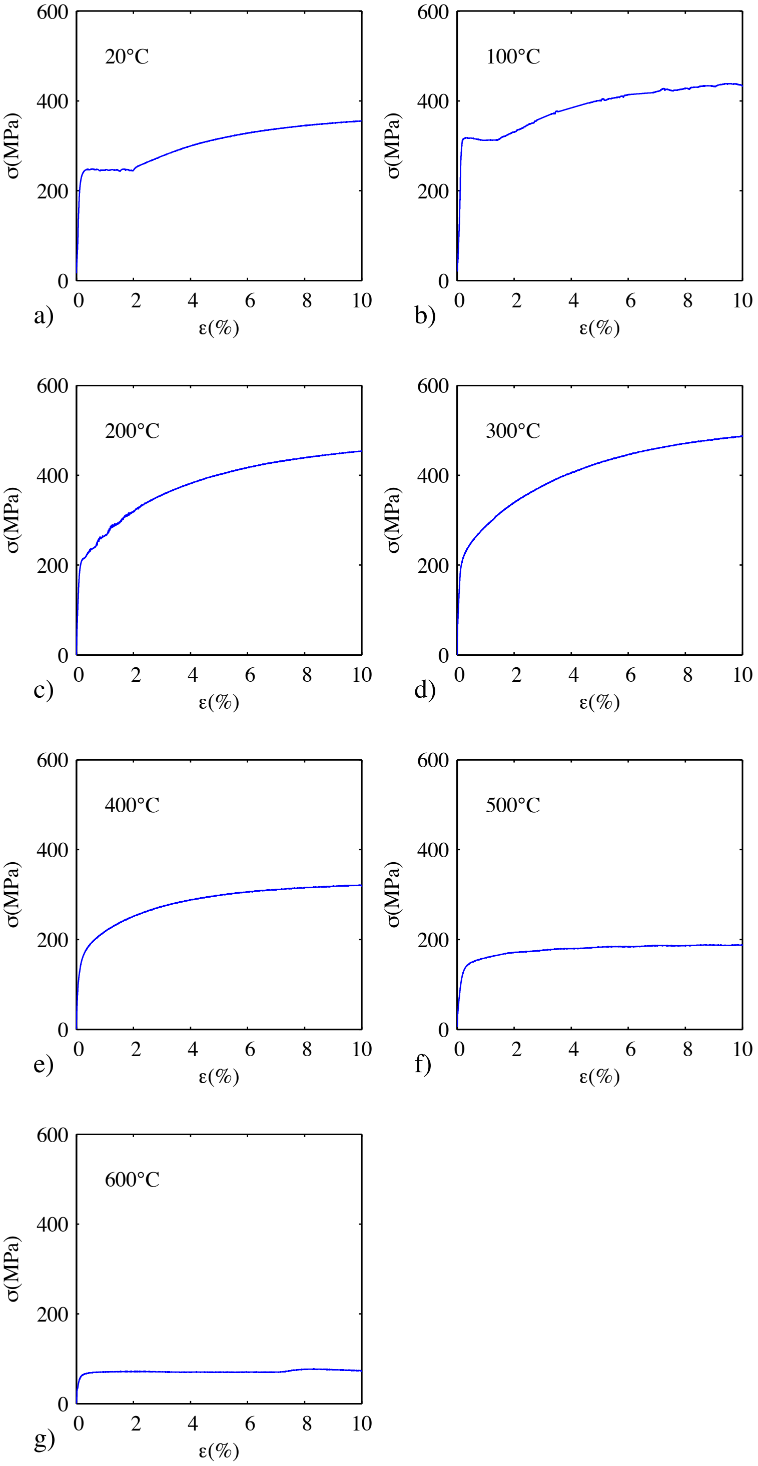

Figure A-1: Stress-strain curves for ASTM A653 with nominal yield stress of 230 MPa [33 ksi] and thickness equal to 1.44 mm [0.0566 in.]

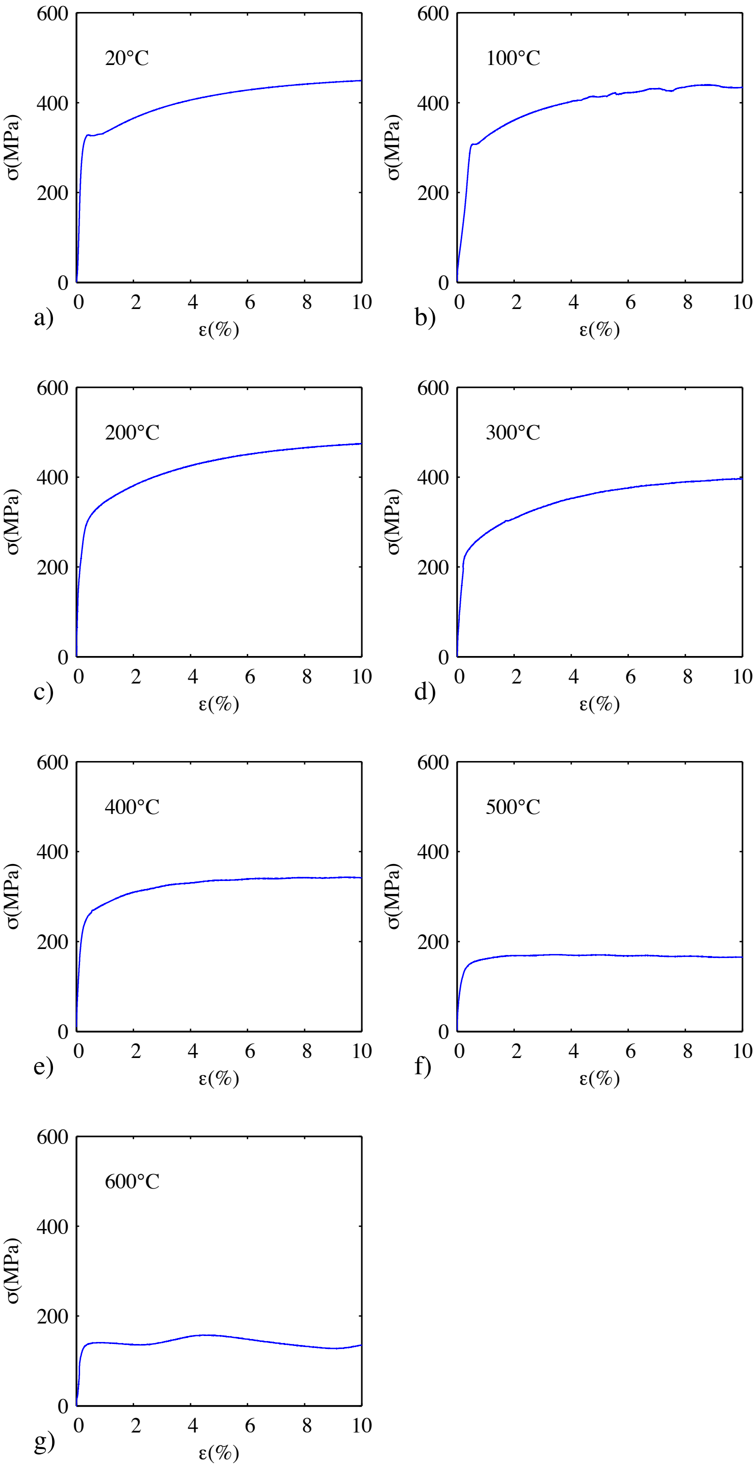

Figure A-2: Stress-strain curves for ASTM A653 with nominal yield stress of 345 MPa [50 ksi] and thickness equal to 2.58 mm [0.1017 in.]

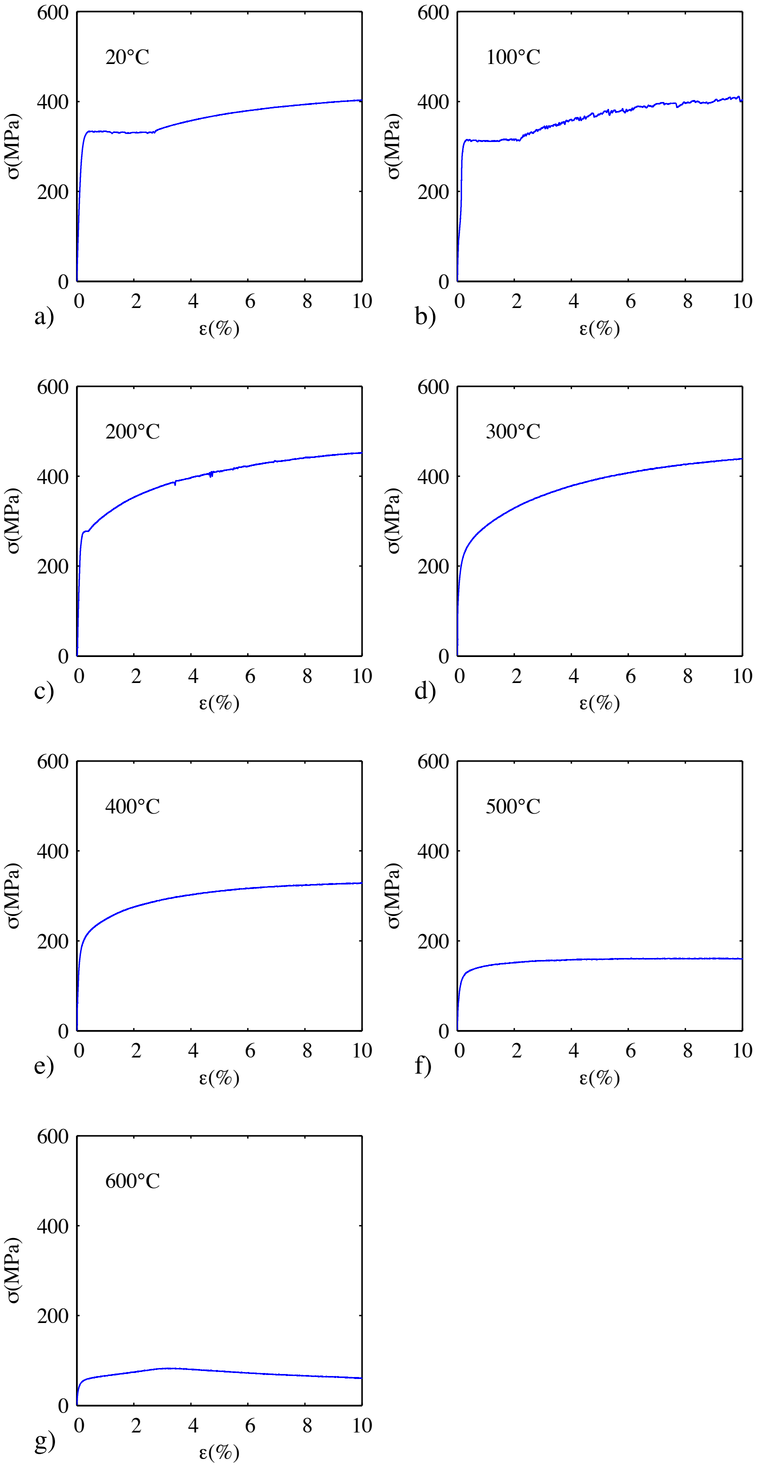

Figure A-3: Stress-strain curves for ASTM A653 with nominal yield stress of 345 MPa [50 ksi] and thickness equal to 1.15 mm [0.0451 in.]

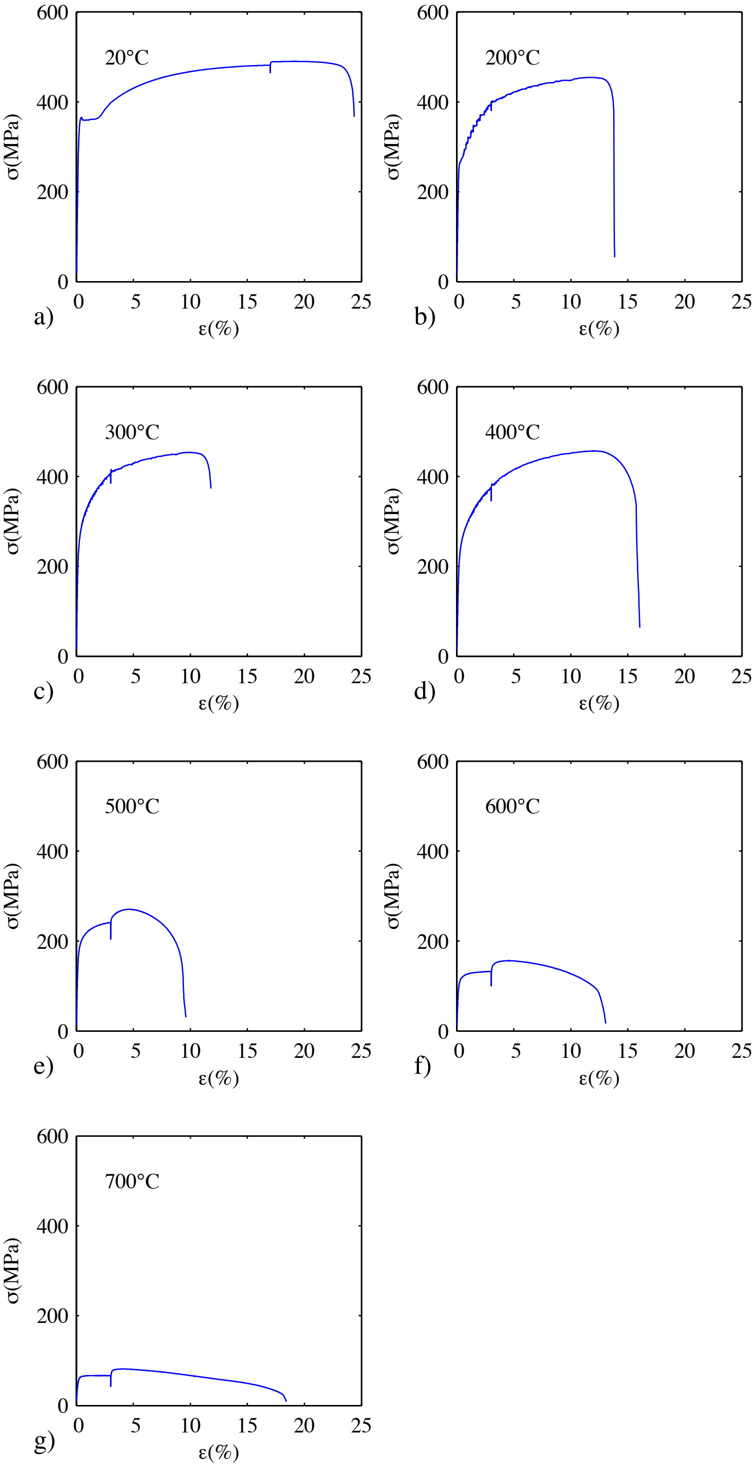

Figure A-4: Stress-strain curves for NBR 7008 ZAR-345 with nominal yield stress of 345 MPa [50 ksi] and thickness equal to 1.55 mm [0.0610 in.]. The discontinuity observed at 3% strain is due to extensometer gage length limit. After 3%, strains were computed based on MTS crosshead displacement.

Appendix B: Load-displacement curves of CFS studs at elevated temperatures

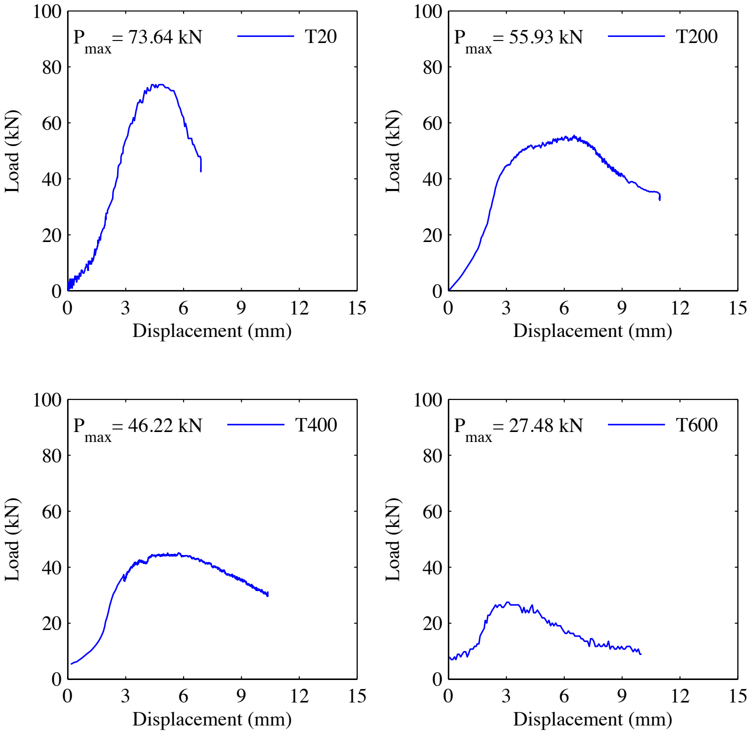

Figure B-1: Compressive load versus displacement of 0.60 m long BARE-BARE studs

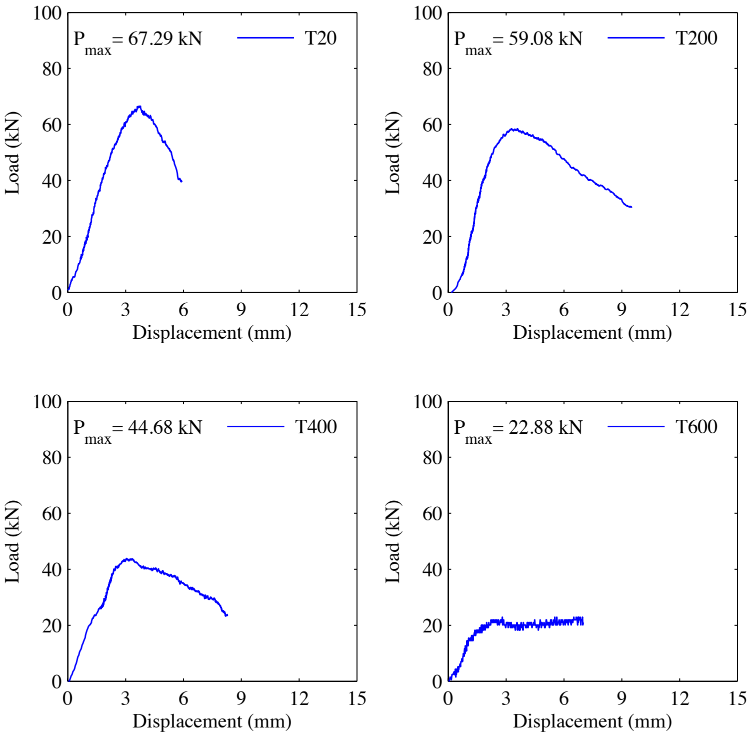

Figure B-2: Compressive load versus displacement of 1.00 m long BARE-BARE studs

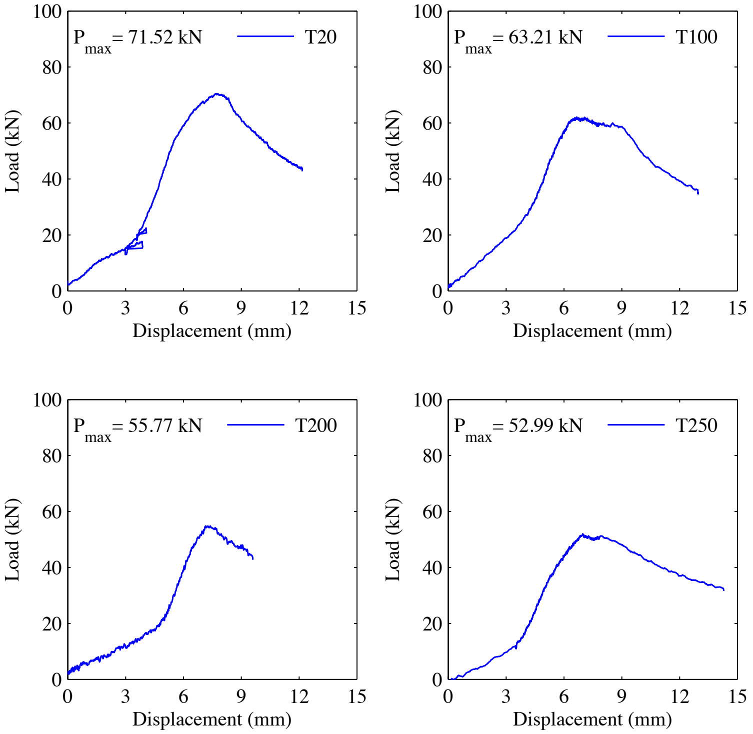

Figure B-3: Compressive load versus displacement of 0.60 m long OB-OSB studs

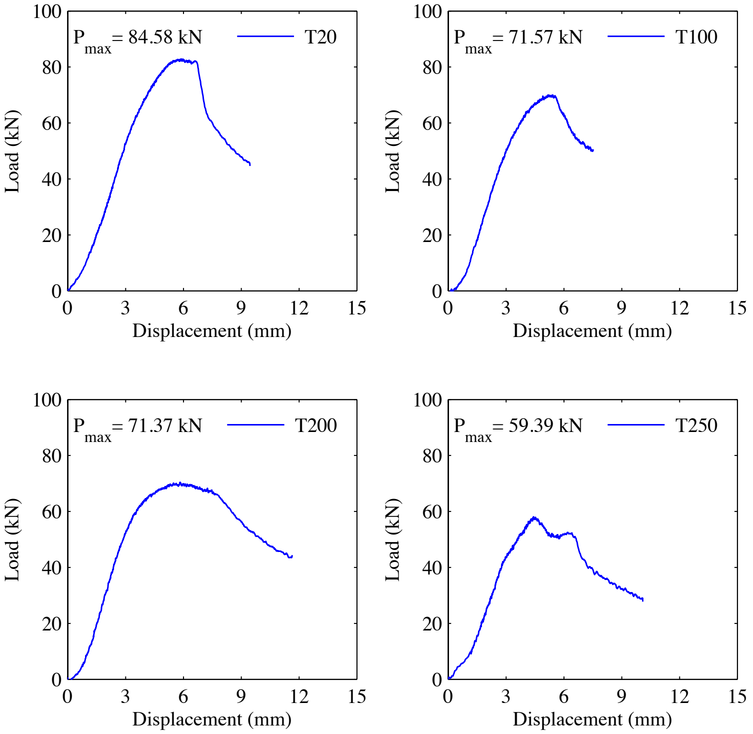

Figure B-4: Compressive load versus displacement of 1.00 m long OSB-OSB studs

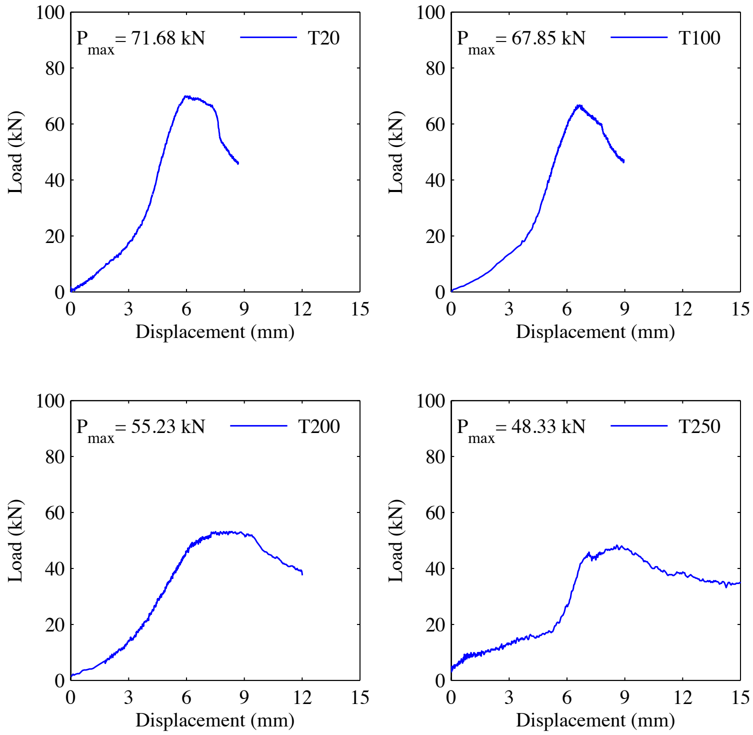

Figure B-5: Compressive load versus displacement of 0.60 m long GYP-OSB studs

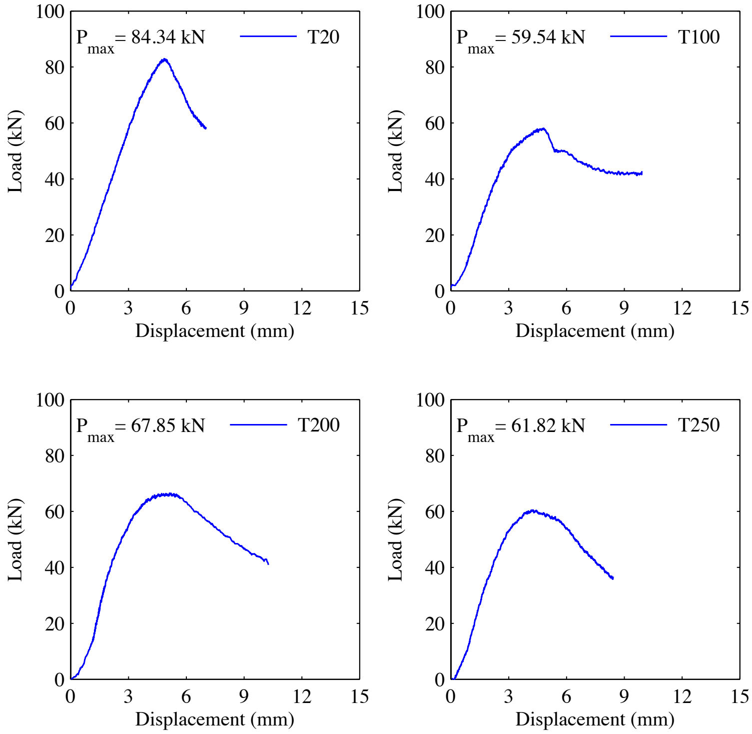

Figure B-6: Compressive load versus displacement of 1.00 m long GYP-OSB studs

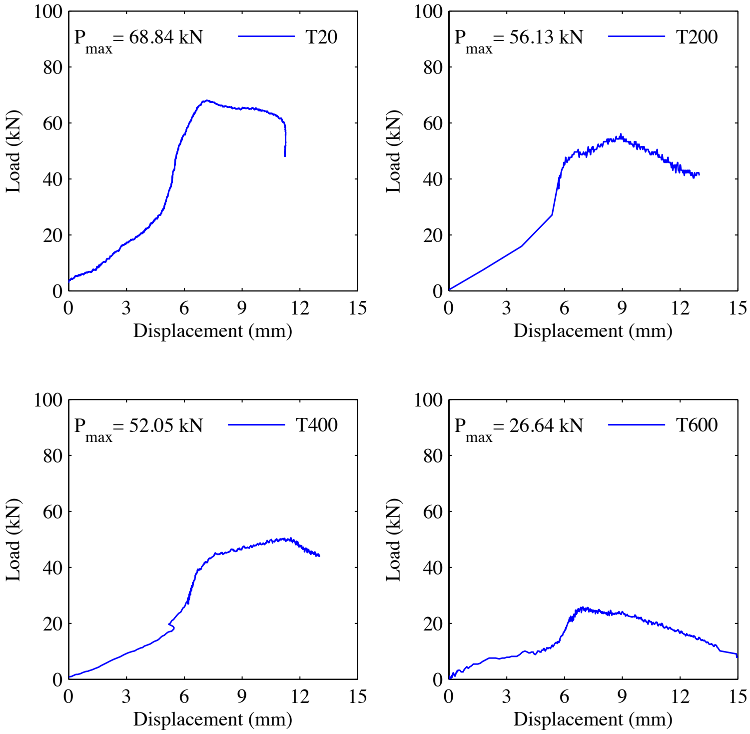

Figure B-7: Compressive load versus displacement of 0.60 m long GYP-GYP studs

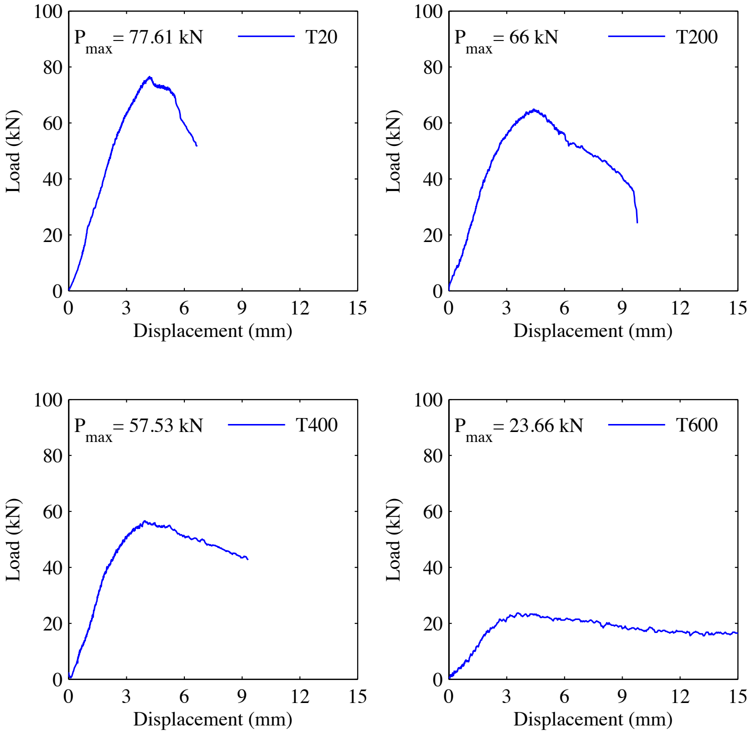

Figure B-8: Compressive load versus displacement of 1.00 m long GYP-GYP studs

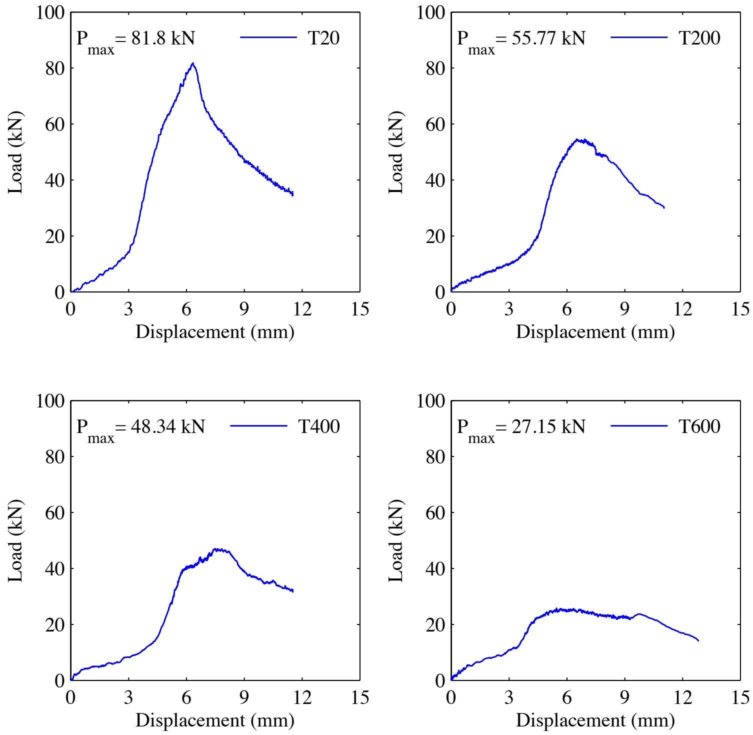

Figure B-9: Compressive load versus displacement of 0.60 m long FRG-FRG studs

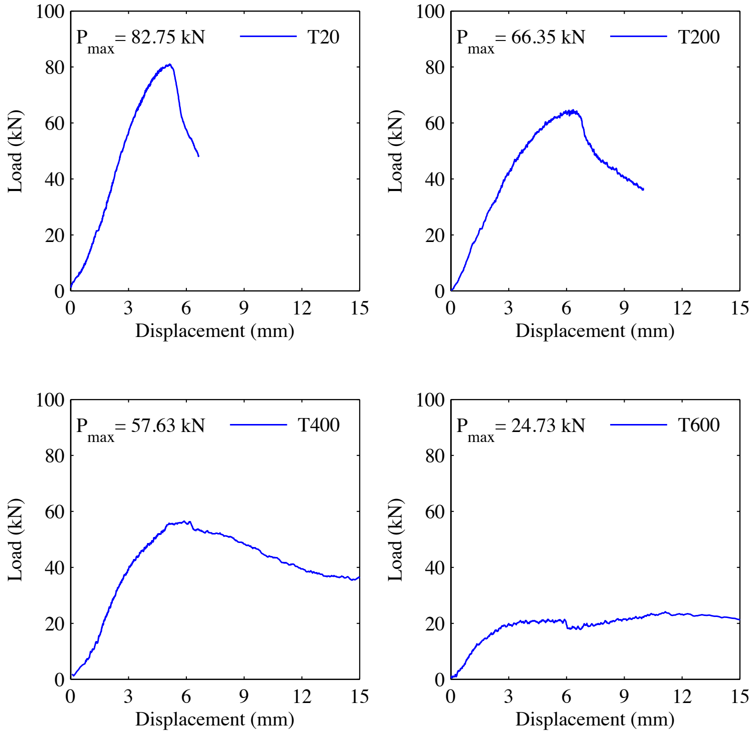

Figure B-10: Compressive load versus displacement of 1.00 m long FRG-FRG studs

Appendix C: In-plane lateral stiffness tests at elevated temperatures

Table C-1: Ambient conditions of in-plane lateral stiffness test specimens

Sheathing	Test	T_{amb} (°C)	Moisture (%)
Gypsum	CT20G1	20.0	11.0
	CT20G2	19.0	11.0
	CT100G1	19.5	10.0
	CT100G2	20.0	11.5
	CT100G3	21.0	10.5
	CT100G4	20.0	12.0
	CT100G5	18.7	11.5
	CT100G6	20.0	11.5
	CT200G1	19.8	16.5
	CT200G2	21.6	14.5
	CT300G1	19.0	15.5
	CT300G2	20.0	13.0
Fire-rated gypsum	CT20Y1	21.9	10.5
	CT100Y1	21.4	7.5
	CT300Y1	21.5	10.5
	CT400Y1	18.0	9.5
Oriented strand board	CT20O1	20.6	2.0
	CT20O2	21.1	2.0
	CT100O1	22.2	2.0
	CT100O2	22.1	2.0
	CT200O1	21.0	2.0
	CT200O2	21.8	2.0
	CT250O1	19.0	2.5
	CT250O2	20.5	2.5
	CT350O1	21.3	2.5
	CT350O2	20.0	2.5

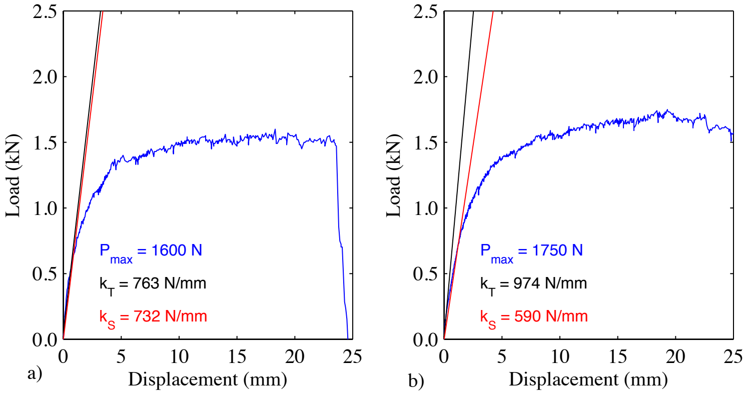

Figure C-1: Tensile load versus displacement of in-plane lateral stiffness tests of gypsum specimens a) CT20G1 and b) CT20G2 at 20 °C

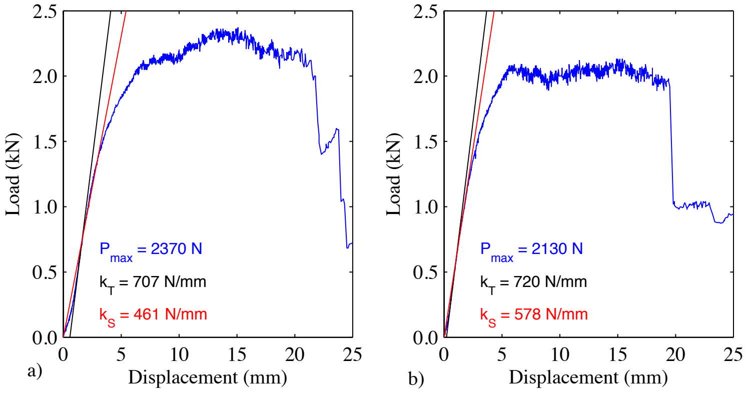

Figure C-2: Tensile load versus displacement of in-plane lateral stiffness tests of gypsum specimens a) CT100G1 and b) CT100G2, tested after 10 minutes at 100 °C

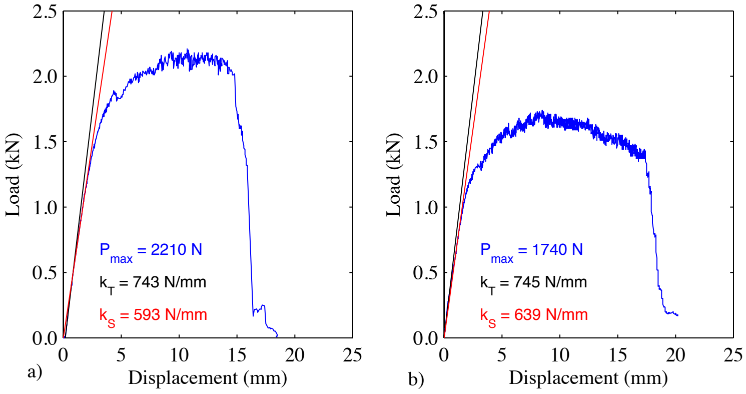

Figure C-3: Tensile load versus displacement of in-plane lateral stiffness tests of gypsum specimens a) CT100G3 and b) CT100G4, tested after 20 minutes at 100 °C

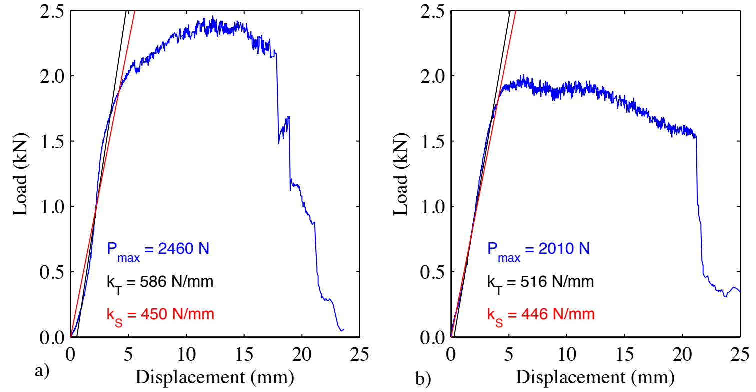

Figure C-4: Tensile load versus displacement of in-plane lateral stiffness tests of gypsum specimens a) CT100G5 and b) CT100G6, tested after 30 minutes at 100 °C and 40 minutes at 100 °C, respectively

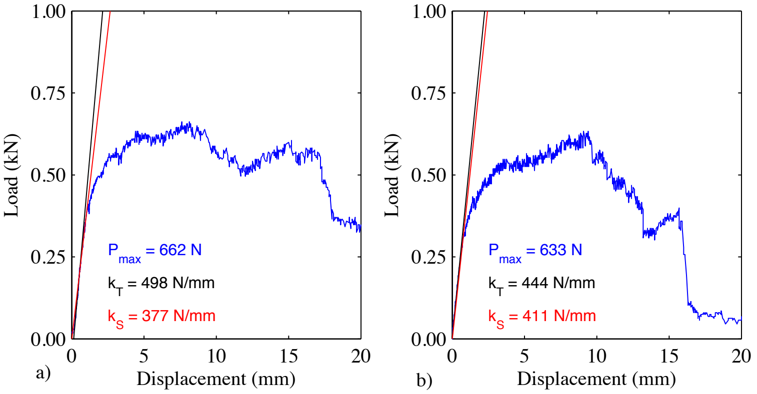

Figure C-5: Tensile load versus displacement of in-plane lateral stiffness tests of gypsum specimens a) CT200G1 and b) CT200G2, tested after 20 minutes at 200 °C

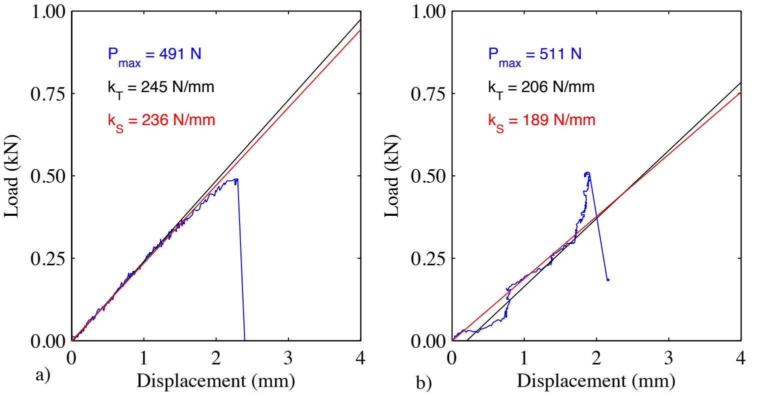

Figure C-6: Tensile load versus displacement of in-plane lateral stiffness tests of gypsum specimens a) CT300G1 and b) CT300G2, tested after 20 minutes at 300 °C

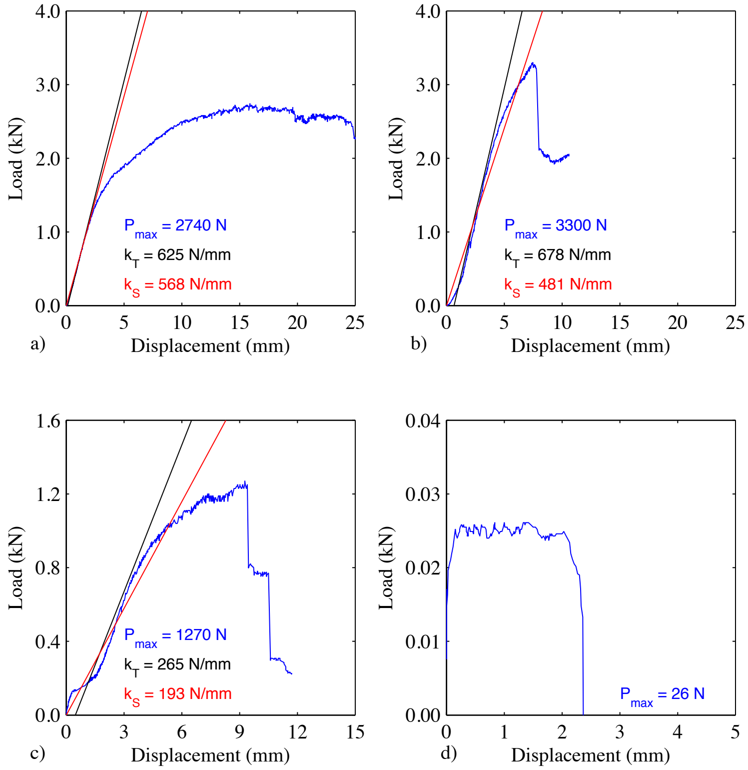

Figure C-7: Tensile load versus displacement of in-plane lateral stiffness tests of fire-rated gypsum specimens a) CT20Y1 and b) CT100Y1, b) CT300Y1 and b) CT400Y1, tested at 20 °C, and after 20 minutes at 100 °C, 300 °C, and 400 °C, respectively

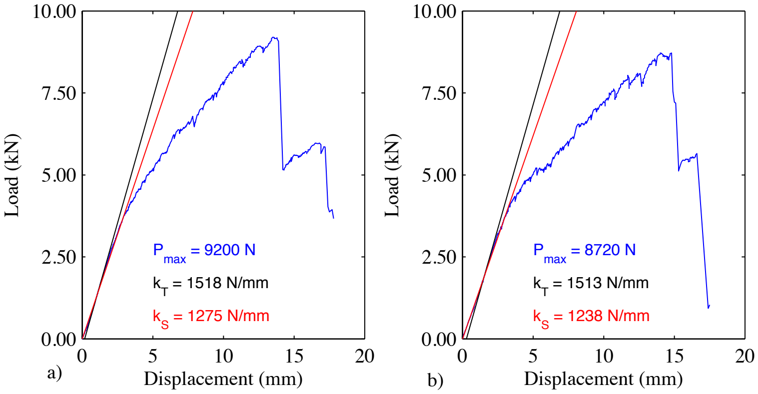

Figure C-8: Tensile load versus displacement of in-plane lateral stiffness tests of oriented strand board specimens a) CT20O1 and b) CT20O2 at 20 °C

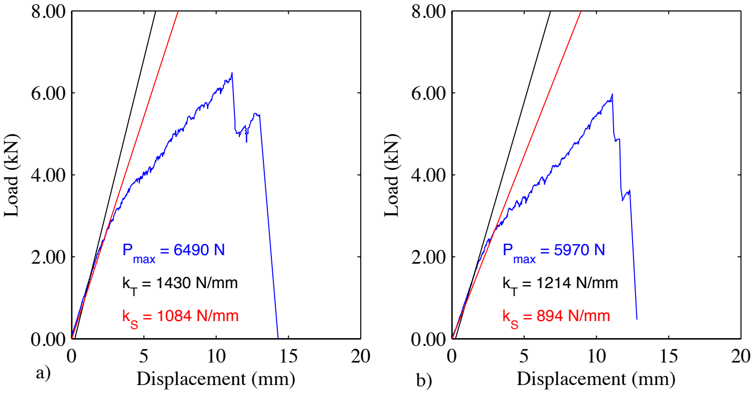

Figure C-9: Tensile load versus displacement of in-plane lateral stiffness tests of oriented strand board specimens a) CT100O1 and b) CT100O2, tested after 20 minutes at 100 °C

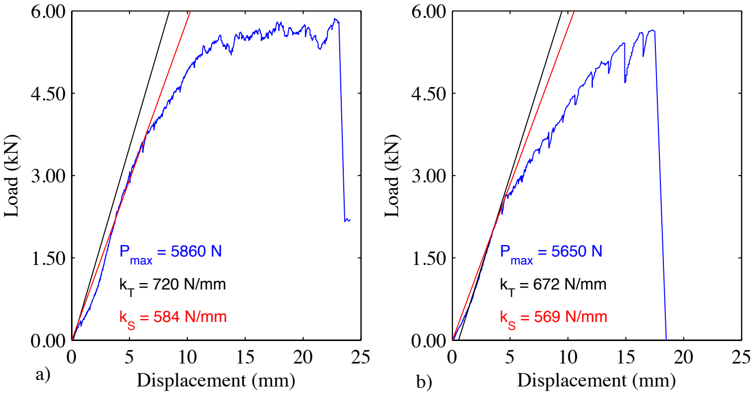

Figure C-10: Tensile load versus displacement of in-plane lateral stiffness tests of oriented strand board specimens a) CT200O1 and b) CT200O2, tested after 20 minutes at 200 °C

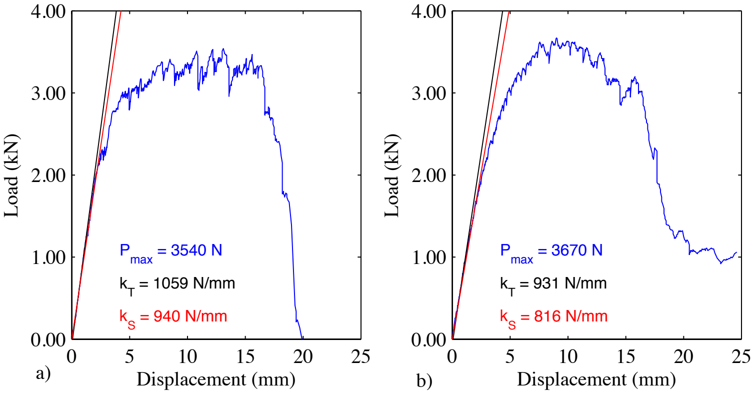

Figure C-11: Tensile load versus displacement of in-plane lateral stiffness tests of oriented strand board specimens a) CT250O1 and b) CT250O2, tested after 20 minutes at 250 °C

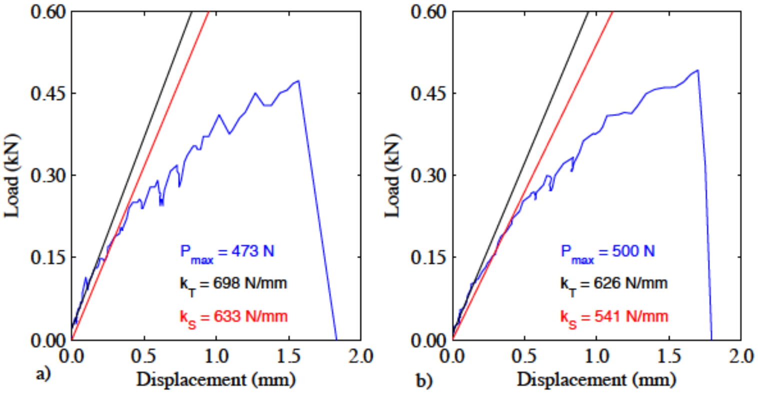

Figure C-12: Tensile load versus displacement of in-plane lateral stiffness tests of oriented strand board specimens a) CT350O1 and b) CT350O2, tested after 20 minutes at 350 °C

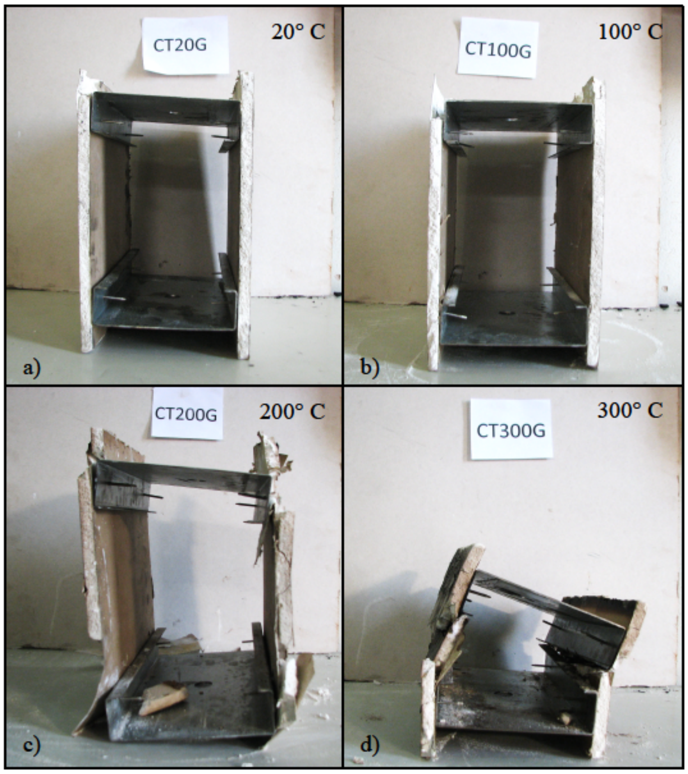

Figure C-13: Gypsum specimens after in-plane lateral stiffness test at a) 20 °C, b) 100 °C, c) 200 °C, and d) 300 °C

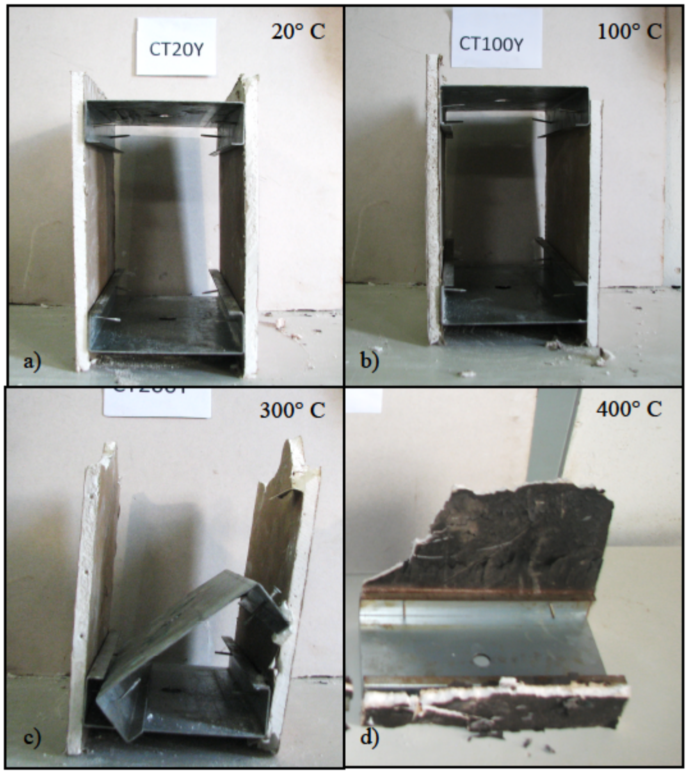

Figure C-14: Fire-rated gypsum specimens after in-plane lateral stiffness test at a) 20 °C, b) 100 °C, c) 300 °C, and d) 400 °C

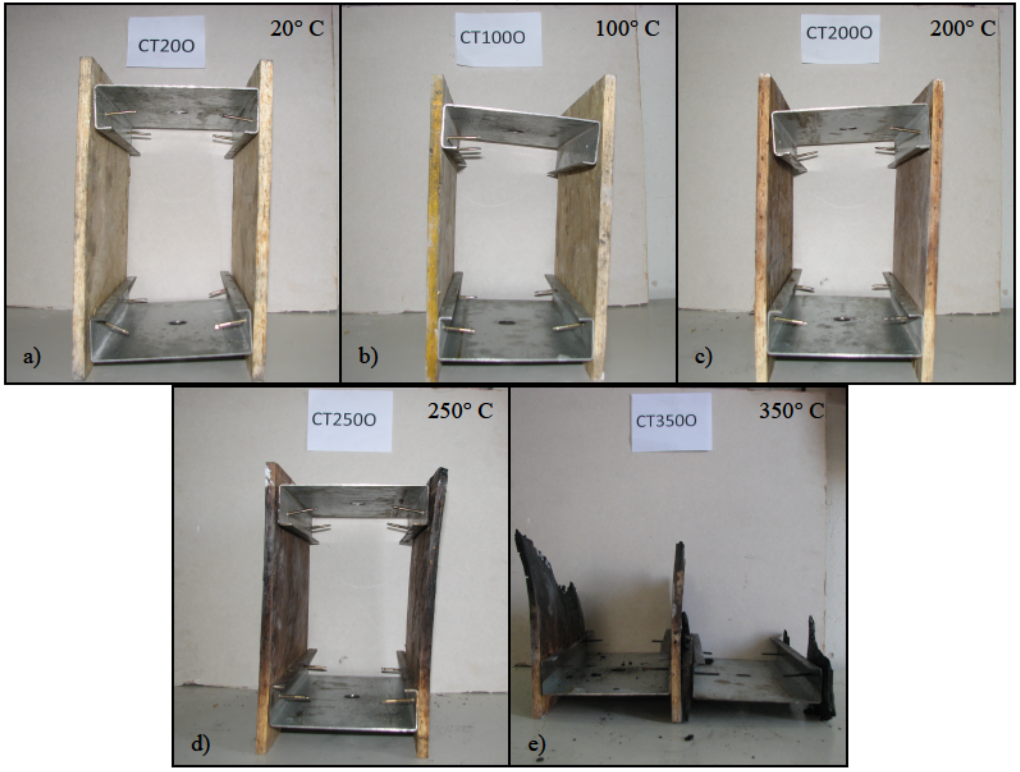

Figure C-15: OSB specimens after in-plane lateral stiffness test at a) 20 °C, b) 100 °C, c) 200 °C, d) 250 °C, and e) 350 °C

Appendix D: Fastener pull-through stiffness tests at elevated temperatures

Table D-1: Ambient conditions of pull-through fastener stiffness test specimens

Sheathing	Test	T_{amb} (°C)	Moisture (%)
Gypsum	FT20G1	20.9	11.5
	FT20G2	20.8	12.5
	FT100G1	25.4	12.0
	FT100G2	25.8	10.5
	FT100G3	21.0	11.0
	FT100G4	20.0	10.5
	FT100G5	18.0	11.0
	FT100G6	18.0	11.5
	FT200G1	21.9	10.5
	FT200G2	21.7	10.5
	FT300G1	25.6	11.0
	FT300G2	23.5	11.0
Fire-rated gypsum	FT20Y1	20.9	11.5
	FT20Y2	21.3	12.5
	FT100Y1	26.7	11.5
	FT100Y2	26.8	11.5
	FT200Y1	23.0	10.5
	FT200Y2	22.2	10.5
	FT300Y1	21.8	11.0
	FT300Y2	22.3	11.0
Oriented strand board	FT20O1	20.0	2.5
	FT20O2	21.5	2.5
	FT100O1	21.3	2.0
	FT100O2	23.0	2.0
	FT200O1	20.2	2.5
	FT200O2	20.7	2.5
	FT300O1	22.9	2.0
	FT300O2	22.3	2.0

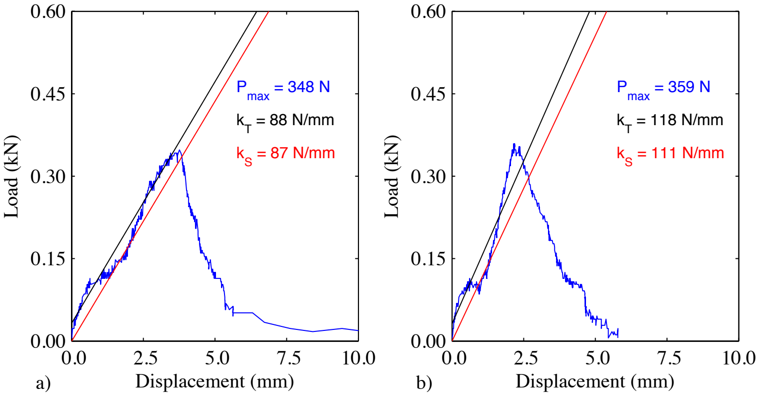

a) b)

Figure D-1: Tensile load versus displacement of fastener pull-through stiffness tests of gypsum specimens a) FT20G1 and b) FT20G2 at 20 °C

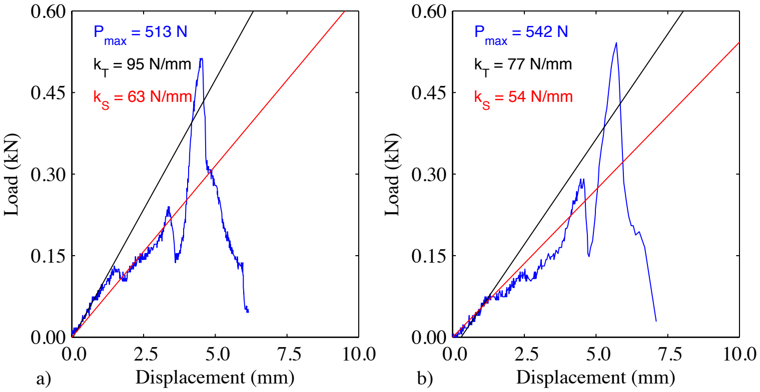

a) b)

Figure D-2: Tensile load versus displacement of fastener pull-through stiffness tests of gypsum specimens a) FT100G1 and b) FT20G2, tested after 10 minutes at 100 °C

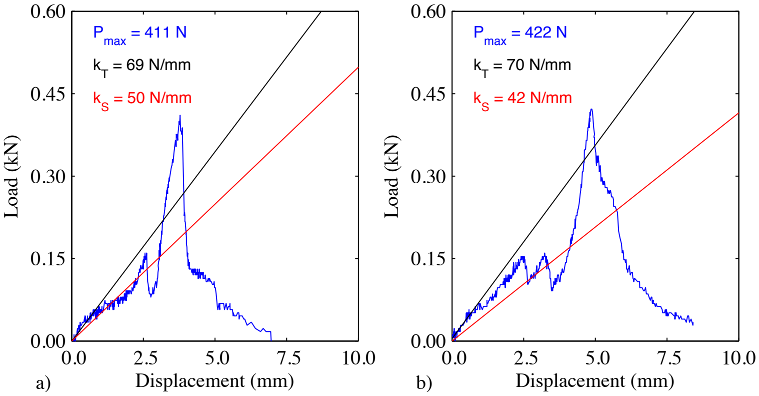

a) b)

Figure D-3: Tensile load versus displacement of fastener pull-through stiffness tests of gypsum specimens a) FT100G3 and b) FT100G4, tested after 20 minutes at 100 °C

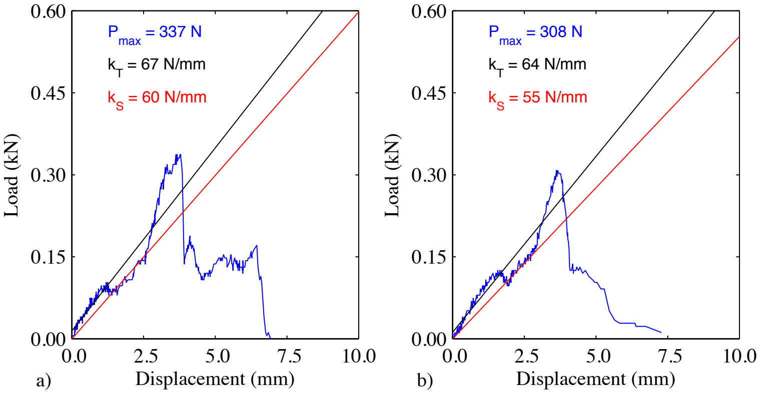

Figure D-4: Tensile load versus displacement of fastener pull-through stiffness tests of gypsum specimens a) FT100G5 and b) FT20G6, tested at 100 °C after 30 and 40 minutes, respectively

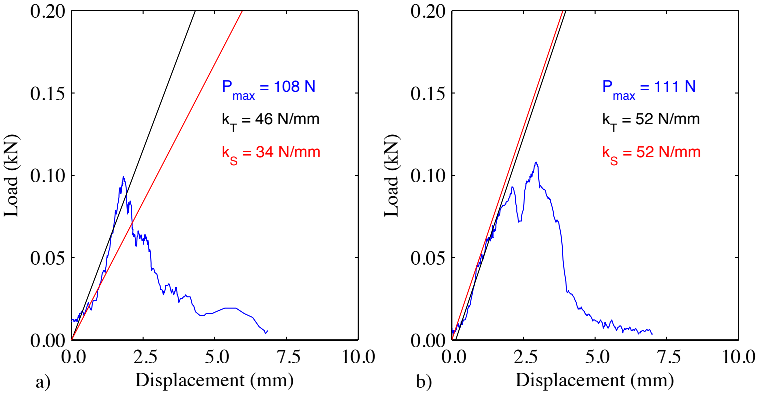

Figure D-5: Tensile load versus displacement of fastener pull-through stiffness tests of gypsum specimens a) FT200G1 and b) FT200G2, tested after 20 minutes at 200 °C

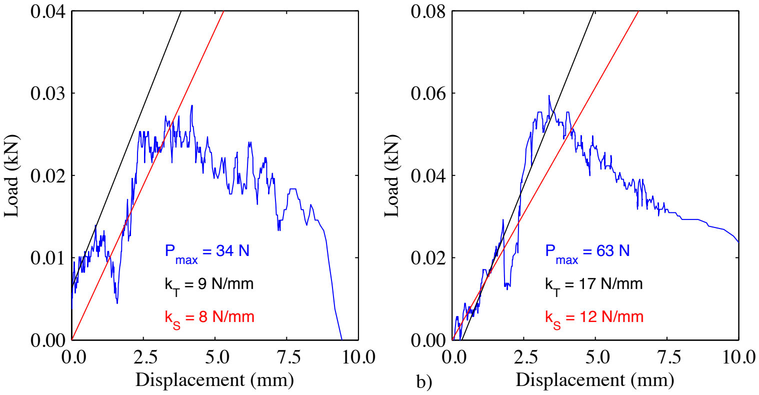

Figure D-6: Tensile load versus displacement of fastener pull-through stiffness tests of gypsum specimens a) FT300G1 and b) FT300G2, tested after 20 minutes at 300 °C

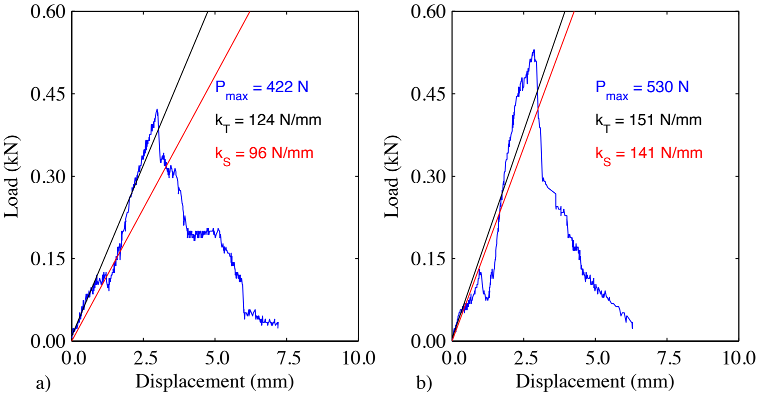

Figure D-7: Tensile load versus displacement of fastener pull-through stiffness tests of fire rated gypsum specimens a) FT20Y1 and b) FT20Y2 at 20 °C

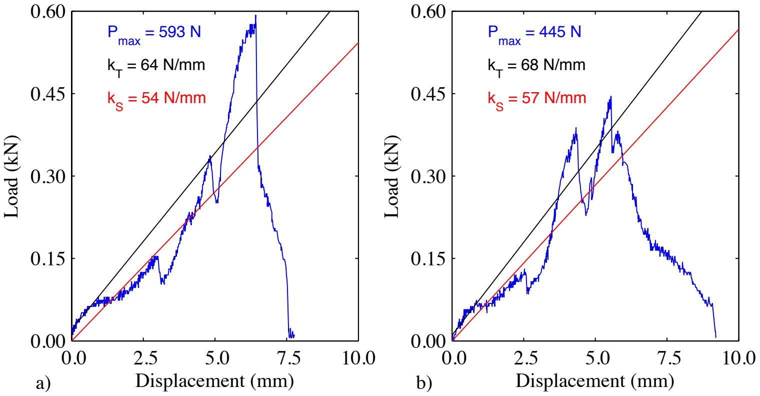

Figure D-8: Tensile load versus displacement of fastener pull-through stiffness tests of fire rated gypsum specimens a) FT100Y1 and b) FT100Y2 at 100 °C

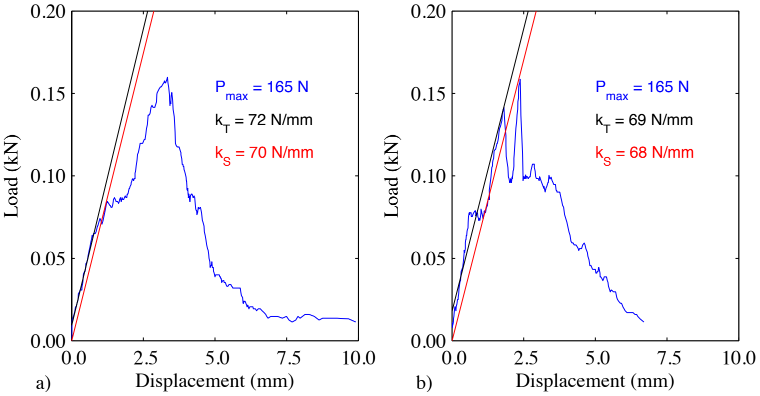

Figure D-9: Tensile load versus displacement of fastener pull-through stiffness tests of fire rated gypsum specimens a) FT200Y1 and b) FT200Y2 at 200 °C

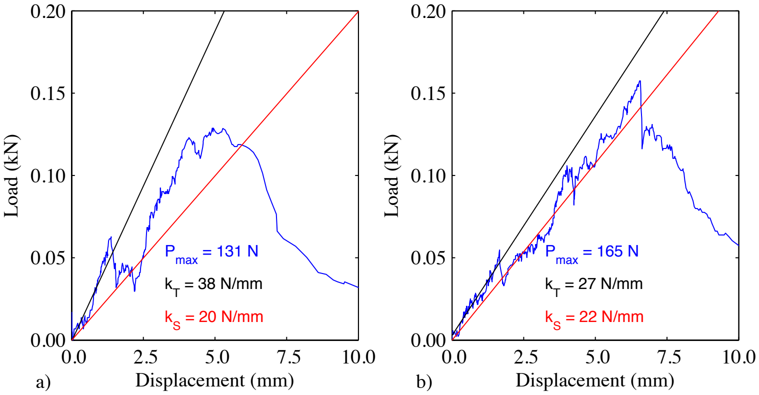

a) b)

Figure D-10: Tensile load versus displacement of fastener pull-through stiffness tests of fire rated gypsum specimens a) FT300Y1 and b) FT300Y2 at 300 °C

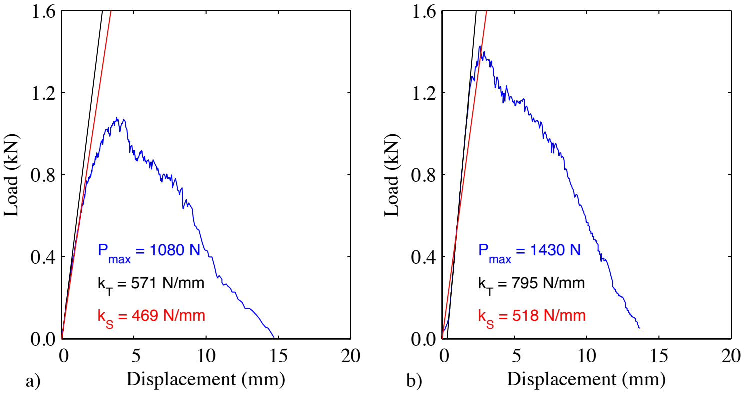

a) b)

Figure D-11: Tensile load versus displacement of fastener pull-through stiffness tests of oriented strand board specimens a) FT20O1 and b) FT20O2 at 20 °C

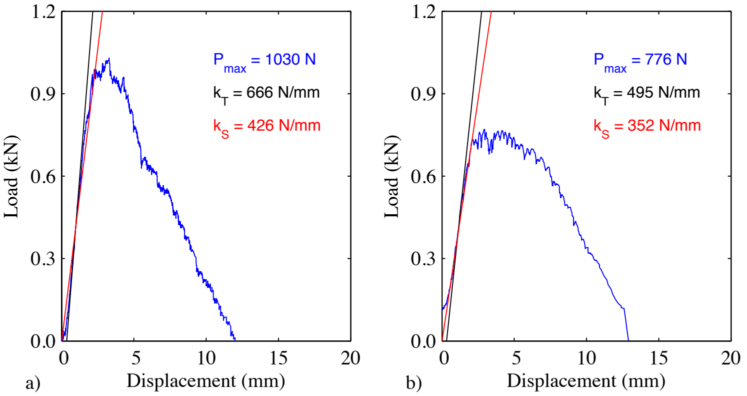

a) b)

Figure D-12: Tensile load versus displacement of fastener pull-through stiffness tests of oriented strand board specimens a) FT100O1 and b) FT100O2, tested after 20 minutes at 100 °C

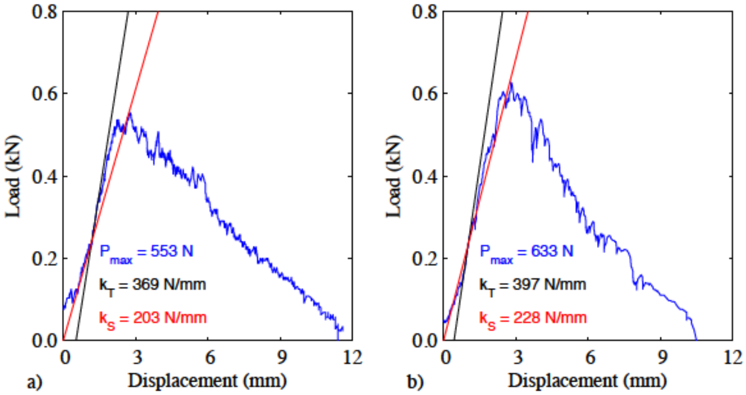

Figure D-13: Tensile load versus displacement of fastener pull-through stiffness tests of oriented strand board specimens a) FT200O1 and b) FT200O2, tested after 20 minutes at 200 °C

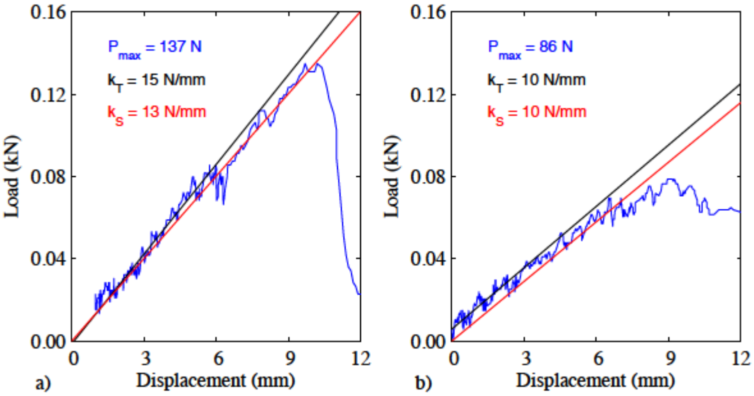

Figure D-14: Tensile load versus displacement of fastener pull-through stiffness tests of oriented strand board specimens a) FT300O1 and b) FT300O2, tested after 20 minutes at 300 °C

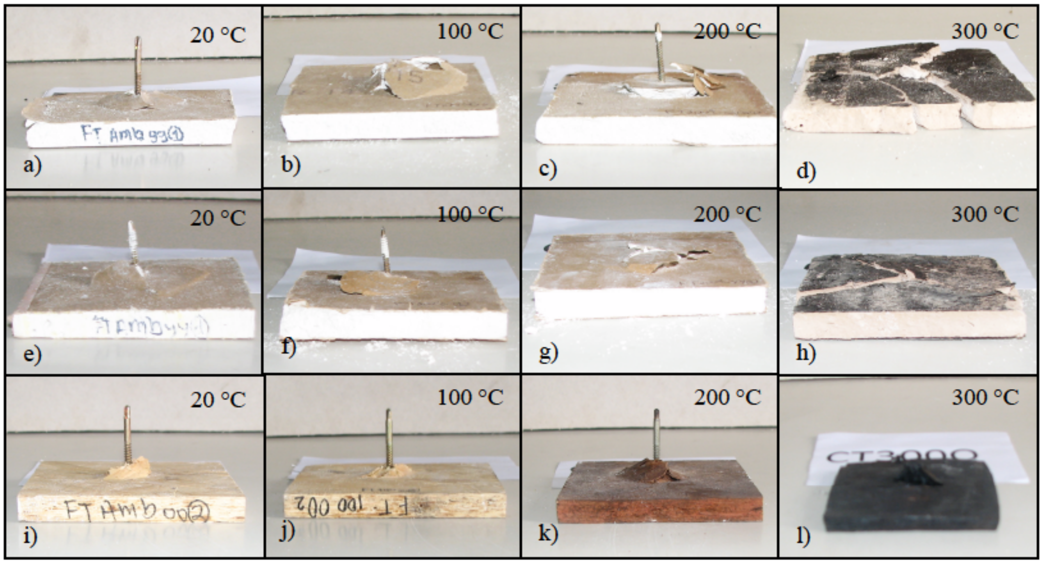

Figure D-15: Specimens after pull-through fastener stiffness test, a-d) gypsum board, e-h) fire-rated gypsum, and i-l) OSB

Appendix E: Squash and elastic buckling loads at elevated temperatures

Table E-1: Squash and elastic buckling loads at elevated temperatures

Sheathing	T (°C)	P_y (kN)	$P_{cr\,l}$ (kN)	$P_{cr\,d}$ (kN)	$P_{cr\,e}$ (kN) L=0.6m	$P_{cr\,e}$ (kN) L=1.0 m
Gypsum (both sides)	20	144.29	43.33	63.67	544.55	505.60
	100	136.79	40.73	59.85	510.54	471.53
	200	127.41	37.48	55.11	437.65	344.34
	300	118.03	34.23	50.12	371.99	237.31
	600	43.14	15.64	22.74	151.79	57.78
	700	18.18	9.45	13.73	91.66	34.89
Fire-rate gypsum (both sides)	20	144.29	43.33	63.46	526.98	456.65
	100	136.79	40.73	59.72	485.21	400.98
	300	118.03	34.23	49.96	368.37	227.23
	600	43.14	15.64	22.74	151.79	57.78
	700	18.18	9.45	13.73	91.66	34.89
OSB (both sides)	20	144.29	43.33	64.26	656.23	1331.66
	100	136.79	40.73	60.22	580.86	1088.27
	200	127.41	37.48	55.15	471.77	716.51
	250	122.72	36.27	53.49	514.05	965.26
	350	105.55	31.13	45.87	412.24	687.66
	600	43.14	15.64	22.74	151.79	57.78
	700	18.18	9.45	13.73	91.66	34.89
Gypsum-OSB	20	144.29	43.33	64.05	569.31	543.84
	100	136.79	40.73	60.15	530.15	504.45
	200	127.41	37.48	55.09	449.46	365.38
	250	122.72	35.85	52.75	423.27	313.48
	600	43.14	15.64	22.74	151.79	57.78
	700	18.18	9.45	13.73	91.66	34.89

Appendix F: Draft specification rules for the analysis and DSM design of CFS for fire

The following equations are proposed for the analysis and design of CFS at elevated temperatures, based on the experimental results and numerical analysis discussed in this dissertation.

After the fire hazard is defined and the temperature distribution on structural and nonstructural components is estimated, the capacity of CFS members can be determined as follows.

F.1 Temperature-dependent mechanical properties of CFS

Calculate the elastic modulus "E(T)", shear modulus "G(T)", and yield stress "$F_y(T)$" of the elements (or strips if Finite Strip Method is used) in the cross-section at elevated temperatures. If elements (or strips) in the cross-section experience different temperatures, mechanical properties (i.e. elastic modulus, shear modulus and yield stress) will be calculated for each element. Poisson's ratio (ν) of 0.3 may be assumed.

Elastic modulus of CFS at elevated temperatures:

$$20^\circ C \le T \le 300^\circ C \rightarrow \frac{E(T)}{E(T_{amb})} = 1.015 - 0.00075T \qquad \text{(Equation F-1-1)}$$

$$300^\circ C \le T \le 700^\circ C \rightarrow \frac{E(T)}{E(T_{amb})} = 1.219 - 0.00143T \qquad \text{(Equation F-1-2)}$$

Shear modulus of CFS at elevated temperatures:

$$G(T) = \frac{E(T)}{2(1+\nu)} \qquad \text{(Equation F-1-3)}$$

Yield stress of CFS at elevated temperatures:

$$20°C \le T \le 300°C \rightarrow \frac{F_y(T)}{F_y(T_{amb})} = 1.013 - 0.00065T \qquad \text{(Equation F-1-4)}$$

$$300°C \le T \le 700°C \rightarrow \frac{F_y(T)}{F_y(T_{amb})} = 1.337 - 0.00173T \qquad \text{(Equation F-1-5)}$$

F.2 Stiffness of fastener-sheathing systems

When designing sheathed CFS members, the effect of sheathing bracing could be included in the analysis by following the method proposed by Schafer (2013) and using the retention factors proposed herein to account for degradation of the connection at elevated temperatures. Local lateral stiffness "k_{xl}" and rotational stiffness "k_ϕ" should be calculated through the method proposed by Schafer (2013) and then reduced according to the temperature of the connection. Use the following equations to obtain the temperature-dependent retention factors for the local lateral stiffness "$k_{xl}(T)$" and rotational stiffness "$k_\phi(T)$".

For gypsum boards:

$$\frac{k_{xl}(T)}{k_{xl}(T_{amb})} = \begin{cases} 1.048 - 0.0024T & \text{if } 20°C \le T \le 300°C \\ 0.660 - 0.0011T & \text{if } 300°C < T \le 600°C \\ 0 & \text{if } T > 600°C \end{cases} \qquad \text{(Equation F-1-6)}$$

$$\frac{k_{\phi}(T)}{k_{\phi}(T_{amb})}=\begin{cases}1.064-0.0032T & if\ 20°C \le T \le 300°C\\ 0.194-0.0003T & if\ 300°C < T \le 600°C\\ 0 & if\ T > 600°C\end{cases} \qquad \text{(Equation F-1-7)}$$

For fire-rated gypsum boards:

$$\frac{k_{xl}(T)}{k_{xl}(T_{amb})}=\begin{cases}1.048-0.0024T & if\ 20°C \le T \le 300°C\\ 0.660-0.0011T & if\ 300°C < T \le 600°C\\ 0 & if\ T > 600°C\end{cases} \qquad \text{(Equation F-1-8)}$$

$$\frac{k_{\phi}(T)}{k_{\phi}(T_{amb})}=\begin{cases}1.056-0.0028T & if\ 20°C \le T \le 300°C\\ 0.426-0.0007T & if\ 300°C < T \le 600°C\\ 0 & if\ T > 600°C\end{cases} \qquad \text{(Equation F-1-9)}$$

For OSB:

$$\frac{k_{xl}(T)}{k_{xl}(T_{amb})}=\begin{cases}1.032-0.0016T & if\ 20°C \le T \le 350°C\\ 1.102-0.0018T & if\ 350°C < T \le 600°C\\ 0 & if\ T > 600°C\end{cases} \qquad \text{(Equation F-1-10)}$$

$$\frac{k_{\phi}(T)}{k_{\phi}(T_{amb})}=\begin{cases}1.068-0.0034T & if\ 20°C \le T \le 300°C\\ 0.078-0.0001T & if\ 300°C < T \le 600°C\\ 0 & if\ T > 600°C\end{cases} \qquad \text{(Equation F-1-11)}$$

F.3 Elastic stability of CFS members

Elastic buckling loads including local, distortional and global buckling loads need to be calculated based on temperature dependent-mechanical properties, the stiffness provided by fastener-sheathing systems (if needed), the geometry of the CFS member and the applied load. Finite strip analysis (recommended), finite element analysis or closed-form solutions might be used.

F-4. CFS member limit states

Current Direct Strength Method equations (AISI-S100 Appendix 1) should be used to estimate the strength of CFS members at elevated temperatures based on the elastic buckling loads determined in Section F.3, and the temperature-dependent squash load "$P_y(T)$" determined as follows. CFS members subjected to uniform elevated temperatures will have uniform yield stress "$F_y(T)$"; whereas CFS members subjected to thermal gradients will have temperature-dependent yield stresses varying in the cross-section. The minimum yield stress in the cross-section "$\min(F_y(T))$" and the gross cross-sectional area "A_g" should be used to compute the squash load.

$$P_y\left(T\right) = \min(F_y(T))A_g \qquad \text{(Equation F-1-12)}$$

References

American Iron and Steel Institute, AISI Standard, AISI S100-2012. North American Specification for the Design of Cold-formed Steel Structural Members. Appendix 1.

Schafer, B. W. (2013). Final Report: Sheathing Braced Design of Wall Studs. Washington, D.C., Johns Hopkins University, prepared for the American Iron and Steel Institute.

Curriculum Vitae

Jean Carlos Batista Abreu was born in Santiago, Dominican Republic, on April 4th, 1986. He attended the Pontificia Universidad Católica Madre y Maestra (PUCMM) in Santiago, Dominican Republic, graduating in 2008 with a Bachelor's Degree in Civil Engineering. After working in the construction industry as a Structural Engineer, he moved to Puerto Rico to pursue a graduate degree in structural engineering. In 2011, he received a M.Sc. degree from the University of Puerto Rico at Mayagüez (UPRM), after studying the impact of fire on the strength and stability of oil storage tanks. Then, Jean joined Johns Hopkins University (JHU) in 2011. Working in the Thin-Walled Structures Lab under Dr. Benjamin W. Schafer, Jean studied the fire performance of cold-formed steel wall assemblies. His research included the execution of an experimental program completed at the University of New Haven, in Connecticut, and the University of Campinas, in Brazil. Concurrently, he performed numerical studies to analyze and design cold-formed steel members and systems at elevated temperatures. During his PhD program, Jean was involved in several research projects in collaboration with researchers from the Institute for NanoBioTechnology at JHU, Cairo University and the National Institute of Standards and Technology. Additionally, Jean served as instructor/mentor for the STEM Achievement in Baltimore Elementary Schools, the Baltimore Polytechnic Institute, and the Center for Talented Youth at JHU. His teaching activities also included working as a teaching assistant in the Department of Civil Engineering at JHU and UPRM. In 2015, Jean was hired as a Visiting Assistant Professor in the Department of Civil and Environmental Engineering at Bucknell University, in Pennsylvania.